Brainstem circuits for locomotor and orienting movements : a functional and connectivity study of V2a neurons

Giovanni Usseglio

THÈSE DE DOCTORAT

NNT : 2022UPASL108

Circuits du tronc cérébral pour les mouvements locomoteurs et d'orientation : étude fonctionnelle et connectomique des neurones V2a

Brainstem circuits for locomotor and orienting movements: a functional and connectivity study of V2a neurons

Thèse de doctorat de l'université Paris-Saclay

École doctorale n° 568 : signalisations et réseaux intégratifs en biologie (Biosigne)
Spécialité de doctorat : Science de la vie et de la santé
Graduate School: Life Science and Health. Référent : Faculté de médicine

Thèse préparée dans l'unité de recherche **Institut des Neurosciences Paris-Saclay (Université Paris-Saclay, CNRS)**, sous la direction de **Julien BOUVIER**, directeur de recherche.

Thèse soutenue à Paris-Saclay, le 8 Décembre 2022, par

Giovanni USSEGLIO

Composition du Jury

Daniel SHULZ DR, NeuroPSI, Saclay	Président
Claire WYART DR, Institut du Cerveau, Paris	Rapportrice & Examinatrice
Matilde CORDERO-ERAUSQUIN DR, INCI, Strasbourg	Rapportrice & Examinatrice
Stéphane DIEUDONNE DR, IBENS, Paris	Examinateur
Pierre-Paul VIDAL DR, Université Paris-Descartes	Examinateur
Micaela GALANTE PU, NeuroPSI, Saclay	Examinatrice

To my uncles Mario and David

Shaolin monastery, Henan Province, China. 2004.

Steve McCurry

TABLE OF CONTENT

1. AKNOWLEDGEMENTS

This is the end of my PhD, a long journey and here I will take the opportunity to thank all the people that have been with me throughout my entire PhD.

First, I would like to thank my PhD supervisor Julien Bouvier. I joined his lab four years ago without really knowing what it meant to be a scientist, and he taught me the rigor and the scientific method. He trained me, technically and intellectually, to be a scientist, he dedicated time to my formation as a researcher and if I am here, now, willing to continue this career, it is because of his mentorship and guidance.

I am so grateful also to all the members of the lab. Aurélie, we almost started at the same time four years ago and she helped me a lot, not only with experiments, but also whenever I had problems or doubts, from dealing with French burocracy to finding microwaves. Edwin, with his computational skills allowed me to make order and sense and of all the experiments I performed. Andrea, who joined the lab in the last few months but it seems he is always been here. Séverine and Coralie, now they moved in other labs and other cities, but we shared the lab life for years, when I arrived they were the experts in the lab and they represented a point of reference for me, especially at the beginning. Alexis, for all the experiments we did together and the willpower he put into doing experiments. Indeed, he did not give up even when experiments did not work for several months. I would also like to thank Maria Giovanna, Diego, Alexandra and Emmanuel: colleagues, carpool mates and, most importantly, friends.

I would like to deeply thank Martina, especially for all the support and advices she gave me from the first time we met, without her everything would have been more problematic, I am simply glad of this. Gianguido, we shared the same city for two years during the master and other two years during my PhD, I was lucky to share with him these two experiences. Filippo, a very long friendship, he arrived with the perfect timing to help me to face the pandemic together with his “risotto alla zucca”. Luca, which helped me in the

moment of real need by hosting me for days at his home almost without notice. In addition, Matteo, Ivan and Anna that joined my journey in the last year, but immediately became part of this adventure.

Furthermore, I would like to thank all my family: my mother, my father, my brother, Desirée and the newcomer Pietro Enea that altogether encouraged and supported me over the years and I knew they were always on my side during my journey. I would like to thank also my relatives, cousins, uncles and aunts. I always felt their encouragement, in particular, my beloved uncles Mario and David that constantly showed me total support on the career I choose. I would like to thank also Sabrina that helped me from the very first moment I arrived in Paris, and I immediately knew that I could have always counted on her.

Furthermore, I want to thank all the people I did not mention explicitly here, that now are still in France or abroad, but also all the Italian friends that, with a visit or just a call, Beatrice also with her painting skills, made me feel better when I needed.

Lastly, I would like to thank Dr. Daniel Shulz, Dr. Claire Wyart, Dr. Matilde Cordero-Erausquin, Dr. Micaela Galante, Dr. Stéphane Dieudonné and Dr. Pierre-Paul Vidal to have accepted to be members of the jury and dedicate their time and energy to evaluate my PhD work.

2. INTRODUCTION

1.1 The general neural basis of motor control

The picture I chose to introduce my PhD project shows, in an amazing way, a human performing an extremely complex motor behavior that requires the coordination of multiple motor actions simultaneously. In order to avoid falling down, indeed, the subject must control every muscle of his own body with high precision and timing. Performing such a composite motor behavior requires the involvement of many regions of the nervous system. The motor task executed by the shaolin monk is difficult, and clearly not all the humans are able to perform it, however, to do the motor behaviors that we, and all vertebrates, accomplish every day to survive, represents one of the major functions of our nervous system. Most of the motor behaviors indeed require the execution of multiple motor actions simultaneously, for example hunting, escaping from predators, interacting with other animal, playing music. These motor behaviors are vital for animals and the ability of the brain to execute and modulate multiple motor actions simultaneously to perform such behaviors with the higher probability of success represents a topic of long-standing interest for neuroscientists.

In particular, for me, understanding how the nervous system recruits multiple motor actions in order to perform a complex/composite motor behavior represents one of the most interesting question to elucidate. Indeed, after a Master's degree in neuroscience, I decided to start a PhD investigation focused on the large-scale neuronal circuits that control composite motor behaviors.

Large-scale neuronal circuits involving multiple brain regions with different functions, from the encephalon to the spinal cord, are necessary to execute the desired motor actions. Indeed, our brain must consider information from the external environment and the inner

body, compute and process such information in concert with our intentions. These brain areas will be referred to as “integrative/cognitive centers”. The neural circuits that are appointed to produce the movements with specific timing and intensity are located along the brainstem and the spinal cord in a somatotopic manner (Figure 1). Such neural circuits will be termed “executory centers” throughout this manuscript. These executory centers comprise the motoneurons contacting the muscles recruited for a given movement and the interneurons that control and tune the motoneural activity (Figure 1C).

However, how the motor signal is transmitted from the integrative/cognitive centers to the executory circuits is far from being completely resolved, and it still represents a big challenge in the field of neural motor control. In the following chapters, I will explain concepts and state-of the art notions that are necessary to understand the starting point and the aim of my PhD project. In particular, since I study the execution of multiple motor actions including orofacial, head, eye movements and locomotion, I will explain in the next chapters the actual notions related to specific motor actions.

1.1.1 Composite motor behaviors - example of orientation

Orientation is a complex motor behavior that requires the execution of multiple actions, for example regulating the speed, changing the locomotor direction, moving the head and the sensory apparatus towards an external cue. Animals can perform these motor actions either individually or simultaneously and can modulate their intensity in response to their needs at any moment. The main structure known to control orienting responses is the superior colliculus (SC, Figure 2) (Basso et al., 2021; Basso and May, 2017; Isa et al., 2021; May, 2006). It is well studied in monkeys, cats and rodents. The homologous structure in the non-mammalian vertebrates is called the optic tectum (Isa et al., 2021).

The SC is located in the dorsal part of the midbrain, and is organized in two divisions: the dorsal visuosensory division, and the ventral motor division (Figure 2). Moreover, the divisions are organized in layers. The stratum zonale (SZ), the startum griseum superficiale (SGS) and the stratum opticum (SO) compose the visuosensory division. The stratum griseum

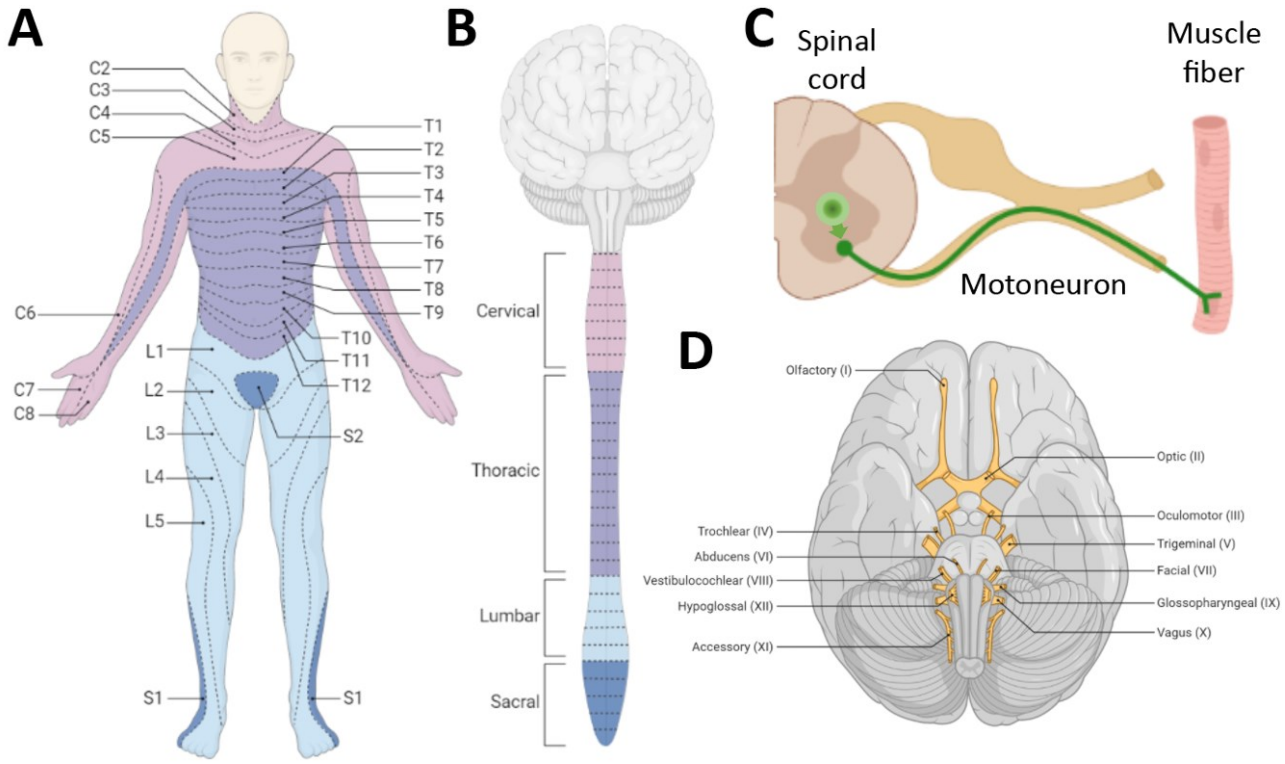

Figure 1. Organization of the executory centers. (A) and (B): the executory centers are distributed in a somatotopic manner throughout the antero-posterior axis of the spinal cord; their position reflects the muscles that they control. (C) Schematic representation of the executory centers (in green) within the spinal cord. The shaded areas represents the circuit that contacts the motoneuron controlling the muscle fiber. (D) Representation of the twelve cranial nerves of the human brainstem. Realized using BioRender.

intermediale (SGI), the stratum album intermediale (SAI), the stratum griseum profondum (SGP), the stratum album profondum (SAP) compose the motor division (Basso and May, 2017; May, 2006).

The visuosensory layers of the superior colliculus receive inputs directly from a vast number of different regions of the brains including the retina, striatum, extrastiatum cortex, lateral geniculate nucleus, parabigeminal nucleus, pretectum and locus coeruleus (Basso et al., 2021; Basso and May, 2017). Notably, the inputs from the retina are segregated into the visuosensory division. Indeed, the retinal inputs from the temporal retina project to the rostral part of the visuosensory layers, while the nasal retinal inputs to the caudal superior colliculus, and inputs from the dorsal and ventral retina project to the lateral and ventral

part (Isa et al., 2021). Therefore, the inputs from the retina are distributed in a retinotopic manner throughout the visuosensory layers. The outputs of the visuosensory division project to the lateral geniculate nucleus, pulvinar, tectopulvinar, parabigeminal nucleus and cortical areas of V3 and middle temporal area of the extrastriate (Albano et al., 1979;

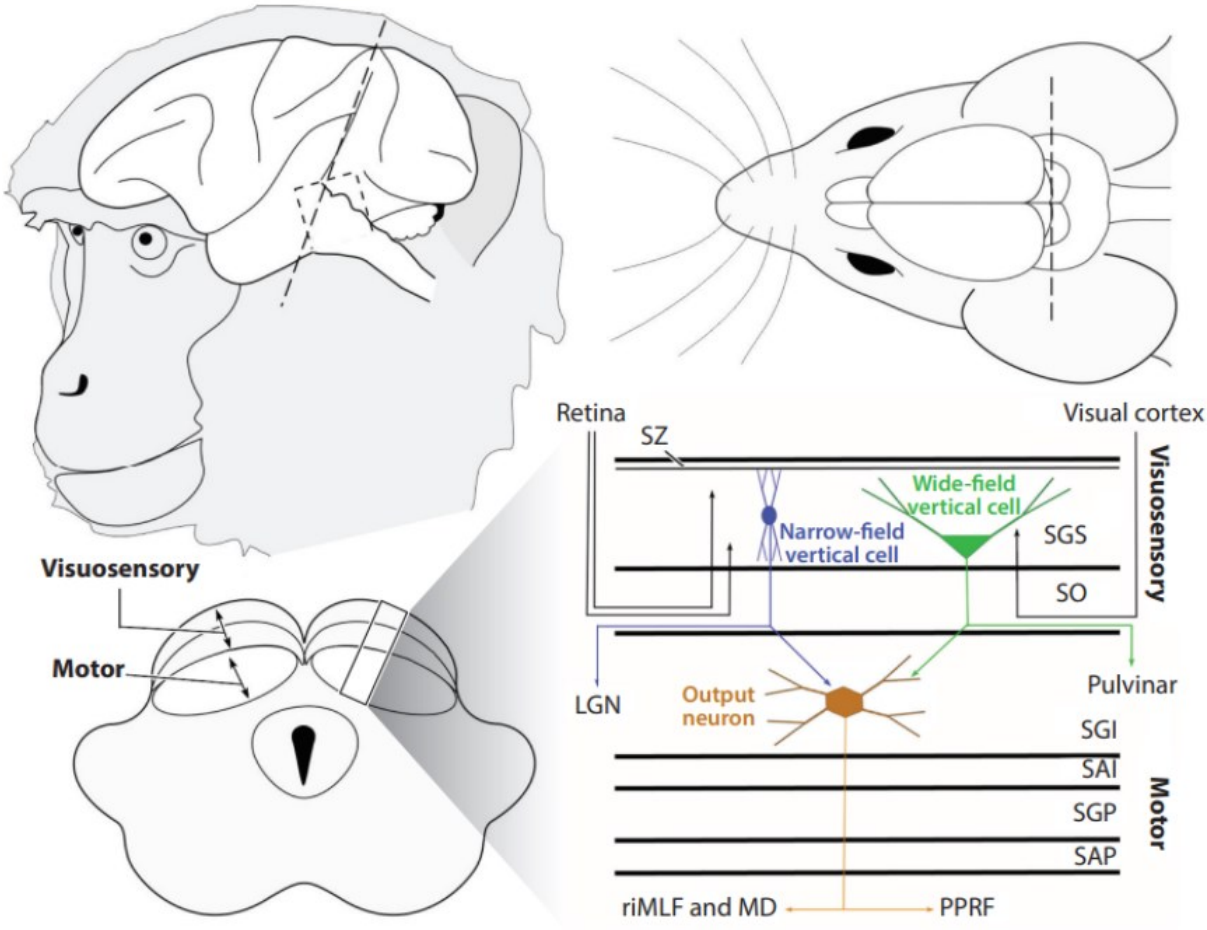

Figure 2. Schematic representation of the brain, highlighting the location of the superior colliculus in two mammalian species, a monkey and a mouse (not to scale). The dashed line indicates an axial cut through the colliculus to reveal the layers. Stratum griseum superficiale (SGS) and stratum opticum (SO) together comprise the visuosensory layers, and the stratum griseum intermediale (SGI) together with the deeper layers comprise the motor layers. The schematic on the right shows the known neuronal types within the colliculus and their projection patterns. Narrow-field vertical cells (*blue*) project to the lateral geniculate nucleus (LGN), and the wide-field vertical cells (*green*) project to the pulvinar. Output neurons of the motor layers (*brown*) project to the rostral interstitial nucleus of the medial longitudinal fasciculus (riMLF) to control vertical eye movements and to the paramedian pontine reticular formation (PPRF) to control horizontal eye movement. The motor layers also project upstream to the medial dorsal nucleus of the thalamus (MD). Abbreviations: SAI, stratum album intermediale; SAP, stratum album profundum; SGP, stratum griseum profundum; SZ, stratum zonale. (Basso and May, 2017).

Bickford et al., 2015; Clower et al., 2001; Gale and Murphy, 2014; Graham et al., 1979; Harting et al., 1991; Lyon et al., 2010). The outputs and the inputs of the motor layers link the SC to almost the entire neuraxis. Notably, extensive projections were found within the medullary reticular formation (Basso et al., 2021; Basso and May, 2017; Isa et al., 2021; May, 2006).

First electrophysiological experiments on SC showed its coupling with saccadic eye movements (rapid eye movement toward an object of interest) (Apter, 1946; Fuchs and Robinson, 1966; Schiller and Stryker, 1972; Wurtz and Goldberg, 1972). Furthermore, the site of electrical stimulation within the retinotopic map (receptive field of the SC) determines the amplitude and the direction of the eye movements, while the frequency of the stimulation controls the speed of the eye movements (Edelman and Goldberg, 2001, 2003; Gnadt et al., 1991; Hikosaka and Wurtz, 1985; Klier et al., 2001; Sparks and Mays, 1990; Stanford et al., 1996; Van Opstal et al., 1990).

The huge network that the superior colliculus forms with almost every region of the brain, with ascending and descending inputs and outputs, suggests a role in processing and transmitting sensory information to a vast number of areas (Goldberg and Wurtz, 1972; Hall and Colby, 2016; White et al., 2009).

Saccadic eye movements is the typical motor action associated to the SC. However, the SC has also been shown to control other typical orienting movements. Indeed, multiple studied demonstrated that SC neurons control fin, limb, head and whisker movements (Alstermark et al., 1987; Apter, 1946; Corneil et al., 2002; Courjon et al., 2004; Courjon et al., 2015; Grantyn et al., 1987; Hemelt and Keller, 2008; Isa and Sasaki, 2002; Iwamoto, 1990; Masullo et al., 2019; Sahibzada et al., 1986; Suzuki et al., 2019).

Altogether, these observations suggest that the SC contributes to the control of multiple orienting motor components. However, how the signal from the SC is converted into a composite orienting behavior remains to be identified.

1.1.2 Composite motor behaviors - example of respiration and locomotion

Another example of combination of multiple motor actions to produce a complex/composite behavior is the coordination of breathing and locomotion. Indeed, when animals, including humans, start running, the breathing frequency immediately increases to match the increased metabolic needs, often coupled with an increase of respiratory amplitude (Dejours et al., 1959; Flandrois et al., 1971; Haouzi et al., 2004; Krogh and Lindhard, 1913; Mateika and Duffin, 1992, 1995; Pearce and Milhorn, 1977; Robinson, 1985; Tsuchiya et al., 2012)

Here, I will explain the general basis of breathing, while that of locomotion will be covered in section 1.1.3 of this manuscript.

Breathing is a fundamental behavior that ensures the constant supply of O2 and the elimination of CO_2. It is composed by two different phases, inspiration and expiration. Inspiration is a systematically active mechanism that involves the concerted muscular contraction of dedicated inspiratory pump muscle groups, of which the diaphragm is the main muscle. Instead, expiration is a passive mechanism at rest due mainly to the relaxation of the inspiratory muscles and lung recoil. However, under certain physiological conditions where the respiratory drive is increased, like during high-level exercise, forced or active expiration takes place (Iscoe, 1998; Jenkin and Milsom, 2014). Breathing is a rhythmic behavior that is controlled by dedicated neurons of the brainstem that form a circuit called respiratory central pattern generator (respiratory CPG) or respiratory rhythm generator (which according to my terminology will form, with the phrenic motorneurons, the respiratory executory center). There are two main structures forming the respiratory CPG (Figure 3A): the preBotzinger Complex (preBötC) and the parafacial respiratory group (pRFG) (Del Negro et al., 2018; Feldman et al., 2013).

The preBötC is the core rythmogenic microcircuit for generating inspiration (Del Negro et al., 2018; Feldman and Del Negro, 2006; Feldman et al., 2003; Smith et al., 1991). Multiple studies demonstrated the existence of the preBötC in different species, including

humans (Mutolo et al., 2007; Pantaleo et al., 2011; Ramirez, 2011; Ramirez et al., 1996; Schwarzacher et al., 2011; Smith et al., 1991; Tupal et al., 2014; Wenninger et al., 2004). The preBötC is located ventrally to the nucleus ambiguous within the ventral medulla and its constitutive neurons express the neurokinin 1 receptor (NK1R) and the neuropeptide somatostatin SST (Feldman et al., 2003; Gray et al., 1999; Stornetta et al., 2003).

The pRFG is located ventrally of the facial motor nucleus (7N). It has been shown that the functional coupling between the pRFG and preBötC is necessary for the generation of the inspiratory rhythm at birth (Mellen et al., 2003; Onimaru et al., 1987; Onimaru and Homma, 2003). pRFG neurons express the transcription factor Phox2b (Onimaru et al., 2008). Notably, the pRFG overlaps with a region called retrotrapezoid nucleus (RTN) known for its chemogenetic role in crucial in detecting pCO_2 changing and the pH variation and regulate the respiratory rhythm (Amiel et al., 2003; Guyenet et al., 2005; Mitchell et al., 1963; Mulkey et al., 2004; Ramanantsoa et al., 2011; Ruffault et al., 2015; Smith et al., 1989; Stornetta et al., 2006).

First studies on breathing and locomotion were performed by stimulating the supraspinal regions diencephalic locomotor region (DLR) and mesencephalic locomotor region (MLR) in cats and lamprey (that are regions known to promote locomotion, I will discuss the MLR later in the manuscript, in section 1.2.1). The stimulation of these areas not only induces an increase of locomotion but also an increase in frequency and amplitude of breathing (DiMarco et al., 1983; Eldridge et al., 1985; Eldridge et al., 1981; Gariepy et al., 2012; Shik et al., 1969).

Furthermore, studies on spinal circuits for locomotion (locomotor CPG, it will be discussed later in the manuscript) demonstrated, on neonatal spinal cord preparation, that the activation of such circuits induced an increase of respiratory frequencies (Le Gal et al., 2020; Le Gal et al., 2014; Morin and Viala, 2002).

A recent study led in my laboratory by another PhD student demonstrated that, during running exercise in mice, there is no lock between breaths and strides, meaning that the respiration phase is independent from the locomotor cycle (Figure 3B) (Herent et al.,

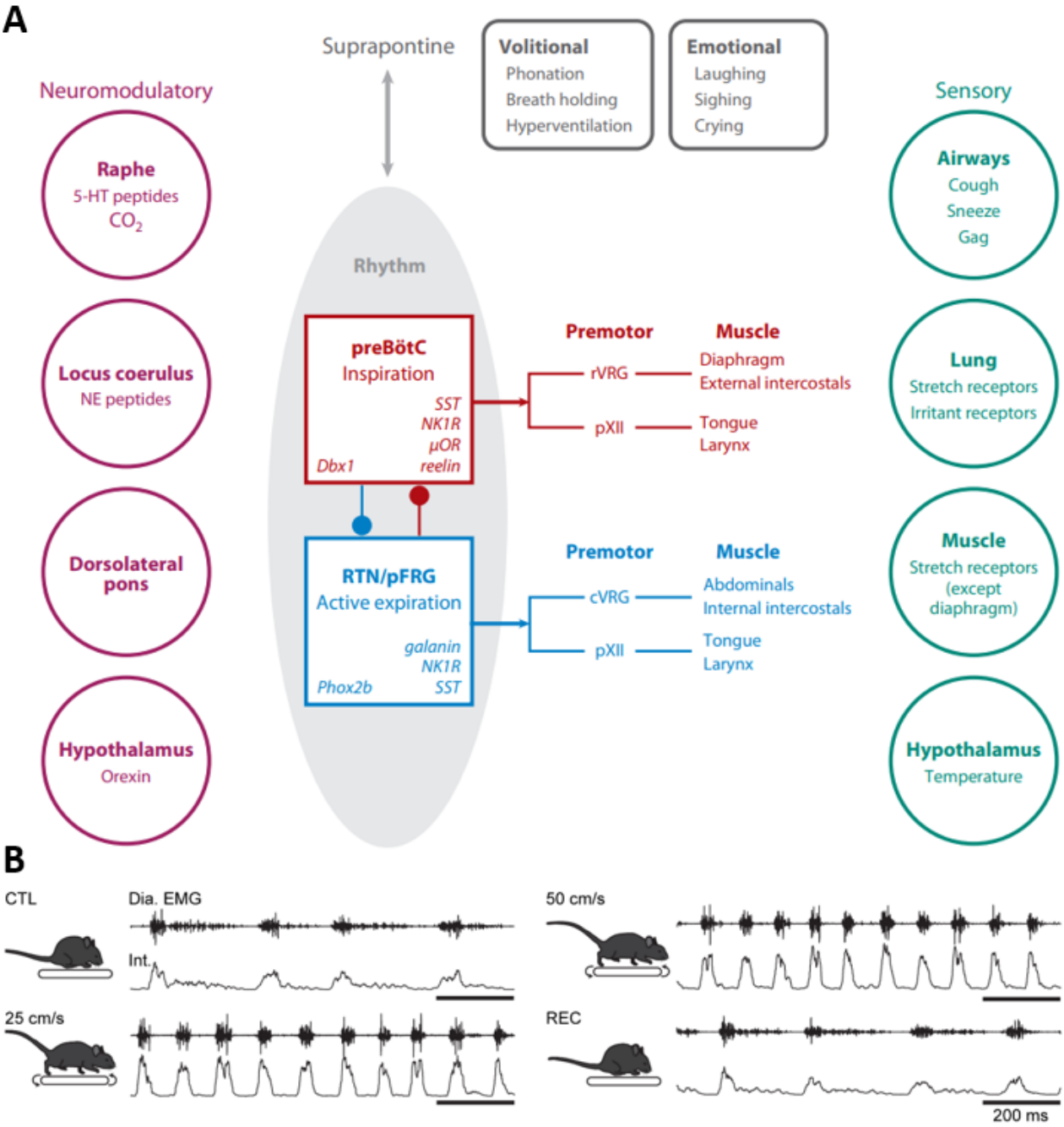

2020). This work suggests that the adaptation to exercise may include different behavior-dependent solutions. Indeed, whilst the transition from rest to moderate exercise could engage a default exercise breathing at fixed frequency, the engagement into faster displacement speeds appears to operate through a further increase of respiratory frequency.

However, whether there is a neural substrate that links locomotor controlling circuits and the breathing CPG to increase the respiratory rate while the locomotor activity increases is not yet determined. Nevertheless, humans asked to imagine performing running exercise

Figure 3. Overview of the central pattern generator for breathing. Core rhythm-generating circuits appear to have two distinct brainstem oscillators: the endogenously active preBotzinger Complex (preBotC) (*red box*) and the conditionally active retrotrapezoid nucleus/parafacial respiratory group (RTN/pFRG) (*blue box*). The preBotC drives inspiratory activity by projections to various premotor populations [rostral ventral respiratory group (rVRG), parahypoglossal (pXII)] that in turn project both to inspiratory muscles that pump air, e.g., the diaphragm and external intercostals, and to inspiratory muscles that modulate airflow resistance, e.g., laryngeal and tongue muscles. The RTN/pFRG has a similar functional path to expiratory muscles. preBotC and RTN/pFRG progenitors and neurons express distinct transcription factors (Dbx1 or Phox2b) and other genes (*right; italics*). Numerous neuromodulatory (*left*), suprapontine (*top*), and sensory (*right*) influences are shown. (Left) Neuromodulation. Respiratory pattern is highly labile. When animals go from quiet sitting to slow walking, the O_2 consumption increases approximately threefold, and if ventilation does not increase rapidly, animals will probably pass out within 100 m. Peptides, serotonin, norepinephrine, and other endogenous neuromodulators—originating in projections from, for example, the raphe, locus ceruleus, and hypothalamus—can affect rhythmogenesis. These actions are essential for normal regulation and may go awry in diseases affecting breathing. The dorsolateral pons, aka pontine respiratory group, including the Kolliker-Fuse and parabrachial nuclei, is also an important modulatory source. (*Top*) Suprapontine inputs are related to volition and emotion. (*Right*) Sensory inputs are essential for the proper regulation of blood gases and for mechanical adjustments related to posture, body mechanics, and likely metabolic efficiency. (Feldman et al., 2013) (B) Breathing rate augments during trotting independently of limb velocity or surface inclination. Diaphragm activity recordings in control condition (CTL), trotting at 25 and 50 cm/s and during recovery after the run (REC). Raw (Dia. EMG) and integrated (Int.) signals are illustrated in each condition. (Herent et al., 2020).

showed an increase of breathing rate, even in the absence of actual exercise (Decety, 1993; Jahn et al., 2008; Karachi et al., 2010; Thornton et al., 2001). Furthermore, as I mentioned above, stimulating the MLR and DLR increase the respiratory rate in cats and lamprey. Interestingly, it has been shown that the MLR projects, in the lamprey, to the paratrigeminal group, considered the homologous structure of the preBötC (Gariepy et al., 2012; Mutolo et al., 2007). Therefore, the preBötC is a prime candidate for integrating locomotor signals and mediating respiratory changes to meet the energetic demand associated with exercise. However, the existence of such mechanism as not been documented yet.

1.1.3 The “executory” centers: where the final drive to the muscles is elaborated

As I already mentioned in the first paragraph, the executory centers (composed by interneurons and motoneurons) are distributed throughout the brainstem and the spinal cord in a somatotopic manner. From the upper spinal cord to the lower spinal cord, these circuits control neck, forelimb, back and hindlimb movements, respectively (Figure 1B). The

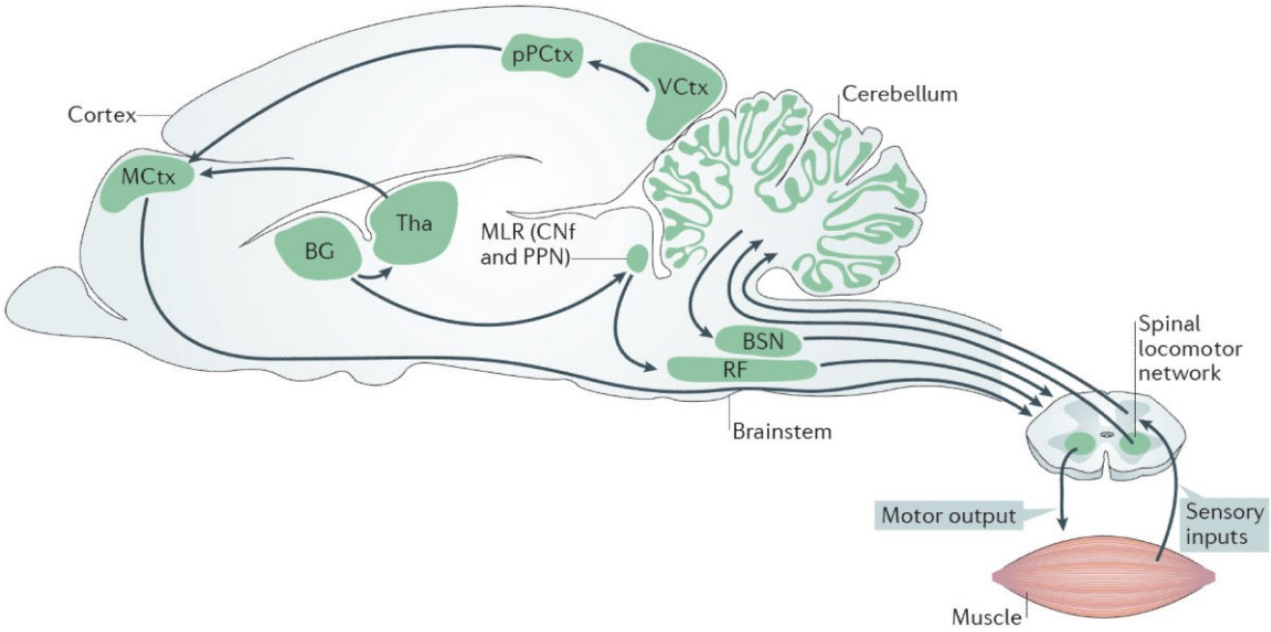

Figure 4. The neuronal control of locomotion in vertebrates. The selection and initiation of locomotion involves various regions of the brain and brainstem. Output neurons of the basal ganglia (BG) project both to the thalamus (Tha) — which sends projections to the motor cortex (MCtx) and other cortical areas — and to areas in the brainstem, including the mesencephalic locomotor region (MLR). Initiation of locomotion is thought to be mediated by the activity of neurons in the MLR including the cuneiform nucleus (CNf) and the pedunculopontine nucleus (PPN). MLR neurons project to neurons in the reticular formation in the brainstem. Neurons in the reticular formation project to locomotor networks in the spinal cord that execute locomotion (the locomotor CPG). Descending fibers from the vestibular and rubrospinal spinal pathways (brainstem nuclei (BSN)) maintain posture and modulatory signals that regulate the ongoing locomotor activity. The cerebellum coordinates locomotor behavior by mediating movement-generated feedback and internal feedback, as well as by modulating the activity in the descending pathways. Proprioceptive sensory feedback modulates the activity of the spinal locomotor network. Cortical activity (MCtx) provides visuomotor (VCtx) correction of locomotion via the posterior parietal cortex (pPCtx). (Kiehn, 2016).

most studied executory center in the spinal cord is the center for controlling locomotion.

Locomotion is a fundamental behavior that encompasses all the animal kingdom, and it can occur in many ways depending on the anatomical characteristics of the animals. Swimming, flying, quadrupedal or bipedal walking are different ways to locomote.

The first hypothesis of the existence of a central spinal program sufficient to produce locomotion was proposed early in the XXth century (Brown, 1911). Years later, was suggested the term locomotor Central Pattern Generator (CPG) (Delcomyn, 1980). Initially the model proposed by Graham was the so-called “Half-centered model”, consisting in two small neuronal networks connected through inhibitory neurons. When one was active, the other one was inhibited. Such model was used to explain the alternation between extensor and flexor muscles during locomotion (Brown, 1914). This model was expanded with the idea of smaller network, called “Unit Burst Generator” (UBG), able to produce intrinsic rhythm activity (Grillner et al., 1981). Pioneering electrophysiological experiments on *ex vivo* spinal cord preparations allowed to study the locomotor CPG in order to record the activity of the ventral roots of the spinal cord, where are located the fibers of the motoneurons contacting specific muscles involved in locomotor behaviors (Kiehn and Kjaerulff, 1996). Independently from the specie and the type of locomotion, the locomotor CPGs in the spinal cord are evolutionary conserved across vertebrates (Grillner and El Manira, 2020; Kiehn, 2006, 2016). These networks contain the sufficient information to activate different muscles and coordinate the cycle and the rhythm of locomotion (Figure 4).

In the brainstem, reside the executory centers for breathing (already explained in section 1.1.2), ocular, and orofacial behaviors. The term orofacial behavior refers to any activity involving muscles of the face, the vibrissae, the jaw, the tongue or the airways, therefore including sniffing, chewing, licking, swallowing and vocalizing (Moore et al., 2013). Notably, such behaviors must be performed without fatal blockages of the airflow. Furthermore, orofacial movements can be performed in synchrony with eye movements, for example during exploration the nose, wiskers and eyes can point towards the same direction in response to an external stimulus. Therefore, these motor actions, if needed in synergy,

must be well-coordinated and require the control of multiple muscles. Indeed, it has been demonstrated that in rats the coordinated activity of 26 pairs of muscles and five cranial nerves are needed to correctly perform eating, drinking and swallowing, that altogether compose the essential complex behavior known as feeding (Barlow, 2009a, b). The motoneurons of the brainstem are organized in nuclei controlling specific muscles (Figure 5). The main nuclei known to control voluntary movements are the oculomotor (III nerve), trochlear (V), abducens (VI) for eye movements, while the trigeminal (V), facial (VII), ambiguous (X) and hypoglossal (XII) for orofacial movements (Cordes, 2001). Examples of motor actions controlled by these motoneurons and executory centers in which they are embedded are the eye and neck movements, whisking, chewing, sniffing and breathing (Guthrie, 2007; Ruder and Arber, 2019).

An orofacial behavior that has been well-studied over the last decades is whisking, that consist in rapid movements of the mystacial vibrissae used for touch, in order to explore the external environment. Notably, the whisker moments are associated and coordinated with sniffing, and therefore, breathing (Moore et al., 2014). The central oscillator for whisking is located in the vibrissa intermediate reticular nucleus (vIRt), a ventral region of the caudal brainstem (Moore et al., 2013). The neurons of the vIRt indeed fire in coordination with the retraction of the vibrissae. It has been proposed that rhythmic whisking is controlled by an oscillatory signal from the inhibitory vIRt neurons to the facial motor nucleus (7N) during the retraction phase (Moore et al., 2013; Moore et al., 2014). Such inhibition might be counterbalanced by an excitatory drive to the motoneurons of the 7N, causing the oscillatory back-and-forth whisker movements (Deschenes et al., 2016). Furthermore, the activity of the vIRt might be controlled by the respiratory CPG (preBotzinger Complex) in order to tightly coordinate whisking and breathing (Deschenes et al., 2016; Kleinfeld et al., 2014; Smith et al., 1991). Recently, it has been showed that vIRt neurons comprises Parvalbumin-expressing inhibitory neurons and that their silencing impairs regular whisking (Takatoh et al., 2021).

Importantly, as I explained before, these executory centers are controlled by integrative/cognitive centers upstream. In the next paragraph, I will describe the classic

organization of descending tracts contacting the executory centers. I will depict the main tracts, and, as I will explain later in the manuscript, my work focuses in particular on the reticulospinal tract.

Nerve	Subtype	Nucleus	Target muscles or ganglia
III	Somatic motor	Oculomotor	Superior, inferior and medial recti muscles; inferior oblique, levator palpebrae superioris
	Visceral motor	Edinger-Westphal	Ciliary ganglion
IV	Somatic motor	Trochlear	Superior oblique
V	Branchiomotor	Trigeminal motor	Muscles of mastication, tensor tympani, anterior belly of digastric, others
VI	Somatic motor	Abducens	Lateral rectus muscle
VII	Branchiomotor	Facial motor	Muscles of facial expression, stapedius, posterior belly of digastric
	Visceral motor	Superior salivatory	Pterygopalatine/sphenopalatine ganglion, submandibular ganglion
IX	Branchiomotor	Nucleus ambiguus	Stylopharyngeus muscle
	Visceral motor	Inferior salivatory	Otic ganglion
X	Branchiomotor	Nucleus ambiguus	Laryngeal and pharyngeal muscles
	Visceral motor	Dorsal motor	Non-striated muscle of thoracic and abdominal viscera
Cranial XI	Branchiomotor	Nucleus ambiguus	Laryngeal and pharyngeal muscles
Spinal XI	Branchiomotor	Accessory nucleus, cervical spinal cord	Sternocleidomastoid and trapezius muscles
XII	Somatic motor	Hypoglossal	Tongue muscles

Figure 5. Cranial nerves and their targets in humans. (Guthrie 2007)

1.1.4 The supraspinal control of executory centers

While the spinal cord and the brainstem executory centers contain all the neural components to produce the motor act itself, their activity is under obligatory control of supraspinal-spinal structures. Over the past decades, scientists dedicated their work in investigating how the nervous system plans and controls motor actions and how it coordinates them in order to perform composite motor behaviors. Efforts were done for identifying the descending pathways that relay a motor signal from the integrative/cognitive centers to the executory centers (Kuypers, 1964, 1981). The classical organization of the mammal brain, groups the descending motor pathways in corticospinal, vestibulospinal,

rubrospinal, cerebellospinal and reticulospinal tract is shown in Figure 6.

The corticospinal tract (i.e., pyramidal tract) originates within the motor cortex and sends axons to the spinal cord with most of the fibers (the percentage varies within different species; about 90% of the fibers in primates, including humans) decussating contralaterally at the level of the pyramids of the brainstem. The corticospinal tract is mostly known for the control for distal muscles. Its main role is to control fine digital movements (Lemon, 2008),

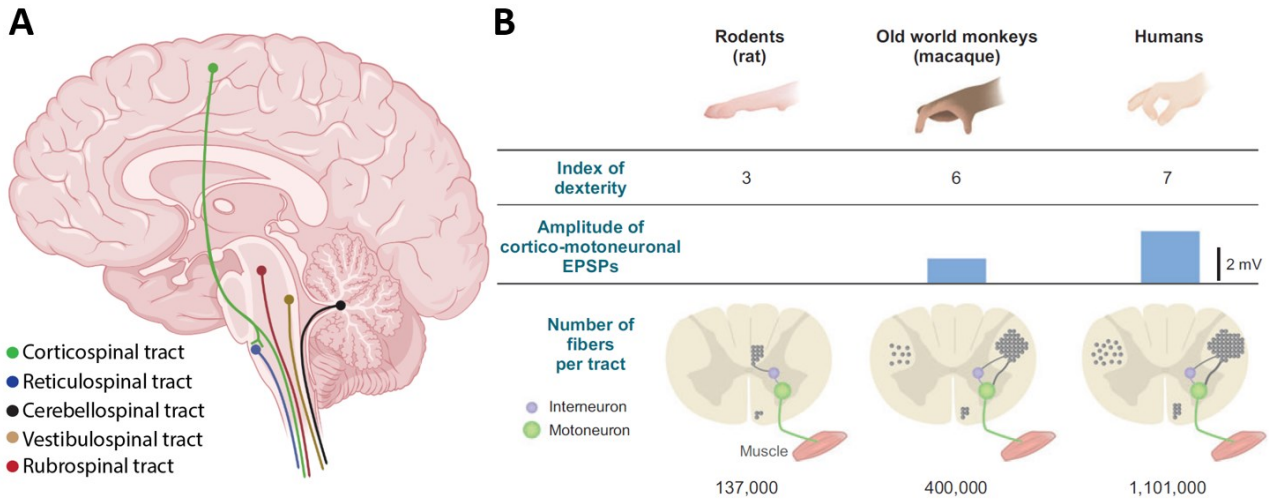

Figure 6. The main descending tracts. (A) Schematic representation of the origin of the five main descending tracts: the corticospinal tract (in green), the reticulospinal tract (in blue), the cerebellospinal tract (in black), the vestibulospinal tract (yellow) and the rubrospinal tract (in yellow). Note that the corticospinal tract sends collateral fibers to the reticular formation, the classical nomenclature referred to this pathway as corticobulbar tract. Realized using BioRender templates. (B) Relationship between the development of the corticospinal tract and the emergence of fine motor control abilities. In rodents, there are no direct connections between corticospinal neurons and the cervical motoneurons which innervate forelimb muscles, but brainstem pathways and spinal interneurons relay cortical input to motor neurons. Most of the corticospinal fibers in rodents travel in the dorsal columns. In non-human primates and humans, direct corticospinal connections with motoneurons have evolved, together with an increase in the size and number of the corticospinal fibers. This is reflected in an increase in the size of the excitatory postsynaptic potential (EPSP) elicited by cortical neurons in hand motoneurons. The primate CST is located mostly in the lateral columns, and a significant proportion of CS fibers (~10%) descend ipsilaterally. The development of the CST correlates with the improvement in the index of dexterity, particularly in the ability to perform finger-thumb precision grip (Lemon, 2008).

Figure 5B. Furthermore, it has been demonstrated that the development of the corticospinal tract presents crucial differences between species (Kuypers, 1981; Lemon, 2008). In particular, it has been demonstrated that in humans, the corticospinal tract forms a direct monosynaptic connection with motoneurons in the cervical spinal cord controlling digital muscles, whilst, in rodents, such connectivity is absent (Alstermark et al., 2004). This might explain why in primates the digital movements are highly skilled. However, in mice, digital movements for behaviors including grasping and grooming are essential. As we will see later in the manuscript, evidences suggest that such behaviors in mice might be controlled by brainstem neurons. Furthermore, in mice, it has been studied that the corticospinal tract does not impact locomotor activity and, in the lumbar spinal cord its main role is to modulate sensory inputs (DiGiovanna et al., 2016; Moreno-Lopez et al., 2021).

The vestibulospinal tract originates in the vestibular nuclei and projects the axons ipsilaterally along the spinal cord and controls primarily the head and eyes movements for body balance (McCall et al., 2017; Sugiuchi et al., 2004). The vestibular nucleus receives inputs from contralateral vestibular nucleus, somatosensory inputs from the spinal cord, from the cerebellum, from multiple areas of the cerebral cortex (Akbarian et al., 1993; Fukushima, 1997; Guldin et al., 1993; Pogossian and Fanardjian, 1992; Wilson et al., 1999). Notably, extensive vestibular projections were observed within the brainstem reticular formation, where originates the reticulospinal tract (Bolton et al., 1992; Peterson and Abzug, 1975; Schor and Yates, 1995).

The rubrospinal tract originates within the magnocellular red nucleus of the brainstem. Rubrospinal projections are more abundant contralaterally. Studies suggest that the rubrospinal tract is involved in controlling the velocity of the execution of the voluntary movements of the limbs (Kuypers, 1981; Lemon, 2008). Interestingly, In humans, the rubrospinal tract seems to be less developed (Yamamoto et al., 2017).

The cerebellospinal tract has been mostly investigated for its role in motor learning, postural adjustments and forelimb movements (Asanuma et al., 1980; Carrea and Mettler, 1954; Fukushima et al., 1977; Liang et al., 2011; Matsushita and Hosoya, 1978; Nudo and

Masterton, 1988; Sathyamurthy et al., 2020; Wang et al., 2018).

The reticulospinal tract originates in the brainstem reticular formation and its projections were observed along the entire spinal cord. In particular, ipsilateral reticulospinal projections are more abundant than contralateral projections. The reticulospinal tract controls multiple voluntary movements including forelimb and orofacial movements, breathing and locomotion. Notably, fibers from other descending tracts have been shown to project and collateralize to the brainstem, as it is demonstrated for the corticospinal and cerebellospinal tracts (Batton et al., 1977; Brodal and Szikla, 1972; Lemon, 2008; Tolbert et al., 1980). These observations suggest that the reticulospinal tract might relay motor signals from the other descending tracts. Indeed, the reticulospinal tract is considered a crucial descending motor pathway that relays the motor command to the executory centers within the spinal cord and the brainstem allowing the animals to perform vital behaviors and survive in the external environment (Brownstone and Chopek, 2018; Humphries et al., 2007). Such role of the reticular neurons represents the starting point of my investigations.

The aim of the following chapter is therefore to accompany the reader to the investigations that were done in the last decades on the study of reticulospinal neurons, and the reticular formation in general, and its involvement in controlling motor actions.

1.2 The Brainstem Reticular Formation

The brainstem reticular formation is a region of the brain that controls many vital, and highly conserved motor behaviors, including orofacial, respiratory, forelimb and locomotor movements but also head and trunk movements as well as uro-genito-sexual functions. The reticular formation is key structure that relays motor commands from the higher brain areas (integrative/cognitive centers) to the executory centers within the spinal cord.

The reticular formation is a vast ventral region with non-discrete boundaries that spans throughout the brainstem (midbrain, pons and medulla oblungata). It receives inputs from multiple brain regions with different functions including the cerebellum, the thalamus, the cortex, visual, vestibular, and auditory pathways. It contacts an incredible number of brain regions with ascending and descending projections: thalamus, cerebellum, red nucleus, basal ganglia, hypothalamus and spinal cord. With such heterogeneous efferences and afferences connectivity, the reticular formation is a major candidate for relaying information from and to different regions of the brains and for controlling multiple motor functions.

However, investigating the functions and the anatomy of the reticular formation has been challenging for decades due to the difficult accessibility of this brain region. Indeed, it is composed most likely by multiple cell types, differing by neurotransmitters, morphology, genetic identity and projections profile, and it is formed by borderless nuclei, but the cells are highly intermingled (Drew et al., 1986; Valverde, 1961). It is also located deep in the brainstem, making access to recording and imaging tools very tedious (Figure 7).

However, the development of new methods of investigation, including optogenetics, chemogenetics and cutting-edge viral tracing, nowadays allows us to thoroughly investigate neural circuits that before were inaccessible and elucidate their anatomy and functions

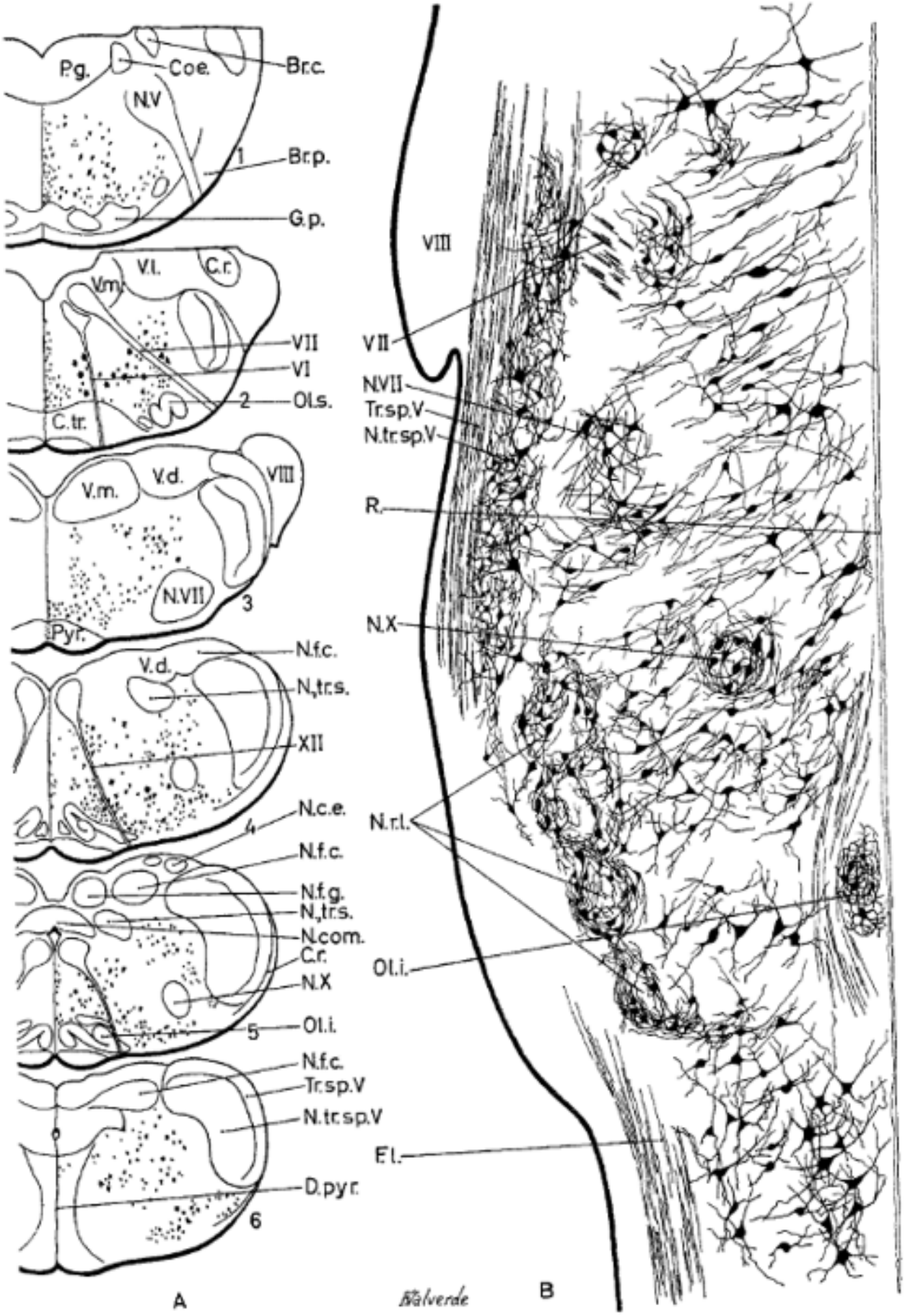
P.g.
Coe.
Br.c.
N.V
1
Br.p.
G.p.
V.l.
C.r.
V.m.
VII
VI
2
Ol.s.
C.tr.
V.m.
V.d.
VIII
N.VII
3
Pyr.
N.f.c.
V.d.
N.tr.s.
XII
N.c.e.
4
N.f.c.
N.f.g.
N.tr.s.
N.com.
C.r.
N.X
5
Ol.i.
N.f.c.
Tr.sp.V
N.tr.sp.V
D.pyr.
6
A
VIII
VII
N.VII
Tr.sp.V
N.tr.sp.V
R.
N.X
N.r.l.
Ol.i.
Fl.
Bâlverde
B

Figure 7. The complex organization of the reticular formation. A, transverse sections at equal distances through the pons and medulla oblongata indicating the size and the grouping of the cells of the reticular formation in an adult albino rat, using a pyridine-silver method. B, horizontal section through the facial and ambiguus nuclei. Rat, 21 days old. Cox method. Abbreviations: A.tr., triangular area containing the fibers to the nucleus dorsomedialis of Astrom. Br.c., superior cerebellar peduncle. Br.p., middle cerebellar peduncle. C.C., canalis centralis. Coe., nucleus coeruleus. C.I., corpus restiforme. C.tr., trapezoid body. D.1., decussation of the medial lemniscus. D.pyr., decussation of the pyramidal tract. F.ar.s.ex., arcuate fibers from the posterior column nuclei. F.c., fasciculus cuneatus. F.g., fasciculus gracilis F.l., funiculus lateralis. F.l.m., medial longitudinal fasciculus. F.s-m., sensitive-motor fascicle. F.v., funiculus ventralis. G.p., griseum pontis. L.m., medial lemniscus. Mg.tr.sp.V, subnucleus magnocellularis nuclei tractus spinalis trigemini caudalis of Meessen and Olszewski. N.c.e., external cuneate nucleus. N.com., commissural nucleus of Cajal. N.c.tr., nucleus of the trapezoid body. N.d-m., nucleus dorsomedialis of Astrom. N.f.c., nucleus cuneatus. N.f.g., nucleus gracilis. N.ic., nucleus intercalatus. N.pr.V, nucleus principalis of the trigeminal nerve. N.r.l., lateral reticular nucleus. N., tr.s., nucleus and tractus solitaries. N.tr.sp.V, spinal nucleus of the trigeminal nerve. N., tr.sp.V, spinal tract and nucleus of the trigeminal nerve. Ol.ac., accessory superior olive. Ol.i., inferior olive. Ol.ped.c., olivary peduncle, crossed part. Ol.s., superior olive. P.g., periaqueductal gray. P1.b.f.v-l., bulbar prolongation of the ventrolateral funiculus of the spinal cord. Pyr., pyramidal tract. R., raphe. R.d.m.o., subnucleus reticularis dorsalis medullae oblongatae of Meessen and Olszewski. R.pc., nucleus reticularis parvicellularis. R.v., nucleus reticularis ventralis. S.g., substantia gelatinosa of dorsal horn and nucleus caudalis of the trigeminal nerve. Str. ac .d., stria acustica dorsalis. T.r-s., rubrospinal tract. Tr.s., tractus solitarius. Tr.sp.V, spinal tract of trigeminal nerve. V.d., descending vestibular nucleus. V.1., lateral vestibular nucleus. V.m., medial vestibular nucleus. V,VI,VII,VIII,IX-X,XIII, rootlets of cranial nerves. N.V,N.VI,N.VII,N.XII, motor nuclei of craial nerves. N.X, nucleus ambiguous. IX-Xef, efferent rootlets of the vago-glosso pharyngeal nerve. G.VII, Genu of the facial nerve. (Valverde, 1961).

(Deisseroth, 2015; Fenno et al., 2014; Roth, 2016; Stepien et al., 2010; Wickersham et al., 2007). For my study, I took advantage from such new techniques to investigate, anatomically and functionally, the reticular formation.

Furthermore, the reticular formation has been proposed to have a role not only in relaying the motor signal between upstream and downstream circuits. Instead, it might be also a region with a certain degree of action selection. Indeed, it has been hypothesized that the reticular formation forms a dense network that might provide the ability to extract

correlated sensory information, the internal connectivity might guarantee the substrate for the coordination of distinct behavioral components, and the individual cells might drive the appropriate motor system (Humphries et al., 2006, 2007).

1.2.1 The Mesencephalic Locomotor Region

As I already mentioned before, one of the most conserved motor behaviors that is performed by all animals is the locomotion. It can be performed in multiple ways: quadrupedal, bipedal, swimming, flying. In non-limbed animals, the execution of locomotion requires the activity of axial muscles that control the body, while in limbed animals, it requires in addition the coordinated activity of limb muscles. Locomotion is composed by three distinct phases: initiation, locomotor episode and termination. These three phases can be performed in multiple ways, based on the speed, gait, limb coordination, direction, depending on the behavioral need at any time.

The neural circuits necessary for the execution of locomotion reside in the spinal cord (locomotor CPG, this concept has been already described previously in the manuscript, section 1.1.3). However, the activity of these executory centers depends from the motor signal coming from supraspinal integrative/cognitive centers. While the executory centers within the spinal cord are well-studied (Kiehn, 2006, 2016), as I explained above in the manuscript the mechanism by which integrative/cognitive centers of the brain contact the executory centers is poorly understood.

One of the most important findings in the field of motor control is the discovery of a region of the brainstem located in the dorsal mesopontine border of the cats that, when stimulated electrically, was inducing locomotion. It was termed the Mesencephalic Locomotor Region (MLR) (Shik et al., 1966; Shik et al., 1969). Furthermore, as the stimulation strength increased, higher speed locomotion is produced, from slow walk to trot and to gallop. This region was found evolutionary conserved in many different species (lamprey, mice, and primates) (Mori et al., 1989; Ryczko and Dubuc, 2013; Shik and Orlovsky, 1976). Moreover, a recent work on MLR, still not peer-reviewed at the time of the writing of this

manuscript, has identify the homologous structure of the MLR in zebrafish (Carbo-Tano et al., 2022).

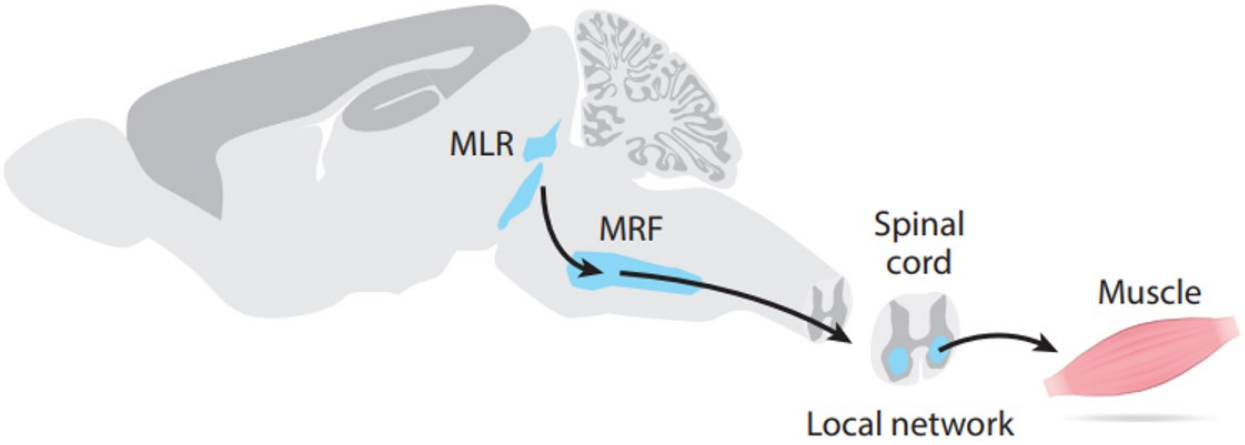

Figure 8. Mesencephalic Locomotor Region (MLR) connections with reticulospinal targets. Schematic view of the MLR that projects to the medullary reticular formation (MRF) with reticulospinal axons that descend to local, executory locomotor networks in the spinal cord through the ventrolateral funiculus.

The MLR is composed of two main subnuclei, the Pedunclopontine nucleus (PPN) and the Cuneiform nucleus (CNF) (Ryczko and Dubuc, 2017). For years, which region of the MLR was involved in promoting movements or whether they were concurring together in inducing locomotion remained unknown. Recent works studied, using novel methods of investigation, the contribution of the two brain structures to the locomotor behavior. Researchers investigated the glutamatergic cells expressing the type 2 vesicular glutamate transporter (VGlut2 neurons), located in both the PPN and CnF, and the cholinergic cells located in the PPN. Using optogenetics, investigators were able to selectively activate these cells and found that the stimulation of VGlut2 neurons in the PPN trigger slow locomotion, whereas the VGlut2 neurons in CnF induce high speed locomotion (Caggiano et al., 2018; Josset et al., 2018). These results suggested that the CnF elicits straight and fast (escape-like) locomotion while the PPN triggers slow, exploratory-like locomotion.

Moreover, studies suggest that MLR might mediate exercise hyperpnea (DiMarco et al., 1983; Eldridge et al., 1985; Gariepy et al., 2010; Kawahara et al., 1989). In lamprey, it has been shown that stimulation of MLR increases respiratory output and that the MLR projects

to the homologous structure of the PreBotc (Gariepy et al., 2012). MLR stimulation in cats induces the respiratory and cardiovascular increases that could occur during locomotor episodes and prior to the movement (Eldridge et al., 1985). These results suggest that the MLR might control in parallel locomotor and autonomic responses, including breathing. Indeed, that is the main topic of the project of onother PhD student within the laboratory, in which I participated.

Interestingly, projections from excitatory neurons of the MLR were found in the reticular formation, suggesting that in the medullary reticular formation there might be neurons relaying the locomotor-promoting signal from the MLR to the spinal cord (Shefchyk et al., 1984). Therefore, it has been proposed that the glutamatergic excitatory neurons in the medullary reticular formation might perform such function. Identifying these neurons might represents a key discovery in investigating the contribution of the reticular formation in the control of movements.

1.2.2 The medullary reticular formation

Within the last century, many scientists focused their investigations in describing the organization of the medullary reticular formation in regions and nuclei. In particular, most of research depicted the anatomy of the rodent reticular formation. The edges of the reticular formation are still not clearly defined and, as well as the name of the structures, they can vary between studies. Therefore, to help the reader, in the following chapter I explain the nomenclature of the medullary reticular formation that I will follow throughout the manuscript.

The classical organization of the reticular formation divides this structure in three regions (median, medial and lateral) (Chopek et al., 2021). The medial medullary reticular formation comprises rostrally the caudal part of the nucleus reticularis pontis caudalis (PnC), continuing with the Gigantocellular nucleus (Gi). The Gi is one of the bigger nuclei of the medullary reticular formation and spans across the ventral pons and the medulla oblongata, from the facial nucleus to the obex (from -5.5 to -7.20 from bregma) (Franklin and Paxinos,

2007; Valverde, 1961). Ventral to the Gi there are the alpha part of the Gi (GiA), more rostrally, and the ventral part of the Gi (GiV), more caudally. Other nuclei of the medullary reticular formation are the dorsal paragigantocellular nucleus (DPGi), the parvocellular reticular nucleus (PCRt), intermediate reticular zone (IRt) and the lateral paragigantocellular nucleus (LPGi). At the most caudal part of the medulla (caudal to -7.20 from bregma), there are the ventral part (MdV) and the dorsal part (MdD) of the medullary reticular formation (Chopek et al., 2021; Franklin and Paxinos, 2007).

One of the main contributions in investigating the organization and the neurons of the medullary reticular formation was done by Valverde in 1961. His work described with an incredible accuracy (especially considering the techniques available at the time) the anatomy of the reticular neurons highlighting the huge variety of the morphology of the cells within the various nuclei of the reticular formation.

"*The nucleus reticularis gigantocellularis […] make up the principal site of origin of the long distance efferent projections of the Reticular Formation. […] The characteristic tendency of the axons of their cells to form a longitudinal tract […]. The tract reaches the spinal cord"*.

With these words, Valverde described the neurons of the reticular formation projecting at different levels of the spinal cord. These neurons, called reticulospinal (RS) neurons, are commonly considered the fundamental cells carrying the motor signal from the integrative/cognitive to the executory centers in order to switch them on or off and modulate their activity. In particular, within the RS, there might be the neurons controlling a fundamental behavior already introduced in this manuscript: locomotion. Indeed, RS neurons are thought to send, in response to MLR activity, the motor command to the locomotor CPG located in the spinal cord (Brownstone and Chopek, 2018; Dubuc et al., 2008; McClellan and Grillner, 1984; Noga et al., 2003). Furthermore, axonal projections of the RS neurons have been found in multiple regions of the spinal cord, suggesting that RS neurons might control also other important motor function beside locomotion (Riddle et al., 2009; Shapovalov, 1972; Sivertsen et al., 2016; Szokol et al., 2008).

In parallel to the anatomical studies, for a functional investigation, first experiments on the brainstem were performed on decerebrated animals. After the lesion, it has been observed that the physiological functions remained intact or, at least, partially active. For decades, this strategy represented the main strategy to investigate brainstem functions. Experiments on decerebrated animals (only the brainstem remained intact), showed in different works that certain motor functions, like locomotion, grooming and responding to acoustic stimuli, remained intact or only partially limited (Bjursten et al., 1976; Roh et al., 2011; Whelan, 1996).

Altogether, these works demonstrated that the brainstem is an essential region of the brain in controlling multiple motor behaviors. Furthermore, these results suggested that, at the level of the brainstem there might be a certain degree of action selection. Indeed, between the regions left intact in decerebrated animals, the reticular formation has been proposed as the main structure for selecting and performing different motor actions (Humphries et al., 2007).

As I mentioned previously, the first obstacle in investigating the reticular formation is represented by the difficult in identifying and manipulate only one neuronal type. This is due to the high level of intermingling of the cells in the reticular formation. Moreover, the nuclei of the reticular formation are deeply located in the ventral part of the brainstem and there is a lack of molecular tools to manipulate them. This represented for decades a huge impediment to anatomically and functionally investigate reticular and reticulospinal neurons.

There are different parameters that we can consider to define the neurons belonging to a cell type: by their location, the neurotransmitter released by the cells, the size of the soma, the axonal projections, the function, the genetic profile. Along the years, using techniques as optogenetics, chemogenetics and viral tracing, different research tried to isolate and study the functions of the reticular neurons according to one or more of these parameters.

In the next paragraphs, I will describe the essential studies focused on the role of the medullary reticular formation in controlling forelimb and orofacial movements, breathing and locomotion.

1.2.3 The medullary reticular neurons and forelimbs movements

As I explained before RS might not control only locomotion, indeed reticular neurons had been studied in the past decades in the context of different motor functions. One of the sets of motor actions discovered to be controlled by the reticular neurons is represented by the forelimb movements. Indeed, in most animals forelimbs are used to reach and grab objects, allowing the animals to perform essential behaviors in exploration, manipulation and grooming. However, whether there are different cell types controlling individual forelimb movements or whether they are controlled by a unique population, is poorly known.

Studies suggested that the lateral regions of the reticular formation might control distal forelimb movements (Kuypers, 1964; Lemon, 2008). Furthermore, recent studies showed that the glutamatergic cells of the ventral part of the reticular formation control grasping and the cells located in the lateral rostral medulla control reaching and food handling (Esposito et al., 2014; Ruder et al., 2021). These studies highlight the complexity of controlling different skilled forelimb movements and rise an important concept that each component of these motor actions might be controlled by different reticular centers instead of a unitary control by extensive collateralization.

1.2.4 The medullary reticular neurons and the orofacial and respiratory movements

Numerous studies over the last decades focused on the reticular formation and its role in motor control. Importantly it has been showed that this complex structure is involved in controlling multiple motor actions including orofacial movements and respiration. As I

already discussed above, with the term orofacial movements, we indicate a vast number of motor actions that are often coordinated with respiration like whisking and sniffing.

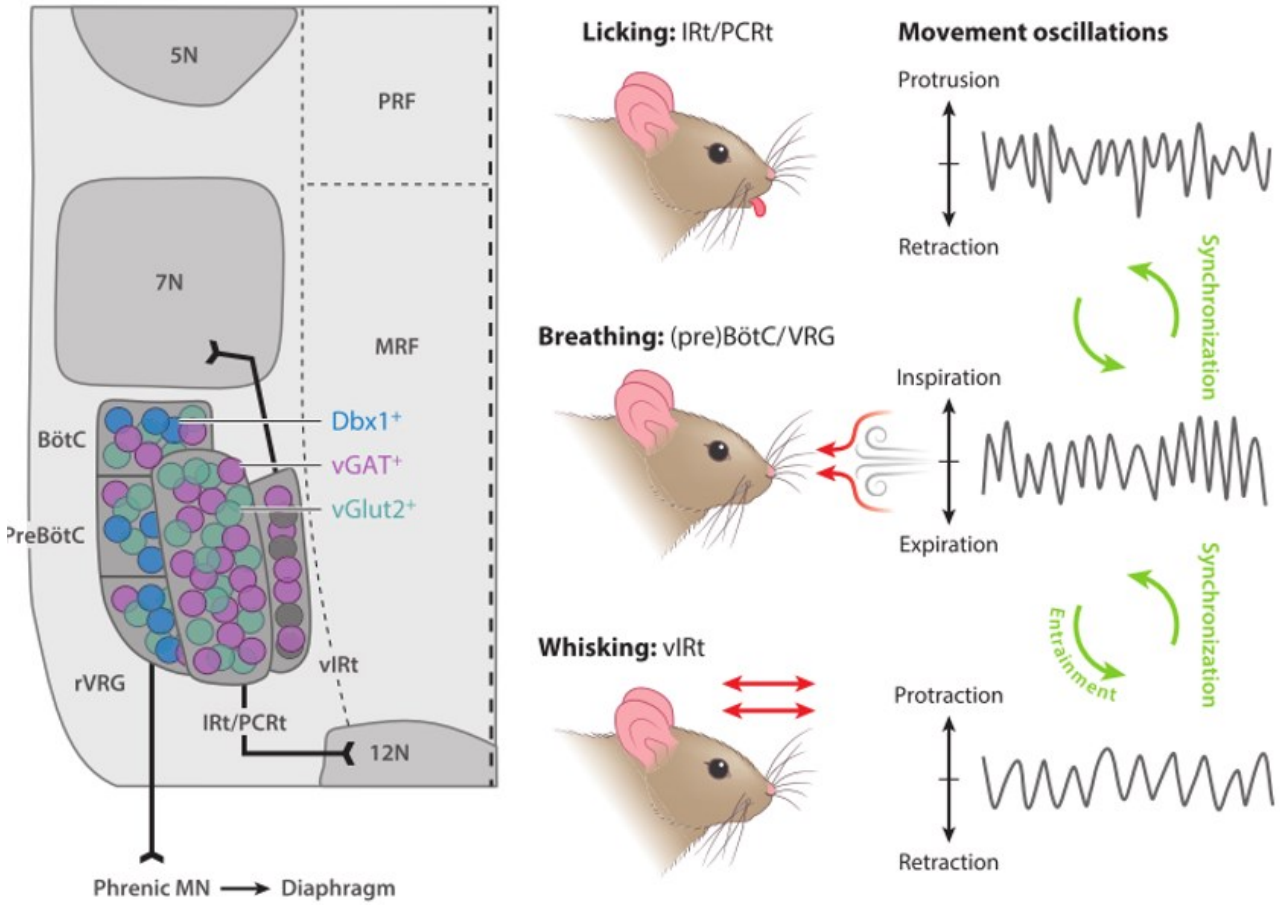

Figure 9. Schematic diagram illustrating the close spatial proximity of brainstem neurons implicated in orofacial and respiratory behaviors. (A) Top-down anatomical depiction of the BötC, preBötC, rVRG, IRt, and PCRt. Excitatory vGlut2 (teal) and inhibitory vGAT (purple) neurons, as well as Dbx1 (blue) neurons, are shown. The rostrocaudal boundary between MRF and PRF is indicated along with relevant cranial motor nuclei (gray). (B) Depiction of licking, breathing, and whisking behaviors with the implicated brainstem structures, and how rhythms between these behaviors can be synchronized. The breathing rhythm can entrain the whisking rhythm, indicating a network between relevant circuit elements. Abbreviations: 5N, fifth motor nucleus; 7N, seventh motor nucleus; 12N, hypoglossal motor nucleus; BötC, Bötzinger complex; Dbx1, developing brain homeobox protein 1; IRt, intermediate reticular nucleus; MN, motor neuron; MRF, medullary reticular formation; PCRt, parvicellular reticular nucleus; preBötC, pre-Bötzinger complex; PRF, pontine reticular formation; rVRG, rostral ventral respiratory group; vGAT, vesicular GABA transporter; vGlut2, vesicular glutamate transporter 2; vIRt, vibrissa zone of the intermediate reticular nucleus (Ruder and Arber, 2019).

Such movements are controlled by dedicated pools of motoneurons located within the brainstem: the cranial motor nuclei (Guthrie, 2007). Understanding the premotor circuits controlling these motor nuclei represents a big challenge. Many studies focus on revealing the presynaptic connectome of the brainstem motor nuclei (Deschenes et al., 2016; Stanek et al., 2014; Takatoh et al., 2013; Takatoh et al., 2021).

Other studies focus on investigating the brainstem circuits that control respiration, and it has been showed that the preBötC complex is a main structure in controlling breathing and it has access to the phrenic nerve via the rostral ventral respiratory group (Del Negro et al., 2018; Feldman et al., 2013) (see section 1.1.2). It is extremely important to mention that different orofacial behaviors might be active synergistically but also can occur isolated from the others depending from the behavioral needs, suggesting that there might be separated circuits for each orofacial behavior but they might be also in communication when they are recruited in coordination (Moore et al., 2013).

1.2.5 The medullary reticular neurons and locomotor movements

Different studies showed that the locomotor-promoting signal from the MLR does not reach directly the spinal cord, but is rather relayed by the medullary reticular formation (Brownstone and Chopek, 2018; Dubuc et al., 2008; Jordan et al., 2008; Noga et al., 2003; Shefchyk et al., 1984). Moreover, in many different species including the lamprey ducks, geese, guinea pig, cats (Marlinskii and Voitenko, 1992; McClellan and Grillner, 1984; Steeves et al., 1987) the medullary reticular formation is crucial in controlling locomotion. Recent work focused on investigating whether the medullary reticular formation neurons relay the motor command from the MLR to the spinal cord. Furthermore, the medullary reticular formation receives inputs from other regions of the brain that are known to control locomotion, from the cerebellar locomotor region (Mori et al., 1998) and the subthalamic locomotor region (Sinnamon and Stopford, 1987).

It has been shown that RS neurons are fast conducting (Degtyarenko et al., 1998; Noga et al., 2003; Orlovskii, 1970a) and that they are active during spontaneous locomotion

(Drew et al., 1986; Matsuyama et al., 2004; Shimamura and Kogure, 1983; Shimamura et al., 1982). Anatomically, RS projections were founded both in the ipsilateral and contralateral ventrolateral funiculus (Steeves et al., 1980) and in different regions of the spinal cord, comprising the lumbar spinal cord, where is located the locomotor CPG (Jankowska, 2008; Matsuyama et al., 2004). However, while in non-mammalian animal models the stimulation of the medullary reticular formation clearly promotes locomotion, experiments on the mammalian medullary reticular formation showed controversial results. Mainly, it has been proposed that the divergent outcomes observed might be due to the cell heterogeneity of the RS neurons (Arber and Costa, 2018; Brownstone and Chopek, 2018; Jordan et al., 2008; Orlovskii, 1970b; Ruder and Arber, 2019). Indeed, RS neurons can differ based on their neurotransmitter and works focused on both excitatory, including glutamatergic and serotonergic, and inhibitory (both GABAergic and glycinergic) RS neurons with the idea that the first type would promote locomotion, while the latter would prevent it (Jordan et al., 2008).

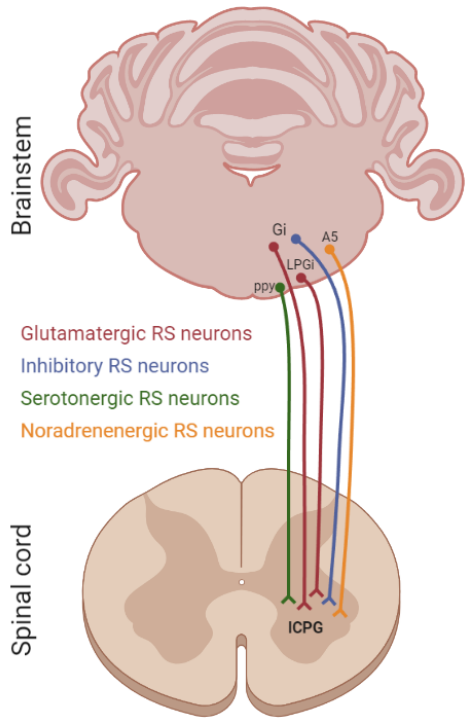

Figure 10. Schematic representation of distinct RS neurons of the medullary reticular formation. The glutamatergic RS neurons (in red) are commonly thought to promote locomotion, while inhibitory RS neurons (in blue) to prevent or block locomotion. The serotonergic RS neurons (in green) are considered to favor the ongoing locomotion. The noradrenergic RS neurons (in yellow) do not alter locomotor activity.

Certainly the most important source of signal that may favor locomotor, and motor actions in general, is thought to be glutamatergic RS neurons. Indeed, the bath application of glutamate is the most effective way to obtain locomotor-like activities on isolated spinal cord preparations from lamprey, rodents and cats (Dale and Roberts, 1984; Douglas et al., 1993; Grillner and El Manira, 2020; Grillner et al., 1981; Kudo and Yamada, 1987). On the contrary, blocking NMDA receptors in the spinal preparation, and in intact animals, impairs locomotion (Chau et al., 2002; Giroux et al., 2003), including that evoked by stimulation of the MLR. Furthermore, it has been showed that the optogenetic stimulation of glutamatergic brainstem neurons on isolated brainstem spinal cord preparation, can promote locomotor-like activities (Hagglund et al., 2010). Recently, the glutamatergic neurons in the lateral paragigantocellular nucleus (LPGi) of the brainstem were shown, when activated with optogenetics, to promote locomotion in freely-moving mice (Capelli et al., 2017). On the contrary, it was reported that the stimulation of the glutamatergic neurons in the adjacent Gi does not initiate locomotion *per se*, but help stabilize postural tone and tune the ongoing pattern (Lemieux and Bretzner, 2019). Others nevertheless argue for a role of Gi glutamatergic neurons in favoring locomotion, notably following spinal cord injury (Engmann et al., 2020). Therefore, while there is accumulating evidence for a role of some glutamatergic RS neurons in promoting movements, including locomotion in response to MLR signals, the identity, nature and location of such locomotor-promoting neurons is still not fully resolved. Furthermore, I will illustrate in the next chapter that considering smaller subsets of neurotransmitter-defined RS neurons will reveal that even excitatory ones can mediate a functional inhibition. Therefore, the glutamatergic status is only a poor predictor of the function of RS neurons and may include a substantial diversity.

Investigations of inhibitory neurons in the medullary reticular formation indicate that they may form a general signal for motor inhibition. One best example that incriminates reticulospinal inhibitory neurons is the induction of muscular atonia of the whole body during REM sleep (Vetrivelan et al., 2009). Regarding inhibition during wakefulness, it was shown in the xenopus tadpole that head contact with obstacles activates GABAergic descending pathways that immediately terminate swimming (Perrins et al., 2002).

Furthermore, the activation of inhibitory neurons located in the GiA, GiV and Gi, blocks ongoing locomotion (Capelli et al., 2017). A motor inhibition signal, including for locomotion, may also be conveyed by inhibitory reticular neurons projecting to subcortical structures, including the thalamus (Giber et al., 2015). Therefore, evidence so far implicate a general role of inhibitory neurons of the medullary reticular formation, being descending or not, in mediating motor arrest. Here again, the possibility for differences among cell-types and spatial location is not documented.

Aside the excitatory and inhibitory amino acids, serotonergic medullary neurons may play a significant role. Although they are not systematically classified as belonging to the reticular formation, one should stress that the raphe nucleus is not the only source of serotonin in the brainstem. In particular, several laboratories have investigated serotonergic RS neurons that are located in the Parapyramidal region (Ppy), largely overlapping with the lateral paragigantocellular reticular nucleus (LPGi). The idea that a descending serotonergic pathway might promote locomotion is prompted from several observations. First, on neonatal spinal cord preparation, the application of serotonin promotes locomotor-like activities (Cazalets et al., 1990; Cazalets et al., 1992; Cowley and Schmidt, 1994, 1997; Schmidt and Jordan, 2000). Secondly, the transplantation of serotonergic cells within the thoracic cord activates locomotion (Ribotta et al., 2000). A more recent research demonstrated that using electrical stimulation of the Ppy region in a brainstem-spinal cord rat preparation elicits fictive locomotion, an effect dependent on spinal serotonergic receptors (Liu and Jordan, 2005). Furthermore, serotonergic neurons, including in the Ppy, show increased expression of the immediate early gene c-fos after MLR-induced locomotion (Opris et al., 2019). Overall, serotonergic descending tracts may play a role in evoking or stabilizing locomotion, although here again, without a clear identification of the incriminated cells nor of their connectivity to the locomotor CPG.

Finally, activation the noradrenergic and dopaminergic receptors elicits fictive locomotion in neonatal rat spinal cord preparation (Gabbay and Lev-Tov, 2004; Kiehn et al., 1999). However, few experiments were performed on noradrenergic and adrenergic RS medullary neurons. Indeed, noradrenergic and adrenergic RS neurons are found in limited

number in two restricted areas of the brainstem: the A5 and A11 cells group of the brainstem Clark (Bjorklund and Skagerberg, 1979; Qu et al., 2006). While the RS dopaminergic neurons of A11 cell group have not been tested, the depletion of noradrenergic RS cells of the brainstem A5 group does not alter the ongoing locomotion (Jasmin et al., 2003; Steeves et al., 1980).

Given the importance of the RS neurons in body movements and in locomotion, it is crucial to consider the RS system as a target for therapies aimed to the recovery of the motor circuits following trauma. In particular, Spinal cord injury (SCI) is an incurable condition which leads to a highly debilitating loss of motor and sensory functions below the injury often including the ability to walk and stand (Sekhon and Fehlings, 2001; Varma et al., 2013; Wilson et al., 2012). The interruption or weakening of the descending neuronal tracts, and in particular of the reticulospinal tract, is the major cause of loss of motor autonomy following SCI. Therefore, strategies aiming at enhancing the survival or regrowth of severed descending axons are highly promising for promoting recovery after SCI. It has been showed that the RS neurons collectively show strong plasticity following SCI (Lu et al., 2012; Pearse et al., 2004; Zorner et al., 2014) and may actually be the tract the most disposed to plasticity (Asboth et al., 2018; Vavrek et al., 2007). RS neurons in the ventral reticular formation can notably sprout across the spinal midline following a hemi-section model and may also have the capacity to regenerate (Lu et al., 2012). Medullary 5-HT RS neurons also show plasticity (Basso et al., 2002; Vavrek et al., 2007). In fact, increasing 5-HT neurotransmission in the spinal cord improves recovery after experimental SCI and in humans (Ghosh and Pearse, 2014; Ribotta et al., 2000; van den Brand et al., 2012; Wenger et al., 2016). A critical step for functional recovery after SCI would thus be the restoration of glutamatergic and/or serotonergic innervation beyond the lesion. Finally, an interesting aspect for both RS and 5-HT neurons is that favoring their activity may stimulate their endogenous plasticity (Hentall and Gonzalez, 2012; Lu et al., 2012).

Altogether, these observations support the notion that RS neurons, within the medullary reticular formation, control multiple motor actions and relay the motor signal from the cognitive/integrative to the executory centers. However, the exact position,

identity, and connectivity of the cells implicated in controlling locomotion, and/or other motor actions are not identified yet. The complexity of the reticular formation has been a major lock for such investigations. We should stress here that although serotonergic, noradrenergic and dopaminergic neurons are often organized in clustered nuclei (therefore not literally belonging to the reticular formation per se, with the exception of the Ppy serotonergic neurons) and represent small populations, the glutamatergic and inhibitory ones are largely spatially intermingled and represent considerably larger populations that might even be heterogeneous. This makes the characterization of a single neurochemical pathway and its partners within the executory circuits a daunting task with classical system neuroscience approaches. Electrical recordings for instance cannot easily discriminate excitatory from inhibitory cell types. Electrical activations are similarly blind to cell-types, and also come with a poor control of the current spread and with the impossibility to disambiguate responses obtained from activating a neuronal somata from passing fibers of distant origin. Mechanical ablations or toxins do not help to resolve cellular specificity and have poor spatio-temporal control. In the next chapter, I will hence cover how novel methods of investigation based on developmental genetics can help to make huge progresses in investigating the medullary reticular formation and its involvement in controlling multiple motor actions by accessing smaller, presumably homogeneous, cellular ensembles.

1.3 Novel approaches to cellular diversity in motor circuits

1.3.1 Spinal cord development

The studies I mentioned in the previous chapters investigated the brain by mostly taking in consideration the location of the neuronal somata or the neurotransmitter released. In the field of spinal cord, one of the main strategies to investigate the function of smaller, and presumably homogeneous neuronal ensembles, has been to imprint tools from developmental biology, and in particular the concept that cells sharing a similar developmental history might share largely similar phenotypic properties (neurotransmitter, localization, electrical properties, connectivity), and thus a similar function. More precisely, reserachers have started to define a "cell-type" by the common history of expression, during development, of transcription factors essential for the cellular development and specification (Goulding, 2009; Kiehn, 2016). By using specific transgenic mouse lines engineered on the basis of such markers, scientists can now see, trace and manipulate a given cell type within a complex and heterogenous structure. This approach has largely been applied to the spinal cord, and I will hence describe its main fundamentals and benefits below. Nevertheless, a similar developmental coding of neuronal diversity applies to the brainstem and should allow new access to cellular diversity in the reticular formation. In fact, my worked investigated the only type of RS neurons defined by such considerations.

The main concept is that during the development of the spinal cord, the levels of expression in progenitor cells of specific developmental genes, namely transcription factors, vary along the dorso-ventral axis of the neural tube. Indeed, the expression oftranscription factors is dependent principally from the protein Sonic hedgehog (Shh) and bone morphogenetic protein (BMP). The concentration of Shh is higher ventrally, while BMP is more concentrated dorsally (Jessell, 2000) (Figure 11). These Shh and BMP gradients along the dorsoventral are fundamental in defining the neural fate of the cells along the axis (Barth et al., 1999; Briscoe and Ericson, 2001; Briscoe et al., 2000; Ericson et al., 1997; Roelink et al., 1995). In particular, the gradient of Shh induces the expression of different transcription

factors that can be grouped in two distinct classes. Class I proteins (Pax6, Bbx2) are repressed by Shh signaling, while Class II proteins (Nkx.2.2, Nkx6.1) are induced by Shh (Briscoe et al., 2000; Briscoe et al., 1999). The selective cross repression interaction between Class I and Class II proteins along the dorsoventral axis defines five domains of progenitors in the ventral spinal cord: p0, p1, p2, PMN, P3 (Briscoe et al., 2000).

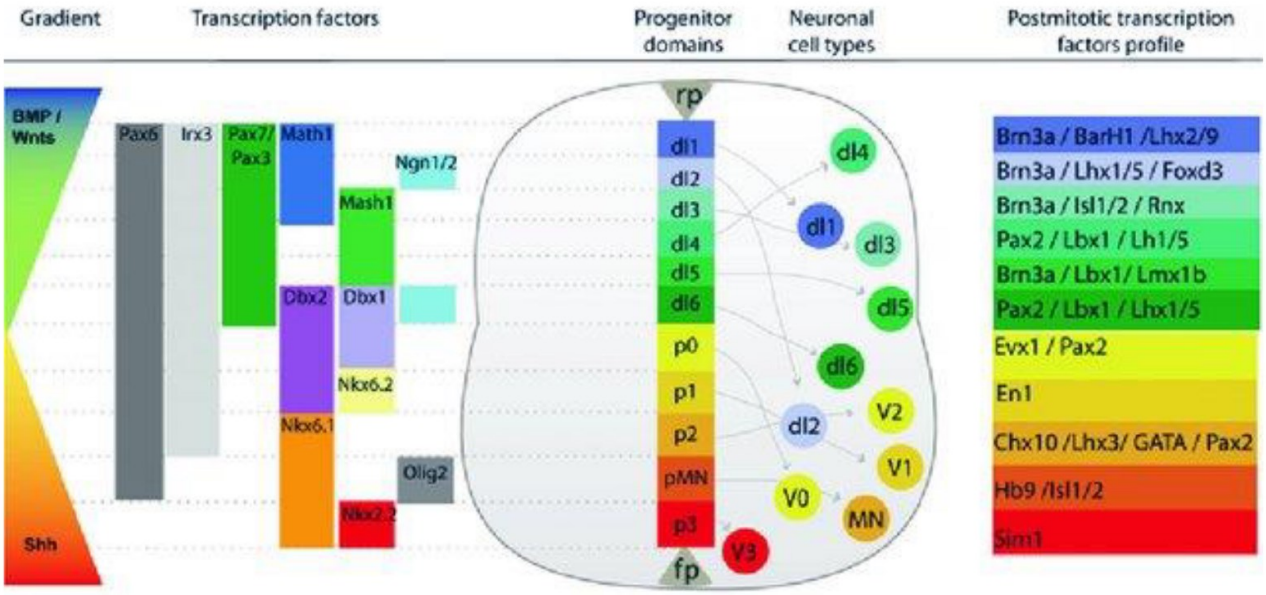

Figure 11. Patterning and cell specification by transcription-factors in the developing spinal cord. Patterning along the dorsoventral axis of the spinal cord is dependent on signaling from early developmental organizing centers. Sonic Hedgehog (Shh) that is secreted ventrally from the notochord and floor plate (fp) triggers the differentiation of ventral cell types. Similarly, Bone morphogenic proteins (BMPs) and Wingless-Ints (Wnts), secreted from the dorsal ectoderm and the roof plate (rp), have an important role in the specification of dorsal cell fates. These secreted proteins act as long-range morphogens, which establish a concentration gradient. In the neural progenitors, a given concentration of morphogens translates in the expression of a given set of transcription factors. Thus, progenitors will organize in "domains" along the dorso-ventral axis, with each domain expressing a unique combination of transcription factors. Dorsally-born progenitors are labelled dI1 to dI6, while ventrally born ones are labelled p0 to p3 for interneurons, and pMN for motoneuronal progenitors. Each progenitor domain will give rise to a discrete set of neuronal cell types, with neurons belonging to one cell type sharing similar properties (i.e. neurotransmitter phenotype, axonal projection...). Neuronal cell types themselves can again be recognized by their specific expression profiles of transcription factors. Interestingly, the final position of the differentiated neurons does not reliably reflect the position of the progenitor domain from

which they are born. Cell-type specific manipulations can thus be achieved by driving the expression of reporter proteins or interfering tools under genetic control a TF (or a combination of TF) that is specific to the cell-type of interest.

When progenitors exit the cell cycle and differentiate into neurons, the dorsal p0 and p1 progenitors generate ventral 0 (V0) and ventral 1 (V1) cells, while the p2, pMN and p3 ventral progenitors generate Ventral 2 (V2) neurons, the somatic motoneurons (sMN) and ventral 3 (V3) neurons (Briscoe et al., 2000; Briscoe et al., 1999). Within these five classes of neurons, scientists determined further subpopulations based on the expression of identified transcription factors (Briscoe and Ericson, 2001).

1.3.2 Benefits to the investigation of spinal executory centers

Thanks to the new insights on the spinal cord development, different research have extensively been using the corresponding genetic tools to manipulate such genetically-defined cell types of the spinal cord. As a result, enormous progresses have been made in understanding how the executory centers within the spinal cord control locomotion.

To understand how the locomotor CPG control locomotion there are hierarchical features that are necessary to take in account: the left-right alternation system, the rhythm generating system and the flexor-extensor patterning system (Kiehn, 2006). On the one hand, the coordination between the two sides of the body is under the control of commissural neurons. These are characterized by axons that cross the midline and make synapses with neurons on the contralateral side of the spinal cord. Several studies converged on the fact that a most important class of neurons for left/right coordination are V0 neurons. They are located in the ventral spinal cord and are born from DBX1-expressing progenitors of the p0 domain (Pierani et al., 2001). It has been showed that the ablation of V0 neurons disrupt left-right alternation (Lanuza et al., 2004). The V0 neurons are subdivided in inhibitory V0d neurons, that coordinate limb alternations at low locomotor frequencies, and excitatory V0v neurons, that control left right alternation at higher frequencies (Talpalar et

al., 2013). From these studies, it has been proposed that V0d neurons are active at low speed of locomotion, while the V0v neurons are active at high speed of locomotion (Bellardita and Kiehn, 2015). An intriguing conclusion of these studies is that part of the contralateral inhibition relies on excitatory neurons (the V0v at high speed). This is counterintuitive for excitatory neurons, but it illustrates very well my earlier postulate that, in complex and heterogeneous structures, neurotransmitter identity is not always accurate to predict function. It also illustrates the importance of post-synaptic targets to appreciate function: that V0d and V0v neurons both mediate contralateral inhibition requires that they each contact different cell types on the opposite side.

On the other hand, the generation of the locomotor rhythm was known to be dependent from excitatory spinal interneurons (Goulding, 2009; Hagglund et al., 2010; Roberts et al., 2008). However, the identity of the underlying neurons remains to be fully elucidated. Experiments on excitatory V2a neurons (expressing the transcription factor Chx10) demonstrated that this population does not affect locomotor rhythm (Crone et al., 2008). In contrast, experiments on spinal excitatory neurons expressing the transcription factor SHOX2+ (expressed in some V2a neurons and some non-V2a neurons) demonstrate that the non-V2a SHOX2+ population has a role in generating the locomotor rhythm (Crone et al., 2008). Silencing the activity of the non-V2a SHox2+ population indeed reduces the rhythmogenicity, however without completely blocking it (Dougherty et al., 2013). Another neural population investigated in the control of rhythm are the neurons expressing HB9, that are located in the ventral spinal cord, and demonstrated that they have rhythmogenic cellular properties supporting a role in rhythm generation (Brownstone and Wilson, 2008; Caldeira et al., 2017).

Finally, the coordination between the activity of motoneurons controlling antagonist muscles (flexor and extensor muscles) of a given limb is another crucial trait of the locomotor behavior. An essential role in regulating this function is made by reciprocal-Ia-inhibitory interneurons, that are activated by the stretch-activated group Ia afferent from muscle spindles. Furthermore, the reciprocal-Ia-inhibitory interneurons inhibit the motoneuron that is antagonist to the motoneuron activated by Ia afferent neurons (Hultborn, 1976;

Talpalar et al., 2011). Another study demonstrated that the ablation of V1 interneurons inhibit flexor activity, while ablation of V2b neurons inhibit extensor activity (Zhang et al., 2014).

As we can conclude from these investigations on the spinal cord network for controlling locomotor activity, the identification of a cell types by their developmental history allowed to describe its function and anatomy. Therefore, it is a common thought that this method of investigation might crucial for studying the medullary reticular formation and its role in motor control. In the next chapter, I will introduce the only RS neural population that has been genetically identified and that represents the starting point of my investigations.

1.3.3 The case of V2a reticular neurons

The concepts from developmental biology that I described in the previous section have seldom been applied to the brainstem reticular formation, although similar principles and combination of transcription factors apply (Briscoe et al., 1999). My supervisor was one of the firsts to benefit from these concepts and apply them to the identification of functional cell types in the reticular formation. He and others notably identified the vital role of brainstem V0 neurons for inspiratory rhythm generation in the preBötC (Bouvier et al., 2010; Gray et al., 1999). Interestingly, these V0 neurons also mediate the characteristic left/right synchronicity of diaphragmatic contractions. This illustrates that developmentally-defined cell types in the brainstem and spinal cord share some similarities (V0 neurons are commissural in both cases) but their functional outcome is obviously distinct (breathing versus locomotion). Even more interestingly, some follow-up work revealed that the same neuronal class (V0 neurons) in the brainstem also constitute the pre-motor output of the preBötC to the phrenic motor neurons. The V0 neuronal class hence has reticulospinal projections, but seems overall tuned for inspiratory control. Other studies have revealed genetic determinants of other important components of the respiratory CPG, including in the PFRG region. Indeed there, the subgroup of neurons relevant for modulating respiratory

rhythm generation, at least in the context of central chemoception are best identified by a combined history of expression of the transcription factors Phox2b and Atoh1 (Ramanantsoa et al., 2011; Ruffault et al., 2015). Other studies have identified crucial neurons of the brainstem reticular formation and linked them to a function, mostly in orofacial control (Hernandez-Miranda et al., 2017).

In contrast, the identification of specific neurons for the control of limb and body movements has progressed slowly. To date, the only genetically-identified class of RS neurons are the V2a neurons, neurons that have expressed Lhx3 and Chx10 (Al-Mosawie et al., 2007). The V2a neurons form a column that span throughout the brainstem and the spinal cord. As already described in previous chapters, V2a neurons located within the spinal cord have been investigated, but less was known about their function in the brainstem. First studies on the V2a neurons of the brainstem were done almost simultaneously on both zebrafish and mice (Bretzner and Brownstone, 2013; Kimura et al., 2013). Kimura and colleagues showed that chx10-expressing neurons in the hindbrain of the zebrafish are active during swimming and when activated with optogenetics, they induce the bending of the body that make the zebrafish swimming (Figure 12 D). Therefore, in Zebrafish, Chx10 neurons seem to trigger locomotion. Furthermore, they identified that there are at least two different types of Chx10 neurons based on electrophysiological properties. In parallel, a research conducted by Bretzner and Brownstone on mice, demonstrated that Chx10 neurons in mice are glutamatergic and projections were found at the level of the spinal cord. Furthermore, they demonstrated that V2a neurons were active during locomotor tasks and they have heterogeneous electrophysiological properties. Moreover, investigations of the calcium transients during MLR stimulation suggest that V2a neurons might receive inputs from this region in order to promote the ongoing locomotion.

A more recent study by my supervisor confirmed the reticulospinal status of V2a neurons at all levels of the medullary reticular formation (Figure 12 A). It also investigated the role these cells in mice during locomotion both in vitro and in in vivo (Bouvier et al., 2015). Surprisingly, the optogenetics activation of the medullary V2a neurons at rest did not evoke any locomotor activity. In contrast, it induced an immediate stop of the ongoing

locomotion if applied during displacement (Figure 12C). Conversely, silencing V2a neurons' activity led to hyperactive mice that could barely stop in an open field paradigm. The locomotor arrest driven by V2a RS neurons was ascribed to a functional inhibition of locomotor-generating properties of the locomotor CPG, rather than to a freezing response. This effect was also limited to a most rostral fraction of V2a neurons, residing in the Gi nucleus. Therefore, these V2a "stop neurons" represent another example (the spinal V0v

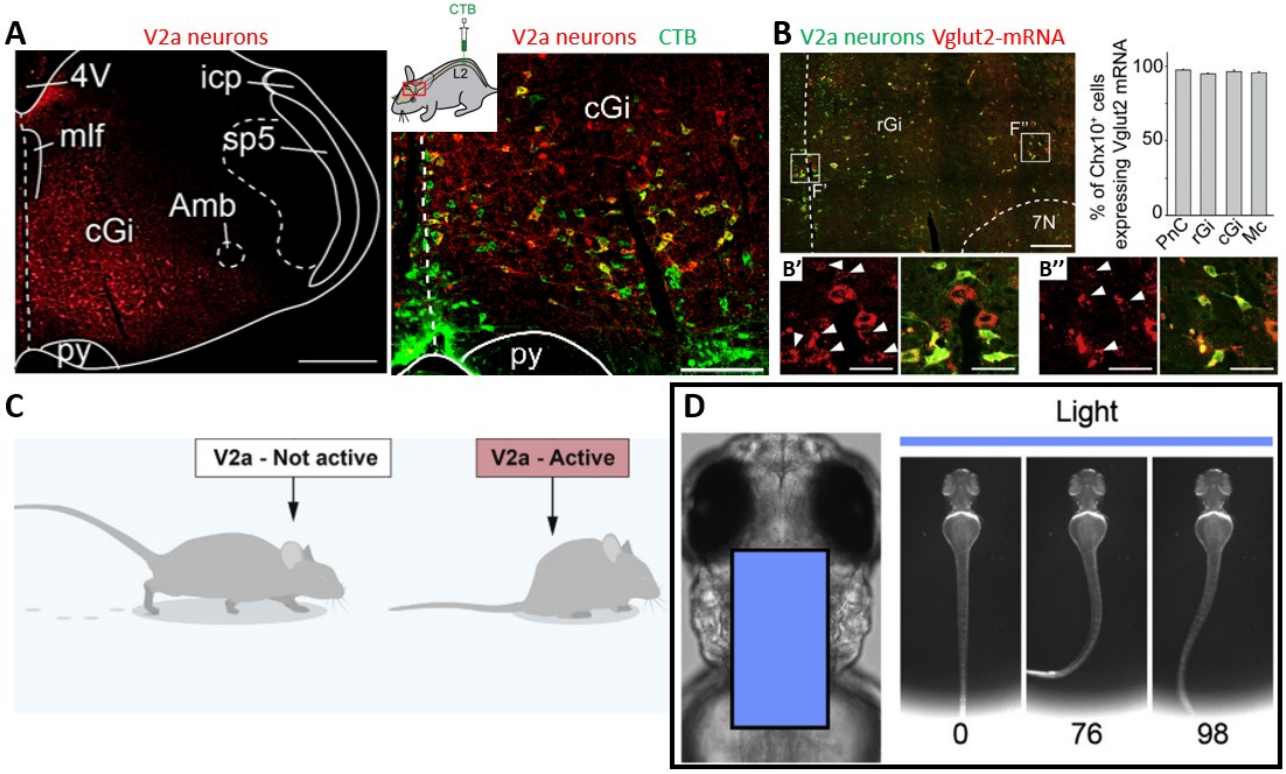

Figure 12. V2a neurons are reticulospinal and their function has been investigated in two species. (A) Left Panel: transverse hemi-sections of the caudal reticular formation stained for V2a neurons (Tdtomato reporter mice line). Small panel on the top-right: schematic representation of the injections of the retrograde marker CTB at the 2nd lumbar segment of the spinal cord. Right panel: transverse hemi-sections of the caudal reticular formation stained for CTB and V2a neurons. (B) Transverse hemi-section in the Gi indicating Vglut2+ glutamatergic (red) V2a neurons (YFP). Bar-graphs show the average percentage of Vglut2+ that are V2a neurons within different regions of the reticular formation. Insets in B' and B'' are magnified views of Vglut2 expression alone (left) and merged with YFP (right) of medially (B') and laterally positioned (B'') V2a neurons. White arrowheads indicate co-expression. (C) In mice, the ability to stop locomotion is regulated by V2a neurons that project to the spinal cord where they depress locomotor rhythm generation. (Bouvier et al., 2015; Kimura et al., 2013). (D) Activation of hindbrain V2a neurons elicits swimming in zebrafish. A flash of blue light was applied to the boxed area (left panel). This evoked swimming-like behavior (right panels).

ones being the first, see section 1.3.2) of an excitatory population that does not act to favor movement. Yet, the physiological role of this population was mysterious. As I will detail in the objectives, this observation prompted by PhD project.

I should note that my first publication on these V2a reticulospinal neurons was in 2020. Therefore, this is the current state of the art that was available to me until publication. Yet, for the sake of completeness, I should also mention here the work that have been published since. For instance, another project run in the lab in parallel than mine was to investigate the endogenous activity of V2a RS neurons in the mouse, during freely-moving displacement. Using calcium imaging performed on *in vivo* freely moving mice, my colleagues confirmed that V2a neurons are indeed active when the animal arrests its locomotion, but that this was only true for a fraction of V2a neurons. Others were active during different motor behaviors (Schwenkgrub et al., 2020). This suggested that the V2a neurons might control not only locomotor arrest, which was also my lead. Another study, this time led by an independent group, demonstrated that the unilateral activation of the medullary V2a neurons induces an ipsilateral turning of the mouse during ongoing locomotion (Cregg et al., 2020). As I will explain in the discussion, this investigation was performed almost in concert with mine, although I had no information about it. The findings are, at least at first glance, similar to mine but we will see that we reach substantially different conclusions on the circuit and mechanistic levels.

The medullary V2a neurons were hence, and still are nowadays, the only medullary RS neurons that are defined genetically and thus tractable. Since they form a subtype of glutamatergic neurons, and since their function seem to diverge from the classical view that excitatory circuits favor movement, they thus represent an exquisite entry-point to study diversity and specialization of RS neurons.

3. OBJECTIVES

The brainstem reticular formation is key for controlling motor actions. Indeed, reticular neurons interface multiple sensory and cognitive modalities upstream, with executory motor circuits downstream. However, how the reticular formation selects, initiates and combines multiple motor actions is largely unknown.

My PhD project is prompted by the above observation. We decided to start my exploration from a cell type of the reticular formation that has been genetically defined, the V2a neurons, but whose intrinsic diversity and function besides arresting locomotion, were not known. From this, my PhD project followed 3 objectives, that were run in parallel:

1. To start replacing these V2a neurons in larger behavioral circuits, and shine light on the behavioral relevance of their "locomotor stop" function, I have explored anatomically the origins of their inputs. For this, I deployed using cutting-edge, rabies-based viral tracing to label neurons located one, and only one synapse upstream the V2a RS neurons and high-throughput microscopy. By this, I aimed at deciphering what are the integrative/cognitive centers sending the command to the V2a neurons.
2. To test whether the V2a neurons control other motor behaviors besides locomotion, I took advantage from optogenetic techniques to unilaterally photo-activate the V2a medullary neurons and examined the consequences on multiple body-scale and orofacial movements. Furthermore, using retrograde tracings and circuit optogenetics, I investigated whether additional actions would be attributed to collaterals of a unique V2a population, or instead to distinct subsets that differ by projection.
3. To start investigating the postsynaptic targets of medullary V2a neurons in different executory centers, I started from the possibility, prompted by our behavioral recordings and some anatomical findings, that some might be directly

connected to specific motoneuronal pools. To demonstrate it, I aimed at revealing the presynaptic connectome of candidate muscles, using intramuscular deliveries of rabies viral vectors on newborn mice.

Furthermore, I participate at the research of another PhD student of the laboratory, Coralie Hérent. Her project aims to investigate the central circuits interfacing locomotor and respiratory centers. In particular, it focuses on the locomotor and respiratory' nodes that mediate the increase of the respiratory rate during running exercise. Indeed, one important request of the reviewers, after the initial submission, was to improve the anatomical mapping of transfected neurons. Since Coralie has left the lab for her postdoc, I got involved in some experiments to address this critic. I perfused animals, imaged brains and mapped neurons for analysis.

My PhD altogether aimed, taking V2a neurons as an entry-point, at decoding the extent to which the genetic classification of RS neurons is sufficient to approach neuronal diversity in the reticular formation. Combined with my contribution to the respiratory/locomotor interaction project, it also aimed at understanding better the neuronal basis of action diversification.

4. RESULTS

4.1. Control of orienting movements and locomotion by projection-defined subsets of brainstem V2a neurons

Article

Current Biology

Control of Orienting Movements and Locomotion by Projection-Defined Subsets of Brainstem V2a Neurons

Graphical Abstract

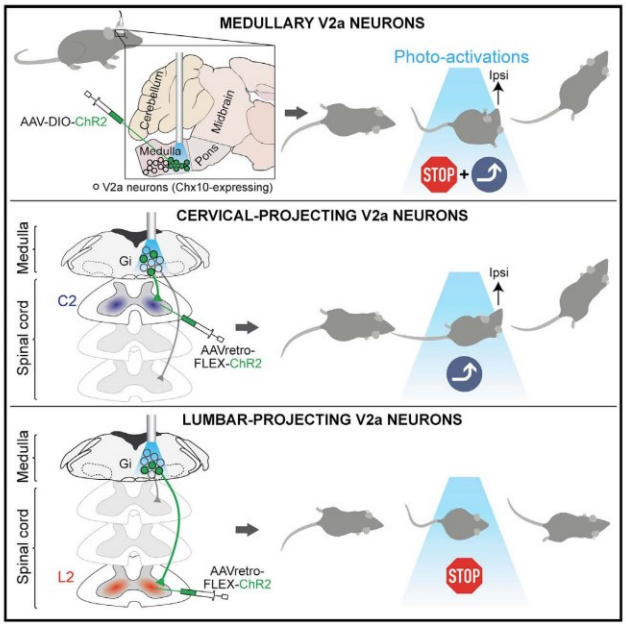

Highlights

- Brainstem V2a neurons control orienting movements, locomotor speed, and trajectory
- Distinct V2a subsets contact the cervical and lumbar spinal segments
- Cervical-projecting V2a neurons govern the head orientation and the path trajectory
- Lumbar-projecting V2a neurons are dedicated to control locomotor velocity

Authors

Giovanni Usseglio, Edwin Gatier, Aurélie Heuzé, Coralie Hérent, Julien Bouvier

Correspondence

julien.bouvier@cnrs.fr

In Brief

Usseglio et al. demonstrate that V2a neurons, a genetically circumscribed class of excitatory reticular neurons, control multiple motor actions linked to orientation. Using viral tracings and circuit optogenetics, they further uncover a modular organization of this neuronal class, with projection-defined subtypes that each support one motor action.

Usseglio et al., 2020, Current Biology *30*, 4665–4681
December 7, 2020
https://doi.org/10.1016/j.cub.2020.09.014

CellPress

Current Biology

CellPress
OPEN ACCESS

Article

Control of Orienting Movements and Locomotion by Projection-Defined Subsets of Brainstem V2a Neurons

Giovanni Usseglio,[1] Edwin Gatier,[1] Aurélie Heuzé,[1] Coralie Hérent,[1] and Julien Bouvier[1,2,*]
[1]Université Paris-Saclay, CNRS, Institut des Neurosciences Paris-Saclay, 91190 Gif-Sur-Yvette, France
[2]Lead Contact
*Correspondence: julien.bouvier@cnrs.fr
https://doi.org/10.1016/j.cub.2020.09.014

SUMMARY

Spatial orientation requires the execution of lateralized movements and a change in the animal's heading in response to multiple sensory modalities. While much research has focused on the circuits for sensory integration, chiefly to the midbrain superior colliculus (SC), the downstream cells and circuits that engage adequate motor actions have remained elusive. Furthermore, the mechanisms supporting trajectory changes are still speculative. Here, using transneuronal viral tracings in mice, we show that brainstem V2a neurons, a genetically defined subtype of glutamatergic neurons of the reticular formation, receive putative synaptic inputs from the contralateral SC. This makes them a candidate relay of lateralized orienting commands. We next show that unilateral optogenetic activations of brainstem V2a neurons *in vivo* evoked ipsilateral orienting-like responses of the head and the nose tip on stationary mice. When animals are walking, similar stimulations impose a transient locomotor arrest followed by a change of trajectory. Third, we reveal that these distinct motor actions are controlled by dedicated V2a subsets each projecting to a specific spinal cord segment, with at least (1) a lumbar-projecting subset whose unilateral activation specifically controls locomotor speed but neither impacts trajectory nor evokes orienting movements, and (2) a cervical-projecting subset dedicated to head orientation, but not to locomotor speed. Activating the latter subset suffices to steer the animals' directional heading, placing the head orientation as the prime driver of locomotor trajectory. V2a neurons and their modular organization may therefore underlie the orchestration of multiple motor actions during multi-faceted orienting behaviors.

INTRODUCTION

Our capacity to continuously adjust our attention and directional heading in response to internal goals or external stimuli is vital. It supports a large panel of behaviors including spatial navigation, exploration of the environment, feeding, and defense. In order to achieve this, animals mobilize lateralized motor actions that are often tightly coupled. In the animal's reference frame, coordinated movements of the head, the eyes, and in rodents, the orofacial sensors represent the primary mean to displace the visual axis and the sensory apparatus toward a point in space [1–3]. When the animal is on the move, these "strict" orienting responses are accompanied by a change in limb activity to reduce locomotor speed, to allow fixation and exploration of a fixed cue, and/or when needed, to change the path trajectory. How the brain orchestrates these multiple motor actions is still only partly resolved. Additionally, the mechanical substrate for trajectory changes during ongoing locomotion, whether it is head orientation [4–6], an asymmetric descending drive to limb controllers [7, 8], or a combination of both, has remained speculative. Much attention has been given to circuits for sensory integration, mainly to the superior colliculus (SC; reviewed in [9]). This midbrain structure synthesizes inputs from different sensory modalities and controls spatially targeted motion in the large sense, including head-eye responses, orofacial movements, and locomotor trajectory [10–14]. However, the cells and circuits that are downstream of the SC and relay orienting commands to the adequate motor groups have remained elusive.

The reticular formation (RF) of the pons and medulla is well known to control movements and is a candidate relay of orienting commands. First, the output layers of the SC project abundantly to the RF [15, 16]. Second, it hosts the circuits for ocular and orofacial movements [17, 18] as well as reticulospinal (RS) neurons that directly reach the spinal cord [19]. In particular, neck motoneurons of the upper cervical spinal cord that control the head orientation are contacted by RS neurons of the gigantocellular (Gi) reticular nucleus [20–22]. The timing and velocity of hindlimb movements, controlled by the lumbar spinal cord [23, 24], are also critically dependent on descending signals from the Gi and adjacent nuclei [25–28]. Third, left-right unbalanced activation or inhibition of the RF has been linked to head orienting movements [26, 29] and to the steering of swimming in the lamprey [8] and of locomotor-like activities on neonatal rat *in vitro* preparations [7]. However, these investigations did not determine the identity of reticular neurons that are downstream of the SC and mediate orienting responses, or examine their

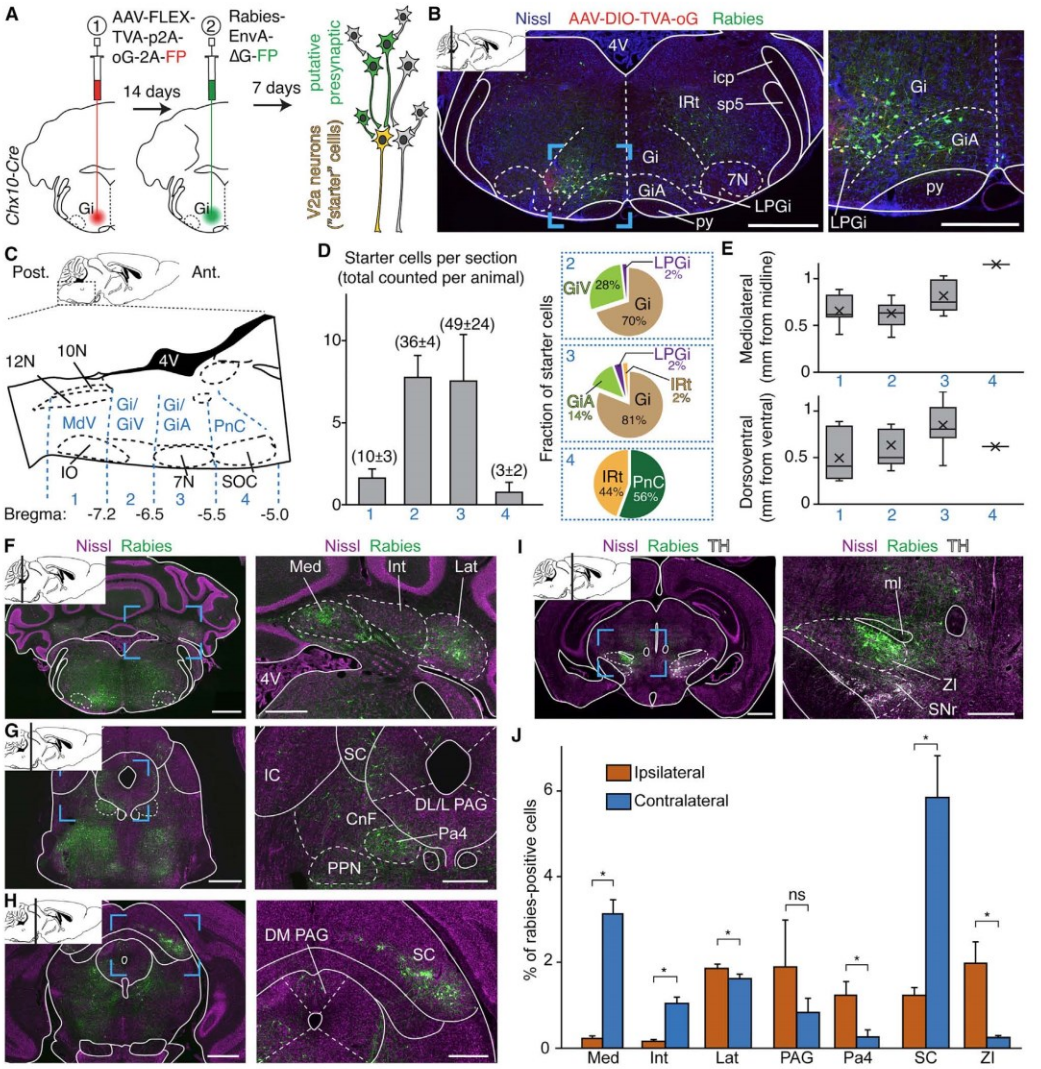

Figure 1. Retrograde Transneuronal Viral Strategy Reveals the Upstream Circuits of V2a Gi Neurons

(A) Schematics of the injection of the helper virus coding TVA and oG (1) and the EnvA-ΔG-rabies (Rb) virus (2) unilaterally in the left Gi of a *Chx10-Cre* adult mouse.

(B) Transverse brainstem section at the level of the injection site showing V2a neurons transfected with the helper virus (red), those co-transfected with the Rb virus ("starter" cells, yellow), and their putative presynaptic partners (Rb only, green), on a Nissl background (blue). Scale bar, 1 mm. Inset to the right is an enlargement of the blue boxed area. Scale bar, 500 μm.

(C) Sagittal schematic of the brainstem indicating the rostrocaudal levels (1 to 4) used for reporting starter cells.

(D) Bar graph showing the average number ± SEM of starter cells per histological section, and in brackets the average total ± SEM per animal, at the 4 rostrocaudal levels (total starter cells counted: 299 from 3 animals; average per animal: 100 ± 29). Pie graphs to the right show the distribution, within rostrocaudal levels 2, 3, and 4, of starter neurons in the indicated subnuclei (in percent of all starter cells at each level, pooled from the 3 animals). All cells at the rostrocaudal level 1 were in the MdV. See STAR Methods for the delineation of brainstem nuclei.

(E) Mediolateral (top, in mm from the midline) and dorsoventral (bottom, in mm from the ventral border) positions of starter cells at each rostrocaudal level (pooled from 299 cells from 3 animals) presented as the mean (crosses) and box-and-whisker plots, which give the median, 25th and 75th percentiles, and range.

(F–I) Transverse sections showing Rb^+ cells (green) at various rostrocaudal locations on a Nissl background (magenta). A tyrosine hydroxylase staining (TH, gray) is added in (I) to identify the SNr. Scale bars, 1 mm and 500 μm (insets).

(legend continued on next page)

implication to trajectory changes during limbed locomotion *in vivo*. Another significant gap of knowledge concerns the possibility for a synergistic control of distinct motor actions by a unique population, or by instead distinct subsets, of reticular neurons. Specifically, movements of the head, orofacial sensors, and locomotor velocity and direction are often tightly coupled [1, 2, 4, 5], and the existence of reticular neurons with branched axonal collaterals [19, 21] raises the possibility for a common control by a unique neuronal population. Yet this remained to be supported experimentally.

Here we investigated the possibility that brainstem V2a neurons, a genetically circumscribed neuronal class defined by the expression of the transcription factor Chx10 [30, 31], may control orienting motor actions. Indeed, they represent a subgroup of excitatory glutamatergic neurons located in the ventral RF, including in the Gi nucleus [32, 33]. Photo-activation of V2a Gi neurons in mice unexpectedly depresses spinal locomotor circuits [34], and this function could participate in steering locomotor trajectory [35]. Second, V2a neurons collectivity send both local and spinal projections [32–36], raising the possibility that this population, or subsets thereof, may drive other motor actions in synergy with limb control. However, these neurons have globally not been incorporated into the framework for studying orientation and nothing is known about their putative diversity.

Using transneuronal viral tracings, we show that V2a Gi neurons receive putative inputs from the contralateral SC, making them candidates for relaying lateralized orienting commands. Next, we found that unilateral photo-activations of V2a Gi neurons both evoked orienting-like motor responses on still animals and can halt and steer the locomotor trajectory when animals are on the move. Finally, and this is a major finding reported here, we reveal distinct functional subsets of V2a RS neurons with at least (1) a lumbar-projecting subset that controls locomotor velocity, but does not impact trajectory even when activated unilaterally, and (2) a cervical-projecting subset dedicated to head orientation and whose activation suffices to steer locomotor trajectory. These findings establish that multiple motor components of orientation are controlled by distinct reticular neurons that share a common genetic identity but that differ in their efferent connectivity. Furthermore, our work argues that the head orientation acts as the prime driver for steering locomotor trajectory.

RESULTS

V2a Gi Neurons Receive Putative Inputs from the Contralateral Superior Colliculus

To address whether V2a Gi neurons are embedded in circuits for orientation, we used a genetically restricted two-virus approach [37] to anatomically reveal their putative inputs (Figure 1A). Specifically, a cre-dependent AAV helper vector (AAV-DIO-TVA-oG-GFP; STAR Methods) was injected unilaterally in the Gi of *Chx10-Cre* adult mice [34, 38, 39], followed by a G-deleted and EnvA-pseudotyped rabies (Rb) virus coding mCherry. We aimed at transfecting V2a neurons unilaterally and located within the intermediate and rostral medullary reticular formation, i.e., rostrocaudal levels that house the Gi and its ventral and alpha parts (GiA/GiV; Figures 1B–1D) where V2a neurons that arrest locomotion are located [34]. Occasional starter cells were found in the adjacent intermediate reticular nucleus (IRt) and the lateral paragigantocellular nucleus (LPGi; Figure 1D), also known to contain V2a neurons [36]. Transneuronally labeled neurons, i.e., expressing only the Rb-driven fluorophore, were detected throughout the brainstem and to a lower extent in the diencephalon. A large proportion of Rb-positive cells was found in the medullary and pontine reticular formations, both ipsilaterally (15% ± 2% of total Rb^+ cells) and contralaterally (15% ± 3%). Aside from this local connectivity, labeling was detected in the deep cerebellar nuclei with various degrees of lateralization (Figures 1F and 1J). In the midbrain, confined labeling was seen in the periaqueductal gray and the mesencephalic reticular formation, notably in what may correspond to the paratrochlear nucleus (Pa4; Figures 1G and 1J). We found no Rb^+ cells in the cuneiform and pedunculopontine nuclei (CnF and PPN; Figure 1G), forming the mesencephalic locomotor region that controls forward locomotion [40, 41]. Importantly, the highest proportion of transneuronally labeled neurons aside from the reticular formation was observed in the SC, predominantly contralaterally (Figures 1H and 1J). Confined labeling was also observed in the zona incerta, mostly ipsilaterally (Figures 1I and 1J). More rostrally, only sparse Rb^+ cells were seen in the somatosensory and motor cortices (data not shown). These experiments indicate that V2a neurons of the Gi and adjacent nuclei are downstream of the SC and may therefore relay lateralized orienting commands.

Activating V2a Gi Neurons Unilaterally Evokes Orienting Motor Responses

To evaluate the capacity of V2a Gi neurons to mediate orienting movements when activated unilaterally, we virally delivered the Channelrhodopsin 2 (ChR2) in the Gi on one side (AAV-DIO-ChR2-eYFP) of *Chx10-Cre* mice and implanted an optic fiber on the same side (Figures 2A and 2B). We confined transfections sites unilaterally and to the rostral medulla, i.e., encompassing the Gi and the adjacent GiA nuclei (Figure S1A), where the strongest inhibitory effect on locomotion was reported [34]. We did not attempt to target smaller contingents (e.g., GiA versus Gi); we will therefore refer to V2a Gi neurons throughout the study.

When light stimulations were delivered unilaterally (500 ms trains of 15 ms pulses at 40 Hz) on stationary mice, the most

(J) Mean percentage ± SEM of Rb^+ cells in a given region over the total amount of Rb^+ cells (n = 3 animals, total cells counted: 8,157; average per animal: 2,719 ± 139). Regions presented are those showing the highest proportions of Rb^+ cells, outside of the RF, which accounted for 15% ± 2% ipsilaterally and 15% ± 3% contralaterally.

4V, fourth ventricle; sp5, spinal trigeminal tract; Gi, gigantocellular reticular nucleus; GiA, gigantocellular reticular nucleus alpha part; GiV, gigantocellular reticular nucleus ventral part; LPGi, lateral paragigantocellular nucleus; IRt, intermediate reticular nucleus; 7N, facial nucleus; py, pyramidal tract; Med, medial (fastigial) nucleus; Int, interposed nucleus; Lat, lateral (dentate) nucleus; IC, inferior colliculus; SC, superior colliculus; LPAG, lateral periaqueductal gray; DLPAG, dorsolateral periaqueductal gray; DMPAG, dorsomedial periaqueductal gray; CnF, cuneiform nucleus; PPN, pedunculopontine nucleus; Pa4, parathroclear nucleus; ml, medial lemniscus; ZI, zona incerta; SNr, substantia nigra pars reticulata.

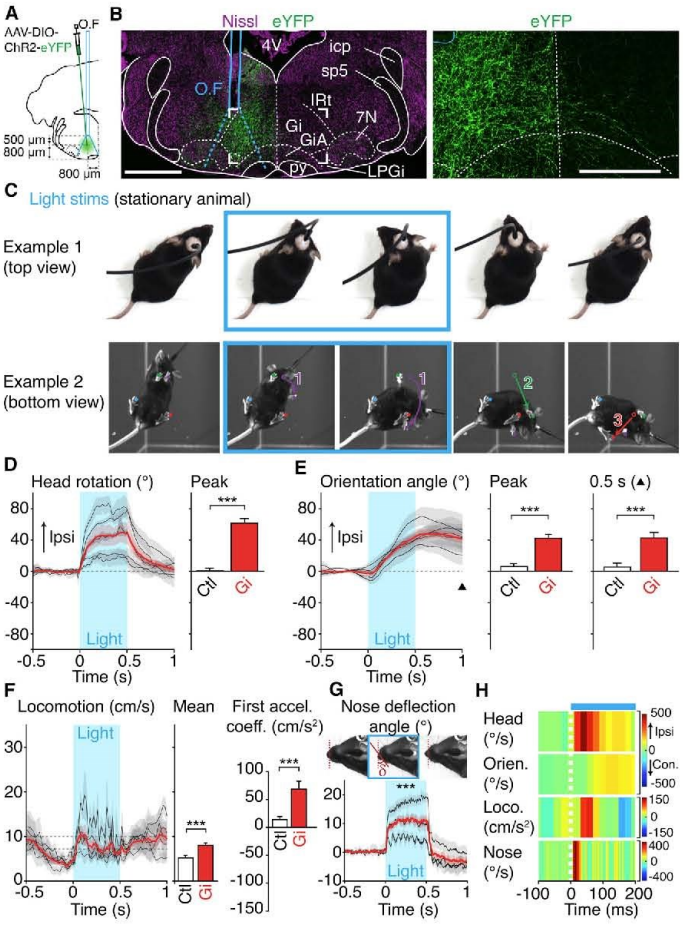

Figure 2. Unilateral Photo-Activations of V2a Gi Neurons Evoke Orienting-like Motor Responses

(A) Experimental strategy for photo-activating V2a Gi neurons. OF, optic fiber. The injection pipette is depicted with an angle for clarity, but the injection was performed without angle.

(B) Left: transverse section at the level of the Gi showing transfected V2a neurons (eYFP, green) on a Nissl background (magenta), the position of the OF, and the theoretical light cone at the fiber tip (dashed blue lines). Scale bar, 1 mm. Right: close-up view over the boxed area showing that transfected neurons are strictly restricted to the ipsilateral side. The vertical dashed line depicts the midline. Scale bar, 500 µm. See also Figure S1A.

(C) Two example snapshots from two animals, showing the typical head yaw rotation and the possible change in orientation evoked by the photo-activation of V2a Gi neurons (15 ms pulses at 40 Hz, for a duration of 500 ms, in blue). On the bottom view, colored numbers indicate the order of limb movements. See also Video S1.

(D–F) Left: mean ± SEM light-evoked changes in head yaw rotation (D), body orientation (E), and locomotor speed (F) for each animal (gray, n = 5 animals, 7 trials each) and across animals (red). The black arrowhead in (E) indicates the time point at 0.5 s after light offset. The dashed zone in (F) indicates the threshold from stationary (<7.5 cm/s) to locomoting (>10 cm/s) conditions. Bar graphs to the right show the mean ± SEM of the peak head rotation during photo-activations (D), the peak change in orientation during photo-activations and the orientation angle 0.5 s after light offset (E), and the mean locomotor speed and the first acceleration coefficient during photo-activations (F) across all trials (Gi, n = 35 trials from 5 mice, 7 trials each) compared with mock trials from control mice (Ctl, n = 44 trials from 4 mice, 11 trials each). ***$p < 0.001$ (unpaired t test). See also Figure S2 for the calculation of movements and the responses of control mice.

(G) Top: snapshots of one head-fixed animal showing the angular displacement of the snout (δ). Bottom: mean angular deflection ± SEM of the snout normalized to the angle during the same time interval before light onset, for each animal (gray) and across animals (red). ***$p < 0.001$ (paired t test between mean values 0.5 s before and during the 0.5 s photo-activations, n = 15 trials from 3 mice, 5 trials each).

(H) Color plot showing the first derivative of the above motor parameters from 100 ms before to 200 ms after light onset (the dashed white line indicates light onset). Note the rapid occurrence of nose deflection (peak change at 15 ms), followed by the head rotation (peak change at 40 ms) and the delayed change in body orientation (peak at 140 ms).

striking response was a robust rotation of the head in the yaw axis and a displacement of the body orientation toward the stimulated side (Figures 2C–2E; Video S1; see STAR Methods and Figures S2A–S2D for movement calculations). These movements were not seen in mock trials on injected and implanted wild-type mice (Figures S2E–S2H), which served as the reference for statistical comparisons in freely moving situations throughout this study (bar graphs in Figures 2D–2F). Photo-activations did not engage animals in sustained locomotor activity, but the forelimbs could perform one or two steps to maintain the body orientation with that of the head (Figures 2C and 2F). Following light offset, animals could regain their initial orientation, but in the majority of trials, they remained oriented toward the stimulated side (Figure 2E; compare also examples in Figure 2C and Video S1). Examinations on head-fixed animals revealed that photo-activations also evoked an immediate horizontal deflection of the snout tip toward the stimulated side (Figure 2G), known to accompany head orienting movements [2]. Finally, to examine the relative temporal occurrences of these motor responses, we computed and color-plotted the first derivative of each parameter after light onset (Figure 2H). This revealed that the change in nose positioning peaked first, on average at 15 ms after light onset, rapidly followed by the head rotation (at 40 ms), suggesting that these are the primary

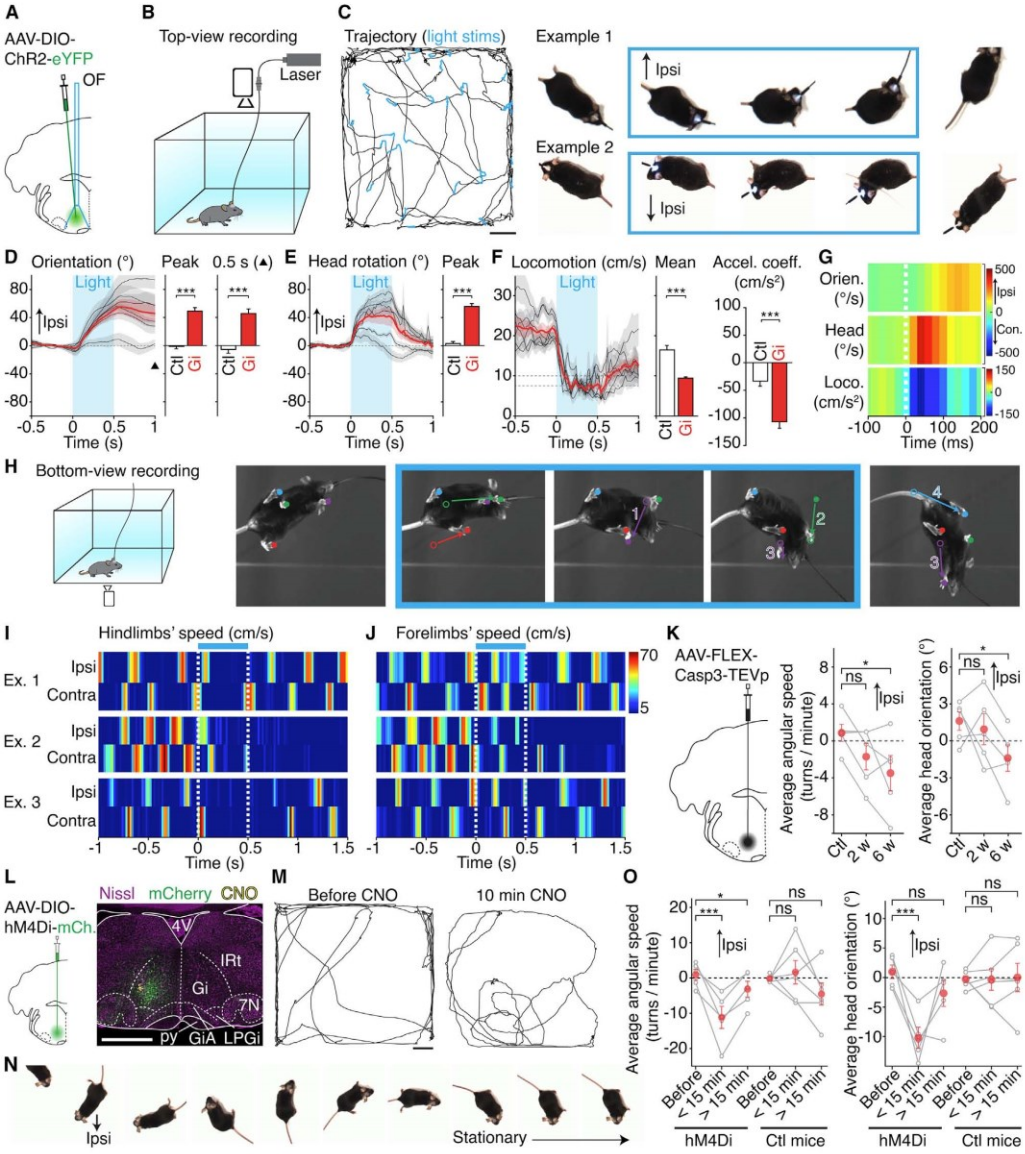

Figure 3. V2a Gi Neurons Control Locomotor Trajectory

(A) Experimental strategy for photo-activating V2a Gi neurons. OF, optic fiber. The injection pipette is depicted with an angle for clarity, but the injection was performed without angle. See also Figure S1A.

(B) Setup for top-view video recordings in an open field.

(C) Left: trajectory of one representative mouse for 3 min showing abrupt photo-evoked directional changes (15 ms pulses at 40 Hz, for a duration of 500 ms, in blue). Scale bar, 10 cm. Right: two example snapshots from two mice showing the typical light-evoked change of locomotor trajectory. See also Video S2.

(D–F) Left: mean ± SEM light-evoked changes in body orientation (D), head yaw rotation (E), and locomotor speed (F) of each animal (gray, n = 6 mice, 8 trials each) and across animals (red). The black arrowhead in (D) indicates the time point at 0.5 s after light offset. The dashed zone in (F) indicates the threshold from stationary (<7.5 cm/s) to locomoting (>10 cm/s) conditions. Bar graphs to the right show the mean ± SEM of the peak change in orientation during photo-activations and the orientation angle 0.5 s after light offset (D), the peak head rotation (E), and the mean locomotor speed and the first acceleration coefficient during

(legend continued on next page)

responses evoked. The change of body orientation occurred later with a peak angular speed at 140 ms. Altogether, these results indicate that activating V2a neurons in the Gi unilaterally evokes known motor components of oriented attention in rodents [2, 14, 42].

Activating V2a Gi Neurons Unilaterally during Locomotion Changes Trajectory

The orienting-like responses described above prompted us to test whether V2a Gi neurons also impact locomotor trajectory when animals are moving. For this, injected and implanted animals were placed in an open field and tracked from above (Figures 3A and 3B) while pulsed light stimulations were delivered during locomotion (i.e., instantaneous speed > 10 cm/s). We observed a striking and pronounced change of locomotor trajectory toward the stimulated side that persisted after light offset (Figures 3C and 3D; Video S2). This orientation change is associated with a rotation of the head (Figures 3C and 3E), reminiscent of the still trials. Additionally, locomotor speed was strongly reduced and animals reached the stationary threshold within 130 ± 30 ms of light onset (Figures 3C and 3F). This progressive locomotor halt, obtained here from strict unilateral activations (Figure S1A), recalls what was reported previously when activating the same cells bilaterally [34]. These motor changes were, however, not seen in, and are thus significantly different from, mock trials in control mice (bar graphs in Figures 3D–3F; see Figures S2I–S2K for responses of control mice). Temporal examination of the evoked motor sequence revealed that the head rotation and the locomotor deceleration occurred first and concomitantly (both peaked at 40 ms), followed by the body orientation (peak at 140 ms; Figure 3G). Manual tracking of the animal's paws showed that, during photo-activations, the hindlimbs terminate the ongoing step before remaining immobile and positioned symmetrically while the forelimbs performed left-right alternating movements toward the stimulated side (Figures 3H–3J; Video S2). When the animals resumed walking after light offset, they did so in the direction pointed by the head. Activating V2a Gi neurons unilaterally during ongoing locomotion therefore imposes a rapid yaw rotation of the head, a bilateral arrest of the hindlimbs, and a displacement of the forelimbs, altogether leading to a change of trajectory. Interestingly, these motor actions can also be expressed during naturally occurring changes in direction. Specifically, however, while the head yaw rotation often precedes the change in body orientation, the relative timing, or even the presence at all, of a locomotor deceleration was more variable (Figures S3A and S3B). Indeed, we found examples of turnings associated with a transient arrest of the 4 limbs followed by a reprise driven by the forelimbs, as well as some with continuing alternating movements of the 4 limbs (Figure S3C). This suggests that the motor sequence evoked by the photo-activation of V2a neurons can be mobilized, in whole or in part, during spontaneous directional changes.

Ablating V2a Gi Neurons or Impairing Their Activity Unilaterally Biases Locomotor Trajectory

We next addressed whether V2a Gi neurons are required for spontaneous changes of locomotor trajectory. We first virally delivered the genetically engineered caspase-3 unilaterally to V2a Gi neurons, to commit them to apoptosis [43]. In an open field test, injected animals showed a time-dependent bias to turn on the contralateral side (Figure 3K). Since this approach may mobilize compensatory circuits and does not allow us to quantify cell death, we next transiently silenced V2a Gi neurons using the inhibitory DREADD hM4Di delivered virally. Four weeks later, intracranial delivery of 1 m CNO was performed by another surgery (Figure 3L). Injections were unilaterally restricted and comparable to those of optogenetic activations, i.e., targeted to the Gi and GiA of the rostral medulla (Figure S1B). When examined immediately after the CNO delivery, animals showed only few episodes of locomotion owing to the partial recovery from anesthesia. Yet when they engaged in walking, either spontaneously or following motivation by the experimenter, they showed a very strong bias toward the contralateral side (Figures 3M–3O; Video S3). Moreover, the head was abnormally bent

photo-activations (F) across all trials (Gi) compared with mock trials from control mice (Ctl, n = 48 trials from 4 mice, 12 trials each). ***$p < 0.001$ (unpaired t test). See also Figure S2 for the calculation of movement changes and responses of control mice.

(G) Color plot of the first derivative of each motor parameter showing their temporal evolution from 100 ms before to 200 ms after light onset (the dashed white line indicates light onset). Note the rapid head movement and locomotor deceleration and the delayed change in body orientation.

(H) Setup for bottom-view video recordings and one example of a photo-evoked trajectory change. Colored numbers indicate the order of limb movements. See also Video S2 for the corresponding video and another example and Figure S3 for naturally occurring turns.

(I and J) Color plots of the velocity of the paws of the hindlimbs (I) and forelimbs (J) from 1 s before to 1 s after the 500 ms photo-activation. The y axis represents 3 example trials from distinct animals; the top one is shown in (H). The color gradient to red indicates speed values in cm/s. During photo-activations, the hindlimbs remain still after having terminated the ongoing step but the forelimbs continue moving.

(K) Caspase3-mediated ablation of V2a Gi neurons leads to a time-dependent increase of spontaneous turns toward the contralateral side, represented as the average angular speed per minute of walking (i.e., instantaneous speed > 10 cm/s), and to a biased orientation of the head. Gray open circles are the means of individual animals, and red circles are the means ± SEM across animals. 2 w, 2 weeks post-injection; 6 w, 6 weeks post-injection. Number of videos: Ctl, 13; 2w, 10; 6w, 11 (from 5 mice). *$p < 0.05$; ns, not significant (unpaired t test).

(L) Transient silencing of V2a Gi neurons by an hM4Di virus followed by intracranial delivery of 1 mM CNO by surgery (detected by fluorescent beads, yellow). Scale bar, 1 mm. See also Figures S1B and S1C.

(M) Trajectory of one representative mouse during 3 min in an open field before and 10 min after intracranial CNO delivery. Scale bar, 10 cm.

(N) Snapshots, taken every 500 ms, of one representative animal injected on the left side, showing a bias in locomotor trajectory and head position, even during stationary periods, toward the contralateral side. See also Video S3.

(O) Average angular speed per minute of walking (left) and average head rotation angle (right) showing the significant bias toward the contralateral side of hM4Di-injected CNO-treated mice (hM4Di, number of videos: before, 13; <15 min, 10; >15 min, 11; from 5 mice), but not following CNO delivery alone using a similar surgical procedure (Ctl mice, number of videos: before, 17; <15 min, 10; >15 min, 12; from 5 mice). Gray open circles are the means of individual animals, and red circles are the means ± SEM across animals. *$p < 0.05$; ***$p < 0.001$; ns, not significant (unpaired t test).

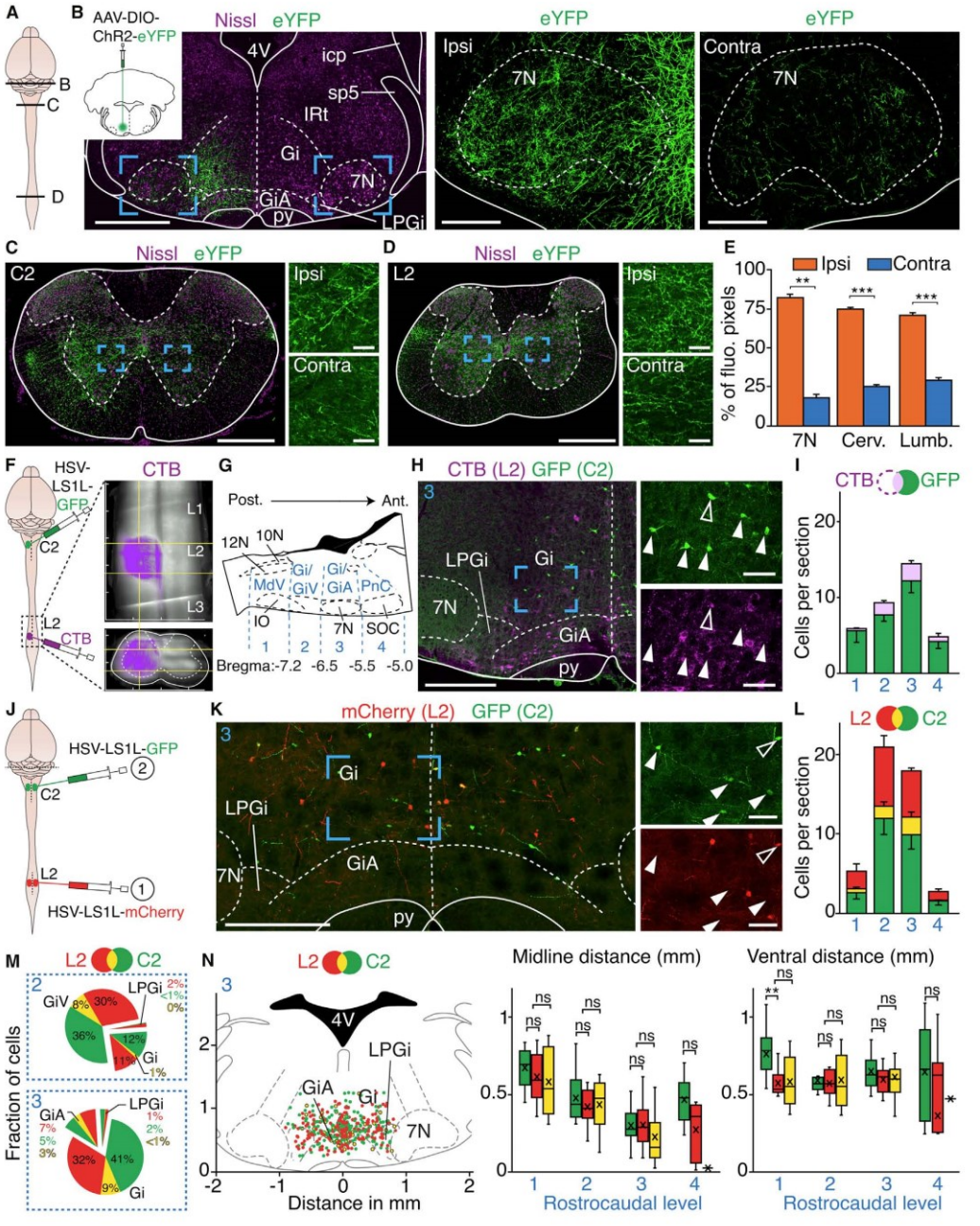

(legend on next page)

toward the contralateral side, an effect also noticeable during stationary periods (Figures 3N and 3O; Video S3). To exclude that these motor abnormalities are caused by the surgical procedure used to deliver the CNO, control (wild-type) mice that did not receive the hM4Di virus underwent a similar procedure, including anesthesia, CNO injection, and behavioral testing. These showed globally no bias toward the ipsilateral or contralateral sides (Figure 3O). The activity of V2a Gi neurons is therefore necessary for controlling locomotor trajectory and may also help to maintain an upright head position.

Distinct Subsets of V2a RS Neurons Show Preferential Projections to Specific Spinal Segments

Since V2a Gi neurons control multiple oriented actions, they should have lateralized access to the corresponding motor circuits. Indeed, V2a axonal projections densely innervate the facial motor nucleus (7N), associated with the whisker and snout musculature [17], as well as the upper cervical and lumbar segments, containing, respectively, the neck [20] and hindlimb [23, 24] motor circuits (Figures 4A–4D). Projections were found on both sides with a predominant ipsilateral contribution (Figure 4E). We next addressed whether these distinct target regions are contacted by a unique population of V2a neurons with branched collaterals or, instead, by distinct subsets with target-specific projections. For the rest of the study, we focused on the head rotation, body orientation, and control of the hindlimbs since these actions are piloted by spinal circuits and may therefore be under a common control by branched RS neurons. We first combined a Cre-dependent retrogradely transported herpes-simplex virus (HSV) [44, 45], injected into the 2nd cervical segment (C2), with cholera toxin B (CTB) injected into the 2nd lumbar segment (L2; Figure 4F). Retrogradely labeled V2a neurons from C2 were found throughout the RF, but only a minority were co-labeled with CTB (14% ± 2% overall; 12% ± 3% at the level of the Gi/GiA where optogenetic activations are performed; Figures 4G–4I). This indicates that the majority of V2a neurons do not have access to both spinal levels. To corroborate this further, we retrogradely labeled V2a neurons from both the C2 and L2 segments conjointly, using two Cre-dependent HSVs each coding a distinct fluorophore (Figure 4J). The majority of labeled V2a neurons were again expressing one, but rarely both, fluorophores (Figures 4K and 4L). Specifically, at rostrocaudal levels where photo-activations are performed, double-labeled V2a neurons represented only 11% ± 2% of all labeled cells. In contrast, when the two HSVs were injected at the same spinal segment (L2) either conjointly or sequentially, we found >90% of co-labeling (Figure S4), confirming previous reports that multiple HSVs can be expressed in individual cells [46]. Therefore, the preferential expression of either fluorophore in the dual C2/L2 HSV injection reflects the existence of distinct V2a subsets each having preferential projections to a specific spinal segment. Interestingly, these subsets were similarly distributed across the different nuclei of the ventral RF (Figures 4L and 4M). Moreover, reporting their mediolateral and dorsoventral positioning did not reveal any spatial segregation except at caudal-most levels (MdV) where the C2-projecting ones tended to be positioned more dorsally (Figure 4N). Finally, using a projection-based delivery of the rabies proteins oG and TVA, we found that both the C2 and L2-projecting V2a subsets receive inputs from the SC and, qualitatively, share similar input structures, albeit in varied proportions and with lower degrees of lateralization than the overall population (Figure S5). These observations altogether demonstrate the existence of distinct

Figure 4. Distinct but Spatially Intermingled V2a RS Neurons Show Preferential Projections to Specific Spinal Segments

(A) Schematic illustrating the position of the sections displayed in the following panels.

(B) Left: transverse section at the level of the Gi, where optogenetic activations are performed, showing the unilateral transfection of V2a neurons with an AAV-DIO-ChR2-eYFP. Scale bar, 1 mm. Right: magnifications of the blue boxed areas showing V2a projections in the ipsilateral and contralateral facial motor nuclei (7N). Scale bar, 200 μm.

(C and D) Transverse spinal cord sections from the same animal (representative of 3 mice), showing V2a projections at the 2nd cervical (C2) and 2nd lumbar (L2) levels. Dashed lines delineate the white matter. Scale bars, 500 μm and 50 μm (insets).

(E) Bar graphs showing the average percentage ± SEM of eYFP^{+} pixels located ipsilaterally and contralaterally in the 7N and in the cervical and lumbar white matter. ***$p < 0.001$; **$p < 0.01$ (unpaired t test; 7N, 10 sections; spinal cord, 12 sections; from n = 3 mice).

(F) Left: experimental strategy for labeling V2a RS neurons projecting to C2 with a Cre-dependent HSV and all L2-projecting neurons with CTB. LS1L, Lox-Stop-Lox. Right: example blend projection along the rostrocaudal (top) and transverse axis (bottom) of a CUBIC-cleared spinal cord imaged with light-sheet microscopy, showing the typical spread of dye load following an injection of CTB at L2 unilaterally. Thick marks, 500 μm.

(G) Sagittal schematic of the brainstem indicating the rostrocaudal levels (1 to 4, in blue), used for reporting labeled neurons.

(H) Transverse section (representative of 4 mice) at the rostrocaudal level 3 showing C2-projecting V2a neurons (GFP) and all lumbar-projecting neurons (CTB). Scale bar, 500 μm. Insets to the right are magnifications of the blue boxed area, showing the scarcity of double-labeled neurons (open arrowheads). Scale bar, 100 μm.

(I) Bar graphs showing, at the 4 rostrocaudal levels, the average number ± SEM of HSV and HSV;CTB-labeled neurons per histological section (n = 4 mice, 756 HSV^{+} cells counted in total; average per animal, 189 ± 24).

(J) Viral strategy for labeling V2a RS neurons projecting to C2 and L2 using Cre-dependent HSVs injected bilaterally.

(K) Left: transverse section (representative of 3 mice) at the rostrocaudal level 3 showing C2- (GFP) and L2-projecting (mCherry) V2a RS neurons. Scale bar, 500 μm. Insets to the right are magnifications of the blue boxed area, showing the scarcity of double-labeled neurons (open arrowheads). Scale bar, 100 μm.

(L) Bar graphs showing, at the 4 rostrocaudal levels, the average number ± SEM per histological section of V2a RS neurons projecting to either or both of the C2 and L2 segments (n = 3 mice; 844 cells counted in total; average cells per animal, 281 ± 33).

(M) Pie graphs showing the distribution, at rostrocaudal levels 2 and 3, of labeled neurons within the indicated subnuclei (in percent of all neurons at each level, pooled from the 3 mice). All cells at level 1 were in the MdV and all cells at level 4 were in the PnC.

(N) Left: transverse position of single- and double-labeled neurons at rostrocaudal level 3 where optogenetic activations are performed. Middle and right: mediolateral (in mm from the midline, absolute values from the left and the right sides are pooled) and dorsoventral (in mm from the ventral border) positions of single- and double-labeled neurons, presented as the mean (crosses) and box-and-whisker plots, which give the median, 25th and 75th percentiles, and range (844 cells pooled from 3 mice). **$p < 0.01$; ns, not significant (unpaired t test). See also Figures S4 and S5.

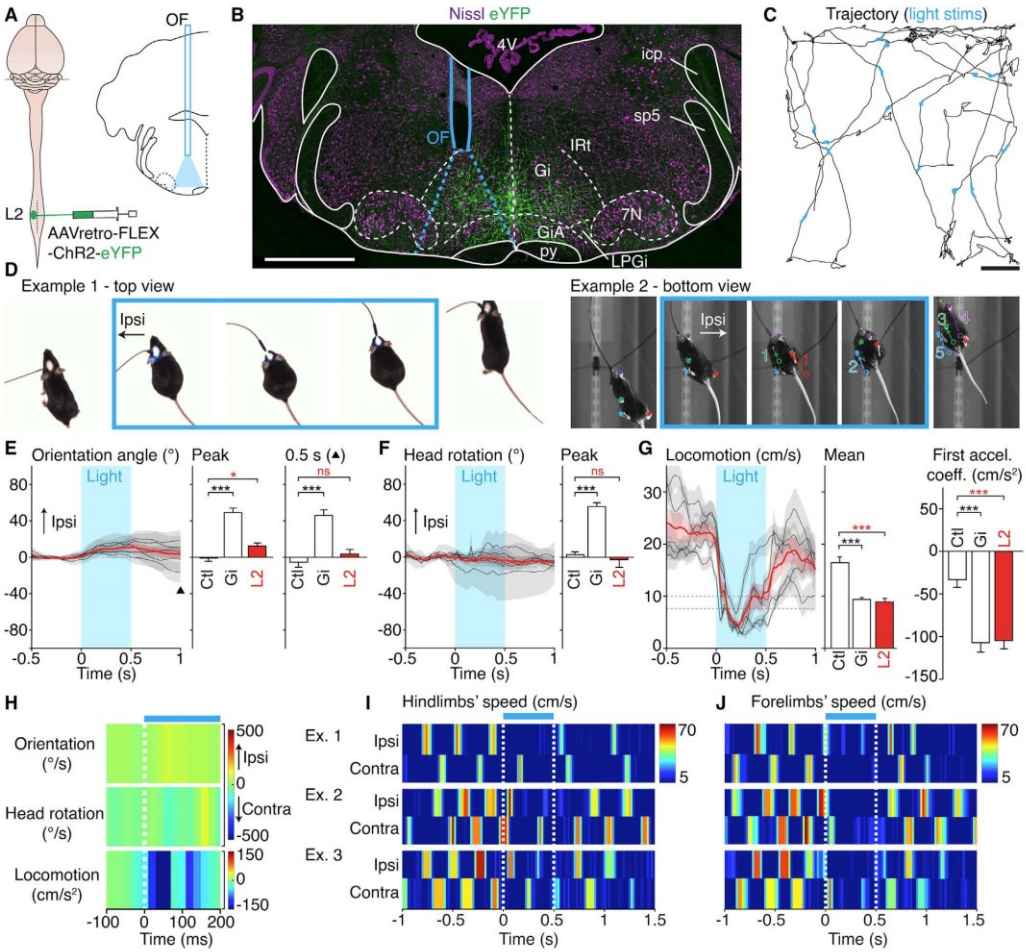

Figure 5. Unilateral Photo-Activations of L2-Projecting V2a Gi Neurons Arrest but Do Not Steer Ongoing Locomotion

(A) Experimental strategy for photo-activating L2-projecting V2a Gi neurons. OF, optic fiber.

(B) Example transverse section showing virally transfected V2a neurons (eYFP) on a Nissl background, the position of the optic fiber (OF), and the theoretical light cone at the fiber tip (dashed blue lines) that restricts activations to the implanted side. Scale bar, 1 mm. See also Figure S1D.

(C) Trajectory of one representative animal for 3 min in the open field. Scale bar, 10 cm.

(D) Example snapshots from two distinct animals, showing the locomotor arrest with no change in trajectory evoked by 500 ms light trains (15 ms pulses at 40 Hz, in blue) delivered unilaterally on the left side. Snapshots are taken 150 ms before light onset; 50 ms, 250 ms, and 450 ms after light onset; and 200 ms after light offset. See also Video S4.

(E–G) Left: mean ± SEM light-evoked changes in body orientation (E), head yaw rotation (F), and locomotor speed (G) of each animal (gray, n = 5 mice, 8 trials each) and across animals (red). The black arrowhead in (E) indicates the time point at 0.5 s after light offset. The dashed zone in (G) indicates the threshold from stationary (<7.5 cm/s) to locomoting (>10 cm/s) conditions. Bar graphs to the right show, for each parameter, the mean ± SEM of all trials when activating L2-projecting V2a neurons (in red, n = 40 trials from 5 mice, 8 trials each) compared with the same measurement in mock trials in control mice (Ctl, n = 48 trials from 4 mice, 12 trials each) and following activation of all V2a Gi neurons (Gi, n = 48 trials from 6 mice, 8 trials each). ***p < 0.001; *p < 0.05; ns, not significant (unpaired t test).

(legend continued on next page)

V2a subsets contacted by the SC but that differ by their segmental projections to the spinal cord.

Differential Control of Head and Hindlimb Movements by Subsets of V2a Gi Neurons

The existence of projection-defined subsets of V2a Gi neurons prompted us to test their respective function. For this, a cre-dependent ChR2 was delivered retrogradely by unilateral injections of an AAVretro-FLEX-ChR2-eYFP [47–49] in the C2 or L2 spinal segments and an optic fiber was placed in the Gi on the same side. Since left-right unbalanced activation of lumbar circuits could steer trajectory [7, 8, 35], we first manipulated the L2-projecting V2a neurons (Figures 5A and 5B; see Figure S1D for implantation sites). Most surprisingly, however, their unilateral activation during locomotion did not change the animals' trajectory (Figures 5C and 5D; Video S4). Specifically, the animal's body orientation only showed a slight and transient bias that was not maintained after light offset (Figure 5E). Animals also did not show any head yaw rotation movements (Figures 5D and 5F). Locomotor speed was nevertheless strongly reduced similarly to the activation of all V2a Gi neurons: animals reached the stationary threshold on average 70 ± 17 ms after light onset (Figures 5D and 5G) and locomotor deceleration peaked at 40 ms after light onset (Figure 5H). Bottom-view examinations revealed that both hindlimbs and forelimbs were halted and positioned symmetrically (Figures 5D, 5I, and 5J; Video S4). On stationary animals, photo-stimulations did not evoke detectable changes in these motor parameters (Figures S6A–S6G and S6O). Hence, L2-projecting V2a neurons, when activated unilaterally, arrest locomotion but do not evoke head and orofacial orienting responses, nor steer trajectory.

The directional change evoked when activating V2a Gi neurons collectively might thus be driven by the C2-projecting subset. Indeed, when ChR2 was retrogradely delivered from the C2 segment and photo-activations performed in the Gi unilaterally during locomotion (Figures 6A and 6B; see Figure S1E for implantation sites), we observed a pronounced change in trajectory toward the stimulated side (Figures 6C and 6D; Video S5). Reminiscent of what we observed when activating V2a neurons collectively, the change in body orientation was highly significant from mock trials in control mice, persisted after light offset (Figure 6E), and was preceded by a rapid rotation of the head (Figure 6F). Remarkably, however, animals did not arrest their locomotion. Specifically, while a locomotor deceleration was observed, it was comparable to that of control mice subjected to mock trials (Figure 6G; see also Figure S2K for the responses of control mice). This ChR2-independent deceleration reflects the limited size of open field, which makes running episodes inevitably short, even in the absence of photo-activation. This locomotor deceleration also occurred later following light onset than when activating all V2a Gi neurons or the L2-projecting ones (Figure 6H; compare with Figures 5H and 3G), suggesting that it is not a primary response from photo-activations. Indeed left-right alternating movements of both hindlimbs and forelimbs persisted during the directional change (Figures 6D, 6I, and 6J; Video S5). Photo-activations on still trials evoked a strong yaw rotation of the head and a re-orientation of the body, and animals could perform a few walking steps toward the stimulated side; there was, however, no deflection of the snout (Figures S6H–S6O). Finally, we excluded a contribution of antidromic activation of C2-located V2a neurons with projections to the brainstem (Figure S7) and found no projections in the reticular formation from Chx10-expressing neurons located in L2 (data not shown). Overall, these results indicate that (1) the C2- and L2-projecting subsets of V2a Gi neurons are specifically dedicated to control head rotation and locomotor speed, respectively, and (2) the former action suffices to steer the animal's trajectory. They also suggest the existence of other V2a Gi neurons with no spinal projections that may control orofacial musculature.

C2-Projecting, but Not L2-Projecting, V2a Neurons Elicit Short-Latency Responses on Neck Muscle Fibers

Since our results underscore the importance of head rotation for locomotor trajectory and since neck premotor circuits reside in the Gi [20–22], we hypothesized that some V2a Gi neurons might be connected to neck motoneurons. We therefore recorded, by electromyography in non-anesthetized awake mice, photo-evoked responses of the splenius muscle, the most vigorously activated during horizontal orienting head movements [20, 50] (Figure 7).

Only animals showing spontaneous activity on both the ipsilateral and contralateral muscles (Figures 7B, 7F, and 7J) were included. When V2a Gi neurons were activated collectively by short (5 ms) light pulses, reliable EMG responses were detected on the ipsilateral side in nearly all trials (Figures 7C and 7D). These occurred at an average latency of 5.57 ± 0.13 ms (min, 3.8 ms; max, 6.8 ms) compatible with the crossing of 2 synapses [51–53]. However contralateral responses were less reliable and significantly more delayed (14.64 ± 0.96 ms, min, 9.6 ms; max, 25 ms). Photo-activating C2-projecting V2a neurons also led short responses ipsilaterally (latency, 6.13 ± 0.10 ms), but not contralaterally (10.74 ± 0.66 ms; Figures 7E–7H). In stark contrast, only occasional responses were observed both ipsilaterally and contralaterally when activating the L2-projecting subset (Figures 7I–7L), and when a response was elicited, its latency was longer on both sides (ipsilateral, 18.39 ± 0.63 ms, min 13.4 ms, max 24.4 ms; contralateral, 19.65 ± 0.65 ms, min 15.6 ms; max 25 ms). Finally, examination of anterograde projections of V2a Gi neurons in the upper cervical spinal cord revealed putative contacts onto motoneurons (Figures 7M and 7N). Overall, these experiments reinforce the existence of distinct functional V2a

(H) Color plot showing the temporal evolution of the motor parameters from 100 ms before to 200 ms after light onset (the dashed white line indicates light onset). Note the absence of trajectory change and head rotation, but a rapid locomotor deceleration (peak at 40 ms) reminiscent of activating V2a Gi neurons collectively (Figure 3G).
(I and J) Color plots of the velocity of the paws of the hindlimbs (I) and forelimbs (J) from 1 s before to 1 s after the photo-activation. A color gradient to red indicates high speed values in cm/s. The y axis represents 3 example trials from distinct animals. The second one corresponds to the snapshots in (D). See also Figure S2 for the responses of control mice and Figure S6 for still trials.

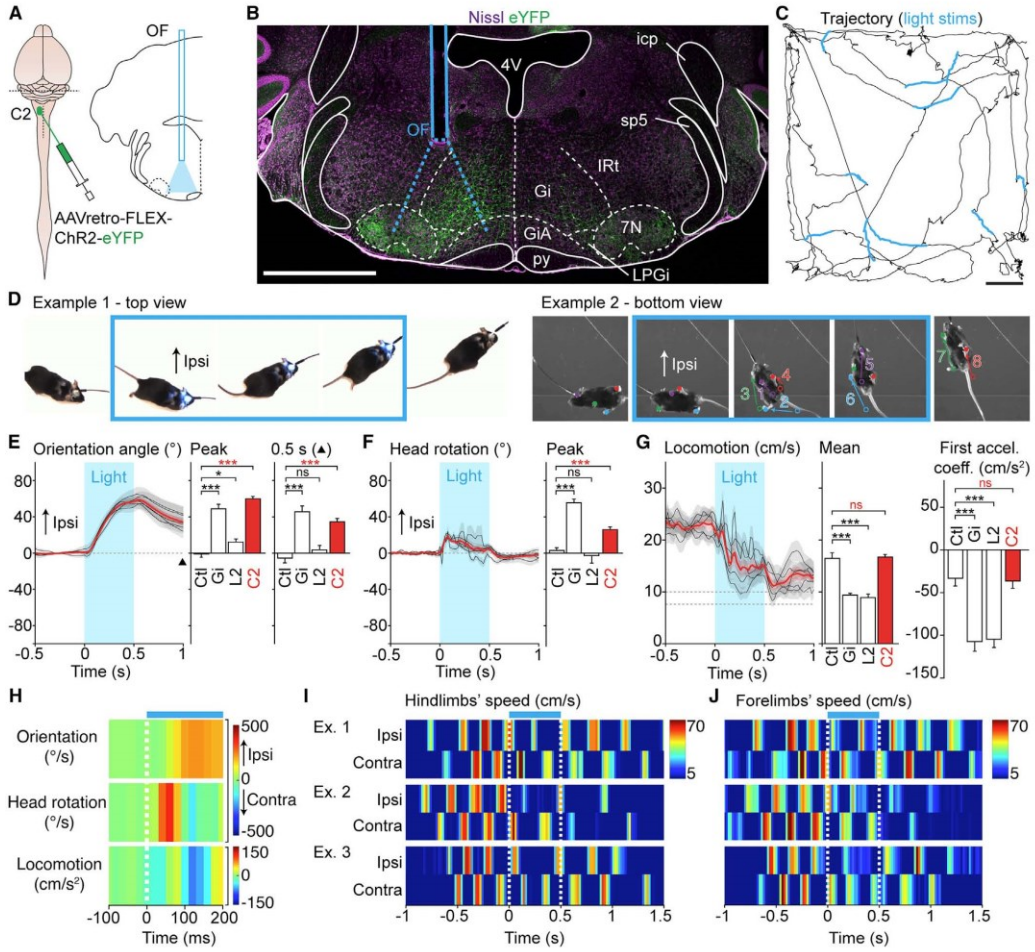

Figure 6. Unilateral Photo-Activations of C2-Projecting V2a Gi Neurons Steer, but Do Not Arrest, Ongoing Locomotion

(A) Experimental strategy for photo-activating C2-projecting V2a Gi neurons. OF, optic fiber.

(B) Example transverse section showing virally transfected V2a neurons (eYFP) on a Nissl background, the position of the optic fiber (OF), and the theoretical light cone at the fiber tip (dashed blue lines) that restricts activations to the implanted side. Scale bar, 1 mm. See also Figure S1E.

(C) Trajectory of one representative animal during 3 min in the open field. Scale bar, 10 cm.

(D) Example snapshots from two distinct animals, showing the change in trajectory without locomotor arrest, evoked by 500 ms light trains (15 ms pulses at 40 Hz, in blue). Snapshots are taken 150 ms before light onset; 50 ms, 250 ms, and 450 ms after light onset; and 200 ms after light offset. See also Video S5.

(E–G) Left: mean ± SEM light-evoked changes in body orientation (E), head yaw rotation (F), and locomotor speed (G) of each animal (gray, n = 5 mice, 23 trials each) and across animals (red). The black arrowhead in (E) indicates the time point at 0.5 s after light offset. The dashed zone in (G) indicates the threshold from stationary (<7.5 cm/s) to locomoting (>10 cm/s) conditions. Bar graphs to the right show, for each parameter, the mean ± SEM obtained across all trials when activating C2-projecting V2a neurons (in red, n = 115 trials from 5 mice, 23 trials each) compared with the same measurement in mock trials in control mice (Ctl, n = 48 trials from 4 mice, 12 trials each) and following activation of all V2a Gi neurons (Gi, n = 48 trials from 6 mice, 8 trials each) or the L2-projecting ones (L2, n = 40 trials from 5 mice, 8 trials each). ***$p < 0.001$; *$p < 0.05$; ns, not significant (unpaired t test).

(H) Color plot showing the temporal evolution of motor parameters from 100 ms before to 200 ms after light onset (the dashed white line indicates light onset). Note the rapid head rotation (peak at 60 ms) and the delayed body orientation (peak at 120 ms), but the absence of rapid deceleration of locomotion.

(I and J) Color plots of the velocity of the paws of the hindlimbs (I) and forelimbs (J) from 1 s before to 1 s after the photo-activations. A color gradient to red indicates high speed values in cm/s. The y axis represents 3 example trials from distinct animals. The first example corresponds to the snapshots in (D). See also Figure S2 for the responses of control mice and Figure S6 for still trials.

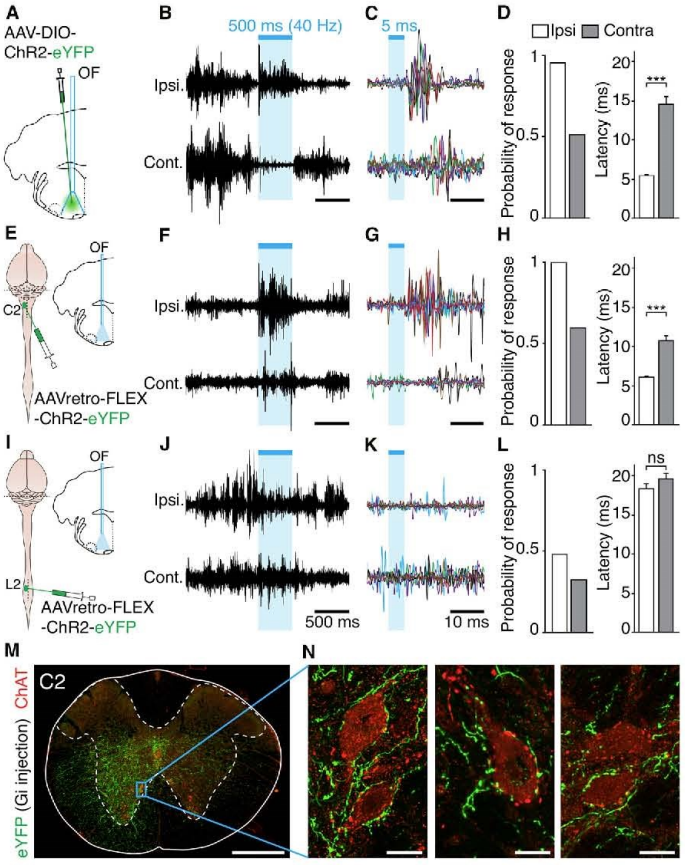

Figure 7. C2-Projecting V2a Neurons Elicit Short-Latency Responses on Neck Muscle Fibers

(A) Experimental strategy for photo-activating V2a Gi neurons. OF, optic fiber.

(B) Example EMG recording showing spontaneous activity on both the ipsilateral and contralateral neck muscles, and the increased activity ipsilaterally following photo-activation of V2a Gi neurons (15 ms pulses at 40 Hz, for a duration of 500 ms).

(C) Six superimposed EMG traces following a single 5 ms light pulse, each shown in a specific color.

(D) Bar graphs showing the presence of reliable (95% success) and low-latency responses (mean, 5.6 ± 0.1 ms; min, 3.8; max, 6.8) ipsilaterally, but not contralaterally (51% success; mean, 14.7 ± 1.0 ms; min, 9.6; max, 25). ***$p < 0.001$ (unpaired t test on n = 68 trials from 3 mice). Data are presented as means across all trials; errors bars in the latency bar graph indicate SEM.

(E–H) Similar recordings and analyses for C2-projecting V2a neurons. Note the reliable and low-latency responses on the ipsilateral (100% success; mean, 6.1 ± 0.1 ms; min, 4.0; max, 8.0), but not on the contralateral muscle (60% success; mean, 10.7 ± 0.7 ms; min, 5.1; max, 19.6). ***$p < 0.001$ (unpaired t test on n = 62 trials from 3 mice).

(I–L) Similar recordings and analyses for L2-projecting V2a neurons. Note the low probability and long latency of responses on both the ipsilateral (48% success; mean, 18.4 ± 0.6 ms; min, 13.4; max, 24.4) and contralateral muscles (33% success; mean, 19.7 ± 0.7 ms; min, 15.6 ms; max, 25 ms). ns, not significant (unpaired t test on n = 78 trials from 4 mice).

(M) Confocal microscopy picture of a transverse section at C2 of an animal injected unilaterally in the Gi with an AAV-DIO-ChR2-EYFP (experimental individual illustrated in Figure 2B), showing anterograde V2a projections (eYFP) and motoneurons (ChAT). Scale bar, 500 μm.

(N) Left: higher magnification of the blue boxed area in (M), showing putative V2a contacts onto 2 motoneurons. The middle and right panels are other examples from the same (middle) and from another (right) animal. Scale bars, 20 μm.

subtypes with specialized projections, and indicate that the C2-projecting, but not the L2-projecting one, has rapid—possibly direct—access to neck motoneurons.

DISCUSSION

Methodological Considerations

A large part of our study relies on projection-based manipulations of neuronal subtypes. While retrogradely transported HSV and AAVretro vectors have already proven to be extremely powerful tools [45, 47–49], notably owing to their restricted entry at terminals [45, 54, 55], there are potential concerns that deserve clarification. First, if wild HSVs can prevent a single cell from being infected by multiple viruses [56], the replication-deficient ones used here are deprived of viral genome [44] and allow multiple infections [46] (Figure S4). Furthermore, little co-labeling was also observed when combining an HSV injection at C2 with CTB at L2 (Figures 4F–4I), unambiguously ascertaining that distinct V2a neurons contact the cervical and lumbar segments. Another concern with dual injections is the risk of severing axons at the rostral site, which can cause an underestimation of neurons projecting more caudally. However, here, all spinal injections were done starting from the lumbar site and performed in the white matter to spare the lateral funiculus where most RS axons travel [19], and animals showed no motor deficits. Furthermore, the existence of distinct V2a subsets is not only supported anatomically but is also demonstrated functionally. Indeed, following a unique injection of a ChR2-coding AAVretro in the L2 segment, i.e., without possible axonal damage at the cervical level, no head movements or short-latency EMG responses on neck muscle fibers were detected (Figures 5 and 7). V2a neurons transfected from L2 therefore do not have a similar access to cervical segments as the overall population or the C2-projecting ones. Finally, the contribution of antidromic activation of spinally located

V2a neurons with projections to the brainstem can be ruled out since (1) motor actions evoked after retrograde delivery of ChR2 are seen when manipulating V2a Gi neurons locally, i.e., without the possibility for distant V2a neurons to express ChR2; (2) activating ascending projections of V2a neurons residing in C2 led to no orienting responses (Figure S7); and (3) Chx10-expressing neurons in L2 do not project to the RF. Overall, the selectivity and convergence of our anatomical (HSV) and functional (AAVretro) investigations firmly establish the existence of distinct functional V2a subsets with preferential projections to the upper cervical or lumbar segments.

The Presynaptic Connectome of V2a Gi Neurons Hints at Their Integrative Function

Aside from the dominant local connectivity, a high fraction of presumed inputs to V2a Gi neurons was found in the SC, in positions matching the output layers known to project to the RF [12, 15]. The majority of SC output neurons are excitatory and the ipsilateral orienting responses we observed are reminiscent of those elicited contralaterally when activating the SC [14, 42]. This suggests that V2a Gi neurons are embedded in an excitatory crossed pathway, as also indicated by a coincident and independent investigation [35]. Interestingly, we found that the SC contacts both the C2- and L2-projecting V2a subsets. Therefore, the latter, while not directly mediating lateralized motor actions, may still relay orientation-related signals. Indeed, the animal's locomotor speed is often encoded together with its directional heading [57, 58], suggesting a tight correlation of these two variables. Allowing a transient arrest of locomotion appears notably pertinent for exploring a fixed object while on the move. Alternatively, the SC projections to L2-projecting V2a neurons may be related to defensive behaviors, also manifested by a behavioral arrest [59]. The role and excitatory or inhibitory nature of the uncrossed pathway from the SC to V2a neurons, less predominant, will need to be uncovered. Finally, the detection of transneuronally labeled neurons in other brain regions known to regulate motor actions or posture [60–62] indicates that V2a Gi neurons may be shared by several modalities that require spatially tuned movements. Here again, examining the neurotransmitter identity of these upstream neurons will be required to fully appreciate their role in mobilizing or inactivating V2a Gi neurons. However, we found no transneuronal labeling in the cuneiform and pedunculopontine nuclei, together forming the mesencephalic locomotor region (MLR) that engages forward locomotion [40, 41]. This could reflect that forward locomotion may be, at least in mice, principally controlled by non-V2a glutamatergic or serotonergic neuronal classes [26, 63]. However, MLR to V2a connections have been suggested functionally *in vitro* [36]. These connections may thus target V2a neurons not investigated here (notably located more caudally) or may be more refractory to rabies transfer.

Differential Control of Head and Hindlimb Movements by Subsets of V2a Neurons

We report here that V2a Gi neurons trigger both "strict" orienting responses ipsilaterally, i.e., lateralized head and orofacial movements, and steer trajectory when activated during locomotion. Conversely, ablating or silencing V2a Gi neurons led to a biased contralateral turning during exploration, in line with a coincident and independent investigation [35]. Such opposite findings from gain and loss of functions exclude that photo-evoked responses owe to an unintentional suppression of activity by over-activation, as previously ruled out for the locomotor aspect [34]. Most importantly, they strongly argue that V2a Gi neurons might be mobilized during—and are causal to—naturally occurring changes of direction. Interestingly, the bias in the head orientation suggests that these neurons might not only be transiently activated at turns, but may also help maintain an upright posture.

The V2a-driven directional change is associated with a bilateral arrest of the hindlimbs, which is reminiscent (i.e., gradual, leading to a stereotypic stationary posture) of what was previously reported when activating the same cells bilaterally [34]. Remarkably, however—and this is certainly the most disruptive finding reported here—the directional change and the locomotor halt are in fact controlled by distinct V2a populations with segment-specific projections. This specialization of V2a neurons is demonstrated both anatomically (Figures 4 and S4) and functionally (Figures 5, 6, 7, and S6). Specifically, activating C2-projecting V2a neurons led to an ipsilateral head yaw rotation followed by a change in trajectory but no locomotor arrest, suggesting that this population does not reach or functionally impact hindlimb-related segments. While these C2-projecting V2a neurons were inevitably activated in previous work [34], their function may have then been hindered by the bilateral nature of the stimulations that may have caused left-right co-contractions of neck muscles (but see [26] for head movements when photo-activating glutamatergic Gi neurons). Conversely, we report a rapid locomotor arrest, but no head rotation, short neck EMG responses, or directional change, when activating L2-projecting V2a neurons (Figures 5 and S6). Therefore, L2-projecting V2a neurons do not reach or functionally impact neck-related cervical segments. Even though our retrograde approach transfects somata on both sides since V2a Gi neurons have crossed projections (Figures 4C–4E), the locomotor halt cannot be due to an unintentional synchronous activation of the left and right sides since (1) the lateral placement of the optic fiber secures unilateral photo-activations [64], and (2) a bilateral arrest is systematically evoked when the ChR2 is delivered locally and unilaterally to the Gi (Figure 3), where there is no possible activation of neurons located across the midline (Figure S1A). This diversification of descending neurons by targeted segment is reminiscent to what was recently uncovered for cerebello-spinal neurons [49]. However, here, we highlight a salt and pepper, body-oriented functional organization at the connectomics levels rather than a spatial topography. While we also detected a numerically smaller subset of V2a neurons with projections to both spinal segments, it is unlikely that it controls head and limb movements synergistically since activating the L2- and C2-projecting subsets evoked mutually exclusive responses. Finally, nose movements were only observed when activating V2a Gi neurons collectively. The snout musculature may thus be controlled by yet another population with only local projections [17]. Therefore, and considering that some brainstem V2a neurons may also modulate breathing [32], this neuronal class appears heterogeneous and may host projection-specialized subsets that each control a specific muscle group.

The Head Orientation as a Prime Driver for Locomotor Trajectory?

On the role of V2a neurons on locomotor trajectory, we converge with a coincident work by Cregg et al. [35]. However, in this independent study, V2a Gi neurons were only manipulated collectively, i.e., regardless of their efferent connectivity. Consequently, our conclusions on the implicated circuits diverge. Cregg et al. propose that locomotor trajectory changes owe to a depression of hindlimb circuits and movements on the side of activated V2a descending neurons. This implies that a unique V2a population steers locomotion when mobilized unilaterally and halts it when mobilized bilaterally. Instead we establish here that the directional change and the locomotor halt are controlled by distinct V2a subsets that differ by their segmental projections and can therefore be experimentally manipulated independently. Our work altogether argues that the impact of V2a Gi neurons on locomotor trajectory is rather primarily supported by their capacity to impose the head orientation. In fact, the head rotation precedes the trajectory changes evoked experimentally (Figure 3G) or occurring spontaneously (Figure S3) and has been postulated as a prime driver for locomotor trajectory in humans [4–6]. In swimming species, trajectory changes are also initiated by a bending of the head and trunk [13]. Our work hence highlights the importance of the head in directing movement path across species. To be clear, we do not dispute that activating V2a Gi neurons collectively—or the C2-projecting subset selectively—leads to asymmetric limb movements [35] (Figures 3H and 6D). Yet we show here that this asymmetry does not appear to be a primary consequence of activated descending V2a neurons reaching the hindlimb controllers in the lumbar spinal cord. It may rather be an adaptive adjustment to the displacement of the body axis, primed by the head (and possibly the forelimbs), which *is* driven by C2-projecting V2a Gi neurons. Changes in body orientation can in fact be imposed by activating V2a neurons on stationary animals (Figures 2C–2E, S6I, and S6J). How such displacement translates in an asymmetric limb pattern while on the move remains to be determined. Limb sensory inputs can adjust stance patterns during mechanically forced directional changes [65, 66] and should notably be examined.

Limitations

Our opposite findings from gain and loss of function indicate that V2a neurons' activity is both causal to, and required for, head orientating movements and trajectory changes. Our results, however, do not speak to whether V2a neurons are mobilized during natural behaviors and at all situations that need oriented movements. Interestingly, natural turnings can be, but do not have to be, associated with a locomotor arrest (Figure S3), suggesting that each subtype could even be recruited independently. Head-mounted microscopes [67] should be considered in future experiments with some developments to overcome the sparsity and deep location of the V2a population. Another intriguing finding reported here is that the two V2a subsets evoke opposing actions: motor excitation for the C2-projecting one, functional inhibition for the L2-projecting one. Yet V2a neurons at all positions of the medullary RF are glutamatergic and do not co-express inhibitory or serotonergic markers [34, 36]. The functional outcome of each subset may therefore owe to the cell types contacted in the spinal cord. Admittedly, we have not examined V2a targets in detail, but the short-latency responses on neck muscles and the putative contacts on cervical motoneurons (Figure 7) raise the possibility that V2a RS neurons may include neck premotoneurons [20, 22]. V2a neurons can indeed be premotoneurons, at least in the spinal cord [68, 69]. Dedicated tracings from muscles [70] will be needed to ascertain this possibility in the brainstem. Instead, the L2-projecting subset may correspond to the previously identified V2a "stop neurons" and may depress locomotor circuits indirectly via inhibitory spinal neurons [34], whose activation can halt locomotion [71]. Characterizing the V2a postsynaptic targets will therefore be extremely informative and should now be achievable with anterograde transneuronal vectors [72]. Finally, while we focused on the rostral medulla (i.e., levels encompassing the Gi and GiA), V2a neurons located more caudally also project to the spinal cord (Figures 4I and 4L) and their function will need to be determined.

General Conclusion

Our work has identified subtypes of reticular neurons that are downstream of the superior colliculus and that control multiple motor actions pertinent for orientation. These subtypes share a common genetic identity and anatomical positioning, but differ by their efferent connectivity. Our study therefore underscores the organization of the reticular formation in functional modules defined by transcription factors, and at the same time argues for a further segregation within modules whereby a functional connectivity organized by muscles or muscle groups may underlie the execution of individual motor actions of a coherent behavior. This represents an entry point to further decipher the neuronal basis for the diversity of motor repertoires and how the brain elaborates complex movements.

STAR★METHODS

Detailed methods are provided in the online version of this paper and include the following:

- KEY RESOURCES TABLE
- RESOURCE AVAILABILITY
  - Lead Contact
  - Materials Availability
  - Data and Code Availability
- EXPERIMENTAL MODEL AND SUBJECT DETAILS
  - Mice
  - Viruses used
- METHOD DETAILS
  - Surgical procedures for injections and implants in the brainstem
  - Surgical procedures for injections in the spinal cord
  - Histology
  - Delineation of brainstem structures and cellular counts
  - Behavioral experiments
  - Electromyographic Recordings
- QUANTIFICATION AND STATISTICAL ANALYSIS
  - Pose estimation using DeepLabCut and quantifications of body and head movements
  - Calculations of limb velocity

- Statistical analysis for optogenetic experiments
- Statistical analysis for ablation and silencing experiments
- Statistical analysis for electromyographic recordings

SUPPLEMENTAL INFORMATION

Supplemental Information can be found online at https://doi.org/10.1016/j.cub.2020.09.014.

ACKNOWLEDGMENTS

This work was funded by an Agence Nationale pour la Recherche grant (ANR-17-CE16-0027) to J.B. and by NeuroPSI, CNRS, and Université Paris-Saclay. G.U. holds a Université Paris-Saclay doctoral fellowship. C.H. holds doctoral fellowships from Région Ile-de-France and Fondation pour la Recherche Médicale. We thank Séverine Diem for assistance with genotyping, Tihana Jovanic for critical reading of the manuscript, and Beatrice Cerocchi for the mouse drawings in the graphical abstract. Other schematics are from Scidraw.io.

AUTHOR CONTRIBUTIONS

J.B. designed the study and supervised the work. G.U. performed experiments with contributions from J.B. and A.H. and analyzed anatomical data. E.G. designed tracking scripts and analyzed the behavioral data with J.B. C.H. helped establish and performed initial transneuronal tracings. G.U. and J.B. prepared figures. J.B. wrote the paper and all authors contributed to its editing.

DECLARATION OF INTERESTS

The authors declare no competing interests.

Received: April 1, 2020
Revised: August 3, 2020
Accepted: September 4, 2020
Published: October 1, 2020

REFERENCES

1. Mitchinson, B., and Prescott, T.J. (2013). Whisker movements reveal spatial attention: a unified computational model of active sensing control in the rat. PLoS Comput. Biol. *9*, e1003236.
2. Kurnikova, A., Moore, J.D., Liao, S.M., Deschênes, M., and Kleinfeld, D. (2017). Coordination of orofacial motor actions into exploratory behavior by rat. Curr. Biol. *27*, 688–696.
3. Guitton, D. (1992). Control of eye-head coordination during orienting gaze shifts. Trends Neurosci. *15*, 174–179.
4. Grasso, R., Glasauer, S., Takei, Y., and Berthoz, A. (1996). The predictive brain: anticipatory control of head direction for the steering of locomotion. Neuroreport *7*, 1170–1174.
5. Dollack, F., Perusquía-Hernández, M., Kadone, H., and Suzuki, K. (2019). Head anticipation during locomotion with auditory instruction in the presence and absence of visual input. Front. Hum. Neurosci. *13*, 293.
6. Grasso, R., Prévost, P., Ivanenko, Y.P., and Berthoz, A. (1998). Eye-head coordination for the steering of locomotion in humans: an anticipatory synergy. Neurosci. Lett. *253*, 115–118.
7. Oueghlani, Z., Simonnet, C., Cardoit, L., Courtand, G., Cazalets, J.R., Morin, D., Juvin, L., and Barrière, G. (2018). Brainstem steering of locomotor activity in the newborn rat. J. Neurosci. *38*, 7725–7740.
8. Fagerstedt, P., and Ullén, F. (2001). Lateral turns in the lamprey. I. Patterns of motoneuron activity. J. Neurophysiol. *86*, 2246–2256.
9. Basso, M.A., and May, P.J. (2017). Circuits for action and cognition: a view from the superior colliculus. Annu. Rev. Vis. Sci. *3*, 197–226.
10. Song, J.H., Rafal, R.D., and McPeek, R.M. (2011). Deficits in reach target selection during inactivation of the midbrain superior colliculus. Proc. Natl. Acad. Sci. USA *108*, E1433–E1440.
11. Stubblefield, E.A., Costabile, J.D., and Felsen, G. (2013). Optogenetic investigation of the role of the superior colliculus in orienting movements. Behav. Brain Res. *255*, 55–63.
12. Felsen, G., and Mainen, Z.F. (2008). Neural substrates of sensory-guided locomotor decisions in the rat superior colliculus. Neuron *60*, 137–148.
13. Saitoh, K., Ménard, A., and Grillner, S. (2007). Tectal control of locomotion, steering, and eye movements in lamprey. J. Neurophysiol. *97*, 3093–3108.
14. Sahibzada, N., Dean, P., and Redgrave, P. (1986). Movements resembling orientation or avoidance elicited by electrical stimulation of the superior colliculus in rats. J. Neurosci. *6*, 723–733.
15. Sparks, D.L., and Hartwich-Young, R. (1989). The deep layers of the superior colliculus. Rev. Oculomot. Res. *3*, 213–255.
16. Redgrave, P., Mitchell, I.J., and Dean, P. (1987). Descending projections from the superior colliculus in rat: a study using orthograde transport of wheatgerm-agglutinin conjugated horseradish peroxidase. Exp. Brain Res. *68*, 147–167.
17. Kleinfeld, D., Moore, J.D., Wang, F., and Deschenes, M. (2014). The brainstem oscillator for whisking and the case for breathing as the master clock for orofacial motor actions. Cold Spring Harb. Symp. Quant. Biol. *79*, 29–39.
18. Sparks, D.L. (2002). The brainstem control of saccadic eye movements. Nat. Rev. Neurosci. *3*, 952–964.
19. Liang, H., Watson, C., and Paxinos, G. (2016). Terminations of reticulospinal fibers originating from the gigantocellular reticular formation in the mouse spinal cord. Brain Struct. Funct. *221*, 1623–1633.
20. Isa, T., and Sasaki, S. (2002). Brainstem control of head movements during orienting; organization of the premotor circuits. Prog. Neurobiol. *66*, 205–241.
21. Sasaki, S., Yoshimura, K., and Naito, K. (2004). The neural control of orienting: role of multiple-branching reticulospinal neurons. Prog. Brain Res. *143*, 383–389.
22. Peterson, B.W., Pitts, N.G., Fukushima, K., and Mackel, R. (1978). Reticulospinal excitation and inhibition of neck motoneurons. Exp. Brain Res. *32*, 471–489.
23. Kiehn, O. (2016). Decoding the organization of spinal circuits that control locomotion. Nat. Rev. Neurosci. *17*, 224–238.
24. Grillner, S., and El Manira, A. (2020). Current principles of motor control, with special reference to vertebrate locomotion. Physiol. Rev. *100*, 271–320.
25. Jordan, L.M., Liu, J., Hedlund, P.B., Akay, T., and Pearson, K.G. (2008). Descending command systems for the initiation of locomotion in mammals. Brain Res. Brain Res. Rev. *57*, 183–191.
26. Capelli, P., Pivetta, C., Soledad Esposito, M., and Arber, S. (2017). Locomotor speed control circuits in the caudal brainstem. Nature *551*, 373–377.
27. Kim, L.H., Sharma, S., Sharples, S.A., Mayr, K.A., Kwok, C.H.T., and Whelan, P.J. (2017). Integration of descending command systems for the generation of context-specific locomotor behaviors. Front. Neurosci. *11*, 581.
28. Ferreira-Pinto, M.J., Ruder, L., Capelli, P., and Arber, S. (2018). Connecting circuits for supraspinal control of locomotion. Neuron *100*, 361–374.
29. Isa, T., and Sasaki, S. (1988). Effects of lesion of paramedian pontomedullary reticular formation by kainic acid injection on the visually triggered horizontal orienting movements in the cat. Neurosci. Lett. *87*, 233–239.
30. Li, S., Misra, K., Matise, M.P., and Xiang, M. (2005). Foxn4 acts synergistically with Mash1 to specify subtype identity of V2 interneurons in the spinal cord. Proc. Natl. Acad. Sci. USA *102*, 10688–10693.
31. Briscoe, J., and Ericson, J. (2001). Specification of neuronal fates in the ventral neural tube. Curr. Opin. Neurobiol. *11*, 43–49.

32. Crone, S.A., Viemari, J.C., Droho, S., Mrejeru, A., Ramirez, J.M., and Sharma, K. (2012). Irregular breathing in mice following genetic ablation of V2a neurons. J. Neurosci. *32*, 7895–7906.

33. Kimura, Y., Satou, C., Fujioka, S., Shoji, W., Umeda, K., Ishizuka, T., Yawo, H., and Higashijima, S. (2013). Hindbrain V2a neurons in the excitation of spinal locomotor circuits during zebrafish swimming. Curr. Biol. *23*, 843–849.

34. Bouvier, J., Caggiano, V., Leiras, R., Caldeira, V., Bellardita, C., Balueva, K., Fuchs, A., and Kiehn, O. (2015). Descending command neurons in the brainstem that halt locomotion. Cell *163*, 1191–1203.

35. Cregg, J.M., Leiras, R., Montalant, A., Wanken, P., Wickersham, I.R., and Kiehn, O. (2020). Brainstem neurons that command mammalian locomotor asymmetries. Nat. Neurosci. *23*, 730–740.

36. Bretzner, F., and Brownstone, R.M. (2013). Lhx3-Chx10 reticulospinal neurons in locomotor circuits. J. Neurosci. *33*, 14681–14692.

37. Kim, E.J., Jacobs, M.W., Ito-Cole, T., and Callaway, E.M. (2016). Improved monosynaptic neural circuit tracing using engineered rabies virus glycoproteins. Cell Rep. *15*, 692–699.

38. Azim, E., Jiang, J., Alstermark, B., and Jessell, T.M. (2014). Skilled reaching relies on a V2a propriospinal internal copy circuit. Nature *508*, 357–363.

39. Romer, S.H., Seedle, K., Turner, S.M., Li, J., Baccei, M.L., and Crone, S.A. (2017). Accessory respiratory muscles enhance ventilation in ALS model mice and are activated by excitatory V2a neurons. Exp. Neurol. *287*, 192–204.

40. Caggiano, V., Leiras, R., Goñi-Erro, H., Masini, D., Bellardita, C., Bouvier, J., Caldeira, V., Fisone, G., and Kiehn, O. (2018). Midbrain circuits that set locomotor speed and gait selection. Nature *553*, 455–460.

41. Josset, N., Roussel, M., Lemieux, M., Lafrance-Zoubga, D., Rastqar, A., and Bretzner, F. (2018). Distinct contributions of mesencephalic locomotor region nuclei to locomotor control in the freely behaving mouse. Curr. Biol. *28*, 884–901.e3.

42. Masullo, L., Mariotti, L., Alexandre, N., Freire-Pritchett, P., Boulanger, J., and Tripodi, M. (2019). Genetically defined functional modules for spatial orienting in the mouse superior colliculus. Curr. Biol. *29*, 2892–2904.e8.

43. Yang, C.F., Chiang, M.C., Gray, D.C., Prabhakaran, M., Alvarado, M., Juntti, S.A., Unger, E.K., Wells, J.A., and Shah, N.M. (2013). Sexually dimorphic neurons in the ventromedial hypothalamus govern mating in both sexes and aggression in males. Cell *153*, 896–909.

44. Neve, R.L., Neve, K.A., Nestler, E.J., and Carlezon, W.A., Jr. (2005). Use of herpes virus amplicon vectors to study brain disorders. Biotechniques *39*, 381–391.

45. Reinhard, K., Li, C., Do, Q., Burke, E.G., Heynderickx, S., and Farrow, K. (2019). A projection specific logic to sampling visual inputs in mouse superior colliculus. eLife *8*, e50697.

46. Coopersmith, R., and Neve, R.L. (1999). Expression of multiple proteins within single primary cortical neurons using a replication deficient HSV vector. Biotechniques *27*, 1156–1160.

47. Tervo, D.G., Hwang, B.Y., Viswanathan, S., Gaj, T., Lavzin, M., Ritola, K.D., Lindo, S., Michael, S., Kuleshova, E., Ojala, D., et al. (2016). A designer AAV variant permits efficient retrograde access to projection neurons. Neuron *92*, 372–382.

48. Ren, J., Friedmann, D., Xiong, J., Liu, C.D., Ferguson, B.R., Weerakkody, T., DeLoach, K.E., Ran, C., Pun, A., Sun, Y., et al. (2018). Anatomically defined and functionally distinct dorsal raphe serotonin sub-systems. Cell *175*, 472–487.e20.

49. Sathyamurthy, A., Barik, A., Dobrott, C.I., Matson, K.J.E., Stoica, S., Pursley, R., Chesler, A.T., and Levine, A.J. (2020). Cerebellospinal neurons regulate motor performance and motor learning. Cell Rep. *31*, 107595.

50. Roucoux, A., Crommelinck, M., and Decostre, M.F. (1989). Neck muscle activity in eye–head coordinated movements. Prog. Brain Res. *80*, 351–362, discussion 347–349.

51. Ueno, M., Nakamura, Y., Li, J., Gu, Z., Niehaus, J., Maezawa, M., Crone, S.A., Goulding, M., Baccei, M.L., and Yoshida, Y. (2018). Corticospinal circuits from the sensory and motor cortices differentially regulate skilled movements through distinct spinal interneurons. Cell Rep. *23*, 1286–1300.e7.

52. Maeda, H., Fukuda, S., Kameda, H., Murabe, N., Isoo, N., Mizukami, H., Ozawa, K., and Sakurai, M. (2016). Corticospinal axons make direct synaptic connections with spinal motoneurons innervating forearm muscles early during postnatal development in the rat. J. Physiol. *594*, 189–205.

53. Palmieri, R.M., Ingersoll, C.D., and Hoffman, M.A. (2004). The hoffmann reflex: methodologic considerations and applications for use in sports medicine and athletic training research. J. Athl. Train. *39*, 268–277.

54. McGavern, D.B., and Kang, S.S. (2011). Illuminating viral infections in the nervous system. Nat. Rev. Immunol. *11*, 318–329.

55. Antinone, S.E., and Smith, G.A. (2010). Retrograde axon transport of herpes simplex virus and pseudorabies virus: a live-cell comparative analysis. J. Virol. *84*, 1504–1512.

56. Criddle, A., Thornburg, T., Kochetkova, I., DePartee, M., and Taylor, M.P. (2016). gD-independent superinfection exclusion of alphaherpesviruses. J. Virol. *90*, 4049–4058.

57. Sargolini, F., Fyhn, M., Hafting, T., McNaughton, B.L., Witter, M.P., Moser, M.B., and Moser, E.I. (2006). Conjunctive representation of position, direction, and velocity in entorhinal cortex. Science *312*, 758–762.

58. Muzzu, T., Mitolo, S., Gava, G.P., and Schultz, S.R. (2018). Encoding of locomotion kinematics in the mouse cerebellum. PLoS ONE *13*, e0203900.

59. Shang, C., Chen, Z., Liu, A., Li, Y., Zhang, J., Qu, B., Yan, F., Zhang, Y., Liu, W., Liu, Z., et al. (2018). Divergent midbrain circuits orchestrate escape and freezing responses to looming stimuli in mice. Nat. Commun. *9*, 1232.

60. Murer, M.G., and Pazo, J.H. (1993). Circling behaviour induced by activation of GABAA receptors in the subthalamic nucleus. Neuroreport *4*, 1219–1222.

61. Supko, D.E., Uretsky, N.J., and Wallace, L.J. (1991). Activation of AMPA/kainic acid glutamate receptors in the zona incerta stimulates locomotor activity. Brain Res. *564*, 159–163.

62. Darmohray, D.M., Jacobs, J.R., Marques, H.G., and Carey, M.R. (2019). Spatial and temporal locomotor learning in mouse cerebellum. Neuron *102*, 217–231.e4.

63. Cabaj, A.M., Majczynski, H., Couto, E., Gardiner, P.F., Stecina, K., Slawinska, U., and Jordan, L.M. (2017). Serotonin controls initiation of locomotion and afferent modulation of coordination via 5-HT7 receptors in adult rats. J. Physiol. *595*, 301–320.

64. Stujenske, J.M., Spellman, T., and Gordon, J.A. (2015). Modeling the spatiotemporal dynamics of light and heat propagation for in vivo optogenetics. Cell Rep. *12*, 525–534.

65. Musienko, P.E., Zelenin, P.V., Lyalka, V.F., Gerasimenko, Y.P., Orlovsky, G.N., and Deliagina, T.G. (2012). Spinal and supraspinal control of the direction of stepping during locomotion. J. Neurosci. *32*, 17442–17453.

66. Karayannidou, A., Zelenin, P.V., Orlovsky, G.N., Sirota, M.G., Beloozerova, I.N., and Deliagina, T.G. (2009). Maintenance of lateral stability during standing and walking in the cat. J. Neurophysiol. *101*, 8–19.

67. Ghosh, K.K., Burns, L.D., Cocker, E.D., Nimmerjahn, A., Ziv, Y., Gamal, A.E., and Schnitzer, M.J. (2011). Miniaturized integration of a fluorescence microscope. Nat. Methods *8*, 871–878.

68. Dougherty, K.J., Zagoraiou, L., Satoh, D., Rozani, I., Doobar, S., Arber, S., Jessell, T.M., and Kiehn, O. (2013). Locomotor rhythm generation linked to the output of spinal shox2 excitatory interneurons. Neuron *80*, 920–933.

69. Kimura, Y., Okamura, Y., and Higashijima, S. (2006). alx, a zebrafish homolog of Chx10, marks ipsilateral descending excitatory interneurons that participate in the regulation of spinal locomotor circuits. J. Neurosci. *26*, 5684–5697.

70. Wu, J., Capelli, P., Bouvier, J., Goulding, M., Arber, S., and Fortin, G. (2017). A V0 core neuronal circuit for inspiration. Nat. Commun. *8*, 544.

71. Caggiano, V., Sur, M., and Bizzi, E. (2014). Rostro-caudal inhibition of hindlimb movements in the spinal cord of mice. PLoS ONE *9*, e100865.

72. Zingg, B., Chou, X.L., Zhang, Z.G., Mesik, L., Liang, F., Tao, H.W., and Zhang, L.I. (2017). AAV-mediated anterograde transsynaptic tagging: mapping corticocollicular input-defined neural pathways for defense behaviors. Neuron *93*, 33–47.

73. Mattis, J., Tye, K.M., Ferenczi, E.A., Ramakrishnan, C., O'Shea, D.J., Prakash, R., Gunaydin, L.A., Hyun, M., Fenno, L.E., Gradinaru, V., et al. (2011). Principles for applying optogenetic tools derived from direct comparative analysis of microbial opsins. Nat. Methods *9*, 159–172.

74. Harrison, M., O'Brien, A., Adams, L., Cowin, G., Ruitenberg, M.J., Sengul, G., and Watson, C. (2013). Vertebral landmarks for the identification of spinal cord segments in the mouse. Neuroimage *68*, 22–29.

75. Ueda, H.R., Ertürk, A., Chung, K., Gradinaru, V., Chédotal, A., Tomancak, P., and Keller, P.J. (2020). Tissue clearing and its applications in neuroscience. Nat. Rev. Neurosci. *21*, 61–79.

76. Franklin, K.B., and Paxinos, G. (2007). The Mouse Brain in Stereotaxic Coordinates, Third Edition (Elsevier).

77. Pearson, K.G., Acharya, H., and Fouad, K. (2005). A new electrode configuration for recording electromyographic activity in behaving mice. J. Neurosci. Methods *148*, 36–42.

78. Mathis, A., Mamidanna, P., Cury, K.M., Abe, T., Murthy, V.N., Mathis, M.W., and Bethge, M. (2018). DeepLabCut: markerless pose estimation of user-defined body parts with deep learning. Nat. Neurosci. *21*, 1281–1289.

STAR★METHODS

KEY RESOURCES TABLE

REAGENT or RESOURCE	SOURCE	IDENTIFIER
Antibodies		
Goat anti-Choline Acetyltransferase (ChAT)	Merck Millipore	Cat #: AB144P; RRID: AB_2079751
Chicken anti-Green Fluorescent Protein (GFP) Antibody	Aves Labs	Cat #: 1020; RRID: AB_10000240
Rabbit anti-Red Fluorescent Protein (RFP)	Rockland	Cat #: 600-401-379; RRID: AB_2209751
Sheep anti-Tyrosine Hydroxylase (TH)	Merck Millipore	Cat #: AB1542; RRID: AB_90755
Bacterial and Virus Strains		
AAV8-hSyn-FLEX-TVA-p2a-eGFP-2a-oG	SALK GT3	RRID: Addgene_85225
HSV1-hEF1a-LS1L-TVA950-T2A-rabiesOG-IRES-mCherry	Rachael Neve	Rachael Neve, Massachusetts General Hospital
HSV1-hEF1a-LS1L-hChR2(H134R)-p2A-EYFP	Rachael Neve	Rachael Neve, Massachusetts General Hospital
EnvA-ΔG-Rabies-mCherry	SALK GT3	RRID: Addgene_32636
EnvA-ΔG-Rabies-GFP	SALK GT3	RRID: Addgene_32635
AAV9-Ef1a-DIO-hChR2(E123T/T159C)-EYFP	Addgene	RRID: Addgene_35509
AAV5-FLEX-taCasp3-TEVp	UNC	RRID: Addgene_45580
AAV8.2-hEF1a-DIO-hM4Di-mCherry-WPRE	Rachael Neve	Rachael Neve, Massachusetts General Hospital
AAVretro-EF1a-doublefloxed-hChR2(H134R)-EYFP-WPRE-HGHpA	Addgene	RRID: Addgene_20298
Chemicals, Peptides, and Recombinant Proteins		
Clozapine N-oxide (CNO)	Enzo Life Sciences	Cat #: BML-NS105-0005
Cholera Toxin B (CTB) – AF647 conjugate	ThermoFisher Scientific	Cat #: C-34778
NeuroTrace 640/660 Deep-Red	ThermoFisher Scientific	Cat #: N21483
NeuroTrace 435/445 blue	ThermoFisher Scientific	Cat #: N21479
Fluoro-Max blue beads	ThermoFisher Scientific	Cat #: B500
Prolong Diamond Antifade Montant	ThermoFisher Scientific	Cat #: P36970
ibidi Mounting Medium	ibidi	Cat #: 50001
Deposited Data		
Original datasets on Mendeley Data	This paper	http://doi.org/10.17632/54x8rjppfz.1
Experimental Models: Organisms/Strains		
Mouse: Chx10-Cre	S. Crone, K. Sharma, L. Zagoraiou, and T.M. Jessell	[34, 38, 39]
Software and Algorithms		
MATLAB R2018a	Mathworks	https://www.mathworks.com/products/matlab.html; RRID: SCR_001622
DeelLabCut	Mathis Lab	http://www.mousemotorlab.org/deeplabcut
ImageJ	https://imagej.net/	RRID: SCR_003070
ZEN Lite	Zeiss	https://www.zeiss.fr/microscopie/produits/microscope-software/zen-lite/zen-2-lite-download.html; RRID: SCR_013672
Leica LASX	Leica	https://www.leica-microsystems.com/products/microscope-software/p/leica-las-x-ls/; RRID: SCR_013673
LabScribe NI	iWorxs	https://www.iworx.com/products/biomedical-engineering/labscribeni/
2nd LOOK	IO Industries	http://ioindustries.com/2ndlook.html
Kdenlive video editor	Kdenlive	https://kdenlive.org/fr/

RESOURCE AVAILABILITY

Lead Contact

Further information and requests for resources and reagents should be directed to and will be fulfilled by the Lead Contact, Julien Bouvier (julien.bouvier@cnrs.fr).

Materials Availability

This study did not generate new unique reagents.

Data and Code Availability

Original data have been deposited to Mendeley Data (http://dx.doi.org/10.17632/54x8rjppfz.1). This study did not generate any computer code.

EXPERIMENTAL MODEL AND SUBJECT DETAILS

Mice

The *Chx10-Cre* was kindly provided by S. Crone, K. Sharma, L. Zagoraiou, and T.M. Jessell [34, 38, 39]. C57BL6 wilt-type mice were obtained by Janvier Labs (Le Genest-Saint-Isle, France). Animals were group-housed with free access to food and water in controlled temperature conditions and exposed to a conventional 12-h light/dark cycle. Experiments were performed on animals of either sex, aged 2 to 3 months at the time of first injection. All procedures were approved by the French Ethical Committee (authorization 2020-022410231878) and conducted in accordance with EU Directive 2010/63/EU. All efforts were made to reduce animal suffering and minimize the number of animals.

Viruses used

For Cre-dependent expression of ChR2 in the Gi we injected unilaterally 100 to 200 nL of an AAV9-Ef1a-DIO-hChR2(E123T/T159C)-eYFP (addgene #35509, titer 3.2×10^{12} vp/mL [73]). For cellular ablation of V2a Gi neurons we used 400 nL of a AAV5-FLEX-taCasp3-TEVp (titer 4.6×10^{12} vp/mL) obtained from UNC (addgene plasmid #45580 [43]). For reversible silencing of V2a Gi neurons we used 400 nL of a AAV8.2-hEF1a-DIO-hM4Di-mCherry-WPRE (titer 2.25×10^{13}) obtained from Dr. Rachael Neve (Gene Delivery Technology Core, Massachusetts General Hospital, USA). For transsynaptic labeling of inputs onto V2a Gi neurons, we used 500 nL of an AAV8-hSyn-FLEX-TVA-p2a-eGFP-2a-oG (titer: 2.8×10^{12} vp/mL) obtained by the GT3 core (Salk Institute). For retrograde labeling of spinally-projecting V2a neurons we used 500nL per injection spot of HSV1-hEF1a-LS1L-TVA950-T2A-rabiesOG-IRES-mCherry and HSV1-hEF1a-LS1L-hChR2(H134R)-p2A-eYFP obtained from Dr. Rachael Neve (Gene Delivery Technology Core, Massachusetts General Hospital, USA). Rabies viruses used were EnvA-ΔG-rabies-mCherry (titer: 3.12×10^{8} vp/mL) and EnvA-ΔG-rabies-GFP (titer: 2.26×10^{8} vp/mL) both obtained by the GT3 core (Salk Institute, USA). For optogenetic manipulations of spinally-projecting V2a neurons we used 500 nL per injection spot of AAVretro-EF1a-doublefloxed-hChR2(H134R)-eYFP-WPRE-HGHpA (Karl Deisseroth, Addgene plasmid # 20298; http://n2t.net/addgene:20298; RRID: Addgene_20298; titer 1.0×10^{13} vp/mL).

METHOD DETAILS

Surgical procedures for injections and implants in the brainstem

Animals were anesthetized with isoflurane throughout the surgery (4% at 1 L/min for induction, and 2%–3% at 0.3 L/min for maintenance). Buprenorphine (0,025 mg/kg) was administered subcutaneously for analgesia before the surgery. The temperature of the mice was maintained at 36°C with a feedback-controlled heating pad. Anesthetized animals were placed on a stereotaxic frame (Kopf) and the skull was exposed. Viral vectors were delivered using a pulled glass pipette connected to a syringe pump (Legato 130, KD Scientific, customized by Phymep, France). The infusion flow was set to 100 nL/min. Coordinates (in mm) used to target V2a Gi neurons were: −6.0 from bregma, 0.8 lateral, and 4.5 from the dorsal brain surface. After the injection, the pipette was held in place for 5 min before being slowly retracted. For optogenetic activations, a 200 μm core 0.39 NA optic fiber (Thorlabs) connected to a 1.25 mm diameter ferrule (Thorlabs) was implanted ~500 μm above the injection site (Figure 2A). This operation was performed during the same surgery as the viral injection when both were targeted to the brainstem. For activating spinally-projecting V2a neurons, the spinal injection was performed first (see below) and the optic fiber was implanted 5 to 7 days later. Dental cement (Tetric Evoflow) was used to secure the implanted ferrules. Animals were followed daily after the surgery.

Surgical procedures for injections in the spinal cord

Animals were anesthetized as described above and spinal injections were performed as previously done [34]. A two cm incision of the skin was performed dorsally on anesthetized animals and the exposed spinal column was fixed with two holders on the left and right sides to a stereotaxic frame to minimize movements. Vertebral spinous processes were used as landmarks to target specific segments [74]. A small incision of the ligamentum Flavum allowed access to the spinal cord. A pulled glass pipette connected to

a motorized syringe pump injector (Legato 130, KD Scientific, customized by Phymep, France) was positioned into the ventromedial area of the L2 (between the 11th and 12th vertebral body) or C2 (between the 1st and 2nd vertebral body) spinal segment using the following coordinates: 400 mm laterally from the dorsal artery and 500 to 850 mm (L2 injections) or 800 to 1200 μm (C2 injections) depth from the dorsal surface. This lateral positioning ensures that the injection pipette does not pass through the lateral funiculus where descending axons of RS neurons travel. A total volume of 500 nL of virus was injected at 100 nL/min in 2 distinct spots separated rostrocaudally by 600 to 800 μm. For CTB injections, we used 500 nL of CTB-AF647 conjugate (Thermofisher Scientific, Cat # C-34778) diluted at 0.5% in sterile saline. Dual HSVs injections (Figures 4J and S4) were done bilaterally to increase the number of labeled cells for quantifications but AAVretro injections (Figures 5, 6, and S6) were done unilaterally. Dual injections of HSVs in both the L2 and C2 spinal segments were performed successively, starting from L2, during the same surgical procedure. For controls, two consecutive HSV injections were performed at L2, either during the same day or at one day apart (Figure S4). After each injection, the pipette was held in place for 5 min before being slowly retracted. The skin was sutured, and animals were followed daily after the surgery. All animals recovered without motor impairments.

Histology

Adult mice were anesthetized with Euthasol Vet (140 mg/kg) and perfused with 4% paraformaldehyde (PFA) in 1X Phosphate Buffered Saline (PBS). Brains and spinal cord were dissected out and fixed overnight in 4% PFA at 4°C. After fixation, tissues were rinsed in 1X PBS. Brain and spinal cord were cryoprotected overnight at 4°C, respectively in 16% and 20% sucrose in PBS. Tissues were rapidly cryoembedded in OCT mounting medium and sectioned at 30 μm using a cryostat. Sections were blocked in a solution of 1X Tris Buffered Saline (TBS), 5% normal donkey serum and 0.5% Triton X-100. The primary antibodies, carried out 24 to 48 h at 4°C, were: goat anti-ChAt (1:500, ref: AB144P, Merck Millipore), chicken anti-GFP (1:500, ref: 1020, Aves Labs), rabbit anti-RFP (1:500, ref: 600-401-379, Rockland) and sheep anti-TH (1:500, ref: AB1542, Merck Millipore). Primary antibodies were detected after 2 h of incubation at room temperature with appropriate secondary antibodies coupled to Alexa Fluor 488, 647, Cy-3 or Cy-5 (1:500, Jackson ImmunoResearch). Sections were counterstained with a fluorescent Nissl stain (NeuroTrace 435/445 blue, ref: N21479, 1:200 or NeuroTrace 640/660 deep-red, ref: N21483, 1:1000, Thermo Fisher Scientific) and mounted in Prolong Diamond Antifade Montant (P36970, Thermo Fisher Scientific) or ibidi Mounting Medium (50001, Ibidi). For counting neurons in the entire brain in transneuronal labeling experiments, all sections were scanned on a Zeiss Axioscan Z1 Digital Slide Scanner (histology platform of the ICM, Paris, France). For all other purposes, sections were acquired with a Leica TCS SP8 confocal microscope (imaging platform of the NeuroPSI Institute, Gif-sur-Yvette, France) with 10x, 25x and 40x objectives. For illustrating a representative spinal cord injection (Figure 4F), whole lumbar spinal cords were cleared using CUBIC-R+ [75] and endogenous CTB fluorescence imaged on a light-sheet microscope (UltraMicroscope II, 4x objective, Miltenyi Biotec).

Delineation of brainstem structures and cellular counts

Brainstem areas were delineated by systematically performing a Nissl stain on experimental sections. The relative distance to Bregma was established by comparing the Nissl stain with that of the Mouse Brain atlas [76]. To examine the distribution of labeled neurons within the rostrocaudal axis of the RF, we considered four major subdivisions, similarly to a previous investigation [34] on the basis of the following criteria (see schematics in Figures 1C and 4G): the most caudal levels (encompassing the MdV) from the rostral edge of the pyramidal decussation caudally, to the opening of the 4th ventricle (obex) rostrally (from approximately −8.0 to −7.2 from Bregma); the caudal extent of the Gigantocellular reticular (Gi) nucleus (encompassing also its ventral part GiV) between the obex caudally and the caudal edge of the facial motor nucleus (7N) rostrally (approximately −6.5 from Bregma); the rostral extent of the Gi nucleus (encompassing its alpha part GiA and the IRt) from the caudal edge of the 7N caudally, to the caudal edge of the superior olivary complex (SOC) rostrally (approximately −5.5 from Bregma); the ponto-medularry junction (encompassing the PnC and the IRt) from caudal edge of the SOC to the motor trigeminal nucleus rostrally (approximately - 5.0 from Bregma). All neurons were counted on 30 μm-thick cryosections. For counting starter cells (Figures 1A–1E and S5) and HSV-labeled neurons (Figures 4 and S4), sections were scanned with a confocal microscope (Leica SP8) using a 25x objective. Counts were done manually with the help of the cell-counter tool in LASX (Leica), in non-adjacent sections. The number of cells per section were averaged per animal, and a grand-mean ± standard error of the mean (SEM) was calculated across animals to produce cells per section bar graphs. At each of the four rostrocaudal subdivision, labeled neurons were allocated into specific subnuclei (e.g., Gi, GiV, GiA, LPGi, IRt, PnC) by overlaying the histological section to the corresponding atlas slide. Pie graphs illustrate the fraction of labeled neurons located in each subnuclei (pooled from all animals) over the total number of labeled contained in the corresponding rostrocaudal subdivision. For counting rabies-labeled neurons, images were obtained from an automated epifluorescence microscope (Zeiss Axioscan Z1 Digital Slide Scanner). For illustrating the percentage of rabies-labeled neurons in each brain area (Figures 1J, S5E, and S5J) neurons in each area were counted using ZEN-Lite (Zeiss) and pooled across all sections for one animal, and expressed as the fraction of the total number of rabies-positive neurons detected automatically by threshold throughout the brain in that same animal. A grand-mean ± SEM was calculated across animals to produce bar graphs. For calculating the fractions of fluorescent anterograde projections in different structures (Figure 4E), maximum z stack projections were made and thresholded. Regions of interests were manually drawn in ImageJ and the densities of fluorescent pixels were measured for 4-5 sections per animal using the Measure plugin. These values were averaged across all sections from all animals and expressed in bar graphs ± SEM.

Behavioral experiments

Optogenetic activations

Behavioral experiments started 15 to 21 days after the viral injection. Implanted animals were connected to a laser source (473 nm DPSS system, LaserGlow Technologies, Toronto, Canada) through a mating sleeve (Thorlabs). In all conditions except EMG recordings, light was delivered in trains of pulses of 15 ms at 40 Hz frequency for a duration of 500 ms. For EMG recordings we also used single pulses of 5 ms duration. We used the minimal laser power sufficient to evoke a response, which was measured to be between 5-12 mW at the fiber tip using a power meter (PM100USB with S120C silicon power head, Thorlabs) to restrict photo-activations unilaterally [64], prevent heat, and exclude an unintentional silencing by over-activation [34].

Behavioral setting and video recordings

For analyzing changes in head movements, trajectory orientation and locomotor speed, animals were placed in a custom open field box (opaque PVC, 60 × 70 cm) without prior habituation and filmed from above at 50 images/sec using a CMOS camera (Jai GO-5000-USB). For analyzing limb movements during optogenetic activations, animals were placed in a custom transparent open-field (40 × 40 cm) and filmed from below at 100 images/sec (Jai GO-2400-USB). For optogenetic activations, open-field recording sessions lasted for a maximum of 30 min per animal. For silencing and ablation experiments, several 3-min videos were recorded per animal. For analyzing snout motion, animals were head-fixed for a maximum of 10 min, and filmed from above at 400 images/sec (Jai GO-2400-USB). Images were streamed to disk on a computer using 2nd Look (IO Industries). Timings of photo-activations were recorded using the TTL output of the laser connected to a National Instruments acquisition card (USB-6211) and the LabScribe NI software (iWorxs). Both recordings were synchronized using hardware trigger. Photo-activations were delivered manually using the NI MAX tool with a minimal interval of 30 s between two consecutive activations. Throughout the manuscript, one trial correspond to one photo-activation. Extracts of videos presented in the supplemental material were edited using Kdenlive (https://kdenlive.org/).

CNO administration

Four weeks following the injection of the hM4Di virus, animals were anesthetized and a surgery was performed as detailed earlier for intracranial viral injection. CNO (Enzo Life science, cat #: BML-NS105-0005) was diluted at 1 mM in freshly made and filtered artificial cerebrospinal fluid (aCSF) of composition (in mM): 126 NaCl; 3 KCl; 1.25 NaH_2PO_4; 2 $MgSO_4$; 26 $NaHCO_3$; 2 CaCl2; 11 D-Glucose. Fluorescent beads (Fluoro-Max blue beads, 0.5 µm, ThermoFischer Scientific, Cat#: B500) were added at a dilution of 1:4000 for subsequent histological validation. A total of 500 nL of CNO/fluorescent beads solution was delivered at the same coordinates used for the hM4Di virus (left side: 4 animals, right side: 1 animal). The pipette was immediately withdrawn after the injection, the skin incision closed rapidly with surgical glue (Vetbond, 3M Cat#: 1469SB) and animals immediately removed from the anesthesia mask. They were kept on an isothermal heating pad (Agnthos, Sweden) for a maximum of 10 min before being placed in the open-field to be filmed from above during 3 min. Since animals had only partially recovered from anesthesia, occasional motivation to move was given by a brief air puff or by the experimenter's hand. Animals were placed back on the heat pad for 2 min, before being filmed again in the open field for 3 min. The 2 videos started within the 15 min that follow the pipette withdrawal are used to produce the "CNO < 15 min" data (Figure 3O). Two or 3 more videos are recorded between 16 and 30 min following pipette withdrawal and used to produce the "CNO > 15 min" data. For controls, similar CNO injections were done on animals that did not receive the hM4Di virus.

Electromyographic Recordings

Electrodes were made of Teflon-insulated silver wire with an outside diameter of 0.14 mm (A-M systems, #793200), inspired by previous work [77]. For each animal, 2 pairs of electrodes were prepared as follows. For each electrode pair, two pieces of wire were lightly twisted together and a knot was placed about 2 cm of one end. A few millimeters from the knot, the Teflon insulation was removed over ~1 mm from each wire so that the two bared regions were separated by about 2 mm. The ends of two wires were glued to a miniature dissecting pin. The opposite ends of the wires were soldered to a miniature connector (Antelec). To implant electrodes in the splenius muscle, animals were anaesthetized using isoflurane and placed in a stereotaxic frame as detailed above. A small incision of the skin was performed dorsally to expose the muscles. The dissecting pin attached to the end of each pair of electrodes was used to draw the twisted pair of wires through the splenius muscle until the knot proximal to the bared regions was firmly against the muscle. The distal end of the electrode exiting the muscle was knotted. The needle was removed by cutting the electrode wires about 0.5 mm distal to this knot. The miniaturized connector was cemented on the skull, caudally to the existing optic fiber. The skin was sutured, and animals were followed daily after the surgery. Between 2 to 3 days following the surgery, implanted animals were connected to an AC amplifier (BMA-400, CWE) and signals were filtered (high-pass: 100 Hz, low-pass: 10 KHz) and collected at 10.000 samples/sec using a National Acquisition card (USB 6211) and the LabScribe NI software (iWorxs). Animals were placed in the open-field and optogenetic activations were delivered manually using the NI MAX tool. A TTL signal from the laser was connected to the same acquisition board for registering the timing of optogenetic activations.

QUANTIFICATION AND STATISTICAL ANALYSIS

Pose estimation using DeepLabCut and quantifications of body and head movements

To compute changes in body orientation, head rotation and locomotor speed, we labeled manually 4 points of interest (POIs) from 3204 frames taken across 80 top-view videos using DeepLabCut version 2.1.5.2 [78]: the head (H), the left and right ears (E_L, E_r) and

the base of the tail (T, see Figure S2A). We then used 95% of the labeled frames to train the network using a ResNet-101-based neural network with default parameters for 1 training iteration. We validated with 3 shuffles, and found that the test error was: 3,84 pixels, train: 3,21 pixels (image size was 2384 by 2048). We then used a p-cutoff of 0,5 to condition the X,Y coordinates for future analyses. This network was then used to analyze all other videos taken with same experimental settings.

Custom scripts were written in MATLAB (Mathworks) and used for computation. The orientation of the animal is defined as the angle α between the vector from T to the median point of E_L and E_R (E_M) and the origin axis $\overrightarrow{x}$ (Figure S2B).

$$\frac{\overrightarrow{TE_M}}{\left\|\overrightarrow{TE_M}\right\|} = \begin{pmatrix} X_1 \\ Y_1 \end{pmatrix}$$

$$\begin{pmatrix} X_1 \\ Y_1 \end{pmatrix} = \begin{pmatrix} \cos(\alpha) & -\sin(\alpha) \\ \sin(\alpha) & \cos(\alpha) \end{pmatrix} * \begin{pmatrix} 1 \\ 0 \end{pmatrix}$$

$$\alpha mod 360 = sign(Y_1) * \cos^{-1}(X_1)$$

The head rotation is defined by the angle β between the vector from T to E_M and the vector from E_L to E_R. A bias of 90° is introduced to set the zero when the 2 vectors are orthogonal, resulting in a positive angle when the head turns to the left and a negative angle when the head turns to the right (Figure S2C).

$$\frac{\overrightarrow{E_L E_R}}{\left\|\overrightarrow{E_L E_R}\right\|} = \begin{pmatrix} X_0 \\ Y_0 \end{pmatrix}$$

$$\begin{pmatrix} X_1 \\ Y_1 \end{pmatrix} = \begin{pmatrix} \cos(\beta) & -\sin(\beta) \\ \sin(\beta) & \cos(\beta) \end{pmatrix} * \begin{pmatrix} X_0 \\ Y_0 \end{pmatrix}$$

$$\beta mod 360 = sign\left(\frac{Y_1 - (X_0 X_1 + Y_0 Y_1) Y_0}{X_0}\right) * \cos^{-1}(X_0 X_1 + Y_0 Y_1) - 90$$

The barycenter (G) of the 4 POIs was computed to generate the locomotor trajectory of each mouse and its position derived to obtained the instantaneous speed (s) of the animal across the recording (Figure S2D).

$$\overrightarrow{s} = \frac{\partial \overrightarrow{u}}{\partial t}$$

With $\overrightarrow{u}$ being the displacement of G

$$\overrightarrow{u} = \overrightarrow{x} + \overrightarrow{y} \text{ and } \begin{cases} \overrightarrow{s_x} = \frac{\partial \overrightarrow{x}}{\partial t}, \overrightarrow{x} \text{ being the displacement of G along the x axis} \\ \overrightarrow{s_y} = \frac{\partial \overrightarrow{y}}{\partial t}, \overrightarrow{y} \text{ being the displacement of G along the y axis} \end{cases}$$

$$\overrightarrow{s} = \overrightarrow{s_x} + \overrightarrow{s_y} \text{ and} \overrightarrow{s_x} \perp \overrightarrow{s_y}$$

$$s = \sqrt{s_x^2 + s_y^2}$$

For optogenetic activations, trials were sorted as during locomotion when the animal's instantaneous speed was above 10 cm/s and during stationary when it was under 7.5 cm/s during 250 consecutive ms prior to light onset. Indeed, when animals were between these 2 speed values, their behavior was difficult to score (some steps interleaved with immobility) and corresponding trials were therefore not included. For each mouse, trials falling into either category (locomoting or stationary) were merged into matrices and each variable computed (var: α, β, speed):

$$A_{var} = \begin{pmatrix} a_{1,1} & \cdots & a_{1,j} \\ \vdots & \ddots & \vdots \\ a_{i,1} & \cdots & a_{i,j} \end{pmatrix}$$

with i the number of trials and j the number of frames per trial.

In the case of angles (ex: α, β), we normalized, at each trial, the changes induced by light stimulation to the average angle during 0,5 s before light onset.

Finally for each type of injection (Gi, C2, L2) and behavioral condition (stationary or locomoting), the mean response of each animal was computed across all trials (the same number of trials per animal, at least 3 trials) and expressed ± standard error (SEM). A grand-mean ± SEM across animals is also illustrated in figures (colored curves).

Calculations of limb velocity

To produce color-plots histograms, we attempted to label the 4 paws using DeepLabCut. However, this led to significant number of errors and inversions between paws. All errors were then manually corrected on 9 videos from 3 mice. Points were then filtered (maximum speed and group cutoff followed by linear interpolation) and the instantaneous speed of each limb speed was then computed, and a color matrix produced using MATLAB.

Statistical analysis for optogenetic experiments

To perform statistical tests for body orientation, we calculated, for each trial, the peak change in orientation of the mouse during photo-activations as well as the orientation 0.5 s after light offset (black arrowhead in graphs). For the head rotation, we calculated the maximum angle variation to baseline during photo-activations. Both the body orientation and head rotation angles of all trials (numbers are given in figure legends) from all mice within each category (i.e., Gi, L2 or C2 injection and stationary or locomoting) were statistically compared to the same measurements obtained from all trials from 4 injected and implanted wild-type mice (stationary: 44 trials from 4 mice, 11 trials each; locomotion: 48 trials from 4 mice, 12 trials each), using unpaired t tests. For evaluating the effect of photo-activations on locomotor speed we took into account the spontaneous gradual deceleration that occurs independently of activating V2a neurons, as seen in mock photo-activation trials in control mice (Figure S2K). This likely owes to the episodic nature of locomotion in this specie and our intentional delivery of photo-activations when animals just engaged in a vigorous locomotor bout which is bound to be short due to the limited size of the open field. We therefore computed, for each trial, the mean locomotor speed during light stimulations as well as the first deceleration coefficient of the first monotonic part of the curve during the light-stimulation as the best fitted linear regression. Both the mean speed and the slope coefficients of all trials of all mice within a given category were statistically compared to those obtained from control mice. For snout motion recordings, the mean position of the nose snout during the 500 ms photo-activations was computed for each trial, and statistically compared to the mean position during the preceding 500 ms.

Statistical analysis for ablation and silencing experiments

We computed, for each video of each mice, i) the instantaneous angular speed of the animal as the first derivative of the body orientation during locomotion (i.e., instantaneous speed > 10 cm/s) and ii) the average head orientation during the entire video recording. These values were statistically compared between appropriate groups (e.g., before and after CNO) using unpaired t tests.

Statistical analysis for electromyographic recordings

EMG recordings were exported to Clampfit (Molecular Devices) and responses to photo-activations were detected manually as events with a pointed peak (either negative of positive), with an amplitude larger than 5 times the mean baseline before the light pulse and occurring within 25 ms following light onset. The latency was defined as the interval between light onset and the time point when the EGM signal reaches the above detection threshold. Data were collected for ~15 trials per animal and a grand-mean ± SEM across all trials was computed to produce bar graphs illustrated in Figure 7. Differences in latency between the ipsilateral and contralateral sides were evaluated by unpaired t tests across all trials.

Current Biology, Volume *30*

Supplemental Information

Control of Orienting Movements and Locomotion by Projection-Defined Subsets of Brainstem V2a Neurons

Giovanni Usseglio, Edwin Gatier, Aurélie Heuzé, Coralie Hérent, and Julien Bouvier

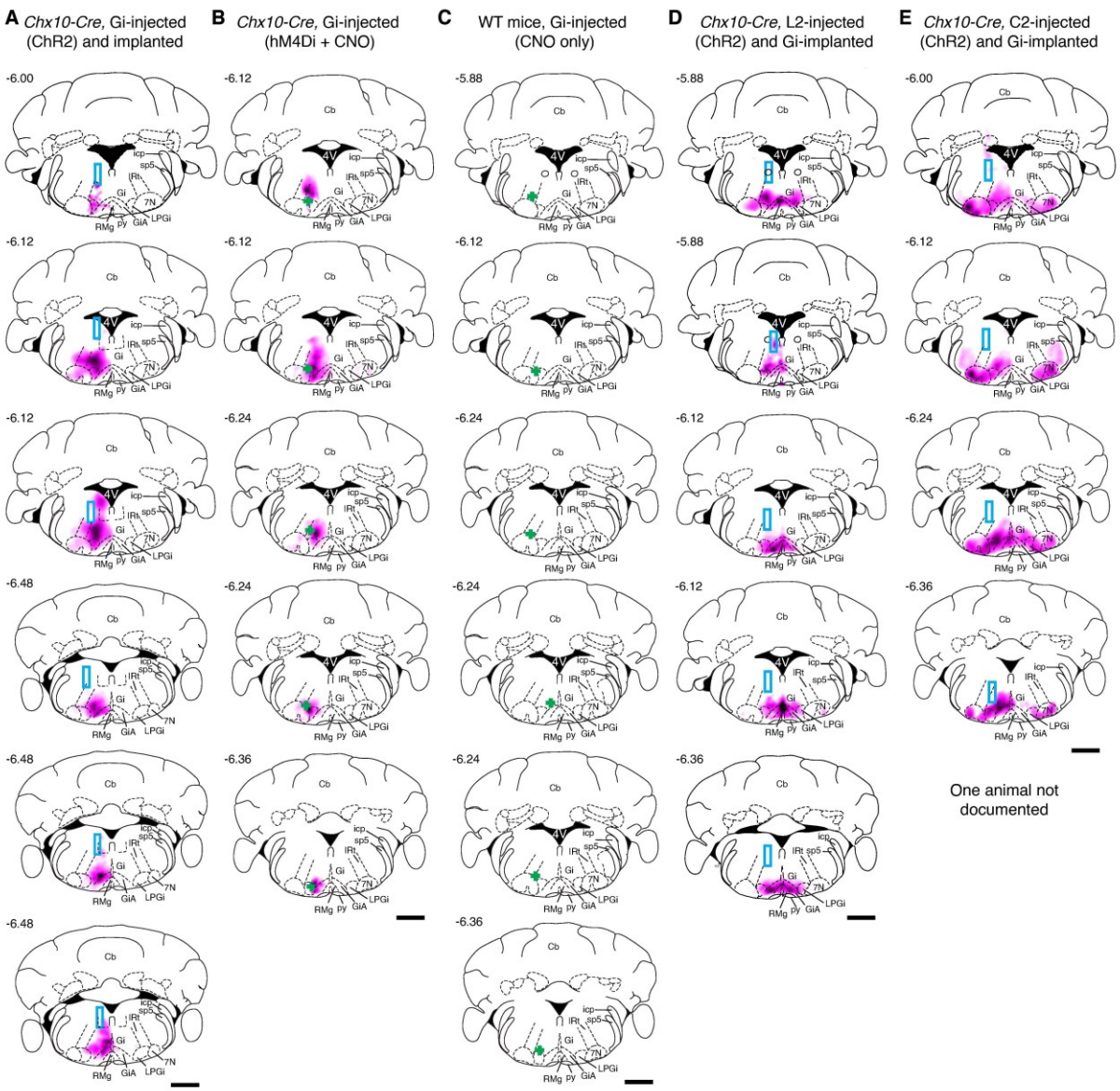

Figure S1. Anatomical sites of viral expression and optic fiber implantations. Related to Figures 2, 3, 5, 6, 7, S6.

Virally-driven fluorescence (both from somata and processes) was color-coded in a pink gradient and mapped onto the stereotaxic mouse brain atlas by Franklin and Paxinos [S1]. Each section is from one animal and sections are ordered from rostral (top) to caudal (bottom). Numbers on the left of each section indicate the approximate rostrocaudal position from Bregma.

(A) Reconstructions following injections of an AAV-DIO-ChR2-eYFP in the Gi of *Chx10-Cre* mice. The blue rectangles depict the locations of the optic fibers.

(B) Reconstructions following CNO-mediated silencing of V2a neurons in the Gi using an AAV-DIO-hM4Di-mCherry followed by intracranial injection of 1 mM CNO in *Chx10-Cre* mice (green crosses, assessed by fluorescent beads injected conjointly).

(C) Reconstructions of injection sites for CNO (green crosses) on wild-types mice, without prior injection of the hM4Di virus.

(D, E) Reconstructions following injections of an AAVretro-FLEX-ChR2-eYFP in the L2 (D) or C2 (E) spinal segments of *Chx10-Cre* mice. The blue rectangles depict the locations of the optic fibers. Altough one animal injected in C2 could not be documented, it was injected using the same procedures, viral volume and coordinates for lens implantation, and it responds similarly to the others to photo-activations; it was therefore not excluded.

Scale bars: 1mm. Cb: cerebellum; RMg: raphe magnus nucleus; Amb: ambiguus nucleus. See Figure 1 for other abbreviations used.

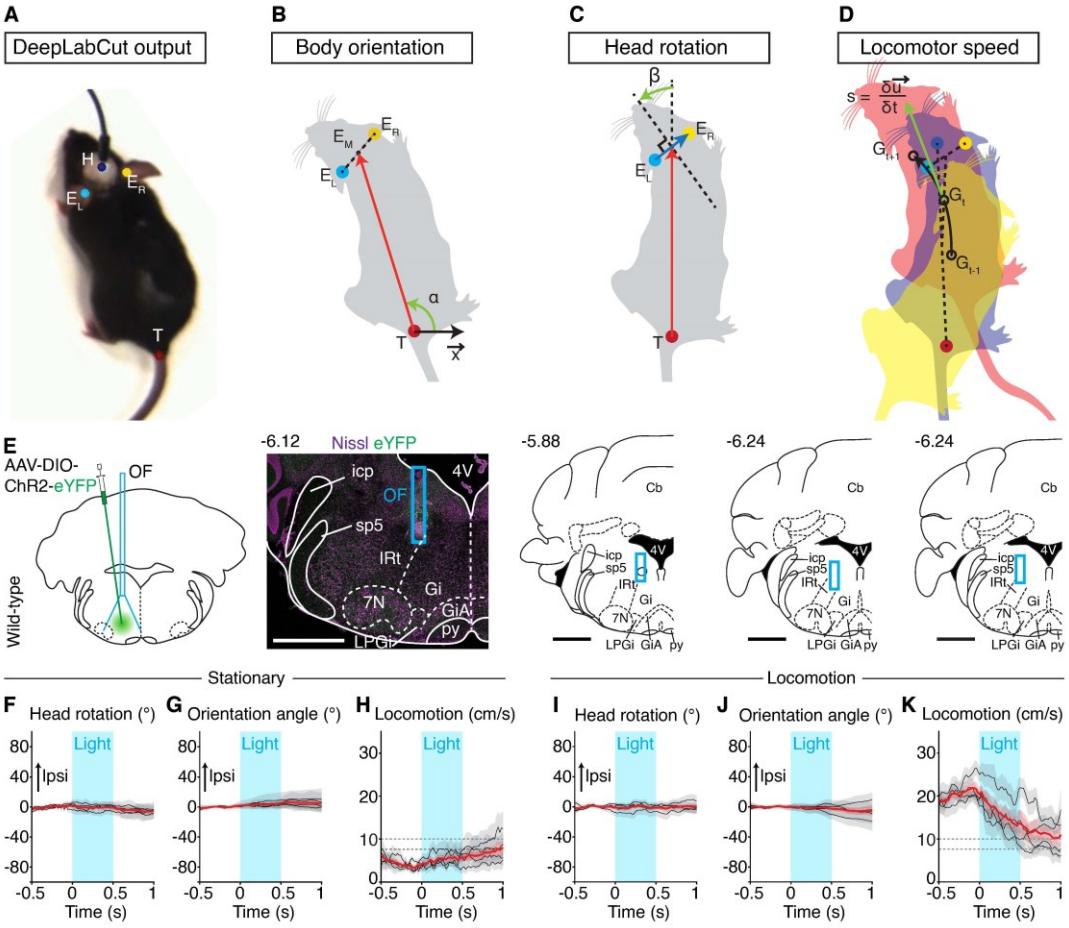

Figure S2. Detection of the animal's body parts and controls for optogenetic activations. Related to Figures 2, 3, 5, 6, S6 and S7.

(A) Snapshot from a mouse filmed from above in the open-field. Using DeepLabCut [S2, S3], we extracted 4 point of interests (POIs) for each frame: the head (H) at the base of the optic fiber implant, the right and left ears (E_R & E_L) and the base of the tail (T).

(B) The angle α between the x-axis of the open field and the vector from the tail to the middle of E_LE_R (TE_M, in red) is computed for each frame, giving the orientation of the body at every instant. This angle is normalized to the average angle during the 500 ms preceding the photo-activations for comparison purposes between trials. See also STAR Methods for details.

(C) The head rotation is defined as the angle β between the body axis vector TE_M (red) and the vector E_LE_R (blue). An offset of 90° is introduced to obtain a left (ipsilateral) head turn as a positive angle and a right (contralateral) head turn as a negative angle. The head rotation angle is normalized to the average angle during the 500 ms preceding the photo-activations for comparison purposes between trials.

(D) The instantaneous speed (s, green arrow) of the animal is computed as the gradient over time of the displacement (u) of the POIs' barycenter (G) at each frame (t). Mouse schematics in (B-D) are from Scidraw.io.

(E) Left: schematic transverse brainstem section depicting the site of viral injection and of the chronic optic fiber (OF) implant on a wild-type mouse. The injection pipette is depicted with an angle for clarity, but the injection was performed without angle. Middle: representative transverse brainstem section at the rostrocaudal level of the injection on a Nissl background, showing the location of the optic fiber and the absence of eYFP-expressing neurons. Right: reconstructions on the mouse brain atlas by Franklin and Paxinos [S1] of optic fiber positions (blue rectangles) of the 3 other wild-type mice; each section is from one animal. Numbers on the left of each section indicate the approximate rostrocaudal position from Bregma. Scale bars: 1 mm.

(F-H) Changes in motor parameters during photo-activations (15 ms pulses at 40 Hz, for a duration of 500 ms, blue area) when animals are stationary. Data are presented as the means ± SEM for each animal (grey, n = 4 mice, 11 trials each) and as the means ± SEM across animals (in red).

(I-K) Similar representations for photo-activations delivered during ongoing locomotion (n = 4 mice, 12 trials each).

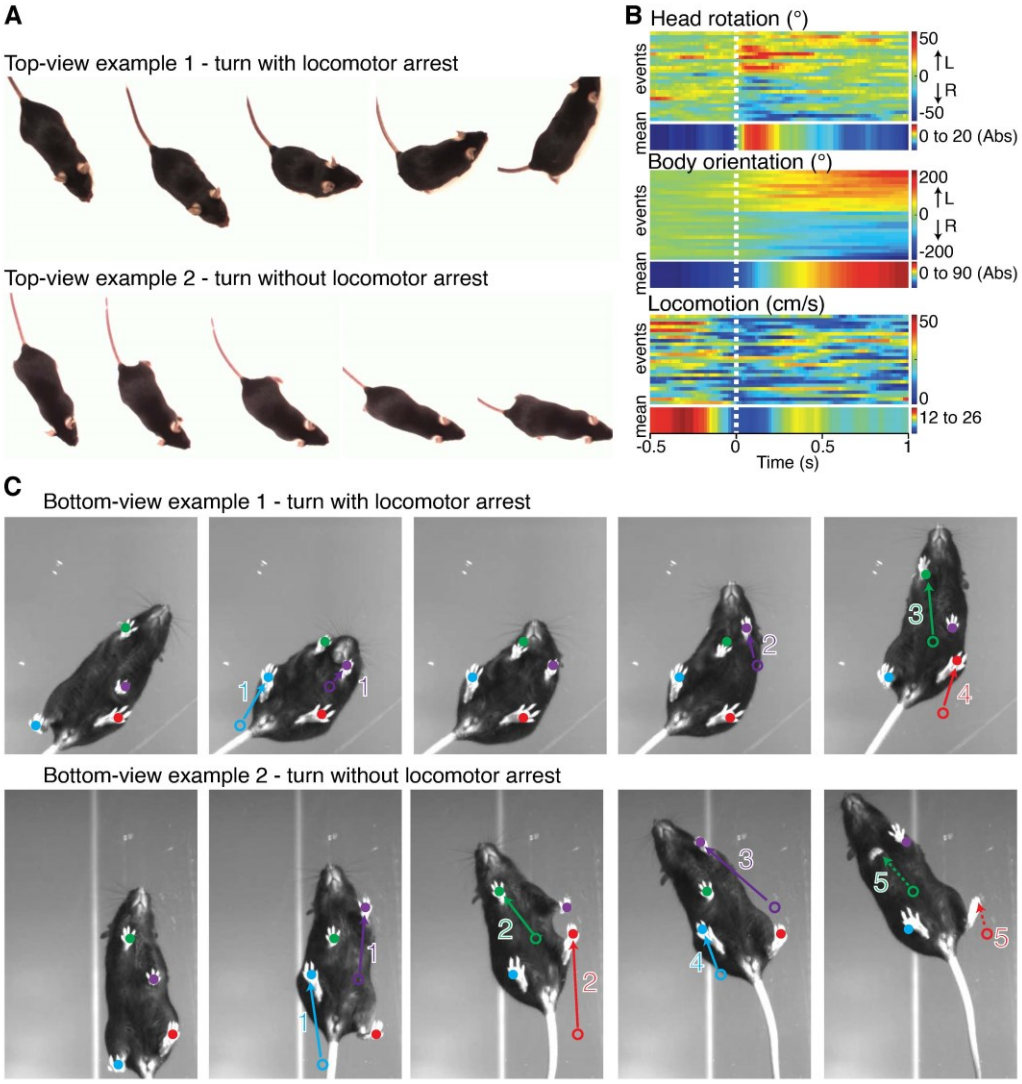

Figure S3. Naturally-occurring directional changes are preceded by a head yaw rotation and can be associated with a decrease in locomotor velocity. Related to Figures 3, 5 and 6.

(A) Two example snapshots of the same wild-type mouse in the open-field. The first one illustrates a change in trajectory associated with a complete locomotor arrest. A rotation of the head precedes the resumption of locomotion in the new direction. In the second example, the mouse does not arrest walking, but note again the rotation of the head towards the new direction.

(B) Color plot of the head rotation, the body orientation and the locomotor velocity for 1.5 s during spontaneously-occurring turns in wild-type mice. For each parameter, 26 turning events from 6 mice are shown on the y axis (events), and the mean across all events is shown below. Events are presented in the same order in the 3 plots. Events are synchronized (time = 0 s, white dashed line) on the peak head rotation velocity (obtained as the first derivative of the head rotation, not shown). The body orientation at each frame is normalized to its mean value during the 500 ms that precede the peak head rotation. For the head rotation and body orientation, the color gradient indicates degrees to the left (positive values, gradient to red) and to the right (negative values, gradient to blue). For the mean color plots, all events were expressed positively regardless of their direction to the left or right side (Abs); blue therefore indicates no change and red a maximal change. For the locomotor velocity, the color gradient to red indicates high values in cm/s.

(C) Two example snapshots of naturally-occurring turnings in a wild-type mouse filmed from below. Colored numbers indicate the order of limb movements. Filled and open circles indicate respectively the current and previous position of the paw. The first example illustrates a change in locomotor trajectory associated with a complete locomotor arrest. Note the symmetric positioning of the 4 limbs and the rotation of the head that precedes the resumption of locomotion in a novel direction which is primed by the forelimbs. In the second example, the mouse does not arrest walking. Note again the rotation of the head towards the new direction.

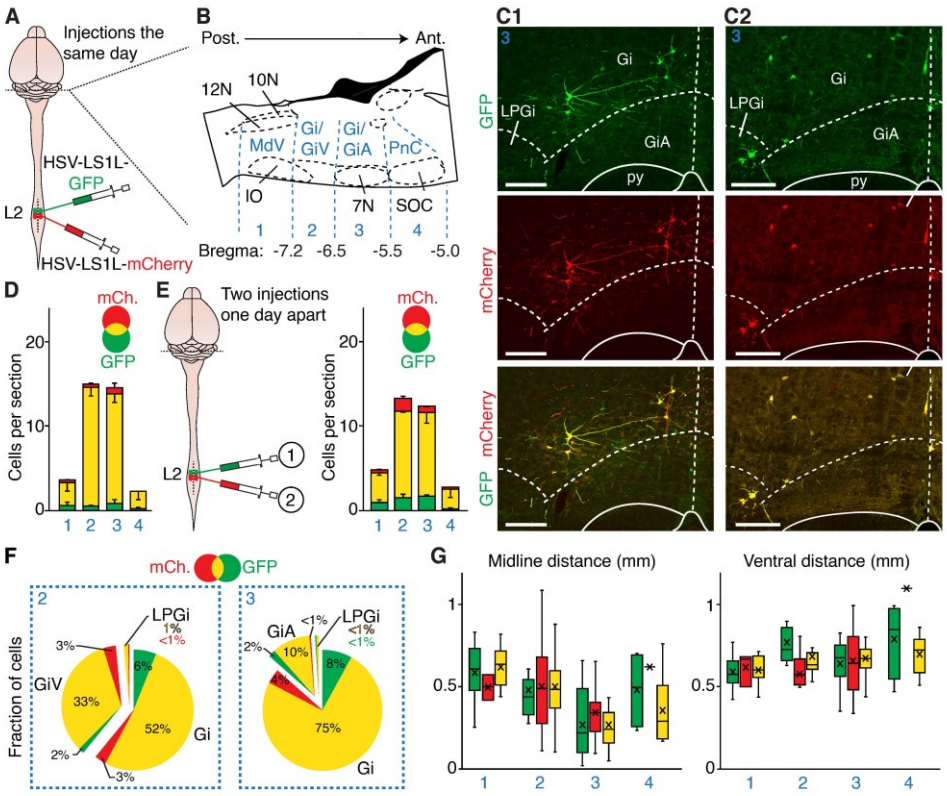

Figure S4. Dual HSV expression in individual V2a neurons. Related to Figure 4.

(A) Injection strategy for labelling L2-projecting V2a RS neurons with two HSVs, each coding a distinct fluorophore and injected sequentially during the same surgery (~15 minutes apart).

(B) Sagittal schematic of the brainstem indicating the rostrocaudal levels (1 to 4, with their approximate distance from Bregma) used to allocate labelled neurons in the subsequent panels.

(C) Transverse brainstem sections at the rostrocaudal level 3, where functional manipulations are performed in this study, showing that the majority of virally-transfected V2a Gi neurons express both HSV-driven fluorophores. C1 and C2 are examples from two distinct animals. Scale bars: 200 μm.

(D) Bar-graph showing, at each rostrocaudal level, the mean number ± SEM of single and double-labelled neurons per histological section (n = 2 mice; total cells counted: 354; average cells per animal: 177 ± 59).

(E) Left: injection strategy for labelling L2-projecting V2a RS neurons with the same two HSVs as in (A), this time injected one day apart. Right: bar-graph showing, at each rostrocaudal level, the mean number ± SEM of single and double-labelled neurons per histological section (n = 2 mice; total cells counted: 442; average cells per animal: 221 ± 43).

(F) Pie-graphs showing the distribution of labelled neurons within the indicated Gi subnuclei at rostrocaudal levels 2 and 3 (in percent of the total number of cells counted at each rostrocaudal level, pooled from the 4 animals shown above). All cells at the rostrocaudal level 1 were in the MdV and all cells at level 4 in the PnC.

(G) Mediolateral (on the left, in mm from the midline) and dorsoventral (on the right, in mm from the ventral border) positions of single and double-labelled cells from the 4 animals illustrated above. Data are presented as the means (crosses) and box-and-whisker plots which give the median, 25th and 75th percentiles, and range.

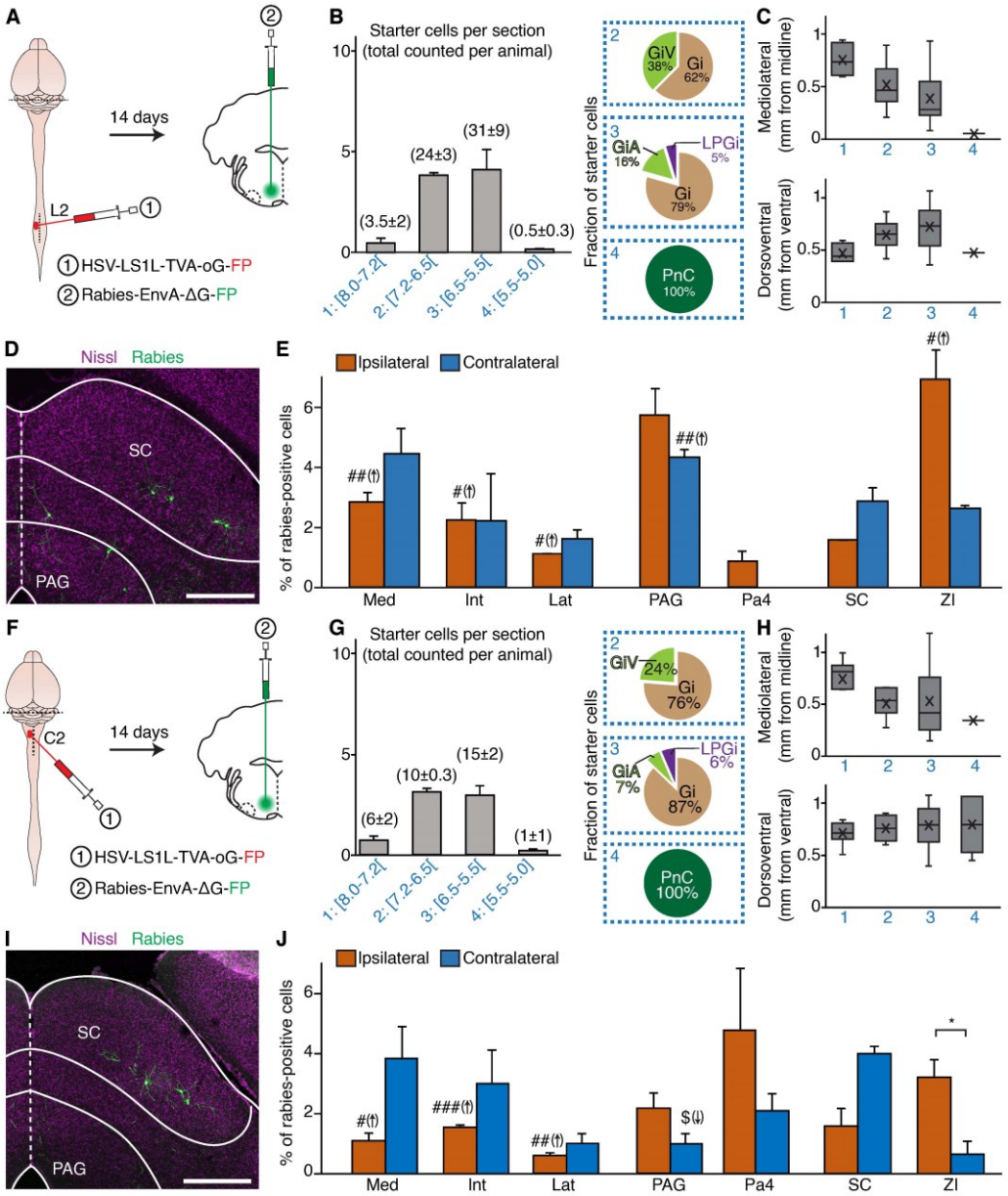

Figure S5. Putative inputs to L2-projecting and C2-projecting subsets of V2a Gi neurons. Related to Figure 4.

(A) Schematic representations of the retrograde transneuronal labelling strategy initiated from L2-projecting V2a neurons. The rabies proteins TVA and oG are retrogradelly-delivered to V2a neurons using a cre-dependent HSV helper, injected in the L2 segment on *Chx10-Cre* adult mice. An EnvA-ΔG-rabies-FP is subsequently injected in the Gi, thereby restricting its entry to V2a Gi neurons that project to the L2 segment.

(B) Left: average number ± SEM of starter cells per histological section at the 4 representative rostrocaudal levels indicated in blue (with the corresponding range of negative coordinates from Bregma, see Figures 1C, 4G & S4B for a schematic representation). Pie-graphs to the right show the distribution of starter cells within the indicated Gi subnuclei at rostrocaudal levels 2, 3 and 4 (in percent of the total number of starter cells counted at each rostrocaudal level). All cells at the rostrocaudal level 1 were in the MdV. See STAR Methods for the delineation of brainstem nuclei. Total starter cells counted: 119 from 2 animals; average per animal: 60 ± 15.

(C) Mediolateral (top, in mm from the midline) and dorsoventral (bottom, in mm from the ventral border) positions of all starter neurons (pooled from the 2 animals) presented as the means (crosses) and box-and-whisker plots which give the median, 25th and 75th percentiles, and range.

(D) Representative transverse section showing rabies$^+$, i.e. putative presynaptic, neurons in the superior colliculus (SC). Scale bar: 500 µm.

(E) Average percentage ± SEM of rabies$^+$ cells in each indicated region over the total amount of rabies$^+$ cells detected in each brain (n = 2 mice, total cells counted: 3476; average per animal: 1738 ± 491). Putative presynaptic neurons in the reticular formation are not shown and accounted for 25 ± 6 % (ipsilaterally) and 28 ± 5 % (contralaterally) of all rabies$^+$ neurons counted. Differences between the ipsilateral and the contralateral sides are not significant (paired t-tests, not represented). $^{\#\#\#}p < 0.001$, $^{\#\#}p < 0.01$, $^{\#}p < 0.05$, unpaired t-test between helper virus injected in the Gi (see Figure 1) and helper virus injected at L2. Non-significant p values are not indicated.

(F-J) Similar representations and quantifications for C2-projecting V2a Gi neurons. Total starter cells counted: 67 from 2 mice; average per mice: 34 ± 6; total rabies$^+$ cells counted: 756; average per animal: 378 ± 170. Putative presynaptic neurons in the reticular formation are not shown and accounted for 35 ± 3 % (ipsilaterally) and 25 ± 3 % (contralaterally) of all rabies$^+$ neurons counted. $^*p < 0.05$, paired t-test between ipsilateral and contralateral sides. $^{\#\#\#}p < 0.001$, $^{\#\#}p < 0.01$, $^{\#}p < 0.05$, unpaired t-test between helper virus injected in the Gi (see Figure 1) and helper virus injected at C2. $^{\$}p < 0.05$, unpaired t-test between helper virus injected in L2 and C2. Non-significant p values are not indicated.

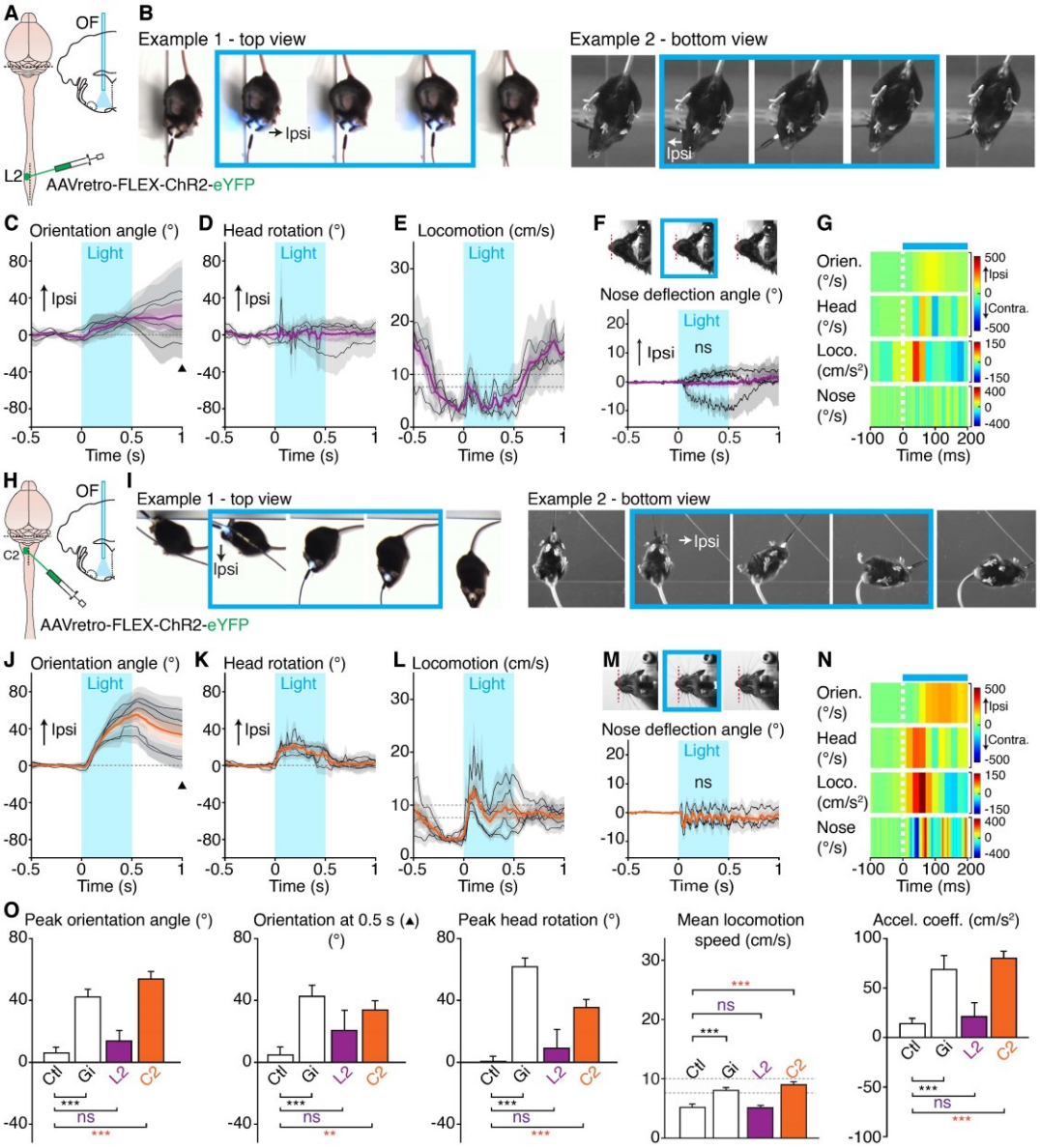

Figure S6. Motor responses when photo-activating L2 or C2-projecting V2a neurons on stationary mice. Related to Figures 5 and 6.

(A) Schematic strategy for photo-activating L2-projecting V2a Gi neurons. See also Figure S1D for all implantation sites.

(B) Example snapshots from two distinct animals (taken 250 ms before light onset, at light onset, 250 ms after onset, just before light offset, and 250 ms after light offset), showing the absence of orienting motor responses during a 500 ms light train (15 ms pulses at 40 Hz) delivered unilaterally.

(C-E) Left: light-evoked changes in the indicated motor parameters. Black lines and grey shaded areas depict the means ± SEM of each animal (n = 4 mice, 3 trials each) and thick purple lines with purple shaded area represent the means ± SEM across animals. The black arrowhead in (C) indicates the time point at 0.5 s after light offset. The dashed zone in (E) indicates the threshold from stationary (< 7.5 cm/s) to locomoting (> 10 cm/s) conditions.

(F) Top: example view of one head-fixed mouse used for measuring the angular displacement of the snout during photo-activations on the left side. Bottom: mean normalized angular deflection ± SEM of the snout, for each animal (grey) and across animals (purple). ns, not significant (paired t-test between the mean angles for 0.5 s before and 0.5 s during photo-activations, n = 24 trials from 4 mice, 6 trials each).

(G) Color plot showing the first derivative of the above motor parameters from 100 ms before to 200 ms after light onset (the dashed white line indicates light onset).

(H-N) Similar illustrations for C2-projecting V2a neurons (orientation/head/locomotion: n = 5 mice, 19 trials each). See also Figure S1E for implantation sites. Note a change in body orientation, in head rotation and the engagement in a few steps of quadrupedal locomotion, but no significant displacement of the snout, in response to photo-activations. In (M): ns, not significant (paired t-test between the mean angles for 0.5 s before and 0.5 s during the photo-activations, n = 21 trials from 3 mice).

(O) Mean ± SEM of the peak change in orientation during photo-activations, the orientation angle 0.5 s after light offset (▲in C and J), the peak head rotation during photo-activations, the mean locomotor velocity and the first acceleration coefficient during photo-activations across all trials for L2-projecting (purple) and C2-projecting (orange) V2a Gi neurons compared with the same measurements in mock trials from control mice (Ctl, n = 44 trials from 4 mice, 11 trials each) and following activation of V2a Gi neurons collectively (Gi, n = 35 trials from 5 mice, 7 trials each). ** $p < 0.01$; *** $p < 0.001$; ns, not significant (unpaired t-test).

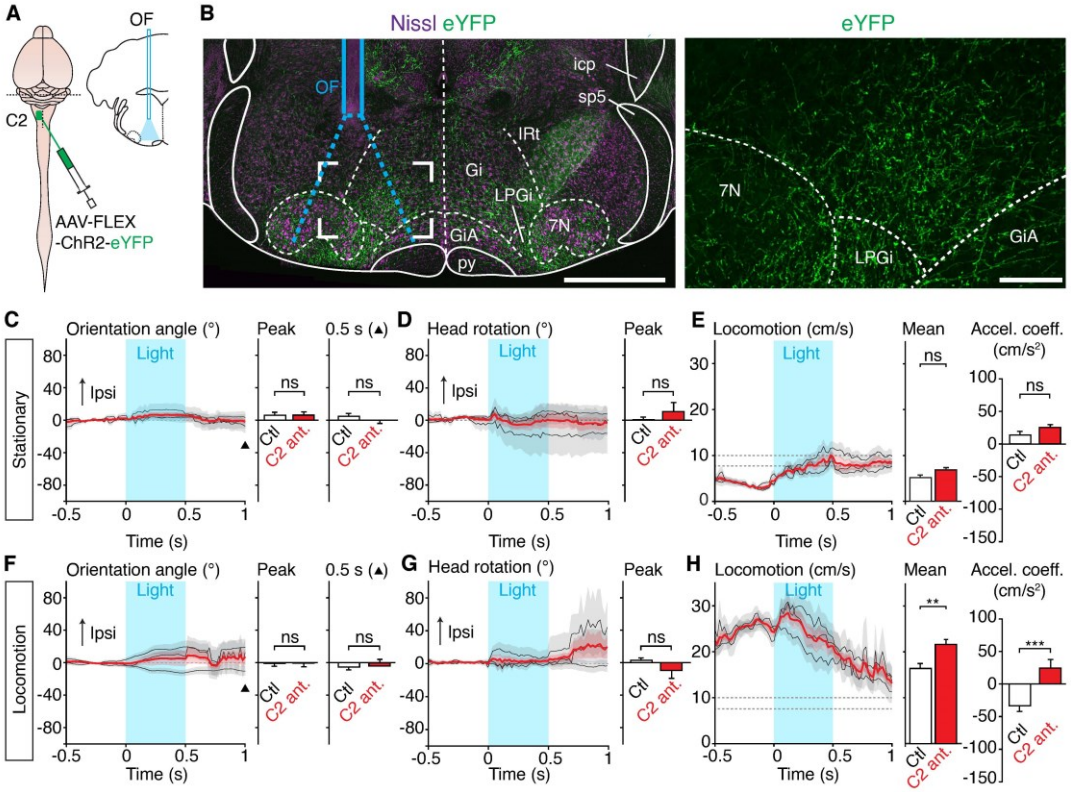

Figure S7. Activating anterograde projections in the Gi of C2-located V2a neurons does not elicit orienting motor responses. Related to Figures 6 and S6.

(A) Experimental strategy for photo-activating, in the Gi, anterograde fibers of V2a neurons residing in the 2nd cervical segment using an AAV-FLEX-ChR2-eYFP. Chx10-expressing neurons located in L2 do not send ascending projections to the reticular formation (not shown).

(B) Example transverse section at the level of the optic fiber implant in the Gi (representative of 3 animals) showing virally-transfected V2a processes (eYFP), the position of the optic fiber (OF) and the theoretical light cone at the fiber tip (dashed blue lines) that restricts activations to the implanted side [S4]. Scale bar: 1 mm. To the right is an enlarged view of the boxed area, showing eYFP processes, but no neuronal somata, in the Gi and adjacent nuclei. Scale bar: 200 µm

(C-E) Left: changes in motor parameters during photo-activations (15 ms pulses at 40 Hz, for a duration of 500 ms, blue area) delivered unilaterally when animals are stationary. Data are presented as the means ± SEM for each animal (grey, n = 3 animals, 56 trials each) and across animals (red). The black arrowhead in (C) indicates the time point at 0.5 s after light offset. The dashed zone in (E) indicates the threshold from stationary (< 7.5 cm/s) to locomoting (> 10 cm/s) conditions. Bar-graphs to the right show the mean ± SEM of the peak change in orientation during photo-activations and the orientation angle 0.5 s after light offset (C), the peak head rotation during photo-activations (D), and the mean locomotor speed and the first acceleration coefficient during photo-activations (E) across all trials (C2 ant., n = 168 trials from 3 mice, 56 trials each) compared with mock trials from control mice (Ctl, n = 44 trials from 4 mice, 11 trials each). ns, not significant (unpaired t-test).

(F-H) Similar illustrations and quantifications during ongoing locomotion (C2 ant.: n = 54 trials from 3 mice, 18 trials each; Ctl: n = 48 trials from 4 mice, 12 trials each). ** $p < 0.01$; *** $p < 0.001$ (unpaired t-test), ns, not significant. See also Figure S2 for the calculation of movements and the responses of control mice.

SUPPLEMENTAL REFERENCES

S1. Franklin, K.B., and Paxinos, G. (2007). The Mouse Brain in Stereotaxic Coordinates 3rd edn. Elsevier.

S2. Mathis, A., Mamidanna, P., Cury, K.M., Abe, T., Murthy, V.N., Mathis, M.W., and Bethge, M. (2018). DeepLabCut: markerless pose estimation of user-defined body parts with deep learning. Nat Neurosci *21*, 1281-1289.

S3. Nath, T., Mathis, A., Chen, A.C., Patel, A., Bethge, M., and Mathis, M.W. (2019). Using DeepLabCut for 3D markerless pose estimation across species and behaviors. Nat Protoc *14*, 2152-2176.

S4. Stujenske, J.M., Spellman, T., and Gordon, J.A. (2015). Modeling the Spatiotemporal Dynamics of Light and Heat Propagation for In Vivo Optogenetics. Cell Rep *12*, 525-534.

4.2. V2a medullary premotoneurons orchestrate upper trunk and orofacial orienting movements

For the following results, that are still not published, I took the initiative to present them here in a paper format.

However, I am fully aware that these data and analysis are not sufficient to complete a peer-reviewed article. Indeed, as the reader will see, the results are not exhaustive, especially for the quantification and analysis.

Moreover, other experiments, that I am currently performing, are required to make these results sufficient for a peer-reviewed article. Some of them indeed are explained in the short discussion that I inserted at the end.

V2a medullary premotoneurons orchestrate upper trunk and orofacial orienting movements

Giovanni Usseglio, Edwin Gatier, Alexis d'Humières, Elisa Toscano, Niccolò Zampieri, Julien Bouvier*

Université Paris-Saclay, CNRS.

Institut des Neurosciences Paris-Saclay. France

Max Delbrück Center for Molecular Medicine, Berlin, Germany

Cluster of Excellence NeuroCure, Charité-Universitätsmedizin Berlin, German

*Correspondance : Dr. Julien Bouvier (julien.bouvier@cnrs.fr)

Introduction

Body movements are necessary for all animals in order to explore the external environment, obtain food, escape for predators and interact with other animals. Most studies have focused on the neuronal circuits for either sensory integration or motor execution. However, the intermediate relay, i.e. the cells that link integrative centers with the executive circuits in the spinal cord, is still poorly documented. This yet represents a fundamental challenge and a prerequisite for designing rehabilitative therapies for patients after spinal cord injuries.

The brainstem reticular formation (RF) is a candidate relay of sensory and goal-directed modalities from multiple higher brain areas to the adequate executive motor circuits of the spinal cord that perform motor actions (Arber and Costa, 2018; Drew et al., 1986; Grillner and El Manira, 2020; Jordan et al., 2008; Leiras et al., 2022; Lemon, 2008; Ruder and Arber, 2019). Indeed, the RF receives inputs from multiple brain regions and hosts reticulospinal (RS) neurons, characterized by long axonal projections contacting different regions of the spinal cord (Caggiano et al., 2018; Ferreira-Pinto et al., 2018; Josset et al., 2018). Furthermore, reticular neurons comprise several cell types differing in their neurotransmitter identity, morphology, developmental history and gene expression (Brownstone and Chopek, 2018; Deliagina et al., 2002; Liu and Jordan, 2005; Valverde, 1961). This cellular heterogeneity suggests that i) each cell type could control a specific motor function, and ii) that different reticular neuronal subtypes might be part of distinct/parallel long-range neural circuits in different descending circuits. However, the functional diversity of reticular neurons and their efferent connectivity to the spinal cord is poorly characterized.

Previous works investigated one class of RS neurons of the Gigantocellular reticular nucleus (Gi) (Franklin and Paxinos, 2007), termed the V2a neurons (defined by the expression of the transcription factor Chx10) (Bretzner and Brownstone, 2013; Kimura et al., 2013). V2a neurons represent a genetically-circumscribable subgroup of excitatory RS neurons in the Gi that, when activated bilaterally, arrests ongoing locomotion (Bouvier et

al., 2015). Such “V2a stop neurons” were then seen as divergent from the classical view that excitatory descending circuits favor movements. Recent works showed that the V2a neurons in the Gi receive inputs from multiple motor-related areas among which the contralateral superior colliculus is the main source (Cregg et al., 2020; Usseglio et al., 2020). This midbrain structure is well-known for its role in spatial orientation (Basso et al., 2021; Basso and May, 2017; Isa et al., 2021; Masullo et al., 2019; May, 2006). Functional investigations indeed confirmed that the activity of V2a neurons control orienting maneuvers (Usseglio et al., 2020). Yet, the same study demonstrated the existence of at least two subsets of V2a neurons controlling different motor components of orientation: one that projects to the lumbar spinal cord arrests locomotion and one that projects to the cervical spinal cord induces a head rotation and change in the trajectory. Yet V2a neurons in the medullary RF are exclusively glutamatergic. Hence, the opposite functional outcome of the two subsets must therefore reflect different targeted cell types in the spinal cord. While lumbar-projecting V2a neurons may exert their function via spinal inhibitory neurons (Bouvier et al., 2015), the post-synaptic targets of cervical projecting V2a neurons remained to be defined.

What’s more, the orienting behavior in the large sense is known to mobilize additional motor components, including eye and snout movements (Basso and May, 2017; Isa et al., 2021; Isa and Sasaki, 2002; May, 2006), actions that are piloted by supra-spinal brainstem circuits. Interestingly, it was recently shown that V2a medullary neurons might comprise a non-spinally projecting population (Chopek et al., 2021), but its functional role was not directly examined. In general, the global efferent connectivity of medullary V2a neurons, as well as their role in controlling other motor actions besides locomotion, head movements and breathing (Crone et al., 2012) are not known.

Our present work demonstrate that the medullary V2a neurons control not only spinal-related motor actions, but also eye movements, an orienting response that is known to be controlled by the superior colliculus (Basso and May, 2017; Isa et al., 2021; Isa and Sasaki, 2002; May, 2006). Furthermore, we demonstrate that there is a subset of V2a neurons contacting the facial motor nucleus (7N), where reside the motoneurons controlling

nose and whiskers movements (Guthrie, 2007). Importantly, the activation of the 7N-projecting V2a subset does not trigger spinal-related movements nor eye movements. Conversely, the C2-projecting and the L2-projecting V2a subsets do not control supraspinal motor actions (snout and eye movements). The different motor outcomes observed during medullary V2a neurons' activation (promoting movements, for the case of neck, eyes, snout movements and arresting motor action, in the case of the stop of locomotion) suggest that there might be distinct post synaptic targets. Indeed, while in the lumbar spinal cord the medullary V2a neurons might exert the stop of locomotion activating inhibitory neurons in the lumbar spinal cord (Bouvier et al., 2015), we demonstrated that the 7N and C2 projecting subsets directly form monosynaptic connections with the motoneurons controlling snout and neck muscles, respectively.

Our work shows that the V2a neurons control both spinal and brainstem-related motor functions, demonstrating a multifunctional ambition of this cell class for orchestrating components of the orienting behavior. Moreover, our results place V2a neurons as an essential premotor population for upper trunk and orofacial orienting actions. Altogether, our study contributes to propel forward our understanding of the complex and multi-function ambition of reticular neurons in the control of composite motor behaviors.

Results

V2a medullary neurons control multiple supraspinal-related motor actions

Previous work showed that the V2a neurons in the Gi control multiple motor components of orientation (Usseglio et al., 2020), including an ipsilateral snout displacement. We hypothesized here that V2a Gi neurons might in addition control eye movements, also typical for orienting behavior and commonly associated to superior colliculus functions (Basso et al., 2021; Basso and May, 2017; Isa et al., 2021). To investigate this, we delivered in Chx10-Cre mice the ChR2 in the Gi ipsilaterally and we implanted an optic fiber on the same side (Figure 1A, B). Then, we placed the mouse in a head-fixed set-up and, using infrared illumination, we tracked the pupil movements during the light activation (Figure 1C) as previously done (Meyer et al., 2020; Michaiel et al., 2020; Sakatani

and Isa, 2007). During the photo-activation (1 single pulse, 500 ms), we observed a horizontal deflection of the ipsilateral eye laterally, away from the nasal edge (Figure 1F, G). This movement was accompanied by a conjugate displacement of the contralateral eye towards the nasal edge (data not shown). In contrast, the pupil movement was virtually absent in the vertical direction (Figure 1).

Furthermore, we also tested whether the eye displacement could be trigger by the photo-activation of spinally-projecting V2a neurons (C2 or L2-projecting). To selectively manipulate spinal-projecting V2a Gi neurons, we took advantage of the INTRSECT viral

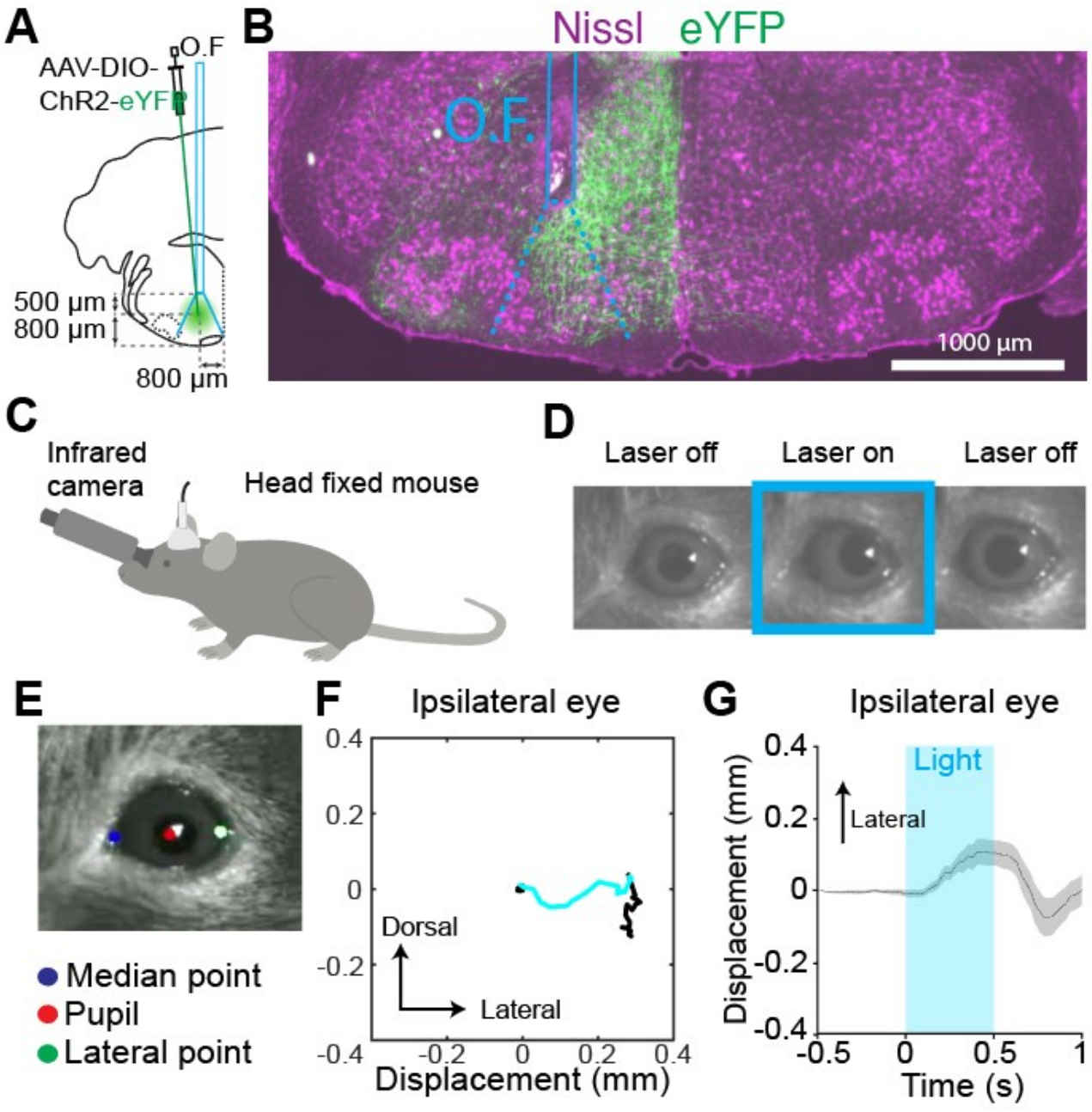

Figure 1. Optogenetic activation of medullary V2a neurons evokes a horizontal displacement of the pupil. (A) Experimental strategy for photo-activating V2a Gi neurons. OF, optic fiber. The injection pipette is depicted with an angle for clarity, but the injection was performed without angle. (B) Left: transverse section at the level of the Gi showing transfected V2a neurons (eYFP, green) on a Nissl background (magenta), the position of the OF, and the theoretical light cone at the fiber tip (dashed blue lines). Scale bar, 1 mm. (C) Schematic representation of the experimental set up. The infrared camera, linked with an infrared light, was placed close to the eye, in a dark room to detect pupil movements. (D) The snapshot on the left shows the position of the pupil before the photo-activation. The snapshot in the centers shows the position of the pupil during the photo-activation (the light is represented with the blue border) The snapshot on the right shows the position of the pupil after the photo-activation. (E) A single frame with three references used for Deep Lab Cut analysis: a median point (in blue close to the nasal edge), the center of the pupil (red point) and the lateral point (green point, away from the nasal edge). (F) Graph showing the horizontal deflection of the pupil during the light activation (blue line). (G) Mean ± SEM changes in pupil deflection during light activation across trials (2 mice, 35 trials).

strategy (Fenno et al., 2014). We injected, in the C2, or L2, spinal cord segement of a Chx10-Cre mouse, a retrogradely-transported AAV coding for the Flp recombinase (AAVretro-flp), and another AAV, activated by both Cre and Flp coding a fluorescent protein and an excitatory channelrhodopsin (Cre_{ON}-Flp_{ON}-ChR2-YFP) in the Gi (Figure 2A,D). In this way, the implantation of an optic fiber above the Gi, allows to activate selectively 7N-projecting V2a neurons (Figure 2A, D). Interestingly, we found no effect (Figure 2). These results showed that V2a neurons control horizontal movements of the pupil, a known a component of orienting, and that such eye movements are not controlled by spinally-projecting (C2 and L2) V2a neurons.

7N-projecting V2a medullary neurons trigger ipsilateral snout movements, but do not control eye movements nor arrest locomotion

We previously revealed that activating V2a Gi neurons, but not those with projections to the cervical or lumbar cord, evokes ipsilateral snout movements, suggesting that this function is a property of locally-projecting V2a Gi neurons. We therefore hypothesized that the snout movement is driven by a dedicated subset of V2a Gi neurons with projections to the 7^{th} facial motor nucleus (7N) and that horizontal eye movements might be controlled by

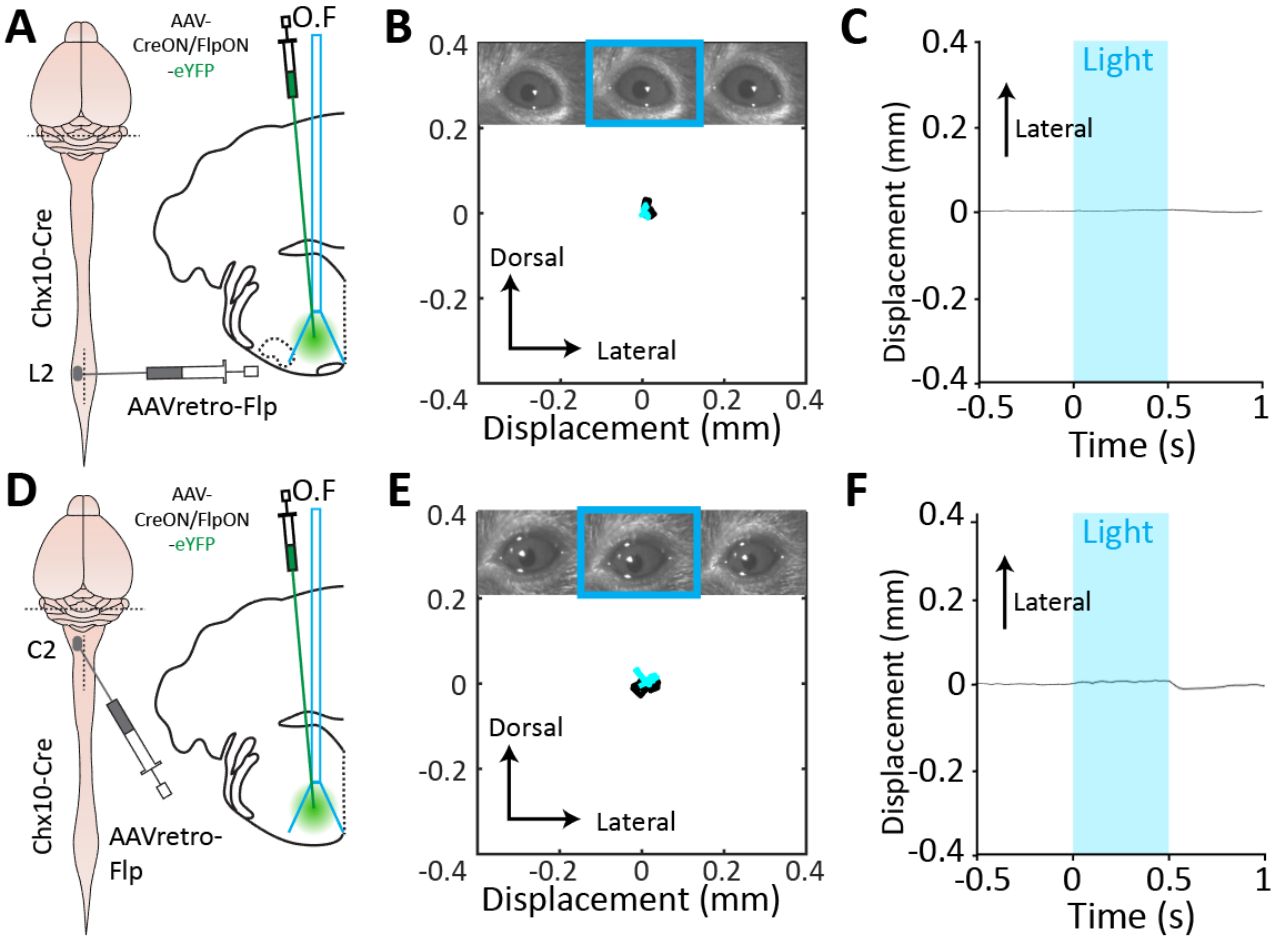

Figure 2. Optogenetic activation of L2 and C2-projecting V2a neurons does not evoke a horizontal displacement of the pupil. (A, D) Experimental strategy for photo-activating V2a Gi neurons projecting to the L2 (A) and C2 (D). OF, optic fiber. The injection pipettes are depicted with an angle for clarity, but the injections were performed without angle. (B, E) Measurement of the horizontal deflection of the pupil during a single event. The snapshots above show the position of the pupil before (left snapshot), during (central snapshot with blue border) and after the light stimulation (right snapshot). (C, F) Mean ± SEM changes in pupil displacement during the light activation across trials (2 animals per experiments).

axonal collaterals of this latter cell class. To selectively manipulate 7N-projecting V2a Gi neurons, we took again advantage of the INTRSECT viral strategy (Fenno et al., 2014). We injected, in the 7N of a Chx10-Cre mouse, a retrogradely-transported AAV coding for the Flp recombinase (AAVretro-flp), and another AAV, activated by both Cre and Flp coding a fluorescent protein and an excitatory channelrhodopsin (Cre_{ON}-Flp_{ON}-ChR2-YFP) in the Gi (Figure 3A). In this way, the implantation of an optic fiber above the Gi, allows to activate selectively 7N-projecting V2a neurons (Figure 3A).

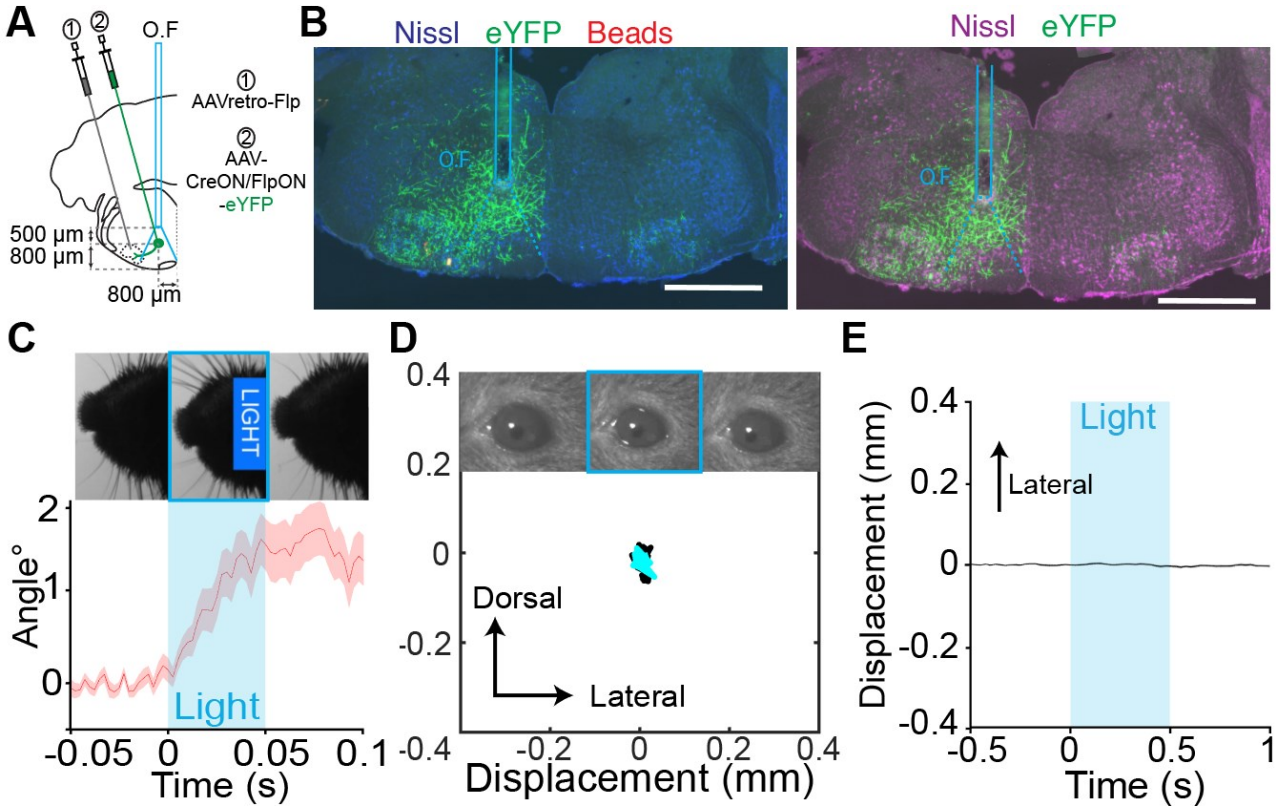

Figure 3. Optogenetic activation of the 7N-projecting V2a neurons evokes snout movement. (A) Experimental strategy for photo-activating V2a Gi neurons projecting to the 7N. OF, optic fiber. The injection pipettes are depicted with an angle for clarity, but the injections were performed without angle. (B) Left: transverse section at the level of the Gi showing transfected 7N-projecting V2a neurons (eYFP, green) on a Nissl background (blue) and the beads (red) to confirm the injection site of the AAVretro-flp at the level of the 7N, the position of the OF, and the theoretical light cone at the fiber tip (dashed blue lines). Scale bar, 1 mm. Right: transverse section at the level of the Gi showing the transfected 7N-projecting V2a neurons (eYFP, green) on a Nissl background (magenta). (C) Mean angular deflection ± SEM of the snout normalized to the angle during the same time interval before the light onset. Snapshots above show the displacement of the snout before (left snapshot), during (central snapshot with blue border) and after the light stimulation (right snapshot). (D) Measurement of the horizontal deflection of the pupil during a single event. The snapshots above show the position of the pupil before (left snapshot), during (central snapshot with blue border) and after the light stimulation (right snapshot). (E) Mean ± SEM changes in pupil displacement during the light activation across trials (2 mice).

We delivered the light when the mouse was in a head-fixed set-up and we recorded the snout activity. The light activation (50 ms) triggers a robust ipsilateral snout movement (Figure 3C). Activating the 7N-projecting V2a neurons therefore engages a similar response of the snout as that observed when activating the entire population of V2a Gi neurons

(Usseglio et al., 2020). Then, we investigated whether activating the 7N-projecting V2a neurons triggers also eye movements. With the same head-fixed set-up, we hence tracked the pupil of the ipsilateral eye during light activation as explained above. Surprisingly, and in stark contrast to photo-activating all V2a Gi neurons, we found here no movement of the eye (Figure 3D, E). These results reveal that the 7N-projecting V2a neurons are responsible for the snout displacement, but that another subset is responsible for eye movements. Hence, the eye movement is likely controlled by a population of locally-projecting V2a neurons that differ from that controlling the snout.

V2a neurons target specific pool of motoneurons to control facial and neck muscles

The observations above suggest that the V2a neurons control different motor components related to orientation through multiple subtypes and project to different regions of the brainstem and spinal cord. It is therefore possible that distinct V2a subsets projecting to different brain regions may contact different postsynaptic targets. The lumbar-projecting V2a RS neurons might contact inhibitory interneurons inducing the arrest of the ongoing locomotion (Bouvier et al., 2015). In contrast, our previous work raised the possibility that cervical-projecting V2a RS neurons might contact directly specific motoneurons of the neck and upper trunk muscles, allowing to rapidly control axial musculature (Usseglio et al., 2020). This might also apply to the 7N-projections. To start addressing such hypotheses, we performed dedicated experiments that employ a trans-neuronal labelling strategy from selected muscle pools (Skarlatou et al., 2020; Stepien et al., 2010).

Firstly, to test our ability to target the motoneurons that control neck movements, we injected a retrogradely-transported Herpes virus coding a fluorophore (HSV-FP), in the dorsal neck muscle (*splenius capitis*) of a newborn mice at P2 (Figure 4A). As expected, this led to the labelling of numerous motoneurons, confined to ventral laminae of the spinal cord and the lower brainstem. On average, we found a total of 12 motoneurons per set of section per animal (only 1 out of 4 sections were imaged), which gives an estimate of 48 motoneurons per animal. The majority of labelled motoneurons were confined within the

first segment of the cervical spinal cord (63%), while less were detected within the second cervical segment (26%) and at the level of the segmental level of the pyramidal decussation where the motoneurons of the 11th cranial nerve are located (11%) (Figure 3). This positioning is in line with the known location of motoneurons of the *splenius capitis*, the main horizontal head flexor.

After having ascertained our capacity to transfect a selected muscle pool with a retrograde HSV, we next took advantage of transsynaptic rabies viral strategies that are widely used to identify the presynaptic connectome of the corresponding motoneurons. The aim was to identify whether some premotor neurons are of V2a identity, and if applicable, to register their position and examine their degree of collateralization to other motor pools. There are multiple strategies used for a pre-motor labelling, and each has its own advantages and caveats and that they all have different rates of success that are summarized in a recent, still not peer-reviewed, review (Ronzano et al., 2022). I should also mention that such strategies had not been used in my lab before, and it hence took time for me to optimize injections, survival, and collect meaningful results. At this stage, we obtained the tools (in terms of viruses and mouse line) to perform two of these complementary strategies, that are represented in figure 5. In Figure 5 A is represented a strategy consisting in injecting in the selected muscle 2 viruses simultaneously: a retrograde virus to deliver the G protein (HSV-G) and a G-deleted-Rabies virus coding for a fluorescent protein. The transfected motoneurons, contacting the targeted muscle, thus express the G protein that allows the rabies to "jump" one synapse upstream and transfect the premotor neurons (Wickersham et al., 2007). However, with this strategy, there is a risk of transfecting the bipolar sensory neurons that contact the targeted muscle. As the rabies could potentially contaminate the distribution of pre-motoneurons via the anterograde ability to transfect the postsynaptic cells of the afferent neurons (Zampieri et al., 2014), there will be therefore a little fraction of cells expressing the fluorescent protein that are not part of the presynaptic connectome of the motoneurons (Figure 5B). On the other hand the second strategy (Figure 5C), consisting in injecting a G-deleted rabies virus in the selected muscle in a Chat-Cre;RGT mouse (expressing the G protein in the cholinergic cells), allows to avoid to transfect

postsynaptic cell of the sensory neurons. However, the limitation of such strategy is represented by the presence of cholinergic spinal interneurons contacting the motoneurons, the V0c (cholinergic V0) that will therefore allow the rabies virus to transfect their presynaptic cells (Figure 5D). Therefore, both strategies come with experimental limitations. Thus, both of them are required to validate the data obtained.

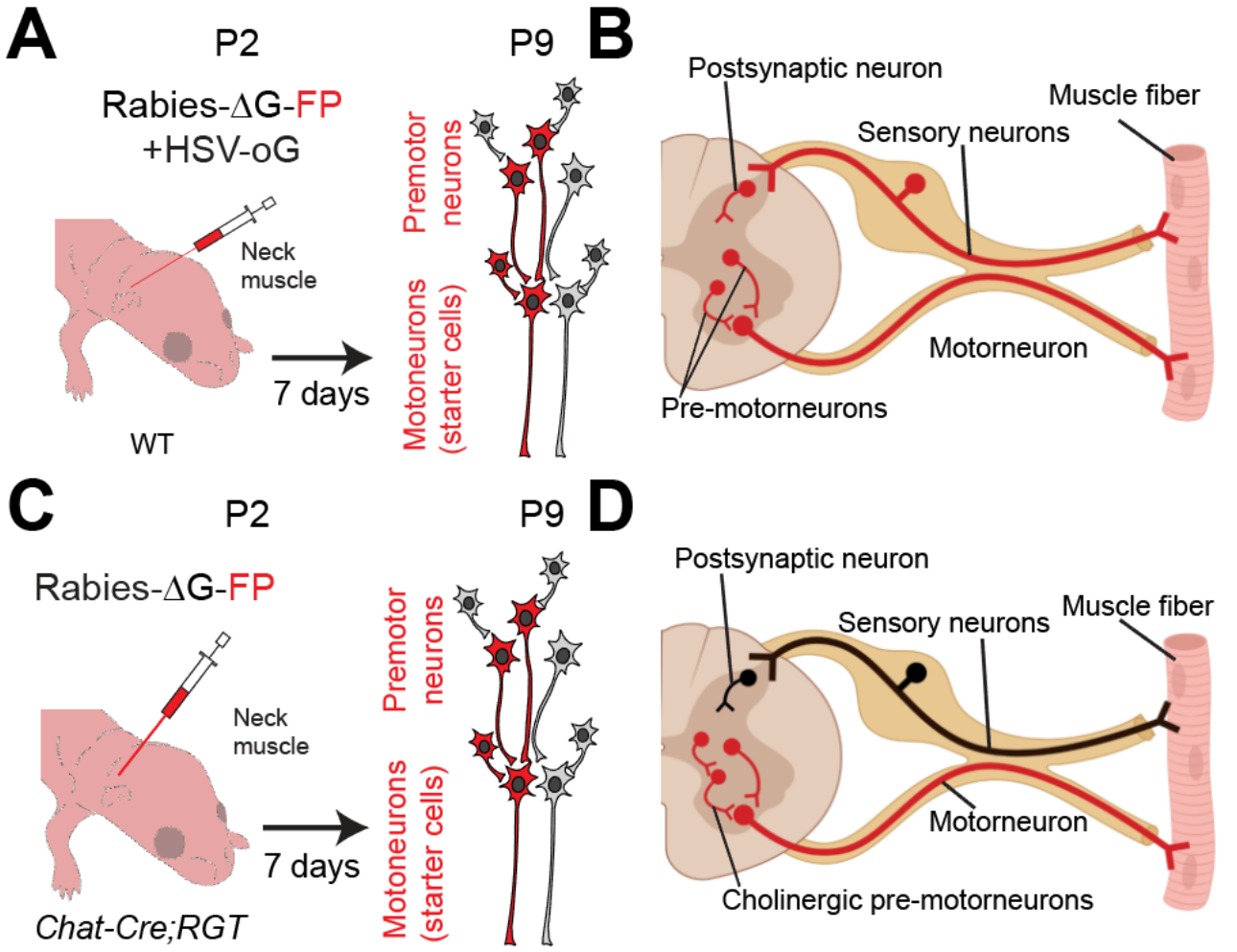

Figure 5. Experimental rabies strategy to reveal presynaptic connectomes of the motoneurons controlling a selected muscle. (A, B) Schematic representation of the injection on a newborn mouse (postnatal day 2). The injection is performed unilaterally in the neck muscle with a mix of viruses: a retrograde HSV to deliver the G-protein in the motoneurons together with a G-deleted rabies virus coding for a fluorescent protein to identify the transfected cells. The injection can be done on wild-type mice (WT) and reveals the Chx10-positive neurons with specific antibody, or on a Chx10-Cre;TdTomato mouse line to identify the V2a neurons. The perfusion is performed seven days after the injection (postnatal day 9). (C, D) Schematic representation of the injection on a newborn mouse (postnatal day 2). The injection is performed unilaterally in the neck muscle with a G-deleted rabies virus. In this strategy the injection must

be done on a Chat-Cre;RGT mouse line that expresses the G protein in all motoneurons. The perfusion is performed seven days after the injection (postnatal day 9).

Firstly, using a monosynaptic Rabies viral strategy (Stepien et al., 2010) consisting in injecting, unilaterally, an HSV-oG and a G-deleted Rabies virus in the neck muscles on newborn mice, we transfected the motoneurons controlling neck muscles and revealed their presynaptic neurons (Figure 6A). Indeed, a large fraction of neurons were found outside of the known location of motoneurons we described in the previous section. In particular, we observed abundant fluorescent neurons in the Gi nucleus (Figure 6B). To question their V2a identity, sections we co-stained with an anti-Chx10 antibody. We indeed observed Chx10-positive neurons co-expressing expressing the fluorescent protein coded by the rabies virus (Figure 6C), i.e., neck premotoneurons of V2a identity. Hence, some V2a RS neurons in the Gi form monosynaptic connections with motoneurons in the upper cervical spinal cord controlling the neck muscles. Moreover, to confirm such data without the potentially confounding contribution of sensory afferences, we used an alternative approach consisting in injecting G-deleted rabies viruses coding for a fluorescent protein in the ipsilateral neck muscles of a newborn Chat-Cre;RGT mouse (Figure 6F). Here again, within the presynaptic connectome of the motoneurons of the neck we observed V2a neurons (Figure 6G). These results demonstrate that some V2a Gi neurons directly control the axial musculature of the neck, presumably allowing a rapid ipsilateral head displacement.

Secondly, we use the rabies transsynaptic strategy on newborn mice to interrogate whether the V2a neurons form a monosynaptic connection with the motoneurons controlling nose muscles (in the 7N motor nucleus). As we did for the motoneurons controlling neck muscles, we targeted the motoneurons that control snout musculature. We injected a retrogradely-transported Herpes virus coding a fluorophore (HSV-FP), in the nose muscles of a newborn mice at P2 (Figure 7A). As expected, this led to the labelling of numerous motoneurons, confined to the 7N. We found a total of 30 motoneurons per set of sections (estimating to 120 for one animal).

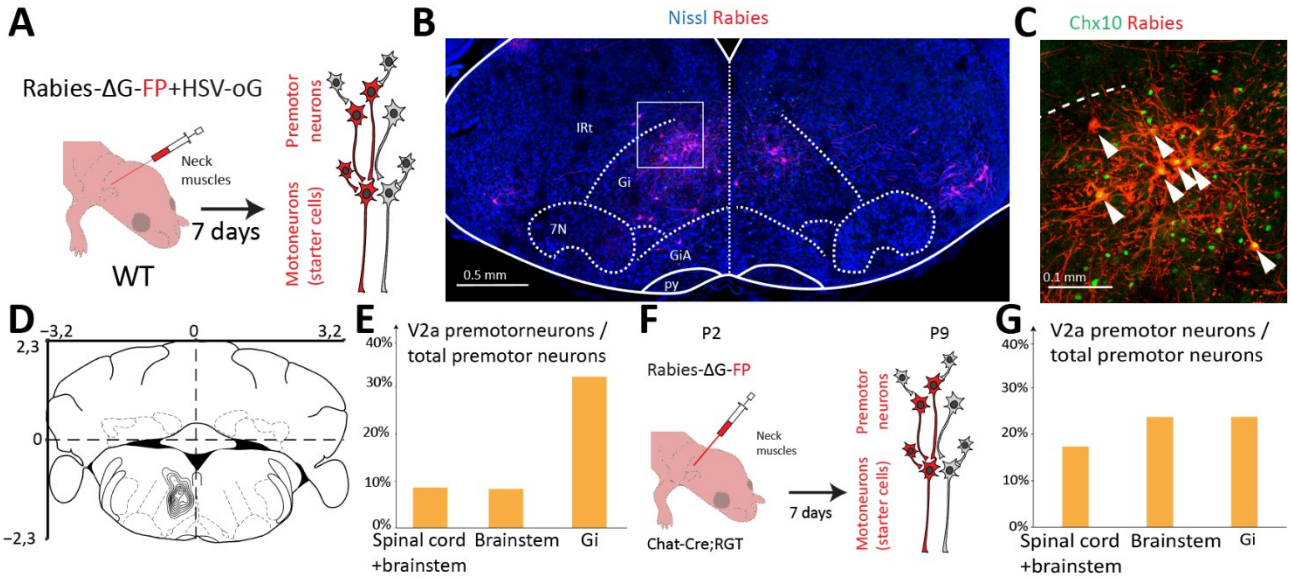

Figure 6. Rabies injection reveals that V2a neurons are premotor of the motoneurons controlling neck musculature. (A) Schematic representation of the injection on a newborn mouse (postnatal day 2). The injection is performed unilaterally in the neck muscle with a G-deleted rabies virus and a retrograde HSV. In this strategy the injection has been done on a wild-type (WT) mouse line. The perfusion is performed seven days after the injection (postnatal day 9). (B) Transverse section of the brainstem at the level of the Gi showing rabies positive neurons (in red) on a Nissl background (in blue). Scalebar: 0.5 mm. (C) Close-up view over the boxed area in (B) showing the rabies-transfected neurons (in red) and Chx10-positive neurons (in green). Scale bar: 0.1 mm. (D) Density map representing the position of the rabies-positive V2a neurons in the RF. (E) Percentage of the number of Chx10-positive neurons expressing the rabies virus over the total number of rabies-positive cells within the brain (brainstem and spinal cord), in the brainstem and in the Gi and associated nuclei (GiA, GiV and LPGi). (2 animals) (F) Schematic representation of the injection on a newborn mouse (postnatal day 2). The injection is performed unilaterally in the neck muscle with a G-deleted rabies virus. In this strategy the injection must be done on a *Chat-Cre;RGT* mouse line that expresses the G protein in all motoneurons. The perfusion is performed seven days after the injection (postnatal day 9). (G) Percentage of the number of Chx10-positive neurons expressing the rabies virus over the total number of rabies-positive cells within the brain (brainstem + spinal cord), in the brainstem and in the Gi and associated nuclei (GiA, GiV and LPGi). (4 animals).

Therefore, we injected rabies G- deleted rabies viruses coding for a fluorescent protein in the snout muscles of a newborn *Chat-Cre;RGT* mouse (Figure 8A). We observe V2a Rabies-positive neurons at all antero-posterior levels of the RF (figure 8B, C) on both the ipsilateral and contralateral sides. Importantly, we found V2a Rabies-positive neurons at

different rostrocaudal positions of the brainstem, not only in the Gi and associated nuclei (GiA, GiV, LPGi), and in the spinal cord (Figure 8D, E, F, G).

These data reveal that some V2a neurons directly contact the motoneurons located within the facial motor nucleus in order to control snout movements.

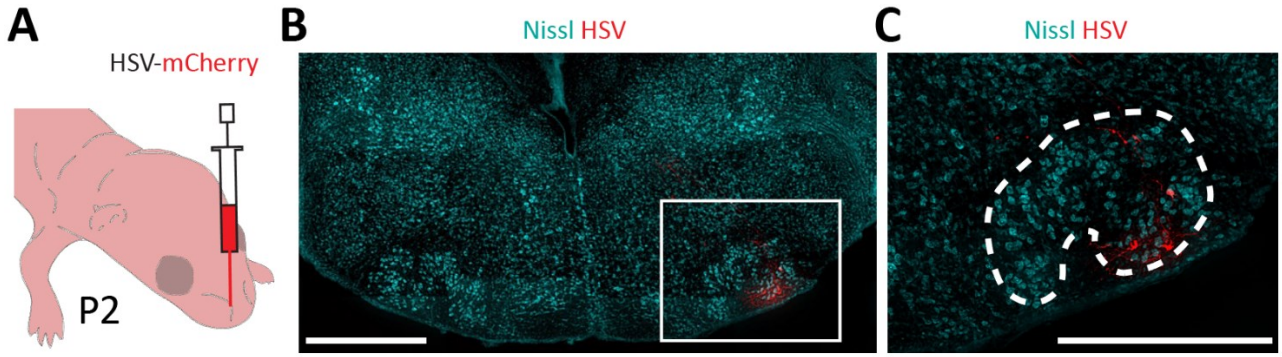

Figure 7. Retrograde injection reveals motoneurons controlling the snout musculature. (A) Schematic representation of the unilateral HSV injection in the snout muscles. (B) Transverse section at the level of the 7N showing transfected motoneurons (mCherry) on a Nissl background (Cyan). Scalebar: 0.5 mm. (C) Close-up view over the boxed area in (B) showing the transfected neurons in the 7N. Scale bar: 0.5 mm.

Discussion

As the superior colliculus is well known to control multiple orienting movements, including eye and orofacial movements (Basso and May, 2017; Isa et al., 2021), and it has been previously shown that the medullary V2a neurons receive inputs from the superior colliculus (Cregg et al., 2020; Usseglio et al., 2020), we focused on whether the V2a neurons might control orienting motor actions associated to supraspinal/brainstem executory circuits. Notably, we observed, with dedicated experiments we designed along the way, that the unilateral activation of medullary V2a neurons triggers an ipsilateral snout movement, as we already demonstrated in our previous study, and a horizontal deflection of the pupil toward the stimulated side. After such observations, we immediately asked whether the V2a neurons control these motor outcomes with dedicated subsets, as the case for the spinally-projecting V2a neurons (Usseglio et al., 2020). Indeed, nose and eye movements were only observed when activating V2a Gi neurons collectively, but when activating any of the

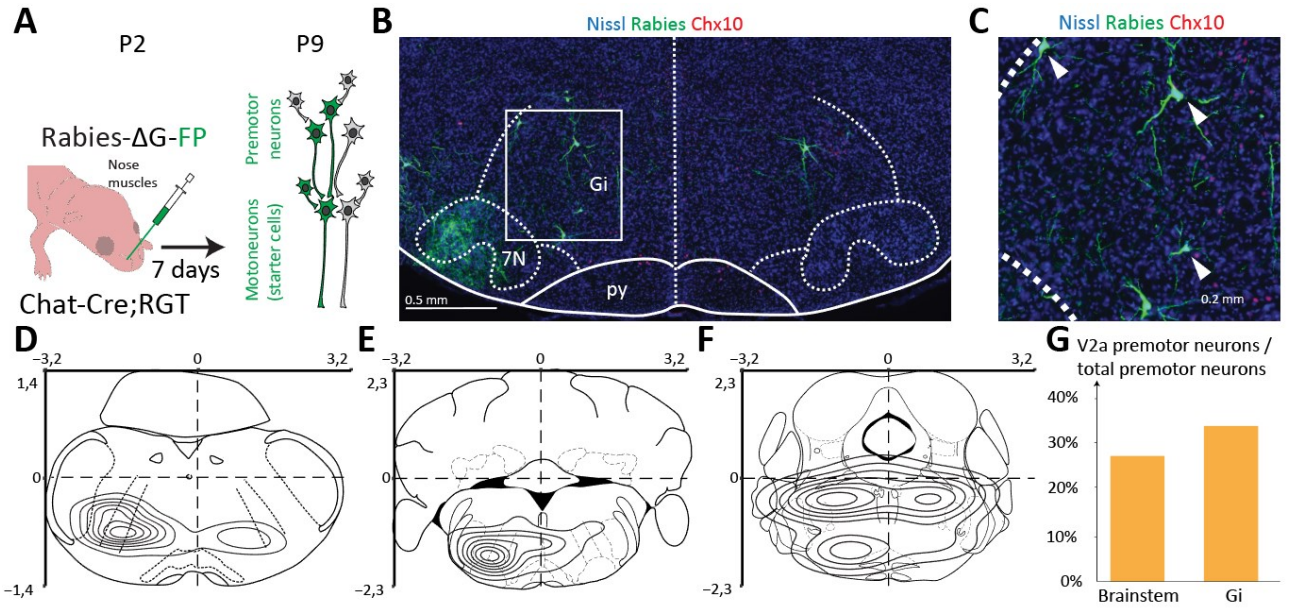

Figure 8. Rabies injection reveals that V2a neurons are premotor of the motoneurons controlling snout muscles. (A) Schematic representation of the injection on a newborn mouse (postnatal day 2). The injection is performed unilaterally in the neck muscle with a G-deleted rabies virus. In this strategy the injection must be done on a *Chat-Cre;RGT* mouse line that expresses the Rabies G protein in all motoneurons. The perfusion is performed seven days after the injection (postnatal day 9). (B) Transverse section of the brainstem at the level of the Gi showing rabies positive neurons (in green) on a Nissl background (in blue). Scalebar: 0.5 mm. (C) close-up view over the boxed area in (B) showing the transfected neurons (in green) and Chx10-positive neurons (in red) on a Nissl background (in blue). Scale bar: 0.2 µm. (D-E-F) density maps representing the position of the rabies-positive V2a neurons in the RF at three different levels along the rostro caudal axis. (G) Percentage of Chx10-positive neurons expressing the rabies virus over the total number of rabies-positive cells within the brain the brainstem and in the Gi and associated nuclei (GiA, GiV and LPGi).

spinally-projecting subset we did not observe any orofacial and eye movements. Moreover, we observed that the V2a neurons projecting to the facial motor nucleus, where reside the motoneurons controlling snout musculature, control selectively nose displacement, but no spinal related motor functions nor eye movements.

A crucial statement is that different V2a subsets can support opposing outcomes at the muscular level: promotion of movement (ipsilateral head rotation, eye and snout movements) for the cervical-projecting and supraspinal subsets, and motor arrest (of the hindlimbs) for the lumbar-projecting subset. These opposite functional outcomes could be

due to the different cell-types contacted by the distinct V2a subsets. Whilst lumbar-projecting V2a neurons may exert their function via spinal inhibitory neurons (Bouvier et al., 2015), the post-synaptic targets of cervical- and facial-projecting V2a neurons remains to be defined. Our investigations, so far, reveal that cervical-projecting V2a RS neurons contact directly specific motoneurons of the neck and upper trunk muscles, known to reside in the upper cervical spinal segments and to be under control from the RF (Isa and Sasaki, 2002; Peterson et al., 1978; Sasaki et al., 2004). However, V2a neurons represent only a fraction of the RS neurons contacting the motoneurons that control neck muscles. It might be of interest to identify the other RS neurons in order to understand how they concur together with V2a neurons to finely control head movements. For example, different RS neurons might be recruited for different motor behaviors, or it could be that they can be recruited simultaneously to regulate the speed and the degrees of the head displacement.

Moreover, as we already mentioned, our study demonstrated that the medullary V2a neurons control eye movements. Up to now, the identification of a V2a subset that controls selectively eye movements has not been provided yet. However, the absence of pupil displacement during the activation of the C2, L2 and 7N-projecting V2a subsets, suggests the existence of a dedicated subset of V2a neurons controlling eye movements. Notably, we observed that the displacement of the ipsilateral pupil during the unilateral activation of the V2a Gi neurons was accompanied by the movement of the contralateral pupil toward the nasal edge. It might be interesting to understand how the V2a neurons control circuits for conjugate eye movements. Investigations could be done for example starting from the analysis of the V2a projections. Indeed, in the brainstem are located the motor nuclei (3rd, 4th, 5th facial motor nucleus) where reside the motoneurons contacting eye muscles (Guthrie, 2007).

Furthermore, we observed that the V2a neurons projecting to the 7N contact directly the motoneurons controlling nose musculature. Therefore, it could be that the V2a subsets are premotor for promoting only certain motor actions (neck and snout movements). The cell type contacted at different levels of the brainstem and the spinal cords might differ based on the subset' function. Thus, it will be extremely interesting to explore further the

postsynaptic targets of the V2a neurons in different regions of the brainstem and spinal cord, and discover what are the molecular and developmental basis that induce such heterogeneity.

As already explained within the results, the experimental rabies strategies we use have limits. Therefore, next step will be to use a third strategy (Figure 9) consisting in injecting a retrograde virus in the selected muscle to deliver the G protein and the TVA receptor. In a second step, the G-deleted Rabies pseutodyped with EnvA (that can transfect only cells expressing TVA receptor) will be injected centrally, within the spinal cord at the level of the motoneurons controlling the selected muscle.

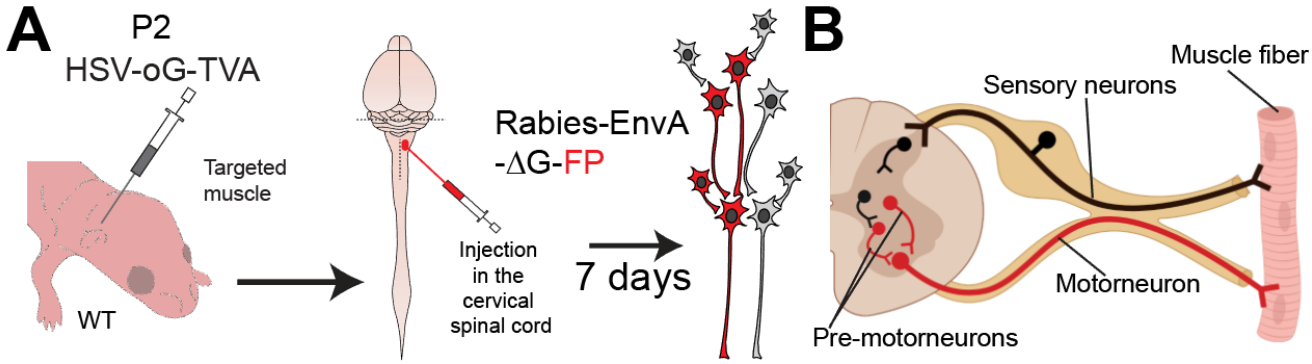

Figure 9. Experimental rabies strategy to reveal presynaptic connectomes of the motoneurons controlling a selected muscle. (A) Schematic representation of the injection on a newborn mouse (postnatal day 2). The injection is performed unilaterally in the targeted muscle (in this case neck musle) with a retrograde HSV-oG-TVA. The injection can be done on wild type mice (WT). After two weeks, a second injection is performed in the upper cervical spinal cord with an EnvA-G-deleted-rabies virus coding for a fluorescent protein to identify the transfected cells. The perfusion is performed seven days after the injection. (B) This rabies strategy reveals the presynaptic connectome of the motoneurons without transfecting the sensory neurons or the cholinergic interneurons within the spinal cord.

Importantly, crucial points remain to address in order to deeply understand the functional connectivity of the V2a neurons: 1) it is necessary indeed to investigate whether the V2a neurons, at different levels of the spinal cord and brainstem, contact distinct cell targets and 2) it is necessary to demonstrate whether the V2a neurons contact motoneurons

only at the level of the cervical spinal cord and the 7N or also at the level of other brain regions. This might elucidate whether the postsynaptic connectivity of the medullary V2a neurons differs at distinct regions of the brainstem and spinal cord, in order to evoke specific responses: promoting (in the case of neck, eye and head movements) and preventing (in the case of the arrest of locomotion) motor action.

Another important open question related to the V2a network is whether the different subsets are interconnected. Recent work from Brownstone and colleagues demonstrated that the locally-projecting V2a neurons contact V2a RS neurons and they observed that these two groups of V2a neurons differ from soma size and electrophysiological properties. However, it is not demonstrated yet whether there is connectivity between the other V2a subsets.

Moreover, the orienting behavior is associated to multiple motor actions including forelimb movements. Therefore, to study forelimb movements during medullary V2a neurons and whether they control extensor and flexor muscles of the forelimb might carry a more detailed overview about the functional and anatomical connectivity of the medullary V2a neurons.

Finally, it is essential to highlight that the V2a neurons represent only one population of the RF. Therefore, future investigations focusing in the other cells of the RF are crucial to understand the neural network within the RF. In particular, an important point is to decipher whether the organization of the V2a neurons is specific and unique for this cell type, or whether the other reticular neuronal types share similar organization in projection-defined subsets controlling unitary motor actions of complex behaviors.

Altogether, these data, combined with results obtained within previous studies (Chopek et al., 2021; Crone et al., 2012; Schwenkgrub et al., 2020; Usseglio et al., 2020), reveal a functional diversity in V2a RS neurons that can be subdivided in two macro-categories, anatomically and functionally, i) one that controls ocular, orofacial and respiratory movements through supra-spinal projections, and ii) another one that controls trunk and limb movements through spinal projections. Within each, a further specialization

by projection site and postsynaptic targets supports the control of individual motor components.

Methods

Mice

The *Chx10-Cre* was kindly provided by S. Crone, K. Sharma, L. Zagoraiou, and T.M. Jessell (Azim et al., 2014; Bouvier et al., 2015; Romer et al., 2017). C57BL6 wild-type mice were obtained by Janvier Labs (Le Genest-Saint-Isle, France). The *Chat-Cre* was obtained from Jackson Laboratories. Animals were group-housed with free access to food and water in controlled temperature conditions and exposed to a conventional 12-h light/dark cycle. Experiments were performed on animals of either sex, aged 2 to 3 months at the time of first injection. All procedures were approved by the French Ethical Committee (authorization 2020-022410231878) and conducted in accordance with EU Directive 2010/63/EU. All efforts were made to reduce animal suffering and minimize the number of animals.

Viruses used

For Cre-dependent expression of ChR2 in the Gi we injected unilaterally 100 to 200 nL of an AAV9-Ef1a-DIO-hChR2(E123T/T159C)-eYFP (addgene #35509, titer 3.2 x 10^{12} vp/ml (Mattis et al., 2011)). For mapping the motoneurons, we used intramuscular injections of 1 µL of HSV-mcherry, obtained from Dr. Rachael Neve (Gene Delivery Technology Core, Massachusetts General Hospital, USA). For premotor labelling from the muscules, we mixed 1µl of HSV-oG with 1µL of ΔG-Rabies made in house (N. Zampieri & E. Toscano) as previously published (Skarlatou et al., 2020).

Surgical procedures for injections and implants in the brainstem

Animals were anesthetized with isoflurane throughout the surgery (4 % at 1 L/min for induction, and 2-3 % at 0.3 L/min for maintenance). Buprenorphine (0,025 mg/kg) was administered subcutaneously for analgesia before the surgery. The temperature of the mice was maintained at 36 °C with a feedback-controlled heating pad. Anesthetized animals were

placed on a stereotaxic frame (Kopf) and the skull was exposed. Viral vectors were delivered using a pulled glass pipette connected to a syringe pump (Legato 130, KD Scientific, customized by Phymep, France). The infusion flow was set to 100 nL/min. Coordinates (in mm) used to target V2a neurons were: -6.0 from bregma, 0.8 lateral, and 4.5 from the dorsal brain surface. Coordinates (in mm) used to target 7N-projecting V2a neurons were: -6.0 from bregma, 1.4 lateral, and 5.1 from the dorsal brain surface. After the injection, the pipette was held in place for 5 min before being slowly retracted. For optogenetic activations, a 200 µm core 0.39 NA optic fiber (Thorlabs) connected to a 1.25 mm diameter ferrule (Thorlabs) was implanted ~500 µm above the injected site. This operation was performed during the same surgery as the viral injection when both were targeted to the brainstem. For activating spinally-projecting V2a neurons, the spinal injection was performed first (see below) and the optic fiber was implanted 5 to 7 days later. Dental cement (Tetric Evoflow) was used to secure the implanted ferrules. Animals were followed daily after the surgery.

Surgical procedures for muscle injection

Animals were anesthetized with isoflurane throughout the surgery (with a variable flow depending on their size. Buprenorphine (0,025 mg/kg) was administered subcutaneously for analgesia before the surgery. Rabies virus was injected through a pulled glass capillary (Harvard apparatus, 1.2 OD x 0.69 x 100L mm), using 10 ms pressure air puffs, delivered by a Picospritzer.

Histology

Adult or p9 mice were anesthetized with Euthasol Vet (140 mg/kg) and perfused with 4% paraformaldehyde (PFA) in 1X Phosphate Buffered Saline (PBS). Brains and spinal cord were dissected out and fixed overnight in 4% PFA at 4°C. After fixation, tissues were rinsed in 1X PBS. Brain and spinal cord were cryoprotected overnight at 4°C, respectively in 16% and 20% of sucrose in PBS. Tissues were rapidly cryoembedded in OCT mounting medium and sectioned at 30 µm using a cryostat. Sections were blocked in a solution of 1X Tris Buffered Saline (TBS), 5% normal donkey serum and 0.5% Triton X-100. The primary

antibodies, carried out 24 to 48 hours at 4°C, were: goat anti-ChAt (1:500, ref: AB144P, Merck Millipore), chicken anti-GFP (1:500, ref: 1020, Aves Labs), rabbit anti-RFP (1:500, ref: 600-401-379, Rockland), sheep anti-Chx10 (1:500, ref: AB9016, Merck Millipore) and Primary antibodies were detected after 2 hours of incubation at room temperature with appropriate secondary antibodies coupled to Alexa-Fluor 488, 647, Cy-3 or Cy-5 (1:500, Jackson ImmunoResearch). Sections were counterstained with a fluorescent Nissl stain (NeuroTrace 435/445 blue, ref: N21479, 1:200 or NeuroTrace 640/660 deep-red, ref: N21483, 1:1000, Thermo Fisher Scientific) and mounted in Prolong Diamond Antifade Montant (P36970, Thermo Fisher Scientific) or ibidi Mounting Medium (50001, Ibidi). For counting neurons, all sections were scanned using a Zeiss Axio Imager-M2. We use the Imaris Microscopy Image Analysis software to count the number of cells per section and define the position of the cells. The density maps were obtained using a custom-made script on R-studio.

Behavioral experiments

Optogenetic activations

Behavioral experiments started 15 to 21 days after the viral injection. Implanted animals were connected to a laser source (473 nm DPSS system, LaserGlow Technologies, Toronto, Canada) through a mating sleeve (Thorlabs). In all conditions light was delivered in trains of pulses of 15 ms at 40 Hz frequency for a duration of 500 ms. We used the minimal laser power sufficient to evoke a response, which was measured to be between 5-12 mW at the fiber tip using a power meter (PM100USB with S120C silicon power head, Thorlabs) to restrict photo-activations unilaterally, prevent heat, and exclude an unintentional silencing by over-activation.

Behavioral setting and video recordings

For analyzing changes in snout and eye movements, animals were placed in a custom made head-fixed set-up for a maximum of 10 minutes without prior habituation and filmed from above (snout) or the side (eye) at 400 images/sec using a CMOS camera (JaiGO 2400 USB). For analyzing eye movements during optogenetic activations, animals were place in a

dark room and we used an IR light to detect pupil displacements. Images were streamed to disk on a computer using 2nd Look (IO Industries). Timings of photo-activations were recorded using the TTL output of the laser connected to a National Instruments acquisition card (USB-6211) and the LabScribe NI software (iWorxs). Both recordings were synchronized using hardware trigger. Photo-activations were delivered manually using the NI MAX tool with a minimal interval of 30 seconds between two consecutive activations. Throughout the manuscript, one trial correspond to one photo-activation.

Quantification and statistical analysis

Pose estimation using DeepLabCut and quantifications of snout and eye movements

To compute changes in eye movements, we labelled manually 3 points of interest (POIs) from 437 frames taken across 22 videos using DeepLabCut version 2.1.5.2. We then used 95% of the labelled frames to train the network using a ResNet-101-based neural network with default parameters for 2 training iteration. We validated with 1 shuffles in the second training, and found that the test error was: 1.79 pixels, train: 1,51 pixels (image size was 120 by 110). We then used a p-cutoff of 0,6 to condition the X,Y coordinates for future analyses. This network was then used to analyze all other videos taken with same experimental settings.

To compute changes in snout movements, we labelled manually 3 points of interest (POIs) from 28 frames taken across 2 videos using DeepLabCut version 2.1.5.2. We then used 95% of the labelled frames to train the network using a ResNet-50-based neural network with default parameters for 1 training iteration. We validated with 1 shuffle, and found that the test error was: 1.26 pixels, train: 1,48 pixels (image size was 928 by 450). We then used a p-cutoff of 0,1 to condition the X,Y coordinates for future analyses. This network was then used to analyze all other videos taken with same experimental settings.

Custom scripts were written in MATLAB (Mathworks) and used for computation. The displacement of the pupil of the animal is defined as the movement of the pupil on the median to lateral axis (Fig 1E).

The snout rotation is defined by the angle β between two instances of the vector from R to N at the first frame and at the current frame. R is the right side of the nose, while N is the tip of the nose.

$$\theta_i = \tan^{-1}\left(\frac{x_{Ni} - x_{Ri}}{y_{Ni} - y_{Ri}}\right) - \tan^{-1}\left(\frac{x_{N0} - x_{R0}}{y_{N0} - y_{R0}}\right)$$

$$with\ R_i = \binom{x_{Ri}}{y_{Ri}}, N_i \binom{x_{Ni}}{y_{Ni}}, i \in [0, number\ of\ frames]$$

References

Arber, S. and R. M. Costa (2018). "Connecting neuronal circuits for movement." Science **360**(6396): 1403-1404.

Azim, E., J. Jiang, B. Alstermark and T. M. Jessell (2014). "Skilled reaching relies on a V2a propriospinal internal copy circuit." Nature.

Basso, M. A., M. E. Bickford and J. Cang (2021). "Unraveling circuits of visual perception and cognition through the superior colliculus." Neuron **109**(6): 918-937.

Basso, M. A. and P. J. May (2017). "Circuits for Action and Cognition: A View from the Superior Colliculus." Annu Rev Vis Sci **3**: 197-226.

Bouvier, J., V. Caggiano, R. Leiras, V. Caldeira, C. Bellardita, K. Balueva, A. Fuchs and O. Kiehn (2015). "Descending Command Neurons in the Brainstem that Halt Locomotion." Cell **163**(5): 1191-1203.

Bretzner, F. and R. M. Brownstone (2013). "Lhx3-Chx10 reticulospinal neurons in locomotor circuits." J Neurosci **33**(37): 14681-14692.

Brownstone, R. M. and J. W. Chopek (2018). "Reticulospinal Systems for Tuning Motor Commands." Front Neural Circuits **12**: 30.

Caggiano, V., R. Leiras, H. Goni-Erro, D. Masini, C. Bellardita, J. Bouvier, V. Caldeira, G. Fisone and O. Kiehn (2018). "Midbrain circuits that set locomotor speed and gait selection." Nature **553**(7689): 455-460.

Chopek, J. W., Y. Zhang and R. M. Brownstone (2021). "Intrinsic brainstem circuits comprised of Chx10-expressing neurons contribute to reticulospinal output in mice." J Neurophysiol **126**(6): 1978-1990.

Cregg, J. M., R. Leiras, A. Montalant, P. Wanken, I. R. Wickersham and O. Kiehn (2020). "Brainstem neurons that command mammalian locomotor asymmetries." Nat Neurosci **23**(6): 730-740.

Crone, S. A., J. C. Viemari, S. Droho, A. Mrejeru, J. M. Ramirez and K. Sharma (2012). "Irregular Breathing in Mice following Genetic Ablation of V2a Neurons." J Neurosci **32**(23): 7895-7906.

Deliagina, T. G., P. V. Zelenin and G. N. Orlovsky (2002). "Encoding and decoding of reticulospinal commands." Brain Res Brain Res Rev **40**(1-3): 166-177.

Drew, T., R. Dubuc and S. Rossignol (1986). "Discharge patterns of reticulospinal and other reticular neurons in chronic, unrestrained cats walking on a treadmill." J Neurophysiol **55**(2): 375-401.

Fenno, L. E., J. Mattis, C. Ramakrishnan, M. Hyun, S. Y. Lee, M. He, J. Tucciarone, A. Selimbeyoglu, A. Berndt, L. Grosenick, K. A. Zalocusky, H. Bernstein, H. Swanson, C. Perry, I. Diester, F. M. Boyce, C. E. Bass, R. Neve, Z. J. Huang and K. Deisseroth (2014). "Targeting cells with single vectors using multiple-feature Boolean logic." Nat Methods **11**(7): 763-772.

Ferreira-Pinto, M. J., L. Ruder, P. Capelli and S. Arber (2018). "Connecting Circuits for Supraspinal Control of Locomotion." Neuron **100**(2): 361-374.

Franklin, K. B. and G. Paxinos (2007). "The Mouse Brain in stereotaxic Coordinates." Elsevier.

Grillner, S. and A. El Manira (2020). "Current Principles of Motor Control, with Special Reference to Vertebrate Locomotion." Physiol Rev **100**(1): 271-320.

Guthrie, S. (2007). "Patterning and axon guidance of cranial motor neurons." Nat Rev Neurosci **8**(11): 859-871.

Isa, T., E. Marquez-Legorreta, S. Grillner and E. K. Scott (2021). "The tectum/superior colliculus as the vertebrate solution for spatial sensory integration and action." Curr Biol **31**(11): R741-R762.

Isa, T. and S. Sasaki (2002). "Brainstem control of head movements during orienting; organization of the premotor circuits." Prog Neurobiol **66**(4): 205-241.

Jordan, L. M., J. Liu, P. B. Hedlund, T. Akay and K. G. Pearson (2008). "Descending command systems for the initiation of locomotion in mammals." Brain Res Rev **57**(1): 183-191.

Josset, N., M. Roussel, M. Lemieux, D. Lafrance-Zoubga, A. Rastqar and F. Bretzner (2018). "Distinct Contributions of Mesencephalic Locomotor Region Nuclei to Locomotor Control in the Freely Behaving Mouse." Curr Biol **28**(6): 884-901 e883.

Kimura, Y., C. Satou, S. Fujioka, W. Shoji, K. Umeda, T. Ishizuka, H. Yawo and S. Higashijima (2013). "Hindbrain V2a neurons in the excitation of spinal locomotor circuits during zebrafish swimming." Curr Biol **23**(10): 843-849.

Leiras, R., J. M. Cregg and O. Kiehn (2022). "Brainstem Circuits for Locomotion." Annu Rev Neurosci **45**: 63-85.

Lemon, R. N. (2008). "Descending pathways in motor control." Annu Rev Neurosci **31**: 195-218.

Liu, J. and L. M. Jordan (2005). "Stimulation of the parapyramidal region of the neonatal rat brain stem produces locomotor-like activity involving spinal 5-HT7 and 5-HT2A receptors." J Neurophysiol **94**(2): 1392-1404.

Masullo, L., L. Mariotti, N. Alexandre, P. Freire-Pritchett, J. Boulanger and M. Tripodi (2019). "Genetically Defined Functional Modules for Spatial Orienting in the Mouse Superior Colliculus." Curr Biol **29**(17): 2892-2904 e2898.

Mattis, J., K. M. Tye, E. A. Ferenczi, C. Ramakrishnan, D. J. O'Shea, R. Prakash, L. A. Gunaydin, M. Hyun, L. E. Fenno, V. Gradinaru, O. Yizhar and K. Deisseroth (2011). "Principles for applying optogenetic tools derived from direct comparative analysis of microbial opsins." Nat Methods **9**(2): 159-172.

May, P. J. (2006). "The mammalian superior colliculus: laminar structure and connections." Prog Brain Res **151**: 321-378.

Meyer, A. F., J. O'Keefe and J. Poort (2020). "Two Distinct Types of Eye-Head Coupling in Freely Moving Mice." Curr Biol **30**(11): 2116-2130 e2116.

Michaiel, A. M., E. T. Abe and C. M. Niell (2020). "Dynamics of gaze control during prey capture in freely moving mice." Elife **9**.

Peterson, B. W., N. G. Pitts, K. Fukushima and R. Mackel (1978). "Reticulospinal excitation and inhibition of neck motoneurons." Exp Brain Res **32**(4): 471-489.

Romer, S. H., K. Seedle, S. M. Turner, J. Li, M. L. Baccei and S. A. Crone (2017). "Accessory respiratory muscles enhance ventilation in ALS model mice and are activated by excitatory V2a neurons." Exp Neurol **287**(Pt 2): 192-204.

Ronzano, R., S. Skarlatou, B. K. Barriga, B. A. Bannatyne, G. S. Bhumbra, J. D. Foster, J. D. Moore, C. Lancelin, A. Pocratsky, M. G. Özyurt, C. C. Smith, A. J. Todd, D. J. Maxwell, A. J. Murray, S. L. Pfaff, R. M. Brownstone, N. Zampieri and M. Beato (2022). "Spinal premotor interneurons controlling antagonistic muscles are spatially intermingled." bioRxiv: 2021.2002.2010.430608.

Ruder, L. and S. Arber (2019). "Brainstem Circuits Controlling Action Diversification." Annu Rev Neurosci **42**: 485-504.

Sakatani, T. and T. Isa (2007). "Quantitative analysis of spontaneous saccade-like rapid eye movements in C57BL/6 mice." Neurosci Res **58**(3): 324-331.

Sasaki, S., K. Yoshimura and K. Naito (2004). "The neural control of orienting: role of multiple-branching reticulospinal neurons." Prog Brain Res **143**: 383-389.

Schwenkgrub, J., E. R. Harrell, B. Bathellier and J. Bouvier (2020). "Deep imaging in the brainstem reveals functional heterogeneity in V2a neurons controlling locomotion." Sci Adv **6**(49).

Skarlatou, S., C. Herent, E. Toscano, C. S. Mendes, J. Bouvier and N. Zampieri (2020). "Afadin Signaling at the Spinal Neuroepithelium Regulates Central Canal Formation and Gait Selection." Cell Rep **31**(10): 107741.

Stepien, A. E., M. Tripodi and S. Arber (2010). "Monosynaptic rabies virus reveals premotor network organization and synaptic specificity of cholinergic partition cells." Neuron **68**(3): 456-472.

Usseglio, G., E. Gatier, A. Heuze, C. Herent and J. Bouvier (2020). "Control of Orienting Movements and Locomotion by Projection-Defined Subsets of Brainstem V2a Neurons." Curr Biol **30**(23): 4665-4681 e4666.

Valverde, F. (1961). "Reticular formation of the pons and medulla oblongata. A Golgi study." J Comp Neurol **116**: 71-99.

Wickersham, I. R., S. Finke, K. K. Conzelmann and E. M. Callaway (2007). "Retrograde neuronal tracing with a deletion-mutant rabies virus." Nat Methods **4**(1): 47-49.

Zampieri, N., T. M. Jessell and A. J. Murray (2014). "Mapping sensory circuits by anterograde transsynaptic transfer of recombinant rabies virus." Neuron **81**(4): 766-778.

4.3. Upregulation of breathing rate during running exercise by central locomotor circuits

Upregulation of breathing rate during running exercise by central locomotor circuits

Coralie Hérent[1,2], Séverine Diem[1,3], Giovanni Usseglio[1], Gilles Fortin[4] and Julien Bouvier[1*]

[1] Université Paris-Saclay, CNRS
Institut des Neurosciences Paris-Saclay
91400, Saclay, France.

[2] Present address:
Champalimaud Neuroscience Program,
Champalimaud Center for the Unknown,
Portugal

[3]Present address:
Institut de Génomique Fonctionelle, University of Montpellier, CNRS, INSERM/
34094 Montpellier Cedex, France.

[4] Institut de Biologie de l'École Normale Supérieure (IBENS),
École Normale Supérieure, CNRS, INSERM, PSL Research University,
75005 Paris, France.

*Correspondence:
Dr. Julien Bouvier
Julien.bouvier@cnrs.fr
ORCID ID: 0000-0002-1307-4426

Abstract

While respiratory adaptation to exercise is compulsory to cope with the increased metabolic supply to body tissues and with the necessary clearing of metabolic waste, the neural apparatus at stake remains poorly identified. Using viral tracing, *ex vivo* and *in vivo* optogenetic and chemogenetic interference strategies in mice, we unravel interactive locomotor and respiratory networks' nodes that mediate the respiratory rate increase that accompanies a running exercise. We show that the mesencephalic locomotor region (MLR) and the lumbar spinal locomotor pattern generator (lumbar CPG), which respectively initiate and execute the locomotor behavior, access the respiratory network through distinct entry points. The MLR directly projects onto the inspiratory rhythm generator, the preBötzinger complex (preBötC), and can trigger a moderate increase of respiratory frequency, prior to, or even in the absence of, locomotion. In contrast, the lumbar CPG projects onto the retrotrapezoid nucleus (RTN) that in turn contacts the preBötC to enforce, during effective locomotion, higher respiratory frequencies. These data expand, on the one hand, the functional implications of the MLR beyond locomotor initiation to a *bona fide* respiratory modulation. On the other hand, they expand the adaptive respiratory role of the RTN beyond chemoception to "locomotor-ception".

Introduction

Breathing is a vital behavior which must combine extreme robustness with continuous adaptability. One striking example is the abrupt augmentation of ventilation at the transition from rest to running in order to maintain homeostasis in spite of increased metabolic demand[1]. This "exercise hyperpnoea" is manifested by an increase in both respiratory frequency and volume. It has long been proposed that its main trigger, at least for acute exercise, is of neuronal nature, i.e., relies on activatory signals from locomotor effectors or circuits impacting onto the respiratory generator in the brainstem[1-3]. However, the underlying cells and circuits are not fully elucidated.

Running hyperpnea can occur without temporal synchronization of breathes to strides[4,5], in the absence of peripheral signals[6], or during mental simulation of exercise[7-9], highlighting that its main neuronal trigger may be of central, rather than peripheral, origin. Of particular interest are therefore brain regions that command or execute locomotor movements and could provide a parallel drive to respiratory centers[10,11]. The mesencephalic locomotor region (MLR) in the dorsal midbrain is considered the main site of locomotor initiation throughout the animal kingdom, likely including humans[12-14]. Stimulation of the MLR, and particularly its cuneiform nucleus (CnF) component, engages forward locomotion at a speed that is commensurate to the intensity of the stimulus[15-19], making it a candidate neuronal encoder and driver of running intensity. Interestingly, the MLR may also upregulate breathing activity[10] and work in the lamprey, an ancestral vertebrate, recently argued for a parallel connectivity of this structure to respiratory centers[20]. This however remains to be investigated in terrestrial mammals. Another central drive to respiratory centers may originate in the circuits of the spinal cord that elaborate the locomotor rhythm and coordinate the motor output during ongoing locomotion, often referred to as a "Central Pattern Generator" or CPG[21,22]. Indeed, pharmacological activation of the lumbar enlargement, where the hindlimb CPG circuit is thought to reside, can upregulate the frequency of respiratory-like activities on *ex vivo* preparations from neonatal rats [23,24]. While this is suggestive of ascending projections to respiratory centers, the underlying circuit and its functionality during running has not been documented.

Another gap of knowledge concerns the identification of the respiratory neurons targeted by descending (e.g., MLR) or ascending (e.g., from the CPG) locomotor drives. In mammals, the respiratory rhythm is driven by neurons of the pre-Bötzinger complex (preBötC) in the ventromedial medulla[25,26]. The preBötC receives inputs from several brain areas including the midbrain[27] and, in the lamprey, MLR neurons were shown to contact a presumed homologue of the preBötC[20,28]. This makes the preBötC a prime candidate for promptly entraining respiration during exercise in mammals. More rostrally, the parafacial (pF) respiratory region may be another contender for respiratory regulation during metabolic challenges including effort. In this region, non-catecholaminergic *Phox2b*-expressing neurons (defining the Retrotrapezoid Nucleus, RTN) can rapidly upregulate respiratory rate in the context of central CO_2 chemoception[29,30] and might support active expiration which is thought to accompany exercise[31-34]. *Phox2b*-positive neurons in the

pF region have been shown to be activated during running[35], during locomotor-like activity on *ex vivo* neonatal rat preparations[23], and their silencing limits exercise capacity in running rats[36].

Here we sought to investigate the central circuits interfacing locomotor and respiratory centers in the resourceful mouse model. We found the existence of both a descending drive from the MLR, and of an ascending drive from the locomotor CPG of the lumbar spinal cord. Remarkably, the MLR is capable of upregulating breathing rate even before the initiation of actual limb movements. We further uncovered that the two systems both have access to respiratory rhythm generation mechanisms albeit through two different synaptic schemes. The MLR directly projects to the preBötC, but not to the pF region, while the lumbar spinal cord targets the pF region which in turns contacts the preBötC. Our work therefore demonstrates two locomotor central drives that may underlie breathing adaptability during running and their synaptic nodes in the respiratory central network.

Results

Glutamatergic CnF neurons project to the preBötC.

We first examined whether locomotor-promoting MLR neurons in mice contact neuronal groups involved in respiratory rhythm generation. The MLR contains two major subdivisions, the cuneiform nucleus (CnF) containing glutamatergic ($Glut^+$) neurons, and the pedunculopontine nucleus (PPN) containing both $Glut^+$ and cholinergic neurons[15-17]. Since locomotor initiation is attributed to the former, we traced the projections of CnF neurons by unilateral stereotaxic injections of a Cre-dependent AAV-eYFP in *Vglut2*^{Cre} adult mice [37] (Figure 1a, b, see Figure S1 for all injection sites). Abundant eYFP-positive fibers were detected in the preBötC, located ventrally to the nucleus ambiguus and containing SST-positive neurons[38]. These projections were found bilaterally with an ipsilateral predominance (Figure 1c, d, g). In contrast, projections were very sparse in the pF respiratory area, located immediately ventral, ventro-median and ventro-lateral to the facial motor nucleus (7N, Figure 1e-g). To verify that CnF neurons synaptically target preBötC neurons, we made use of a genetically restricted two-virus approach[39] to reveal preBötC putative inputs anatomically. PreBötC neurons can be delineated as $Glut^+$ neurons with commissural projections[40,41]. We therefore injected a retrograde Cre-dependent rabies helper virus (HSV-LSL-TVA-oG [42]) in the preBötC on one side followed by an EnvA-ΔG rabies (Rb) virus in the contralateral preBötC (Figure 1h). As demonstrated previously[43], this leads to the expression of the Rb virus in projection-defined neurons (here commissural $Glut^+$ preBötC neurons, Figure 1i) and in their presynaptic partners by transsynaptic spread. The latter were detected in the CnF and PPN nuclei bilaterally (Figure 1j). Other putative preBötC presynaptic partners were detected in the contralateral preBötC, the periaqueductal grey, the superior colliculus and the NTS, and only few in the pF region (Figure S2 and data not shown). Altogether, these anterograde and retrograde tracings demonstrate that $Glut^+$ CnF neurons directly contact candidate respiratory rhythm generating neurons in the preBötC, but not in the pF region.

Glutamatergic CnF neurons modulate inspiratory rhythm generation.

We next tested the ability of Glut$^+$ CnF neurons to functionally impact the preBötC. One hallmark of preBötC responses to phasic incoming inputs is their phase-dependency to the ongoing rhythm [44,45]. To evaluate this for CnF-evoked preBötC responses, we virally delivered the excitatory Channelrhodopsin 2 (ChR2) in Glut$^+$ CnF neurons on one side of *Vglut2^{Cre}* adult mice, and implanted an optic fiber over the injection site (Figure 2a). Breathing cycles were measured with whole body plethysmography (WBP, Figure 2b) while single-pulse (50 ms) photoactivations were delivered randomly during the respiratory cycle during quiet breathing in awake and alert animals. Photostimuli did not elicit any noticeable body movements but indeed evoked individual breaths. We calculated the resultant phase-shift, expressed as the perturbed cycle duration over the duration of the control cycle as done previously[44,45] (Figure 2b, see methods). We found that unilateral photostimulation of Glut$^+$ CnF neurons elicited an ectopic inspiratory burst and shortened the respiratory cycle but that this effect was most prominent when delivering light-pulses during early expiration (phase: 0.5 - 0.6, phase shift: 0.77 ± 0.10, $p < 0.0001$, Figure 2c). In contrast, the effect was only minimal in late expiration. We also observed a shortening (although less drastic) of the next two subsequent cycles, suggesting that activation of the CnF also determines a longer lasting modulatory action on preBötC rhythm generation (Figure S3a-d). No alteration of the respiratory cycle was however seen in mock trials in control mice that do not express ChR2 (Figure S4a, b). Likewise, activating Glut$^+$ neurons of the vlPAG, located laterally to the CnF but at the same dorso-ventral depth (Figure S5a-c), or those of the inferior colliculus, located dorsally but at the same medio-lateral location as the CnF (Figure S5e-g) did not impact the respiratory cycle. Therefore, the phase-dependent shortening observed when targeting the CnF cannot be attributed to thermal confounds [46] nor to the few cells in adjacent structures that are occasionally transfected (Figure S1). To ascertain that this CnF-driven modulation of respiratory rhythm generation owes to direct projections to the preBötC, we next photoactivated ChR2-expressing fibers in the preBötC following viral injection in the CnF (Figure 2d). This led to similar phase-dependent shortenings of the respiratory cycle, again maximal when light-activations are delivered in early expiration (phase: 0.5 - 0.6; phase shift: 0.79 ± 0.15, $p < 0.0001$, Figure 2e, f). This effect disappeared after the 2nd subsequent respiratory cycle (Figure S3e-h). Light deliveries in the preBötC of control mice that do not express ChR2 did not produce any noticeable effect (Figure S4d, e). Overall, the direct projections of the Glut$^+$ CnF neurons indeed conform to phase-dependent activation of preBötC neurons, highlighting excitatory modulations of inspiratory burst generation.

Glutamatergic CnF neurons modulate breathing in synergy with locomotion.

Through their access to rhythm generating neurons in the preBötC, Glut$^+$ CnF neurons might be capable of upregulating breathing frequency in synergy with locomotor initiation. To access respiratory

parameters during vigorous displacement movements, we made use of our recently-developed method for chronic electromyographic recordings of the diaphragm (DiaEMG), the main inspiratory muscle[4]. *Vglut2*^{Cre} animals were made to express ChR2 in Glut^{+} CnF neurons as above, EMG-implanted, and placed in a linear corridor. Light was delivered in 1 s trains at increasing pulse frequencies when animals were quietly breathing, alert, and stationary at one end of the corridor (Figure 3). Animals were filmed from the side and their displacement speed computed using markerless video-tracking as performed previously[4,47]. In line with numerous studies[15-18], we found that photoactivating Glut^{+} CnF neurons at 15 Hz or more engages animals in forward locomotion (Figure 3a, b), and that higher stimulation frequencies impose faster regimes, shorten the delay between light onset and locomotor initiation and increase the occurrence of left-right synchronous gaits (Figure S6). Our photoactivations did not induce any rearing, grooming, handling behaviors or arrest behaviors that would be expected from light accessing Glut^{+} PPN neurons immediately ventral to the CnF [15,48]. Furthermore, we never observed defensive freezing or orienting behaviors that are typical of activations of, respectively, the adjacent ventrolateral periaqueductal grey (vlPAG[49], Figure S5a-b) or the superior or inferior colliculus ([50,51], Figure S5e, f). This, together with the posthoc confirmation of optic fiber placement (Figure S1), argues for accurately restricted activations of the CnF. Importantly, CnF photostimulations were associated with an increased respiratory rate (Figure 3b, c), an effect that was not seen in control mice that do not express ChR2 (Figure S4c). Remarkably, during CnF photoactivations that effectively engage running, respiratory rate increased in a two-step sequential manner. In a first step, that we term the "pre-loco" phase, a modest increase was seen immediately at light onset but before the first locomotor movements (i.e., during the delay between light onset and the initiation of locomotion, Figure 3d). The mean respiratory rate during this "pre-loco" phase was significantly higher than baseline but not correlated to the photostimulation frequency (Figure 3e). In a second step, when the animals effectively engage in locomotion ("loco" phase), the respiratory rate was further augmented (Figure 3d). There, respiratory rate was still not strongly dependent on stimulation frequency but it was proportional to the actual displacement speed (Figure 3f). The amplitude of DiaEMG was not significantly changed during the pre-loco phase but was increased during the loco phase (Figure 3e, f), supporting a further ventilatory effort when animals run. We also found that the respiratory and locomotor rhythms were never temporally synchronized (Figure S7), similarly to the situation in spontaneously running mice[4]. These results indicate that the respiratory frequency during CnF-evoked locomotion is upregulated immediately at light onset before the initiation of locomotion, and further upregulated during actual locomotion. The former observation suggests that Glut^{+} CnF neurons can independently modulate respiratory activity and limb movements. Demonstrating this further, photostimulations below the threshold for locomotor initiation (5 and 10 Hz, Figure 3g, Figure S6b) were sufficient to significantly increase the respiratory frequency and the amplitude of DiaEMG from baseline (Figure 3h). The same subthreshold stimulations targeted to the vlPAG or to the inferior colliculus neurons located in proximity to the CnF however evoked no significant changes in breathing rate (Figure S5d, h), further excluding a confounding effect of the occasional viral expression in these structures.

Altogether, these analyses demonstrate that i) Glut^{+} CnF neurons can upregulate breathing rate before, or even in the absence of, locomotor movements, ii) during CnF-evoked locomotion, the highest increase in breathing rate from rest occurs when actual locomotor movements are engaged, iii) respiratory frequency increase during the "loco" phase is proportional to the displacement speed, and iv) breaths are not phase-locked to cyclic limb movements.

The spinal locomotor circuits project to the pF respiratory region.

We then reasoned that the engagement in actual locomotor movements may be associated with a stronger drive onto respiratory centers which could originate from activated lumbar locomotor circuits. We thus performed large-volume injections of a Cre-dependent AAV-eYFP bilaterally in the lumbar spinal cord of *Vglut2*^{Cre} mice, to cover most of the thoraco-lumbar enlargement where neurons that generate the locomotor rhythm and set its speed are distributed[52-54] (Figure 4a, b), and examined projections in the brainstem respiratory regions. In contrast to the anterograde tracings from the CnF, this revealed very few, if any, eYFP-positive fibers in the preBötC but their abundant (and ubiquitous) presence flanking all but dorsal margins of the 7N (ventral, anterior, posterior, medial, and lateral), thus the pF respiratory region (Figure 4c-f). To discriminate passing fibers from putative synaptic contacts, we first repeated these spinal cord injections with an AAV that drives expression of a presynaptic, synaptophysin-fused fluorophore[55], and indeed observed fluorescent puncta in the pF (Figure 4g). We also performed similar spinal injections using an AAV vector that enables transsynaptic Cre expression in postsynaptic target neurons (AAV1-Syn-Cre[56]) followed by a Cre-dependent AAV-eYFP vector in the pF region. This led to numerous eYFP-expressing cells (Figure 4h, i) in all subdivisions of the pF. Since the pF does not project to the lumbar spinal cord (Figure S8), the Cre-dependent labelling is not brought about by retrograde transport of the AAV1-Syn-Cre virus but witnesses its anterograde synaptic transfer. Therefore, ascending spinal projections synaptically target the pF respiratory region.

Lumbar locomotor circuits upregulate breathing rate through the RTN$^{Phox2b/Atoh1}$ *ex vivo*.

To investigate functionally the possibility that lumbar locomotor circuits can upregulate breathing, we used *ex vivo* isolated brainstem/spinal cord preparations from neonatal mice. Although long-used for monitoring locomotor[54] or respiratory-like[25] activities, monitoring both simultaneously during drug-evoked locomotor-like activity had only been achieved on rat preparations[23,24]. We adapted the method to the neonatal mouse and used a split-bath for independent pharmacological manipulation of the brainstem and spinal cord through superfusion of dedicated artificial-cerebrospinal fluids (aCSFs, see methods). In these conditions, we recorded respiratory-like activity on the 4th cervical ventral root and locomotor-like activity on the 2nd lumbar ventral root (Figure 5a).

When both the brainstem and spinal cord were superfused with control aCSF, only respiratory-like activities were detected. Bath-application of the neuroactive substances N-methyl-D-aspartate (NMDA) and

serotonin (5-HT) in the spinal compartment evoked locomotor-like activities associated with an increased frequency of the respiratory-like activity (by 162 ± 30 % of baseline, Figure 5b, c). To rule out drug leakage from the spinal compartment, we first verified that this frequency increase of respiratory-like activities was abolished following a cervical transection (Figure S9a-c). We also found a similar acceleration of respiratory-like activity by targeted optogenetic activations of lumbar Glut^{+} neurons (170 ± 38 % from baseline, Figure S9d-f). Altogether, these experiments indicate that the activation of lumbar spinal circuits that contain the locomotor CPG exerts an excitatory effect on respiratory activity.

Since our anatomical observations place the pF respiratory region as a candidate target of ascending pathways from the spinal cord (Figure 4), we next addressed the functional contribution of this region. We first eliminated physically the pF by a complete transection below the facial motor nucleus (Figure 5d). Respiratory-like activities persisted on the 4th cervical root, but pharmacological activation of lumbar circuits no longer significantly upregulated their frequency (Figure 5e, f). We also examined specifically the contribution of RTN neurons in the pF region[29,30], making use of the fact that RTN neurons relevant for modulating respiratory rhythm generation, at least in the context of central chemoception, i) are best identified by a combined history of expression of the transcription factors *Phox2b* and *Atoh1*[57,58] (thereafter RTN$^{Phox2b/Atoh1}$ neurons;) and ii) can be deleted when expressing a mutated allele of PHOX2B (*Phox2b*^{27Ala}) in rhombomeres 3 and 5 (*Egr2*^{cre}*;Phox2b*^{27AlaCKI} background[57,58]; Figure S10). We thus recorded respiratory- and locomotor-like activities from *Egr2*^{cre}*;Phox2b*^{27AlaCKI} RTN mutant pups (Figure 5g). Preparations showed persistent inspiratory-like activity on the 4th cervical root, but pharmacological activation of lumbar circuits no longer upregulated its frequency (Figure 5h, i). These experiments highlight the capacity of spinal lumbar circuits to upregulate respiratory-like activities through RTN$^{Phox2b/Atoh1}$ neurons in the pF respiratory region.

Silencing RTN$^{Phox2b/Atoh1}$ neurons reduces respiratory increase during running exercise *in vivo*.

The importance of RTN$^{Phox2b/Atoh1}$ neurons revealed above *ex vivo* prompted us to address their contribution to respiratory activity during running in behaving mice. For this, we used an intersectional background in which Cre expression is conditioned by both *Atoh1* and *Phox2b* expression[58] (*Atoh1*^{FRTCre}*;Phox2b*^{Flpo}), and injected in the pF region bilaterally a Cre-dependent AAV coding the inhibitory DREADD receptor hM4Di (Figure 6a, b). Diaphragmatic EMG electrodes[4] were then implanted and respiratory parameters were measured before and 2-3 h after the administration of the DREADD ligand Clozapine-N-Oxide (CNO) at rest or during treadmill running. At rest, CNO administration had no significant effect on the mean inspiratory frequency, inspiratory and expiratory durations, DiaEMG amplitude (Figure 6c, d) and breathing variability (coefficient of variation <0.1), supporting previous findings that the RTN only minimally contributes to the baseline breathing rate[36]. When animals were made to run at 40 cm/s they showed, prior to CNO administration, an augmented respiratory frequency (269 % increase) and amplitude (263% increase), in agreement with previous work[4]. However, following CNO administration, their breathing rate and DiaEMG amplitudes were significantly reduced compared to the pre-CNO measurements at the same running speed

(Figure 6e, f). Furthermore, CNO-treated mice showed a less pronounced reduction in their expiratory time (Te). Administration of saline in hM4Di-injected mice or of CNO on wild-type mice changed neither the breathing rate, expiratory and inspiratory times, nor the DiaEMG amplitude both at rest and during running sessions (Figure S11). We also did not observe any impact of CNO or saline alone on breathing regularity (coefficient of variation < 0.1). This excludes any non-specific effects of CNO alone, as previously reported for the same concentration[59]. These experiments indicate that the activity of RTN$^{Phox2b/Atoh1}$ neurons is required for upregulating ventilatory frequency during running exercise.

RTN$^{Phox2b/Atoh1}$ neurons project to the preBötC inspiratory generator.

The reduced breathing rate following the silencing of RTN$^{Phox2b/Atoh1}$ neurons suggests that this genetically defined neuronal subset may have access to the main inspiratory generator, the preBötC. While the pF region was shown to send projections to the ventral respiratory column and possibly the preBötC[60,61], this had not been determined for RTN$^{Phox2b/Atoh1}$ neurons. To examine it, similarly to what we did for CnF neurons (Figures 1, 2), we injected a Cre-dependent AAV vector coding ChR2 and a fluorescent protein in the pF region of *Atoh1^{FRTCre};Phox2b^{Flpo}* animals and implanted an optic fiber above the injection site (Figure 7a, b). Anatomically, we observed and quantified abundant eYFP-labelled varicosities of RTN$^{Phox2b/Atoh1}$ neurons in the preBötC region with a strong ipsilateral dominance (Figure 7c, d). To demonstrate the capacity of RTN$^{Phox2b/Atoh1}$ neurons to directly modulate rhythm generation mechanisms in the preBötC, we examined respiratory responses to 50 ms single-pulse photoactivations with the same analytic tools described earlier for CnF activations (Figure 2). We found that unilateral photostimulation of RTN$^{Phox2b/Atoh1}$ neurons could elicit an ectopic inspiratory burst and shorten the respiratory cycle (Figure 7e, f). However, when compared to CnF photostimulation, shortenings of the respiratory peaked earlier during the inspiration phase (phase 0.2 - 0.3 and 0.3 - 0.4; phase shift: 0.70 ± 0.13 and 0.69 ± 0.09; $p < 0.0001$) and, contrary to the CnF, stimulation during late expiration caused a significant lengthening of the respiratory cycle (phases 0.9 - 1; phase shift: 1.11 ± 0.12; $p = 0.0004$). Here again, stimulation of RTN$^{Phox2b/Atoh1}$ neurons led to phase dependent inspiratory responses in keeping with the preBötC excitability dynamics. Yet unlike the CnF, no shortening of the subsequent cycles following the stimulus was observed (Figure S12). Moreover, 1 s light stimulations of the RTN$^{Phox2b/Atoh1}$ neurons resulted in significant augmentations of respiratory frequency during the stimulus, mostly accounted for by a decrease of Te, even at the lowest stimulation frequencies (Figure 7g, h). RTN$^{Phox2b/Atoh1}$ to preBötC connectivity is further corroborated by the detection of eYFP puncta in the preBötC following the injection of a Cre-dependent AAV coding a synaptophysin-fused eYFP in the pF area on *Atoh1^{FRTCre};Phox2b^{Flpo}* animals (Figure 7i, j). Altogether, these results demonstrate that the genetically defined subset of RTN$^{Phox2b/Atoh1}$ neurons can upregulate respiratory rate through direct projections to the preBötC.

Discussion

A neuronal substrate for hyperpnea during running has long been proposed but its underlying cells and circuits had remained speculative. We uncover here two systems by which the central locomotor network can enable respiratory rate augmentation in relation to running activity (Figure 8). On the one hand, we reveal the capacity of the MLR subnucleus CnF, a conserved locomotor controller [12,15-19], to upregulate breathing. On the other hand, we demonstrate that when active, the lumbar enlargement of the spinal cord containing the hindlimb CPG, also potently upregulates breathing rate. Using cell-type specific circuit tracing and functional interferences, we further characterize each locomotor drive by identifying its specific neuronal target in the respiratory network.

Multiple locomotor drives set respiratory rhythm frequency.

A remarkable finding reported here is the function of the CnF beyond locomotor control. We should stress again here that our injection scheme only minimally transfects, and likely does not photoactivate, neurons in the adjacent PAG and IC (Figure S1). While these structures may modulate breathing in specific contexts[62], they do not contribute to the modulations reported here (Figure S5). One intriguing feature we observed with CnF stimulations is that respiratory rate is upregulated before the engagement of locomotor movements, or for stimulations that are below the threshold for locomotor initiation (Figure 3). This might be consequent to the direct access of the CnF to the preBötC (Figures 1, 2), while its access to the limb circuits requires the crossing of multiple synapses, including reticulospinal relay neurons[16,63] (Figure 8b). The regulation of breathing by the CnF in the absence of locomotor movements places the CnF as a *bona fide* respiratory modulator structure. Admittedly, we could not assess the necessity of these neurons for the development of the ventilatory response during spontaneous exercise since their silencing itself impairs the capacity of the animal to actually run, and therefore exercise[16]. Nevertheless, in the lamprey, spontaneous swimming bouts are preceded by a marked increase in respiratory frequency [20,28]. Activity of the CnF prior to movement initiation may hence bear physiological relevance as an anticipatory mechanism to the planned motor action. Men informed of an upcoming exercise or imagining performing an exercise[7-9], also show increased ventilation and cardiovascular responses, although less drastic than during actual movements. These adjustments are reminiscent of the “pre-loco” phase resulting here from CnF stimulations (Figure 3). Interestingly, the CnF is associated with escape-like fast regime running[15,16], and may be part of a larger command system for defensive behaviors in the broad sense[64,65]. It may therefore bear output connectivity allowing to engage a composite response with both cardiovascular[65], respiratory (this study and[20]), and if needed, locomotor components. Data in the lamprey indicate that locomotor and respiratory centers are contacted by distinct MLR neurons[20]. Pending an equivalent examination in mice, it is possible that the MLR may, similarly to other descending motor pathways[43], host projection-defined subsets that each control one trait of a multi-faceted behavior.

We also report the existence of a modulation of breathing rate upon activation of the lumbar spinal segments that contains the hindlimb locomotor circuits[21,22] (Figure 8c). Such an ascending drive, previously suggested in rats[23,24], is demonstrated here in mice by local pharmacological (Figure 5) or optogenetic (Figure S9) activations of the lumbar enlargement on reduced preparations *ex vivo.* Indeed, *ex vivo*, the absence of the MLR and of peripheral structures as well as the experimental control of the extracellular solution, allow to isolate the functional contribution of the spinal ascending drive from descending, peripheral feedbacks, and central chemoceptive ones. We hence propose that active locomotor executive circuits (through projections to the RTN, see below), continuously inform respiratory centers on the state of ongoing locomotion and are, at least partly, causal to the further increase of respiratory rate seen when animals engage in locomotion (i.e., the "loco" phase) following CnF stimulations (Figure 8). This is further supported by the recent report of increased respiratory-like activity after activation of the lumbar enlargement in rat neonatal preparations[23]. Yet, we cannot rule out a persisting activity of CnF neurons during the running exercise[16]. This leaves open the possibility that the two locomotor drives, i.e., from the CnF and the lumbar spinal cord, may synergize to set the respiratory frequency during ongoing running.

Different respiratory nodes integrate distinct locomotor drives.

Another intriguing observation is that the two revealed locomotor drives target different nuclei in the respiratory rhythm generating network. The CnF connects to the preBötC, the main site of inspiratory rhythm generation[25,26], while the lumbar CPG contacts the pF respiratory region, and possibly the RTN$^{Phox2b/Atoh1}$ previously implicated in central CO_2 chemoception[29,30,57,58] that in turn projects onto the preBötC (Figure 8 b, c).

For the former, the connectivity is first demonstrated anatomically by the detection of anterogradely-labelled fibers, and a transsynaptic labelling approach initiated from Glut$^+$ preBötC neurons (Figure 1). This connectivity is also supported functionally, by the capacity of Glut$^+$ CnF neurons or their projections in the preBötC to impact respiratory rhythm mechanisms (Figure 2). In contrast, we found that ascending projections from the lumbar spinal cord were virtually absent in the preBötC but were dense in the pF (Figure 4), in an area compatible with that of the RTN. The synaptic nature of these ascending projections was ascertained using a synaptic labelling (Figure 4g) and an anterograde transsynaptic strategy[56] (Figure 4h). The functionality of these ascending projections and the identity of their neuronal targets as RTN$^{Phox2b/Atoh1}$ neurons were demonstrated both by silencing experiments *in vivo* (Figure 6) and by *ex vivo* experiments on RTN null mutants (Figure 5). In the latter situation, peripheral chemoreceptors, sensory activation or other metabolic factors do not contribute. Hence, the spinal locomotor circuits provide at least one source of RTN$^{Phox2b/Atoh1}$ neuron excitation, which may be complemented *in vivo* by other sources including neighboring adrenergic C1 neurons[29,66] or somatic afferents[67]. The requirement of the RTN is further supported by the perturbed respiratory-like activity following bilateral lesions of the RTN in rat neonatal preparations[23], and the increased c-Fos expression in RTN neurons following exercise in rats[35]. Furthermore, a broader silencing

of RTN and neighboring adrenergic neurons, defined by *Phox2b* expression alone, was previously shown to limit the running capacity in rats[36]. Therefore, the RTN$^{Phox2b/Atoh1}$ subset may be the prominent integrator of the ascending locomotor drive, at least for the setting of respiratory frequency. A previous study (in rats) of the role of the RTN in mediating changes in the respiratory activity during exercise concluded that the RTN does not appear to be involved in triggering the initial increases in ventilation at the onset of exercise but is rather critical in maintaining increased respiratory effort during sustained exercise[36]. Our work strikingly substantiates this view. The CnF would pre-empt and trigger heightened metabolic demand at the onset of exercise while the RTN, by adjusting the respiratory effort to the engaged and sustained locomotion, might determine exercise capacity.

We also show that the RTN$^{Phox2b/Atoh1}$ neurons in turn project to the preBötC (Figure 7). This makes the preBötC inspiratory generator a final integrator of both the descending (from the CnF, Figure 8c) and the ascending (from the lumbar spinal cord, Figure 8b) locomotor drives and raises the question of the identity of the targeted neurons. Our transsynaptic tracing scheme from the preBötC demonstrates that the CnF targets glutamatergic preBötC neurons (Figure 1h-j). Comparatively however, the number of transsynaptically labeled neurons in the pF area was much lower (Figure S2d, e). Moreover, brief CnF photostimulations were most effective to shorten the respiratory cycle when delivered during early expiration but failed when delivered during inspiration (Figure 2). This is reminiscent to what was observed when directly stimulating glutamatergic preBötC neurons collectively[45] or the *Dbx1*-expressing V0 subset[44], the main rhythmogenic candidates[40]. In contrast, when stimulating the RTN$^{Phox2b/Atoh1}$, the shortening of the respiratory cycle is most efficient during inspiration and a significant lengthening of the respiratory cycle is observed when photoactivations are delivered in late expiration (compare Figure 2c with Figure 7f). This permissive action in inspiration and the lengthening in expiration recalls what others have reported when specifically activating inhibitory, but not excitatory, preBötC neurons[45]. The RTN$^{Phox2b/Atoh1}$ and the CnF might thus preferentially target different cell-types in the preBötC: inhibitory neurons for the former, and glutamatergic ones for the latter. Note that such a bias towards preBötC inhibitory target neurons for the RTN$^{Phox2b/Atoh1}$ compared to the CnF could would be mechanistically compatible with switching from CnF-induced “pre-loco” moderate respiratory frequency increase, to the higher “loco” respiratory frequency range associated to actual locomotion. Indeed, the current model ascribes a limited ability of preBötC excitatory neurons compared to inhibitory neurons at entraining high frequency rhythms[45]. Although our data are compatible with such a working model, the proposed connectivity will need to be investigated directly by future work.

Limitations and perspectives

While both the CnF and spinal locomotor circuits have the capacity to upregulate breathing frequency, further adjustments can be achieved by changes in tidal volume and by the mobilization of active expiration, a candidate signature of exercise hyperpnea. The expiratory motor drive was not directly

monitored here and recording the activity of abdominal respiratory muscles would be required. The possibility that the spinal ascending locomotor drive contributes to onset of active expiration, is yet likely given that i) Te was found considerably reduced in ventilatory responses to 1 s photostimulations of RTN$^{Phox2b/Atoh1}$ neurons (Figure 7h) as expected from induction of an active expiratory phase, ii) the widespread projections onto the pF region, including its lateral aspect (Figure 4f) thought to host an expiratory oscillator[26,68], and iii) the recent demonstration that optogenetic activation of CO_2 chemoceptive RTN neurons induces active expiration[34]. Finally, while our results localize the locomotor ascending drive to the lumbar spinal cord, the identity of incriminated neurons will remain to be characterized. Our spinal injections were intentionally targeted to the entire thoraco-lumbar enlargement, since the locomotor-promoting circuits are distributed across multiple segments[54]. Spinal neurons of V2a, $V0_V$ or V3 genetic identity as well as *Shox2* and *Hb9*-expresing ones stand as candidates, by virtue of their glutamatergic nature and their direct contribution to locomotor rhythm and pattern[21,69]. In any case, should these neurons and possibly the ensuing ascending drive be rhythmically modulated during locomotion, this fails to translate in a phased entrainment of breathing (this study and[4]).

General conclusion

We provide here a firm demonstration and a circuit characterization of two central neuronal drives for breathing adaptation during running. The circuit revealed highlights the multi-functional ambition of cell-types and pathways that are typically regarded as “locomotor” or “respiratory” related. This represents an entry point to further decipher the nodes and links through which distinct motor programs necessarily cooperate.

Methods

Mice

C57BL/6J wild-type mice were obtained by Janvier Labs (Le Genest-Saint-Isle, France). *VGlut2-IRES-Cre* animals (therefafter *Vglut2^{Cre}*, [37] and *Ai32(RCL-ChR2(H134R)/EYFP)* (thereafter *ChR2^{floxed}*, [70]) were obtained from Jackson Laboratories. To manipulate RTN$^{Phox2b/Atoh1}$ neurons we used the following mouse lines: *Egr2^{Cre}* [71] crossed with *Phox2b^{27AlaCKI}* [57] and *Atoh1^{FRTCre}; Phox2b^{Flpo}* [58] mouse lines. Animals were group-housed with free access to food and water in controlled temperature conditions and exposed to a conventional 12-h light/dark cycle. Experiments were performed on animals of either sex, aged 2 to 3 months at the time of first injection and data from males and demales were pooled. All procedures were approved by the French Ethical Committee (authorization 2020-022410231878) and conducted in accordance with EU Directive 2010/63/EU. All efforts were made to reduce animal suffering and minimize the number of animals.

Viruses used

For anterograde tracing and photostimulation of the CnF and its projection in the preBötC, as well as for photoactivations of IC and the PAG, we used a Cre-dependent AAV9-Ef1a-DIO-hChR2(E123T/T159C)-eYFP (Addgene #35509, titer 7.7e12 vp/ml [72]) unilaterally (40 to 100 nL). No labelling was seen in wild-type animals (see also [72] and [43] for validation studies). For anterograde tracing from the lumbar spinal cord, the same virus was injected bilaterally (600-750 nL/side) in the second lumbar segment, and for RTN$^{Phox2b/Atoh1}$ photostimulation, the injection was unilateral (350-500 nL). For reversible silencing of RTN$^{Phox2b/Atoh1}$ neurons, we used bilateral injections (350-500 nL/side) of an AAV8.2-hEF1a-DIO-hM4Di-mCherry-WPRE[43] obtained from Dr. Rachael Neve (Gene Delivery Technology Core, Massachusetts General Hospital, USA, titer: 5.6e12 vp/ml). No labelling was seen in wild-type mice. For transsynaptic labelling of inputs onto preBötC neurons, we used 500 nL of a HSV1-hEF1a-LS1L-TVA950-T2A-rabiesOG-IRES-mCherry obtained from Dr. Rachael Neve (Gene Delivery Technology Core, Massachusetts General Hospital, USA), and 200 nL of EnvA-ΔG-rabies-GFP obtained by the GT3 core (Salk Institute, USA, titer: 9.59e9 vp/ml). For anterograde transsynaptic tracing, we used injection of an AAV2/1-hSyn-Cre-WPRE-hGH (UPenn Vector Core, titer: 6.68e13 vg/ml, validated in [56]) bilaterally in the lumbar spinal cord (600-750 nL/side) and the same AAV (Addgene # 35509) as for anterograde tracing and optogenetic stimulations bilaterally in the pF area (300 nL/side). For anterograde synaptic tracing from the RTN$^{Phox2b/Atoh1}$, we used unilateral injection (350-500 nL) of an AAV8.2-hEF1a-DIO-synaptophysin-eYFP[55] obtained from Dr. Rachael Neve (Gene Delivery Technology Core, Massachusetts General Hospital, USA, titer: 5.4e12 vp/ml). No labelling was seen in wild-type mice.

Surgical procedures

Injections and implants in the brainstem

Animals were anesthetized with isoflurane throughout the surgery (4 % at 1 L/min for induction; 2-3 % at 0.2 L/min for maintenance). Buprenorphine (0,025 mg/kg) was administered subcutaneously for analgesia before the surgery. The temperature of the mice was maintained at 36 °C with a feedback-controlled heating pad. Anesthetized animals were placed on a stereotaxic frame (Kopf) and the skull was exposed. Viral vectors were delivered using a pulled glass pipette connected to a syringe pump (Legato 130, KD Scientific, customized by Phymep, France). Infusion flow was set to 100 nL/min. Coordinates (in mm) used to target CnF neurons (Figures 1-3) were: 4.4 caudal to bregma, 1.3 lateral, and 2.8 mm from skull surface. Coordinates used to target PAG neurons (Figure S5) were: 4.4 caudal to bregma, 0.3 lateral, and 2.8 mm from skull surface. To target IC neurons (Figure S5), they were: 4.4 caudal to bregma, 1.3 lateral, and 1.7 mm from skull surface. In both cases, the volume injected was 50 nL. RTN$^{Phox2b/Atoh1}$ neurons were targeted unilaterally (Figure 7) or bilaterally (Figures 4, 6) using the following coordinates: 6.0 caudal to bregma, 1.25 lateral, and 5.8 from skull surface. preBötC injections (Figure 1) were performed at the following coordinates: -7.2 from bregma, 1.25 lateral, and 5.7 from skull surface. After the injection, the pipette was held in place for 5 to 10 min before being slowly retracted. For CnF, CnF fibers in the preBötC, RTN$^{Phox2b/Atoh1}$, PAG and IC optogenetic activations, a 200 µm core 0.39 NA optic fiber connected to a 1.25 mm diameter ferrule (Thorlabs) was implanted 0.4

mm above targeted sites. Optic fibers were secured to the skull with dental cement (Tetric Evoflow). Animals were followed daily after surgery.

Injections in the spinal cord

Animals were anesthetized as described above and spinal injections were performed as previously done [43,73]. A two cm skin incision was performed dorsally on anesthetized animals and exposed spinal column was fixed with two holders on the left and right sides to a stereotaxic frame to minimize movements. Vertebral spinous processes were used as landmarks to target specific segments [74]. A small incision of the ligamentum Flavum allowed access to the spinal cord. A pulled glass pipette connected to a motorized syringe pump injector (Legato 130, KD Scientific, customized by Phymep, France) was positioned into the ventromedial area of the L2 (2nd lumbar segment, between the 11th and 12th vertebral body) using the following coordinates: 350 µm laterally from the dorsal artery and 800 µm depth from the dorsal surface. This lateral positioning ensures that the injection pipette does not pass through the lateral funiculus where ascending and descending axons travel. The volume injected was 600-750 nL/side to allow for transfection of neurons across multiple thoraco-lumbar segments (see Figure 4a, b). For Cholera Toxin B (CTB) experiments (Figure S8), we injected 600-750 nL of CTB-AF647 conjugate (ThermoFisher Scientific, ref. # C-34778) diluted at 0.5 % in sterile water on each side of the spinal cord. After each injection, the pipette was held in place for 5 to 10 min before being slowly retracted. The skin was sutured, and animals were followed daily after the surgery. All animals recovered without motor impairments.

Diaphragm EMG recordings

The protocol was described previously[4]. In brief, a 12 cm pair of electrodes was prepared from Teflon-coated insulated steel wires with an outside diameter of 0.14 mm (A-M systems, ref. # 793200). Two wires were lightly twisted together, and a knot was placed 5 cm from one end. At 1 cm from the knot, the Teflon insulation was stripped over 1 mm from each wire so that the two bared regions were separated by about 2 mm. The ends of the two wires were soldered to a miniature dissecting pin. The free ends of the electrodes, and a 5 cm ground wire were soldered to a micro connector (Antelec). Nail polish was used to insulate the wires at the connector.

For diaphragm implantation, animals were anaesthetized, placed in a stereotaxic frame and hydrated by a subcutaneous injection of saline solution (0.9 %) as previously reported[4]. Their temperature was maintained at 36°C with a feedback-controlled heating pad. This step was crucial to ensure post-surgery survival. The skull was exposed and processed to secure the micro connector using dental cement (Tetric Evofow). The ground wire was inserted under the neck's skin and the twisted electrodes were tunneled towards the right part of the animal guided by a 10 cm silicon tube of 2 mm inner diameter. The animal was then placed in supine position, the peritoneum was opened horizontally under the sternum, extending laterally to the ribs, and the silicon tube containing the electrodes was pulled through the opening. The

sternum was clamped and lifted upwards to expose the diaphragm. A piece of stretched sterile parafilm was placed on the upper part of the liver to avoid friction during movement of the animal and to prevent conjunctive tissue formation at the recording sites. The miniature dissecting pin was pushed through the right floating ribs. The pin was then inserted through the sternum, leaving the bare parts of the wires in superficial contact with the diaphragm. The electrodes' position was secured on both sides of floating ribs and sternum using dental cement. The pin was removed by cutting above the secured wires. The peritoneum and abdominal openings were sutured and a head bar was placed on the cemented skull to facilitate animal's handling when connecting and disconnecting EMG cables during behavioral sessions. Buprenorphine (0.025 mg/kg) was administered subcutaneously for analgesia right after surgery and animals were observed daily following the surgery and treated with Buprenorphine if needed.

Histology

Adult mice were anesthetized with Euthasol Vet (140 mg/kg) and perfused with 4 % paraformaldehyde (PFA) in 1X Phosphate Buffered Saline (PBS). Brains and spinal cords were dissected out and fixed overnight in 4 % PFA at 4 °C. After fixation, tissues were rinsed in 1X PBS. Brain and spinal cord were cryoprotected overnight at 4 °C, respectively in 16 % and 20 % of sucrose in PBS. Tissues were rapidly cryo-embedded in OCT mounting medium and sectioned at 30 µm using a cryostat. Sections were blocked in a solution of 1X Tris Buffered Saline (TBS), 5 % normal donkey serum and 1 % Triton X-100. Primary antibodies, carried out 48 hours at 4 °C, were: goat anti-ChAt (1:500, ref. # AB144P, Merck Millipore), chicken anti-GFP (1:500, ref. # 1020, Aves Labs), rabbit anti-RFP (1:500, ref. # 600-401-379, Rockland), rabbit anti-SST (1:500, ref. # T-4103, BMA Biomedicals), and sheep anti-TH (1:500, ref. # AB1542, Merck Millipore). Primary antibodies were detected after 2 hours of incubation at room temperature with appropriate secondary antibodies coupled to Alexa-Fluor 488, 647, Cy-3 or Cy-5 (1:500, Jackson ImmunoResearch). Sections were counterstained with a fluorescent Nissl stain (NeuroTrace 435/445 blue, ref. # N21479, 1:200 or NeuroTrace 640/660 deep-red, ref. # N21483, 1:1000, Thermo Fisher Scientific) and mounted in Prolong Diamond Antifade Montant (P36970, Thermo Fisher Scientific). Sections were acquired with a Leica TCS SP8 confocal microscope (NeuroPICT imaging platform of the NeuroPSI Institute) using 10x and 25x objectives, or on a motorized Zeiss AxioImager at 10x.

The preBötC was defined as located ventrally to the cholinergic ChAT$^+$ neurons of the nucleus ambiguus (na) where somatostatin$^+$ (SST) neurons are detected[38] (Figures 1, 4, 7; from 7.0 to 7.4 mm caudal to bregma). The pF respiratory region was defined as immediately ventral, ventro-median and ventro-lateral to facial motor neurons[75] (7N; Figures 1, 4, 6, 7; from 6.7 to 5.7 mm caudal to bregma).

Behavioral experiments

Optogenetic activations

Behavioral experiments started 4 to 5 weeks after the viral injection. Implanted animals were connected to a laser source (473 nm DPSS system, LaserGlow Technologies, Toronto, Canada) through a mating sleeve (Thorlabs). The laser was triggered by the output of a National Instruments interface (NI-USB 6211) and the timings of light activations were delivered using the NI MAX software. For CnF, RTN$^{Phox2b/Atoh1}$, PAG or IC long photostimulation, light was delivered in trains of pulses of 20 ms (5 to 20 Hz) and of 15 ms (30 and 40 Hz) frequency for a duration of 1 s. Each frequency stimulation was repeated three times with several minutes of rest between trials. We used the minimal laser power sufficient to evoke a response, which was measured to be between 5-12 mW at the fiber tip using a power meter (PM100USB with S120C silicon power head, Thorlabs) to restrict photoactivations unilaterally[46], prevent heat, and exclude an unintentional silencing by over-activation. For randomized short light-pulses, 50 ms light stimulations (50-70 pulses/experiment) were applied randomly in the respiratory cycles.

Plethysmography recordings

To analyze the effect of short photoactivations of the CnF, CnF fibers in the preBötC (Figure 2), RTN$^{Phox2b/Atoh1}$ (Figure 7), and PAG and IC (Figure S5) on burst timing, ChR2-injected animals were placed inside a hermetic whole-body plethysmography (WBP) chamber[58], customized to allow the passage of the optical patch-cord, four weeks after viral injection. The plethysmography signal was recorded over a period of 10 minutes using a National Instruments Acquisition card (USB-6211) and the LabScribe NI software (iWorxs).

Locomotion in a linear runway

Four to five weeks following the injection of the ChR2-expressing virus in the CnF, animals were implanted with a diaphragm EMG as explained previously (Figure 3). One week following EMG implantation, animals were placed in a linear corridor (80 x 10 cm), and familiarized for 1 h/day for 3 days prior to experiments. Implanted animals were filmed from the side at 200 fps and 0.5 ms exposure time using a CMOS camera (Jai GO-2400-USB) and images were streamed to a hard disk using the 2nd LOOK software (IO Industries). The start of the EMG recordings was hardware-triggered by the start of the video-recordings using the frame exposure readout of the video camera, so that the two recordings are synchronized. When animals were immobile at one end of the corridor and their respiration was stable, we delivered CnF optogenetic activations with frequencies ranging from 5 to 40 Hz. For each frequency, the stimulation was repeated three times with several minutes of rest between trials.

Chemogenetic silencing and treadmill experiment

Three weeks following the injection of the hM4Di virus in the RTN$^{Phox2b/Atoh1}$, animals were implanted for diaphragm EMG recordings as explained above (Figure 6). Non-injected C57BL/6J wild-type mice were also implanted as controls to test for CNO side effects (Figure S11). One week following EMG implantation, animals were familiarized on a stationary custom-made motorized treadmill with adjustable speed range (Scop Pro, France, belt dimensions: 6 cm x 30 cm) for 30 min/day for 3 days prior to the experiments. In

addition, implanted animals were exercised during this time for a total of 5 min at 40 cm/s each day. Mice could rest for 5 min after running before being placed back in their cage. This step was crucial to obtain stable running animals during experimental sessions. Following this short training, implanted mice were connected with custom light-weight cables to an AC amplifier (BMA-400, CWE Inc.) and neurograms were filtered (high-pass: 100 Hz, low-pass: 10 kHz), collected at 10 kHz using a National Instruments acquisition card (USB-6211) and live-integrated using the LabScribe NI software (iWorxs). Animals were first placed on the stationary treadmill to monitor basal respiration. Animals were then challenged to trot at 40 cm/s for 1.5 min before being administered intraperitoneally with CNO (Enzo Life science, ref. #: BML-NS105-0005) at 10 mg/kg[59] or saline (0.9 %). Animals were placed again on the treadmill with the same paradigm 2-3 h and 5 h after CNO or saline administration to measure respiration in resting and running conditions. During experiments, animals were filmed from the side in the same way as above to monitor the stability of running episodes.

Ex vivo brainstem-spinal cord experiments

Pups aged 1-2 days were used in all experiments. Neonates were anaesthetized with isoflurane, decerebrated and the brainstem still attached to the spinal cord was dissected and isolated in ice-cold Ringer's solution that contained (in mM): 111 NaCl, 3 KCl, 25 $NaHCO_3$, 1.25 $MgSO_4$, 1.1 KH_2PO_4, 2.5 $CaCl_2$ and 11 D-Glucose, and oxygenated in 95 % O_2, 5 % CO_2 to obtain a pH of 7.4. Isolated brainstem-spinal cords were transferred into a recording chamber and pinned to a Sylgard 184 resin. Preparations were partitioned in two compartments at the level of lower thoracic segments (T11) using a Vaseline wall, to restrict bath application of locomotor drugs on the lumbar spinal cord (Figure 5). The lumbar compartment was continuously perfused with the above Ringer's solution while the rostral compartment containing the brainstem was superfused with a Ringer's solution that contained (in mM): 111 NaCl, 8 KCl, 25 $NaHCO_3$, 3.7 $MgSO_4$, 1.1 KH_2PO_4, 1.25 $CaCl_2$ and 30 D-Glucose. All recordings were done at room temperature (25°C) after allowing 30 min recovery period after the dissection. Respiratory- and locomotor-like activities were recorded respectively on the 4th cervical (C4) and the 2nd lumbar (L2) ventral roots using extracellular suction glass pipettes (120F-10, Harvard Apparatus). Drug-evoked locomotor-like activities were induced by bath-applying 10 to 14 µM of N-methyl-D-aspartate (NMDA, Tocris) and serotonin (5-HT, Sigma-Aldrich, Figure 5), or using blue light on the lumbar spinal cord of ChR2-expressing pups (*Vglut2^{Cre}; ChR2^{floxed}*, Figure S9d-f). Signals were collected and band-passed filtered at 100 Hz to 1 kHz with an AC amplifier (Model 1700, A-M Systems) and live-integrated (Neurolog NL703, Digitimer) with a time constant of 100 ms (C4) or 200 ms (L2). Signals were sampled using Clampex 11 (Molecular Devices) at 5 kHz. To control for locomotor drugs leakage, some preparations were transected at the level of the cervical spinal cord (Figure S9a-c). For brainstem transection experiments, the rostral part of the brainstem containing the pF respiratory region was physically removed (Figure 5d-f). *Egr2^{Cre};Phox2b^{27AlaCKI}* pups were used to genetically eliminate RTN$^{Phox2b/Atoh1}$ neurons[57,58] (Figure 5g-i).

Quantifications and statistical analysis

Registration of CnF injection sites

To evaluate the extent of viral expression in the CnF and neighboring areas (anterograde tracing, Figure 1; photostimulations, Figures 2, 3), we registered the position of all infected cells using ImageJ Cell Counter plugin from one coronal plane at sites of injection. The position of reporter-positive cells from each coronal section as well as optic fiber placement are shown in Figure S1.

Axonal projection and cell quantifications

To quantify axonal projections from CnF (Figure 1g), lumbar (Figure 4e), and RTN$^{Phox2b/Atoh1}$ (Figure 7d) neurons to brainstem respiratory areas, we manually defined i) the pF region as immediately ventral, ventro-median, ventro-lateral and lateral to facial motor neurons[75] (bregma - 6.7 to -5.7 mm), and ii) the preBötC as a 400 x 400 µm square residing ventrally to the ChAT$^+$ nucleus ambiguus, where somatostatin$^+$ cells are detected[38] (bregma -7.0 to -7.4 mm). We used three rostro-caudal coronal sections from preBötC and/or pF and measured the number of fluorescent pixels per µm² bilaterally (Figures 1, 7) or unilaterally (Figure 4) using the ImageJ Measure plugin. All values were averaged across animals (3 sections/animal) and a grand mean ± SD across n animals was calculated per hemi-section.

To evaluate the rostro-caudal organization of projections and transfected cells within the pF, we delineated pF subregions as follows: bregma -5.7 (rostral), -6.1 (intermediate), and -6.7 (caudal, see Figure 4f). Each pF subregion was further divided into lateral vs medial portions. We used one coronal section per subregion per animal to quantify i) projections from the lumbar spinal cord (Figure 4f) using ImageJ Measure plugin, and ii) the number of infected pF (Figure 4i) and RTN$^{Phox2b/Atoh1}$ (Figures 6b, 7b) neurons using ImageJ Cell Counter. All values were averaged across animals and a grand mean ± SD across n animals was calculated per hemi-section.

To assess the rostro-caudal distribution of transfected cells in the spinal cord (Figure 4b), we used one coronal section from seven segments of the spinal cord: the 12th (T12) and 13th (T13) thoracic, and the 1st to 5th lumbar (L1 to L5) segments. Cells were counted using ImageJ Cell Counter. All values were averaged across animals (1 section/animal) and a grand mean ± SD across n animals was calculated per hemi-section.

Phase-shift analysis

The durations of the respiratory cycle containing the light stimulus (perturbed cycle, θ) and the previous respiratory cycle (control cycle, ϕ, Figures 2 and 7) were measured. One respiratory cycle was defined from the onset of inspiration to the subsequent inspiratory onset. The phase of light-stimulation ϕ_S was defined from the onset of the perturbed cycle to the onset of the light pulse. The perturbed cycle θ was defined as from the onset of the inspiration that precedes the light stimulation to the onset of the subsequent inspiration. The perturbed phase (phase-shift) was calculated as the ratio of the perturbed cycle divided by the control cycle (θ/ϕ). The light phase was defined as the ratio of the stimulated cycle divided by the control

cycle (ϕ_s/ϕ). The perturbed phase was then plotted against the light phase for all events from all animals. A phase shift <1 (perturbed cycle duration lower than the control one) indicates a shortening of the respiratory cycle, a phase shift >1 (perturbed cycle duration higher than the control) indicates a lengthening, and a phase shift equal to 1 (perturbed cycle duration equal to the control) indicates no effect. The number of events (N) and animals (n) are given in the corresponding figures for all tested condition. In addition, the average perturbed phase was plotted against the average light phase in 0.1 ms bins as mean ± SD. Inspiratory time (I) was measured, averaged for each animal and a grand average was calculated and annotated in the corresponding figures for all tested condition. Expiratory time (E) was calculated from respiratory cycle and inspiratory (I) times.

Locomotor parameters analysis

To track the mouse displacement and measure its speed, we used DeepLabCut (version 2.1.5.2, [47]) and manually labelled the positions of the head from 50 frames of each video. We then used 95 % of the labelled frames to train the network using a ResNet-50-based neural network with default parameters for 3 training iterations. This network was then used to analyze videos from similar experimental settings. For treadmill experiments (Figure 6), the head X coordinate was used as a control for running stability on the treadmill. For CnF stimulations on the corridor (Figure 3), the head X coordinate was used to calculate the animal's speed s_x using the gradient over time.

$$\overrightarrow{s_x} = \frac{\partial \vec{x}}{\partial t}, \vec{x}\ being\ the\ displacement\ of\ the\ head\ along\ the\ x\ axis$$

Head X coordinate (treadmill) and calculated velocity (corridor) were then exported to Clampfit (Molecular Devices) and interpolated to 10 kHz to match the acquisition framerate of diaphragmatic EMG recordings. Both sets of signals (head X and diaphragm, or speed and diaphragm) were merged in single files, before being processed offline in Clampfit. The animal's instantaneous speed is illustrated on Figure 3. The mean speed, defined from movement onset to the end of the photostimulation, was then calculated using the statistic function in Clampfit for each CnF stimulation (5 to 40 Hz). All values were averaged across trials for each animal (3 trials/animal), and a grand mean ± SD across n animals was calculated per stimulation frequency (Figure S6b).

Locomotor onset delay (Figure S6c) were defined as latency between the onset of the CnF stimulation and the onset of movement for each CnF stimulations. All values were averaged across trials (3 trials/animal) and a grand mean ± SD across n animals was calculated per stimulation frequency.

For gait analysis during CnF photostimulations (Figure S6d), we manually annotated the paw of a reference hindlimb (ipsilateral) and registered the timings of footfalls (when the paw first touches down). Each reference locomotor cycle was then defined as the duration from one footfall (ipsi_FF_n) to the next

(ipsi_FF$_{n+1}$). The time of occurrence of the contralateral hindlimb footfall within the reference locomotor cycle was annotated manually (contra_FF) and the synchronicity rate was then computed as follows:

$$synchronicity\ rate = \frac{t_{contra\_FF} - t_{\text{ipsi\_FFn}}}{t_{\text{ipsi\_FFn+1}} - t_{\text{ipsi\_FFn}}}$$

A custom MATLAB script was used to categorize synchronized (synchronicity rate $\in$[0, 0.25[$\cup$[0.75, 1]) or alternated (synchronicity rate $\in$[0.25, 0.75[) ipsi- and contralateral hindlimb steps. Synchronicity rates were averaged across animals (3 trials/animal) and a grand mean ± SD across n animals was calculated per stimulation frequency.

Locomotor/respiratory coordination

The temporal coordination of breaths to strides (Figure S7) was represented with circular statistics, similarly to what we performed recently[4] and imprinting from numerous studies having investigated the cycle-to-cycle correlations of motor activities[53,54,76]. The phase of each individual inspiratory burst within the locomotor cycle (ΦInsp, around 15 bursts) is represented as position, from 0 to 1, of diamond marks on the outer circle (see Figure S7d). For each animal, we also computed the mean phase of consecutive inspiratory bursts and represented it as a colored circle (the mean phases of different animals are in different colors). The distance R of the mean phase to the center of the circle indicates the concentration of individual phase values around the mean, as established by [54]. If inspiratory and locomotor movements are temporally correlated, then individual phase values will be concentrated around a preferred phase value (for instance 0 or 1, at the top of the circle, if the two motor activities were in phase). The mean value would then be positioned at a significant distance from the center. Conversely, if inspiratory and locomotor movements are not coupled, individual phases will be evenly distributed across the circle. Consequently, the mean phase value will be at a short distance from the diagram center, illustrating the dispersion of values around the mean. The inner circles of the circular diagrams depict the threshold for mean phase values to be considered significantly oriented (R < 0.3) as commonly done [4,53,54,76]. Circular plots were obtained using a custom macro in Excel.

In vivo respiratory changes analysis

To analyze breathing changes resulting from CnF (EMG recordings; Figure 3), RTN$^{Phox2b/Atoh1}$, PAG and IC photostimulation (WBP recordings; Figures 7, S5), instantaneous inspiratory frequencies and amplitude were detected over a 1 s window, using the threshold search in Clampfit before, during and directly after a 1 s light stimulation for all frequencies (5 to 40 Hz). For CnF stimulations that triggered locomotor episodes (15 to 40 Hz), the recovery period was measured as soon as the animal returned to immobility. Breaths detected from the onset of the light stimulus to the onset of movement were categorized as “pre-loco” phase (Figure 3d-e). Breaths detected from movement onset to the offset of the light stimulus were categorized as “loco”

phase (Figure 3d, f). All values were averaged across animals (3 trials/animal) and a grand mean ± SD across n animals was calculated per stimulation frequency.

For treadmill running (Figure 6), the mean diaphragm frequency was analyzed prior to exercise (resting condition) and from stable trotting moments, i.e., when the animal's speed was in phase with the treadmill, inferred by the absence of changes in head's X coordinates (running condition). For each condition, i.e., before (CTL), during (CNO/saline) and after (REC) administration of either CNO or saline, we measured instantaneous respiratory frequency and amplitude using the threshold search in Clampfit. Inspiratory (Ti) and expiratory (Te) times were quantified manually before (CTL), during (CNO/saline) and after (REC) administration of either CNO or saline. These measurements were done using 2 to 3 windows of 6 s each taken during resting conditions and at any stable moment of the 1.5 min run (excluding the first 20 seconds to avoid possible stress-induced changes when the treadmill is just engaged). Measurements were averaged to give the mean value for each animal. Averaged mean values were expressed as mean ± SD across n animals.

Ex vivo respiratory-like activities analysis

Instantaneous respiratory-like frequencies were analyzed offline using the threshold search in Clampfit (Molecular Devices) before, during and after bath application of NMDA and 5-HT (Figure 5). Respiratory frequency changes during drug and washout conditions were normalized and expressed as a percent of control values. A grand mean ± SD across n animals was calculated.

Statistical Analysis

All data are expressed as mean ± SD. Statistical tests were performed using GraphPad Prism 7 and are spelled out in figure legends, as well as the number of trials (N) and animals (n) used for each experiment. Changes were considered as not significant (ns) when $p > 0.05$ and as significant when $p < 0.05$. Significance levels are reported between conditions (*) and with control condition (§; Figure 7) as follows: * or §, $p < 0.05$; ** or §§, $p < 0.01$; *** or §§§, $p < 0.001$; and **** or §§§§, $p < 0.0001$.

Acknowledgements

This work was funded by Agence Nationale de la Recherche (ANR-17-CE16-0027 and ANR-20-CE16-0026 to JB and ANR-15-CE16-013-02 to GF) and CNRS, Université Paris-Saclay and NeuroPSI. CH held a doctoral fellowship from Région Ile-de-France. CH and GU held a fellowship extension from Fondation pour la Recherche Médicale (contract FDT201904007982 to CH and FDT202106013165 to GU). We thank Aurélie Heuzé for lab management and genotyping animals, Edwin Gatier for help with DeepLabCut and analytic scripts, Jean-François Brunet for providing the *Atoh1*^{FRTCre}*; Phox2b*^{Flpo} animals, and the NeuroPSI animal facility for housing animals.

Author Contributions

JB and GF designed the study and provided funding. JB supervised the work. CH performed and analyzed all experiments with contributions from SD and JB. GU contributed to the revision work. CH and JB prepared figures. JB wrote the paper and CH and GF contributed to its editing.

Competing Interests

The authors declare no competing interests.

Data Availability

The data that support the findings of this study will be made available in the Source Data provided with the paper. Microscopy data are available from the corresponding author upon reasonable request.

719 **Figures and legends**

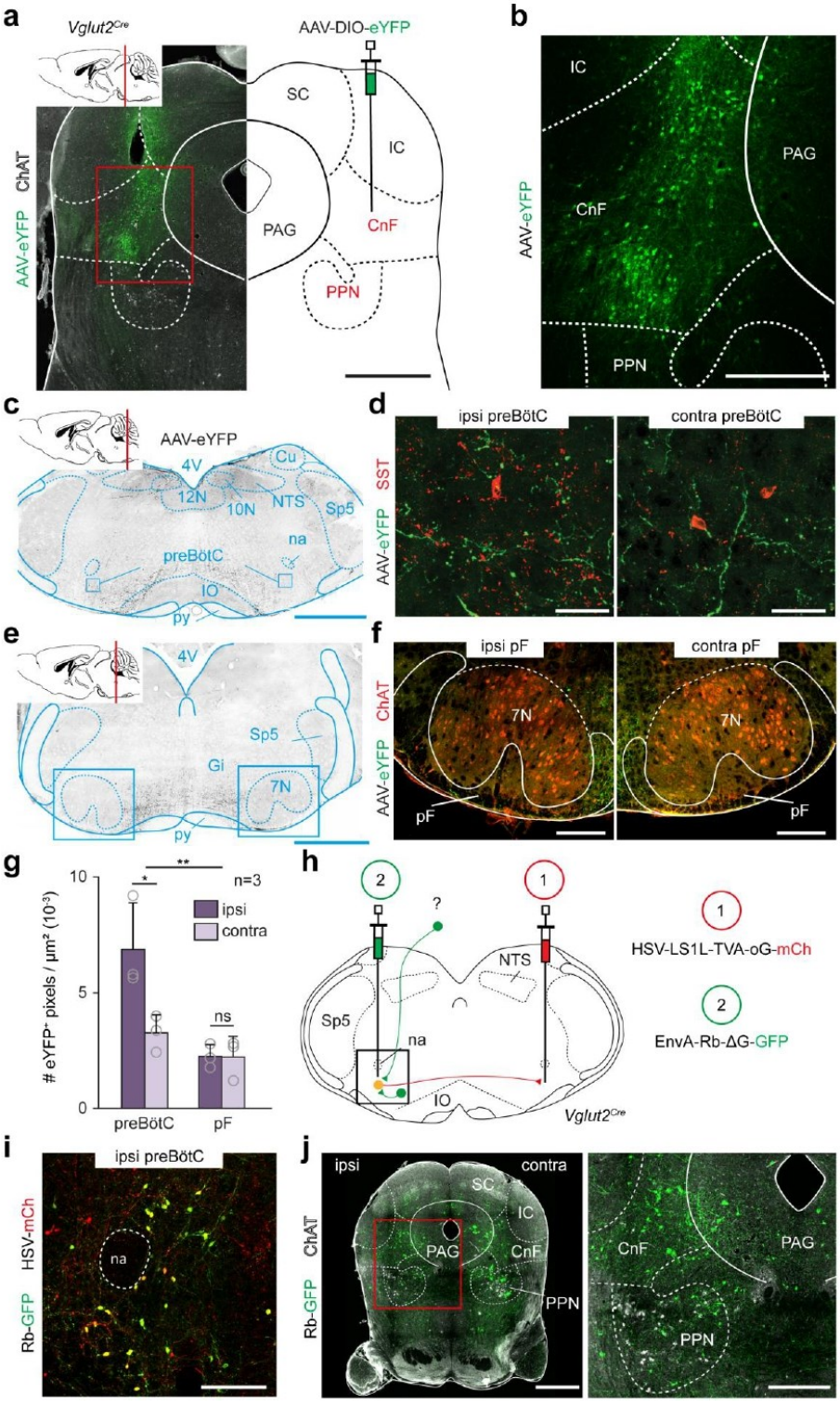

Figure 1: CnF glutamatergic neurons contact the preBötC inspiratory generator.

(a) Transverse section showing the experimental strategy for tracing glutamatergic (Glut$^+$) CnF projections in *Vglut2^{Cre}* adult mice. Cholinergic PPN neurons are identified by Choline Acetyl Transferase (ChAT) expression. Scale bar, 1 mm.

(b) Magnification showing transfected eYFP$^+$ cells concentrated in the CnF. Scale bar, 400 µm.

(c) Transverse section in the caudal medulla showing CnF projections in the ventral reticular formation including the preBötC. Scale bar, 1 mm.

(d) Magnifications over ipsilateral and contralateral preBötC containing somatostatin-expressing (SST$^+$) cells. Note that the CnF projects to both sides with an ipsilateral predominance. Scale bar, 40 µm.

(e) Transverse section in the rostral medulla showing the distribution of CnF projections at the level of the pF respiratory area. Scale bar, 1 mm.

(f) Magnifications over ipsilateral and contralateral pF areas delineated around Choline Acetyl Transferase (ChAT$^+$) facial motoneurons (7N). Note that Glut$^+$ CnF neurons project very little to the pF area. Scale bar, 250 µm. Panels (**a-f**) are representative of n=3 animals.

(g) Mean density ± SD of eYFP$^+$ fluorescent pixels in the preBötC and the pF areas on either side. Gray open circles are mean values of n individual mice. **, $p < 0.01$; *, $p < 0.05$; ns, not-significant (Wilcoxon matched-pairs tests; preBötC and pF: 9 sections per side).

(h) Experimental design for retrograde transsynaptic monosynaptic tracing from Glut$^+$ commissural preBötC neurons in *Vglut2^{Cre}* adult mice. An HSV-LS1L-TVA-oG-mCherry is first injected in the contralateral preBötC followed by a G-deleted and EnvA pseudotyped rabies virus (EnvA-ΔG-Rb-GFP) in the ipsilateral preBötC.

(i) Magnification over the ipsilateral preBötC showing double-transfected "starter" cells. Scale bar, 200 µm.

(j) *Left*: transverse section at the MLR level showing putative presynaptic cells (Rb-GFP$^+$). Scale bar, 1 mm. *Right*: magnification showing Rb-GFP$^+$ cells in CnF and PPN. Scale bar, 250 µm. Panels (**h, j**) are representative of n= 3 animals.

See also Figures S1, S2.

Abbreviations used in all figures: PAG: periaqueductal gray; IC: inferior colliculus; SC: superior colliculus; PPN: pedunculopontine nucleus; CnF: cuneiform nucleus; 4V: fourth ventricle; 10N: dorsal motor nucleus of vagus ; 12N: hypoglossal motor nucleus; NTS: nucleus tractus solitarius; py: pyramidal tract; IO: inferior olive; Cu: cuneate nucleus; na: nucleus ambiguus; preBötC: pre-Bötzinger complex; pF: parafacial respiratory area; Sp5: spinal trigeminal nucleus; 7N: facial nucleus; Gi: gigantocellular reticular nucleus.

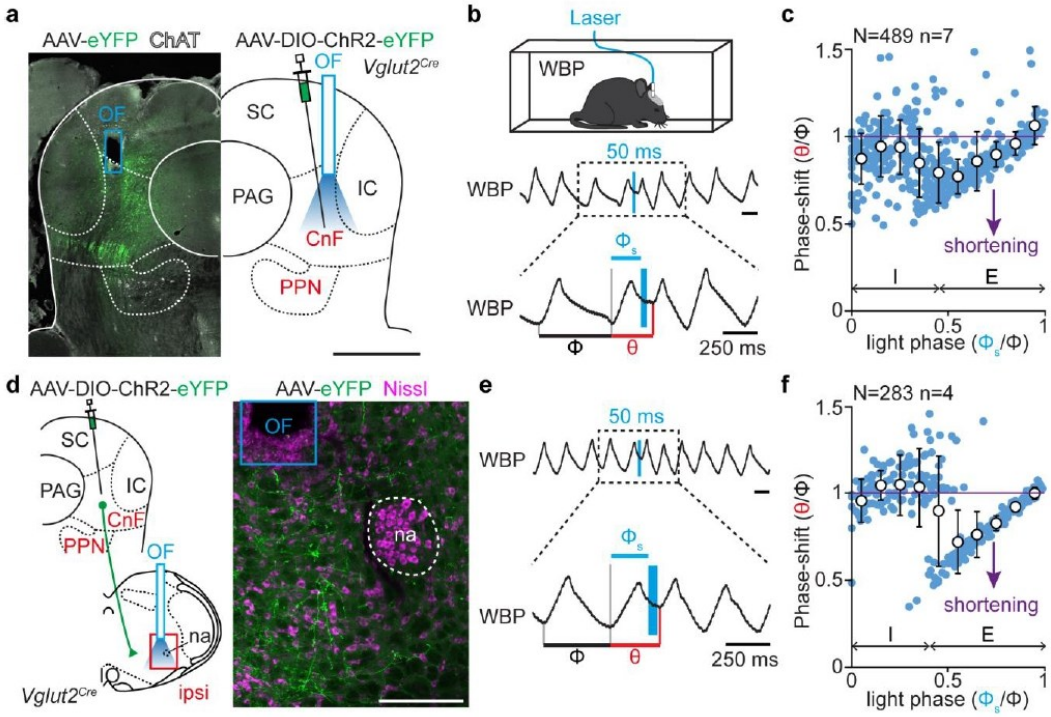

748 **Figure 2: Photoactivation of glutamatergic CnF neurons impacts respiratory rhythm generation in the preBötC.**

749 **(a)** Transverse section showing the experimental strategy for photostimulating Glut$^+$ CnF neurons in *Vglut2^{Cre}* adult mice.
750 ChAT, Choline Acetyl Transferase. Scale bar, 1 mm.

751 **(b)** *Top*: setup for recording ventilation using whole-body plethysmography (WBP) during CnF optogenetic activations.
752 *Middle*: WBP recordings around a single 50 ms light pulse (vertical blue bar) of Glut$^+$ CnF neurons during the expiratory
753 phase of one respiratory cycle (inspirations are upwards, expirations are downwards). Note that the stimulation
754 shortens the respiratory cycle. *Bottom*: magnification showing the control cycle (ϕ, black), the phase of light-simulation
755 (ϕ_s, blue), and the perturbed cycle (θ, red).

756 **(c)** Plot of the phase-shift (perturbed cycle normalized to control cycle: θ/ϕ) as a function of the phase of light-
757 stimulation normalized to the control cycle (ϕ_s/ϕ). Values < 1 (purple line) indicate a shortening of the perturbed cycle.
758 Inspiration (I) and expiration (E) mean durations are indicated. Note that the phase-shift is shortened when the light
759 pulse occurs during expiration. Blue circles represent individual data from N random trials from n mice. White circles
760 are averages ± SD across all trials within 0.1 ms bins.

761 **(d)** *Left*: experimental strategy for photostimulation of Glut$^+$ CnF fibers in the ipsilateral preBötC in *Vglut2^{Cre}* adult mice.
762 *Right*: transverse section at the level of the preBötC showing CnF eYFP$^+$ projections and optic fiber placement in the
763 preBötC. Scale bar, 200 µm

764 **(e-f)** Same as in (**b-c**) during a single 50 ms light-stimulation of CnF projections to the ipsilateral preBötC. Note that the
765 respiratory cycle is shortened when light is delivered during expiration. N random trials from n mice. See also Figures
766 S3, S4, S5.

767

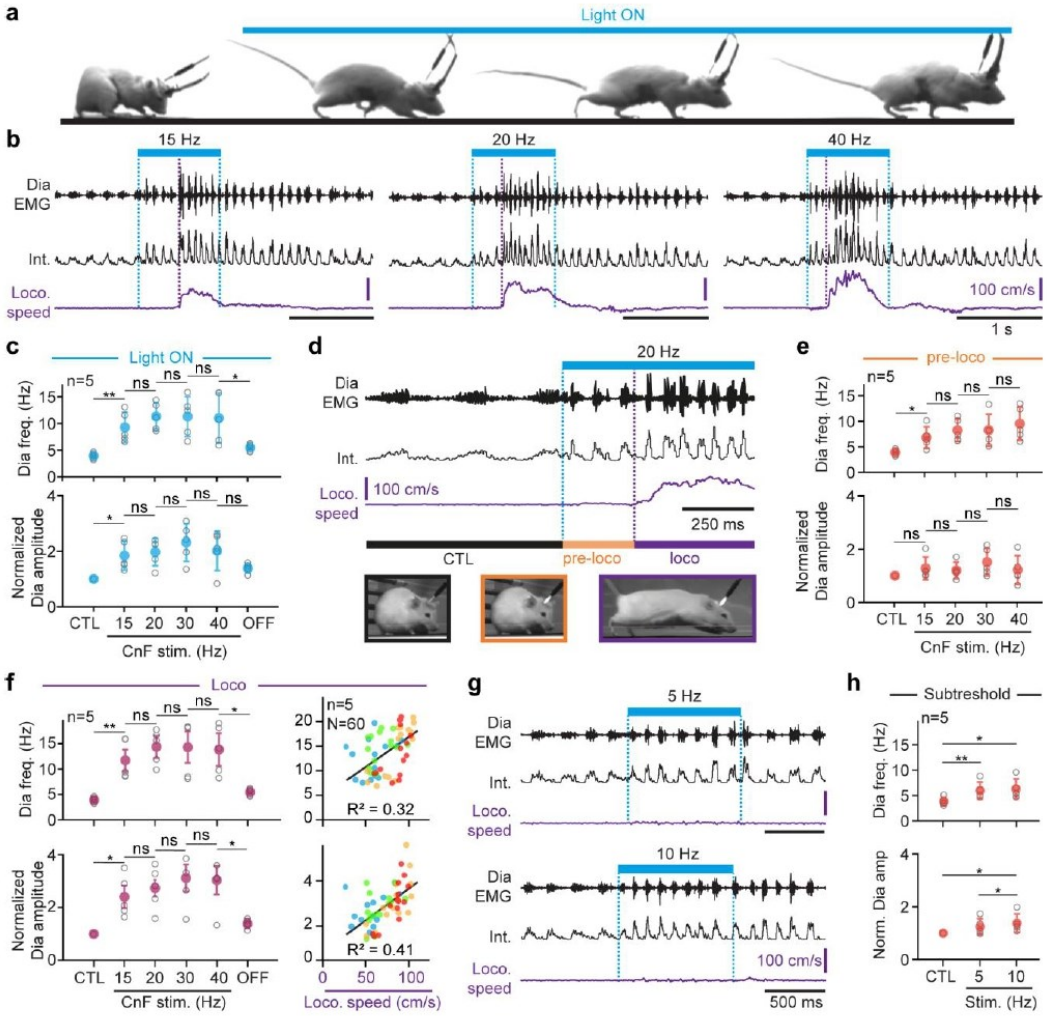

Figure 3: Glutamatergic CnF neurons upregulate breathing in synergy with, and even in the absence of, locomotion.

(a) Photostimulation of Glut$^+$ CnF neurons for 1 s at 20 Hz triggers running. Injection and implantation strategies are similar to Figure 2a.

(b) Raw (DiaEMG) and integrated (Int.) electromyogram of the diaphragm and instantaneous locomotor speed during 1 s CnF photostimulations at 15, 20 and 40 Hz. Note that breathing frequency increases at light onset, before the animal starts running, and increases further upon running.

(c) Quantification of diaphragmatic frequency and amplitude at rest (CTL), during 1 s CnF photostimulation at increasing frequencies, and following light offset (OFF). Amplitudes are normalized to CTL.

(d) Enlarged EMG recording of one representative animal in CTL and during 1 s CnF photostimulation at 20 Hz. In the "pre-loco" phase, the animal remains still, while during "loco" phase the animal engages in running.

(e) Quantification of diaphragmatic frequency and amplitude in CTL and during the "pre-loco" phase at increasing CnF photostimulation frequencies.

(f) *Left*: similar quantifications during the "loco" phase. *Right*: color plot showing diaphragm frequency and normalized amplitude in relation to locomotor speed. Note that 32 % of inspiratory frequency and 41 % of the amplitude correlate with locomotor speed (R^2).

(g) Example EMG recordings from one representative animal during CnF photostimulations at 5 and 10 Hz. Note that while such subthreshold stimulations do not initiate running, breathing frequency and amplitude increase.

(h) Quantifications of diaphragm frequency and amplitude in CTL and during subthreshold CnF stimulations.

In all graphs, gray open circles are means of 3 trials per animal and colored circles are means ± SD across n mice. ns, not significant. *, $p < 0.05$, **, $p < 0.01$ between stimulation frequencies. (matched-pairs t-tests).
See also Figures S1, S4, S5, S6 and S7.

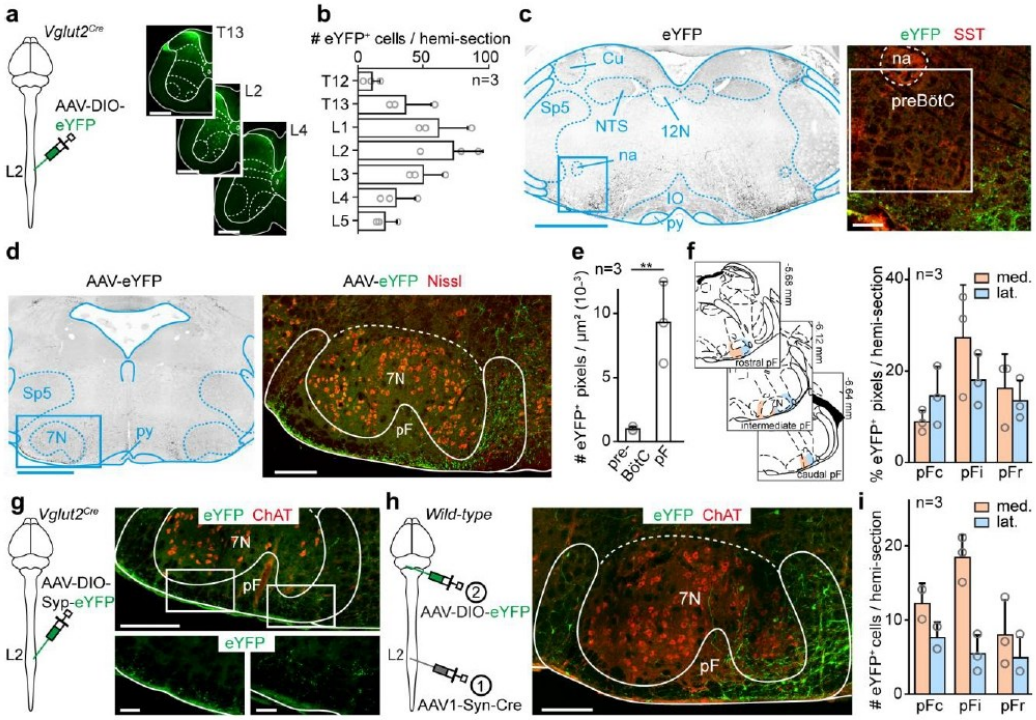

Figure 4: Glutamatergic lumbar spinal cord neurons contact the pF respiratory area.

(a) *Left*: experimental strategy for labelling projections of Glut$^+$ thoraco-lumbar neurons bilaterally in *Vglut2^{Cre}* adult mice. *Right*: transverse sections at the level of thoracic (T13) and lumbar (L2, L4) segments showing transfected spinal neurons. Scale bars, 500 µm.

(b) Bar-graphs showing the distribution (mean number ± SD per hemi-section) of eYFP$^+$ transfected spinal cells in different thoraco-lumbar segments. Gray open circles are mean values of n individual mice.

(c) *Left*: transverse section at the preBötC level showing eYFP$^+$ spinal projections. Scale bar, 1 mm. *Right*: magnification of the preBötC area containing SST$^+$ cells. Note the absence of spinal projections. Scale bar, 100 µm.

(d) Transverse brainstem section at the level of the pF showing eYFP$^+$ spinal projections. Scale bar, 1 mm. *Right*: magnification showing abundant eYFP+ spinal projections in the pF area, ventrally and ventro-medially to the 7N motoneurons.

(e) Mean density ± SD across n mice of eYFP$^+$ fluorescent pixels in preBötC and pF hemi-sections. Gray open circles are the mean values of individual mice. **, $p < 0.01$ (Wilcoxon matched-pairs tests; 9 sections per area).

(f) *Left*: delineation of rostro-caudal (from top to bottom) and medio-lateral (orange and blue) subdivisions of the pF. *Right*: distribution of fluorescent pixels in the different pF subdivisions. Bars are means ± SD across n mice and gray open circles are mean values of individual mice. See methods for details.

(g) *Left*: experimental strategy for labelling synaptic boutons of Glut$^+$ thoraco-lumbar neurons in *Vglut2^{Cre}* adult mice. Injections were done bilaterally. *Right*: transverse section showing putative synaptic boutons in the pF area. Scale bars, 250 (top) and 50 (bottom) µm.

(h) *Left*: experimental strategy for labelling pF neurons contacted by spinal neurons through anterograde transsynaptic transfer of an AAV1-Syn-Cre in adult *wild-type* mice. Injections were done bilaterally. *Right*: transverse section showing eYFP$^+$ neurons in the pF area demonstrating that spinal ascending projections make synaptic contacts with pF neurons. Representative of n = 3 mice. Scale bar, 200 µm.

(i) Quantification of transsynaptically labelled neurons in the pF subdivisions defined in (**f**). See methods for details.

See also Figure S8.

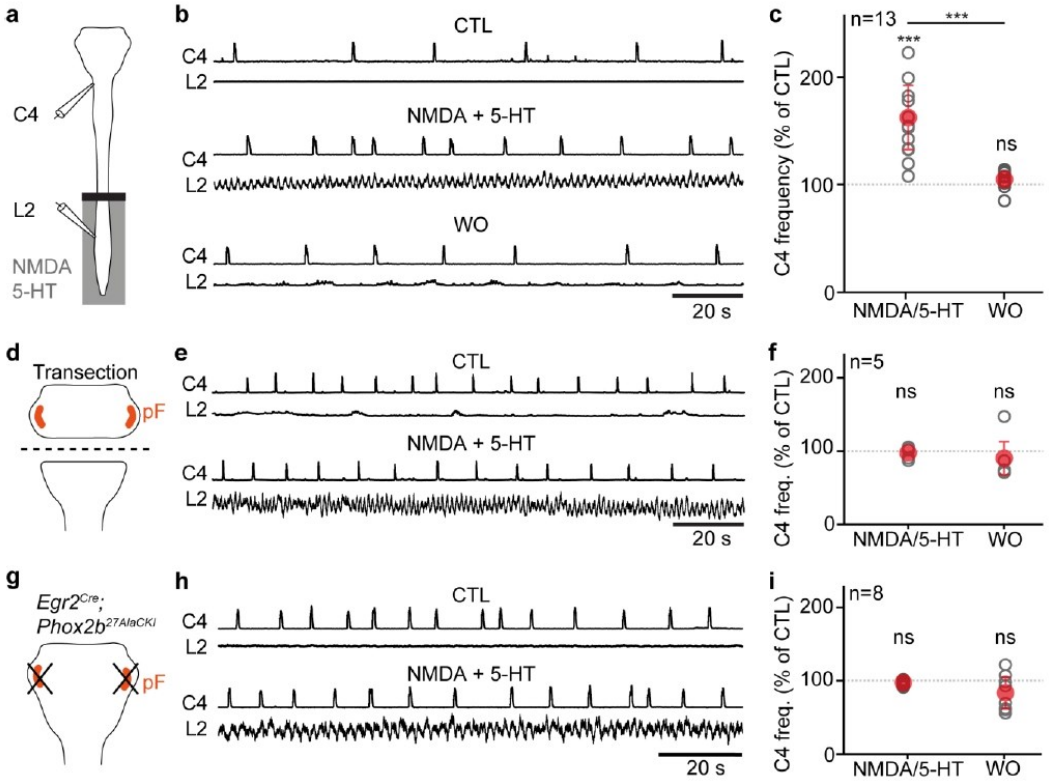

Figure 5: Pharmacological activation of locomotor-like activities increases inspiratory-like frequencies *ex vivo*, which requires RTN$^{Phox2b/Atoh1}$ integrity.

(a) Experimental strategy for recording respiratory- (C4) and locomotor-like (L2) motor activities on isolated *ex vivo* brainstem-spinal cord neonatal preparations. The lumbar spinal cord compartment is superfused with control or locomotor drugs enriched (NDMA and 5-HT) aCSF while the brainstem compartment remains in control aCSF.

(b) Recordings of C4 and L2 integrated activities of one representative preparation before (CTL), during (NMDA/5-HT), and after (WO) perfusion of locomotor drugs in the lumbar spinal cord compartment. Note that C4 frequency increases when locomotor-like activities are triggered.

(c) Quantification of the C4 frequency change (percent change to CTL) during and after drug-induced locomotor-like activity.

(d-f) Similar experiments as in (**a-c**) in preparations that underwent a brainstem transection to physically remove the pF respiratory area. No change of respiratory-like activity is seen during the application of locomotor drugs on the lumbar compartment.

(g-i) Similar experiments as in (**a-c**) performed in *Egr2^{Cre};Phox2b^{27AlaCKI}* neonates. These lack pF neurons that express *Phox2b* and are derived from rhombomere 5, a genetic intersection that recapitulates the genetically-defined RTN$^{Phox2b/Atoh1}$. No change of respiratory-like activity is seen during the application of locomotor drugs on the lumbar compartment.

In all graphs, gray open circles are means of individual preparations, and red circles are means ± SD across n preparations. ***, $p < 0.001$; ns, not significant (Wilcoxon matched-pairs tests).

See also Figures S9 and S10.

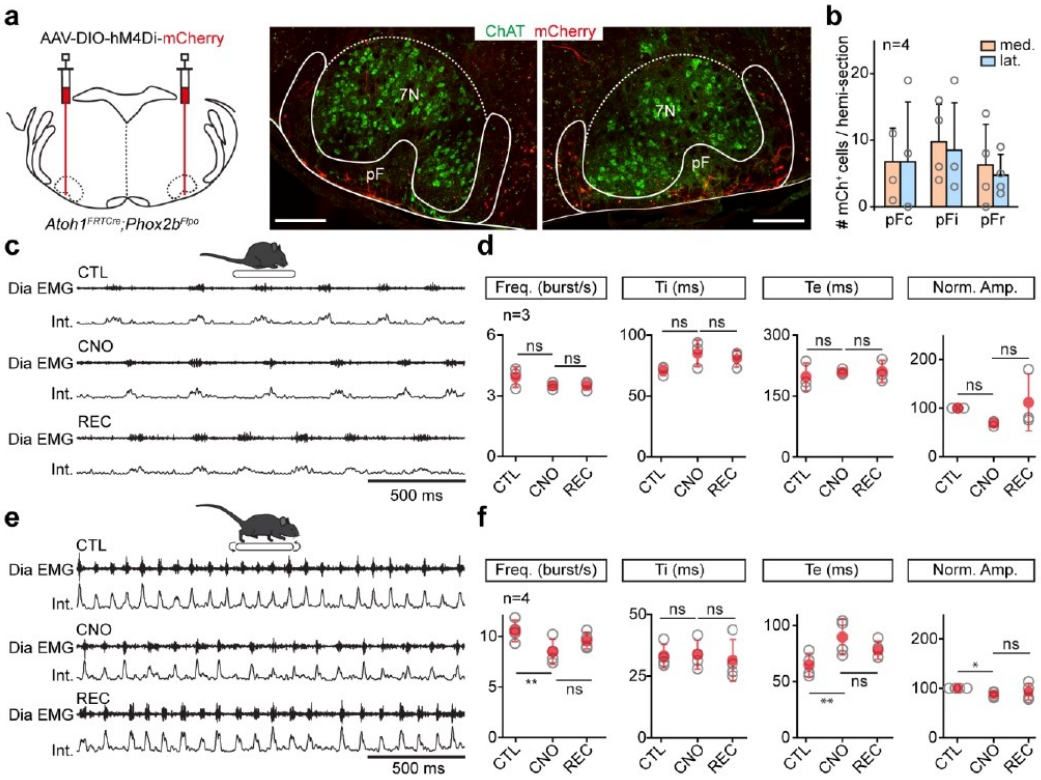

Figure 6: Silencing RTN$^{Phox2b/Atoh1}$ neurons reduces respiratory frequency during running.

(a) *Left*: experimental strategy for silencing RTN$^{Phox2b/Atoh1}$ neurons bilaterally using the virally-driven inhibitory DREADD receptor hM4Di in *Atoh1*^{FRTCre};*Phox2b*^{Flpo} adult mice. *Right*: transverse sections showing bilaterally transfected neurons in the pF area around the 7N motoneurons identified by Choline Acetyl Transferase (ChAT) expression. Scale bar, 250 µm.

(b) Number and distribution of transfected (mCherry^{+}) neurons across pF subregions as defined in Figure 4f. Bars are means ± SD across n mice and gray circles are mean values of individual mice. See methods for details.

(c) Raw (DiaEMG) and integrated (Int.) recordings of diaphragm activity of one representative animal at rest before (CTL), during (CNO), and after (REC) administration of CNO at 10 mg/kg.

(d) Quantification of respiratory parameters before, during and after CNO administration: frequency, inspiratory (Ti) and expiratory (Te) times, and normalized amplitude. Note that silencing RTN$^{Phox2b/Atoh1}$ neurons does not alter basal respiratory parameters.

(e, f) Similar representations as in (**c, d**) in mice running on a treadmill at 40 cm/s. Note the significantly lower diaphragm frequency and increased expiratory time (Te) when RTN$^{Phox2b/Atoh1}$ neurons are silenced.

In all graphs, grey open circles are means of individual mice and red circles are means ± SD across n mice. ns, not significant. **, $p < 0.01$ (Wilcoxon matched-pairs test in **d** and paired t-test in **f**).

See also Figure S11.

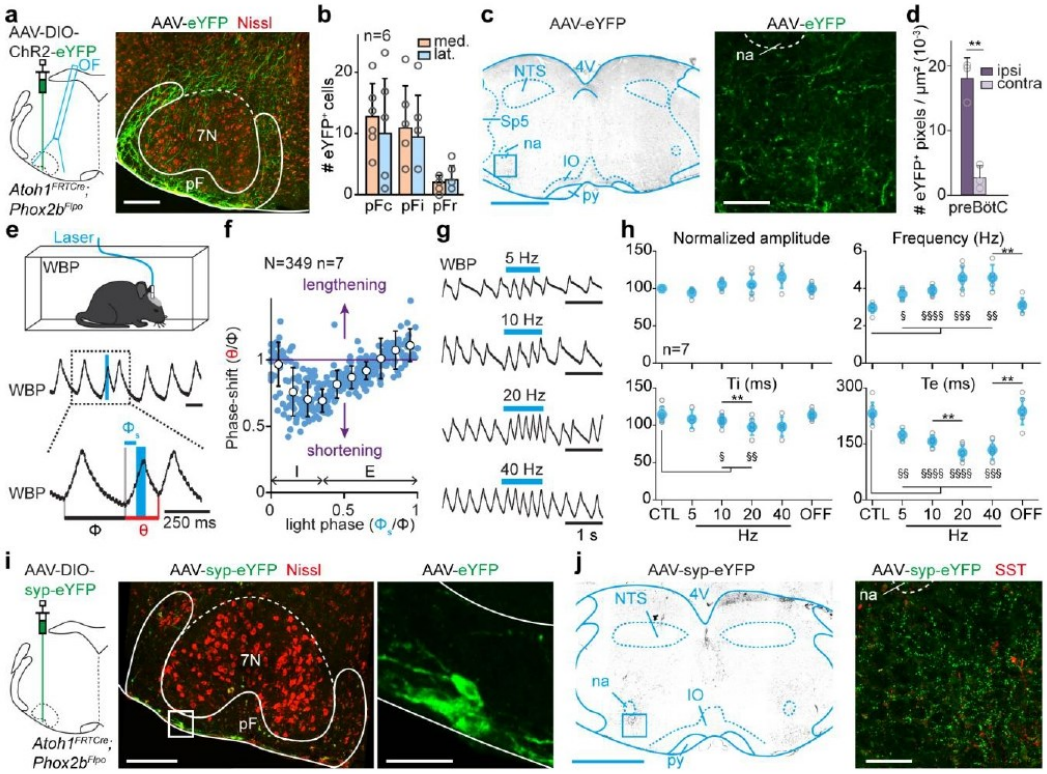

Figure 7: RTN$^{Phox2b/Atoh1}$ neurons contact the preBötC and impact respiratory rhythm generation.

(a) *Left*: experimental strategy for labelling and photoactivating RTN$^{Phox2b/Atoh1}$ neurons unilaterally in *Atoh1*^{FRTCre};*Phox2b*^{Flpo} adult mice. *Right*: transverse section showing unilaterally transfected RTN$^{Phox2b/Atoh1}$ somas. Scale bar, 250 µm.

(b) Number and distribution of transfected eYFP$^+$ neurons across pF subregions as defined in Figure 4f. Bars are means ± SD across n mice and gray circles are mean values of individual mice. See methods for details.

(c) *Left*: transverse section at the preBötC level showing eYFP$^+$ projections from RTN$^{Phox2b/Atoh1}$ neurons. Scale bar, 500 µm. *Right*: magnification of the preBötC area showing abundant eYFP$^+$ projections. Scale bar, 100 µm.

(d) Density and distribution of eYFP$^+$ projections in ipsilateral and contralateral preBötC. Bars are means ± SD across n mice and gray circles are mean values of individual mice. **, $p < 0.01$ (Wilcoxon matched-pairs test).

(e) *Top*: setup for recording ventilation using whole-body plethysmography (WBP) during optogenetic activations of RTN$^{Phox2b/Atoh1}$ neurons (inspirations are upwards, expirations are downwards). *Middle*: WBP recordings around a single 50 ms light-stimulation of RTN$^{Phox2b/Atoh1}$ neurons during inspiration. Note that RTN$^{Phox2b/Atoh1}$ stimulation shortens the respiratory cycle. *Bottom*: magnification showing control cycle (ϕ, black), the phase of light-simulation (ϕ_s, blue), and perturbed cycle (θ, red).

(f) Plot of the phase-shift (perturbed cycle normalized to the control cycle: θ/ϕ) as a function of the phase of light-stimulation normalized to the control cycle (ϕ_s/ϕ). Inspiration (I) and expiration (E) mean durations are indicated. Note that the phase-shift is shortened (values < 1, purple line) when the light pulse occurs in the mid-I/early-E and lengthened (values > 1) during late-E. Blue circles represent individual data from N random trials from n mice. White circles are averages ± SD across all trials within 0.1 ms bins.

(g) WBP recordings of ventilation during photoactivation of RTN$^{Phox2b/Atoh1}$ neurons at increasing train frequencies.

(h) Quantification of the respiratory parameters before (CTL), during and after (OFF) photostimulations of RTN$^{Phox2b/Atoh1}$ neurons at different frequencies: normalized amplitude, frequency, inspiratory (Ti) and expiratory (Te) times. Gray open circles are means of 3 trials for individual animals and filled colored circles are means ± SD across n mice. Statistics

between frequencies (*) or compared to CTL (§) are depicted as follows: * or §, $p < 0.05$; ** or §§, $p < 0.01$, §§§, $p < 0.001$; §§§§, $p < 0.0001$ (Amplitude: Wilcoxon matched-pairs test; frequency, Ti and Te: paired t-tests).

(i) *Left*: experimental strategy for labelling the synaptic contacts of $RTN^{Phox2b/Atoh1}$ neurons using a virally-driven synaptophysin-eYFP fusion protein injected unilaterally (syp-eYFP). *Middle*: transverse section showing transfected $RTN^{Phox2b/Atoh1}$ somas in the pF area. Scale bar, 250 µm. *Right*: magnification of $RTN^{Phox2b/Atoh1}$ transfected somas. Scale bar, 50 µm. Representative of n=4 animals.

(j) *Left*: transverse section at the preBötC level. Scale bar, 1 mm. *Right*: magnification of the preBötC area. Note the abundant $eYFP^+$ synaptic contacts of $RTN^{Phox2b/Atoh1}$ neurons. Scale bar, 100 µm.

See also Figure S12.

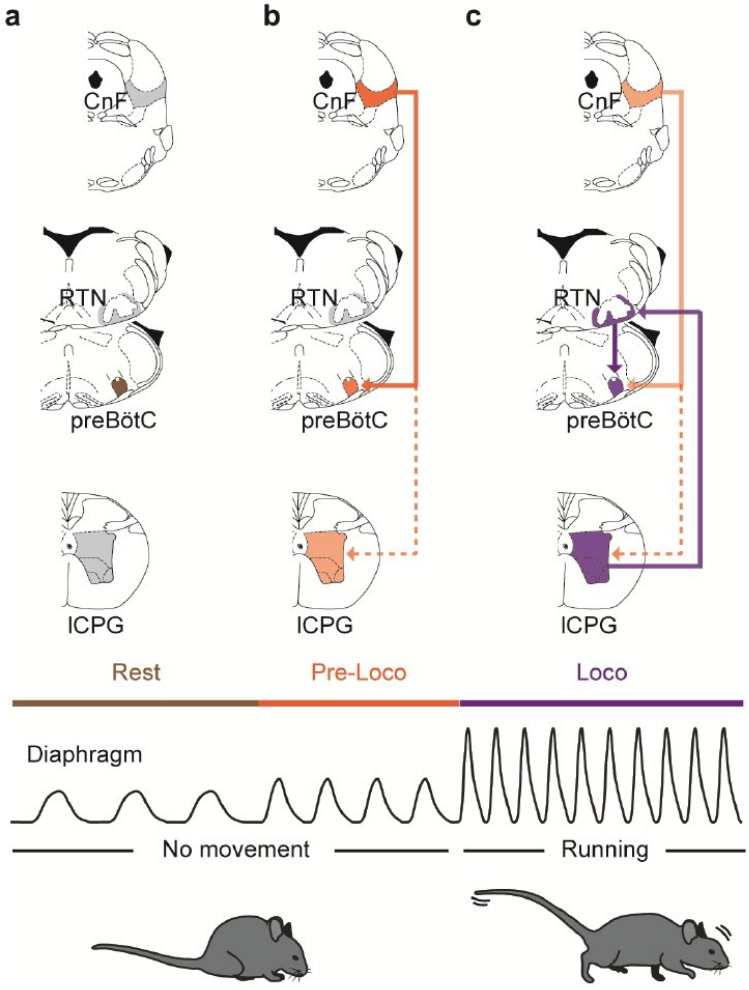

Figure 8: Graphical representation of revealed circuits.

(a) At rest, and in the absence of locomotor initiation signal from the CnF to the locomotor central pattern generator (lCPG), the preBötC drives the basal inspiratory rate.

(b) CnF activation leads to an augmented ventilation before the animal engages in effective running. This "pre-loco" phrase is attributed to the CnF sending a direct and rapid activatory signal to the preBötC (thick line). In contrast, the CnF signal crosses multiple synapses before reaching the locomotor CPG[16,63] (dashed line), which may support a longer latency to locomotor onset.

(c) CnF activation eventually leads to a running episode, during which ventilation is augmented further. This effect is attributed to the activated lCPG sending direct projections to the pF respiratory area, and in particular to the RTN$^{Phox2b/Atoh1}$ neurons, which in turns contact and activate the preBötC (thick lines).

References

1. Mateika, J.H. & Duffin, J. A review of the control of breathing during exercise. *Eur J Appl Physiol Occup Physiol* **71**, 1-27 (1995).
2. Gariepy, J.F., Missaghi, K. & Dubuc, R. The interactions between locomotion and respiration. *Prog Brain Res* **187**, 173-188 (2010).
3. Duffin, J. The fast exercise drive to breathe. *J Physiol* **592**, 445-451 (2014).
4. Hérent, C., Diem, S., Fortin, G. & Bouvier, J. Absent phasing of respiratory and locomotor rhythms in running mice. *eLife* **9**(2020).
5. Iscoe, S. Respiratory and stepping frequencies in conscious exercising cats. *J Appl Physiol Respir Environ Exerc Physiol* **51**, 835-839 (1981).
6. Fernandes, A., Galbo, H., Kjaer, M., Mitchell, J.H., Secher, N.H. & Thomas, S.N. Cardiovascular and ventilatory responses to dynamic exercise during epidural anaesthesia in man. *J Physiol* **420**, 281-293 (1990).
7. Decety, J., Jeannerod, M., Durozard, D. & Baverel, G. Central activation of autonomic effectors during mental simulation of motor actions in man. *J Physiol* **461**, 549-563 (1993).
8. Tobin, M.J., Perez, W., Guenther, S.M., D'Alonzo, G. & Dantzker, D.R. Breathing pattern and metabolic behavior during anticipation of exercise. *J Appl Physiol (1985)* **60**, 1306-1312 (1986).
9. Thornton, J.M., Guz, A., Murphy, K., Griffith, A.R., Pedersen, D.L., Kardos, A., Leff, A., Adams, L., Casadei, B. & Paterson, D.J. Identification of higher brain centres that may encode the cardiorespiratory response to exercise in humans. *J Physiol* **533**, 823-836 (2001).
10. Eldridge, F.L., Millhorn, D.E., Kiley, J.P. & Waldrop, T.G. Stimulation by central command of locomotion, respiration and circulation during exercise. *Respir Physiol* **59**, 313-337 (1985).
11. Eldridge, F.L., Millhorn, D.E. & Waldrop, T.G. Exercise hyperpnea and locomotion: parallel activation from the hypothalamus. *Science* **211**, 844-846 (1981).
12. Le Ray, D., Juvin, L., Ryczko, D. & Dubuc, R. Chapter 4--supraspinal control of locomotion: the mesencephalic locomotor region. *Prog Brain Res* **188**, 51-70 (2011).
13. Leiras, R., Cregg, J.M. & Kiehn, O. Brainstem Circuits for Locomotion. *Annu Rev Neurosci* (2022).
14. Sébille, S.B., Rolland, A.S., Faillot, M., Perez-Garcia, F., Colomb-Clerc, A., Lau, B., Dumas, S., Vidal, S.F., Welter, M.L., Francois, C., Bardinet, E. & Karachi, C. Normal and pathological neuronal distribution of the human mesencephalic locomotor region. *Movement disorders : official journal of the Movement Disorder Society* **34**, 218-227 (2019).
15. Josset, N., Roussel, M., Lemieux, M., Lafrance-Zoubga, D., Rastqar, A. & Bretzner, F. Distinct Contributions of Mesencephalic Locomotor Region Nuclei to Locomotor Control in the Freely Behaving Mouse. *Curr Biol* **28**, 884-901 e883 (2018).
16. Caggiano, V., Leiras, R., Goni-Erro, H., Masini, D., Bellardita, C., Bouvier, J., Caldeira, V., Fisone, G. & Kiehn, O. Midbrain circuits that set locomotor speed and gait selection. *Nature* **553**, 455-460 (2018).
17. Roseberry, T.K., Lee, A.M., Lalive, A.L., Wilbrecht, L., Bonci, A. & Kreitzer, A.C. Cell-Type-Specific Control of Brainstem Locomotor Circuits by Basal Ganglia. *Cell* **164**, 526-537 (2016).
18. Dautan, D., Kovács, A., Bayasgalan, T., Diaz-Acevedo, M.A., Pal, B. & Mena-Segovia, J. Modulation of motor behavior by the mesencephalic locomotor region. *bioRxiv*, 2020.2006.2025.172296 (2020).
19. van der Zouwen, C.I., Boutin, J., Fougère, M., Flaive, A., Vivancos, M., Santuz, A., Akay, T., Sarret, P. & Ryczko, D. Freely Behaving Mice Can Brake and Turn During Optogenetic Stimulation of the Mesencephalic Locomotor Region. *Frontiers in neural circuits* **15**, 639900 (2021).
20. Gariepy, J.F., Missaghi, K., Chevallier, S., Chartre, S., Robert, M., Auclair, F., Lund, J.P. & Dubuc, R. Specific neural substrate linking respiration to locomotion. *Proc Natl Acad Sci U S A* **109**, E84-92 (2012).
21. Kiehn, O. Decoding the organization of spinal circuits that control locomotion. *Nature reviews* **17**, 224-238 (2016).

22. Grillner, S. & El Manira, A. Current Principles of Motor Control, with Special Reference to Vertebrate Locomotion. *Physiological reviews* **100**, 271-320 (2020).

23. Le Gal, J.P., Juvin, L., Cardoit, L., Thoby-Brisson, M. & Morin, D. Remote control of respiratory neural network by spinal locomotor generators. *PLoS ONE* **9**, e89670 (2014).

24. Le Gal, J.P., Colnot, E., Cardoit, L., Bacque-Cazenave, J., Thoby-Brisson, M., Juvin, L. & Morin, D. Modulation of respiratory network activity by forelimb and hindlimb locomotor generators. *Eur J Neurosci* (2020).

25. Smith, J.C., Ellenberger, H.H., Ballanyi, K., Richter, D.W. & Feldman, J.L. Pre-Botzinger complex: a brainstem region that may generate respiratory rhythm in mammals. *Science* **254**, 726-729 (1991).

26. Del Negro, C.A., Funk, G.D. & Feldman, J.L. Breathing matters. *Nature reviews* **19**, 351-367 (2018).

27. Yang, C.F., Kim, E.J., Callaway, E.M. & Feldman, J.L. Monosynaptic Projections to Excitatory and Inhibitory preBötzinger Complex Neurons. *Front Neuroanat* **14**, 58 (2020).

28. Gravel, J., Brocard, F., Gariépy, J.F., Lund, J.P. & Dubuc, R. Modulation of respiratory activity by locomotion in lampreys. *Neuroscience* **144**, 1120-1132 (2007).

29. Abbott, S.B., Stornetta, R.L., Coates, M.B. & Guyenet, P.G. Phox2b-expressing neurons of the parafacial region regulate breathing rate, inspiration, and expiration in conscious rats. *J Neurosci* **31**, 16410-16422 (2011).

30. Abbott, S.B., Stornetta, R.L., Fortuna, M.G., Depuy, S.D., West, G.H., Harris, T.E. & Guyenet, P.G. Photostimulation of retrotrapezoid nucleus phox2b-expressing neurons in vivo produces long-lasting activation of breathing in rats. *J Neurosci* **29**, 5806-5819 (2009).

31. Iscoe, S. Control of abdominal muscles. *Progress in neurobiology* **56**, 433-506 (1998).

32. Abraham, K.A., Feingold, H., Fuller, D.D., Jenkins, M., Mateika, J.H. & Fregosi, R.F. Respiratory-related activation of human abdominal muscles during exercise. *J Physiol* **541**, 653-663 (2002).

33. Ainsworth, D.M., Smith, C.A., Eicker, S.W., Henderson, K.S. & Dempsey, J.A. The effects of locomotion on respiratory muscle activity in the awake dog. *Respir Physiol* **78**, 145-162 (1989).

34. Souza, G., Stornetta, R.L., Stornetta, D.S., Abbott, S.B.G. & Guyenet, P.G. Differential Contribution of the Retrotrapezoid Nucleus and C1 Neurons to Active Expiration and Arousal in Rats. *J Neurosci* **40**, 8683-8697 (2020).

35. Barna, B.F., Takakura, A.C. & Moreira, T.S. Pontomedullary and hypothalamic distribution of Fos-like immunoreactive neurons after acute exercise in rats. *Neuroscience* **212**, 120-130 (2012).

36. Korsak, A., Sheikhbahaei, S., Machhada, A., Gourine, A.V. & Huckstepp, R.T.R. The Role Of Parafacial Neurons In The Control Of Breathing During Exercise. *Scientific reports* **8**, 400 (2018).

37. Vong, L., Ye, C., Yang, Z., Choi, B., Chua, S., Jr. & Lowell, B.B. Leptin action on GABAergic neurons prevents obesity and reduces inhibitory tone to POMC neurons. *Neuron* **71**, 142-154 (2011).

38. Stornetta, R.L., Rosin, D.L., Wang, H., Sevigny, C.P., Weston, M.C. & Guyenet, P.G. A group of glutamatergic interneurons expressing high levels of both neurokinin-1 receptors and somatostatin identifies the region of the pre-Botzinger complex. *J Comp Neurol* **455**, 499-512 (2003).

39. Kim, E.J., Jacobs, M.W., Ito-Cole, T. & Callaway, E.M. Improved Monosynaptic Neural Circuit Tracing Using Engineered Rabies Virus Glycoproteins. *Cell Rep* (2016).

40. Bouvier, J., Thoby-Brisson, M., Renier, N., Dubreuil, V., Ericson, J., Champagnat, J., Pierani, A., Chedotal, A. & Fortin, G. Hindbrain interneurons and axon guidance signaling critical for breathing. *Nat Neurosci* **13**, 1066-1074 (2010).

41. Koshiya, N. & Smith, J.C. Neuronal pacemaker for breathing visualized in vitro. *Nature* **400**, 360-363 (1999).

42. Neve, R.L., Neve, K.A., Nestler, E.J. & Carlezon, W.A., Jr. Use of herpes virus amplicon vectors to study brain disorders. *Biotechniques* **39**, 381-391 (2005).

43. Usseglio, G., Gatier, E., Heuzé, A., Hérent, C. & Bouvier, J. Control of Orienting Movements and Locomotion by Projection-Defined Subsets of Brainstem V2a Neurons. *Curr Biol* (2020).

44. Cui, Y., Kam, K., Sherman, D., Janczewski, W.A., Zheng, Y. & Feldman, J.L. Defining preBotzinger Complex Rhythm- and Pattern-Generating Neural Microcircuits In Vivo. *Neuron* **91**, 602-614 (2016).

45. Baertsch, N.A., Baertsch, H.C. & Ramirez, J.M. The interdependence of excitation and inhibition for the control of dynamic breathing rhythms. *Nat Commun* **9**, 843 (2018).

46. Stujenske, J.M., Spellman, T. & Gordon, J.A. Modeling the Spatiotemporal Dynamics of Light and Heat Propagation for In Vivo Optogenetics. *Cell Rep* **12**, 525-534 (2015).

47. Mathis, A., Mamidanna, P., Cury, K.M., Abe, T., Murthy, V.N., Mathis, M.W. & Bethge, M. DeepLabCut: markerless pose estimation of user-defined body parts with deep learning. *Nat Neurosci* **21**, 1281-1289 (2018).

48. Ferreira-Pinto, M.J., Kanodia, H., Falasconi, A., Sigrist, M., Esposito, M.S. & Arber, S. Functional diversity for body actions in the mesencephalic locomotor region. *Cell* (2021).

49. Tovote, P., Esposito, M.S., Botta, P., Chaudun, F., Fadok, J.P., Markovic, M., Wolff, S.B., Ramakrishnan, C., Fenno, L., Deisseroth, K., Herry, C., Arber, S. & Luthi, A. Midbrain circuits for defensive behaviour. *Nature* **534**, 206-212 (2016).

50. Sahibzada, N., Dean, P. & Redgrave, P. Movements resembling orientation or avoidance elicited by electrical stimulation of the superior colliculus in rats. *J Neurosci* **6**, 723-733 (1986).

51. Masullo, L., Mariotti, L., Alexandre, N., Freire-Pritchett, P., Boulanger, J. & Tripodi, M. Genetically Defined Functional Modules for Spatial Orienting in the Mouse Superior Colliculus. *Curr Biol* **29**, 2892-2904 e2898 (2019).

52. Hagglund, M., Borgius, L., Dougherty, K.J. & Kiehn, O. Activation of groups of excitatory neurons in the mammalian spinal cord or hindbrain evokes locomotion. *Nat Neurosci* **13**, 246-253 (2010).

53. Talpalar, A.E., Bouvier, J., Borgius, L., Fortin, G., Pierani, A. & Kiehn, O. Dual-mode operation of neuronal networks involved in left-right alternation. *Nature* (2013).

54. Kjaerulff, O. & Kiehn, O. Distribution of networks generating and coordinating locomotor activity in the neonatal rat spinal cord in vitro: a lesion study. *J Neurosci* **16**, 5777-5794 (1996).

55. Inoue, S., Yang, R., Tantry, A., Davis, C.H., Yang, T., Knoedler, J.R., Wei, Y., Adams, E.L., Thombare, S., Golf, S.R., Neve, R.L., Tessier-Lavigne, M., Ding, J.B. & Shah, N.M. Periodic Remodeling in a Neural Circuit Governs Timing of Female Sexual Behavior. *Cell* **179**, 1393-1408.e1316 (2019).

56. Zingg, B., Chou, X.L., Zhang, Z.G., Mesik, L., Liang, F., Tao, H.W. & Zhang, L.I. AAV-Mediated Anterograde Transsynaptic Tagging: Mapping Corticocollicular Input-Defined Neural Pathways for Defense Behaviors. *Neuron* **93**, 33-47 (2017).

57. Ramanantsoa, N., Hirsch, M.R., Thoby-Brisson, M., Dubreuil, V., Bouvier, J., Ruffault, P.L., Matrot, B., Fortin, G., Brunet, J.F., Gallego, J. & Goridis, C. Breathing without CO(2) chemosensitivity in conditional Phox2b mutants. *J Neurosci* **31**, 12880-12888 (2011).

58. Ruffault, P.L., D'Autreaux, F., Hayes, J.A., Nomaksteinsky, M., Autran, S., Fujiyama, T., Hoshino, M., Hagglund, M., Kiehn, O., Brunet, J.F., Fortin, G. & Goridis, C. The retrotrapezoid nucleus neurons expressing Atoh1 and Phox2b are essential for the respiratory response to CO(2). *eLife* **4**(2015).

59. Jensen, V.N., Seedle, K., Turner, S.M., Lorenz, J.N. & Crone, S.A. V2a Neurons Constrain Extradiaphragmatic Respiratory Muscle Activity at Rest. *eNeuro* **6**(2019).

60. Li, P., Janczewski, W.A., Yackle, K., Kam, K., Pagliardini, S., Krasnow, M.A. & Feldman, J.L. The peptidergic control circuit for sighing. *Nature* (2016).

61. Smith, J.C., Morrison, D.E., Ellenberger, H.H., Otto, M.R. & Feldman, J.L. Brainstem projections to the major respiratory neuron populations in the medulla of the cat. *J Comp Neurol* **281**, 69-96 (1989).

62. Lefler, Y., Campagner, D. & Branco, T. The role of the periaqueductal gray in escape behavior. *Curr Opin Neurobiol* **60**, 115-121 (2020).

63. Jordan, L.M., Liu, J., Hedlund, P.B., Akay, T. & Pearson, K.G. Descending command systems for the initiation of locomotion in mammals. *Brain research reviews* **57**, 183-191 (2008).

64. Ryczko, D. & Dubuc, R. The multifunctional mesencephalic locomotor region. *Curr Pharm Des* **19**, 4448-4470 (2013).

65. Korte, S.M., Jaarsma, D., Luiten, P.G. & Bohus, B. Mesencephalic cuneiform nucleus and its ascending and descending projections serve stress-related cardiovascular responses in the rat. *Journal of the autonomic nervous system* **41**, 157-176 (1992).

66. Guyenet, P.G., Stornetta, R.L., Bochorishvili, G., Depuy, S.D., Burke, P.G. & Abbott, S.B. C1 neurons: the body's EMTs. *American journal of physiology* **305**, R187-204 (2013).

67. Kanbar, R., Stornetta, R.L. & Guyenet, P.G. Sciatic nerve stimulation activates the retrotrapezoid nucleus in anesthetized rats. *J Neurophysiol* **116**, 2081-2092 (2016).

68. Huckstepp, R.T., Cardoza, K.P., Henderson, L.E. & Feldman, J.L. Role of parafacial nuclei in control of breathing in adult rats. *J Neurosci* **35**, 1052-1067 (2015).

69. Dougherty, K.J. & Ha, N.T. The rhythm section: An update on spinal interneurons setting the beat for mammalian locomotion. *Curr Opin Physiol* **8**, 84-93 (2019).

70. Madisen, L., Mao, T., Koch, H., Zhuo, J.M., Berenyi, A., Fujisawa, S., Hsu, Y.W., Garcia, A.J., 3rd, Gu, X., Zanella, S., Kidney, J., Gu, H., Mao, Y., Hooks, B.M., Boyden, E.S., Buzsaki, G., Ramirez, J.M., Jones, A.R., Svoboda, K., Han, X., Turner, E.E. & Zeng, H. A toolbox of Cre-dependent optogenetic transgenic mice for light-induced activation and silencing. *Nat Neurosci* **15**, 793-802 (2012).

71. Voiculescu, O., Charnay, P. & Schneider-Maunoury, S. Expression pattern of a Krox-20/Cre knock-in allele in the developing hindbrain, bones, and peripheral nervous system. *Genesis* **26**, 123-126 (2000).

72. Mattis, J., Tye, K.M., Ferenczi, E.A., Ramakrishnan, C., O'Shea, D.J., Prakash, R., Gunaydin, L.A., Hyun, M., Fenno, L.E., Gradinaru, V., Yizhar, O. & Deisseroth, K. Principles for applying optogenetic tools derived from direct comparative analysis of microbial opsins. *Nature methods* **9**, 159-172 (2011).

73. Bouvier, J., Caggiano, V., Leiras, R., Caldeira, V., Bellardita, C., Balueva, K., Fuchs, A. & Kiehn, O. Descending Command Neurons in the Brainstem that Halt Locomotion. *Cell* **163**, 1191-1203 (2015).

74. Harrison, M., O'Brien, A., Adams, L., Cowin, G., Ruitenberg, M.J., Sengul, G. & Watson, C. Vertebral landmarks for the identification of spinal cord segments in the mouse. *NeuroImage* **68**, 22-29 (2013).

75. Guyenet, P.G. & Mulkey, D.K. Retrotrapezoid nucleus and parafacial respiratory group. *Respir Physiol Neurobiol* (2010).

76. Skarlatou, S., Herent, C., Toscano, E., Mendes, C.S., Bouvier, J. & Zampieri, N. Afadin Signaling at the Spinal Neuroepithelium Regulates Central Canal Formation and Gait Selection. *Cell Rep* **31**, 107741 (2020).

Supplementary Figure 1

a ***Vglut2*^{Cre} CnF-injected and implanted**

Figure 1a-f, anterograde tracing: n=3 mice.
Figure 2a-c, photostimulations in the plethysmograph: all mice used (n=7).
Figure 3, CnF photostimulations in the corridor: n=5 mice.

b ***Vglut2*^{Cre}, CnF-injected and preBötC-implanted**

Figure 2d-f, photoactivations in the plethysmograph: n=4 mice

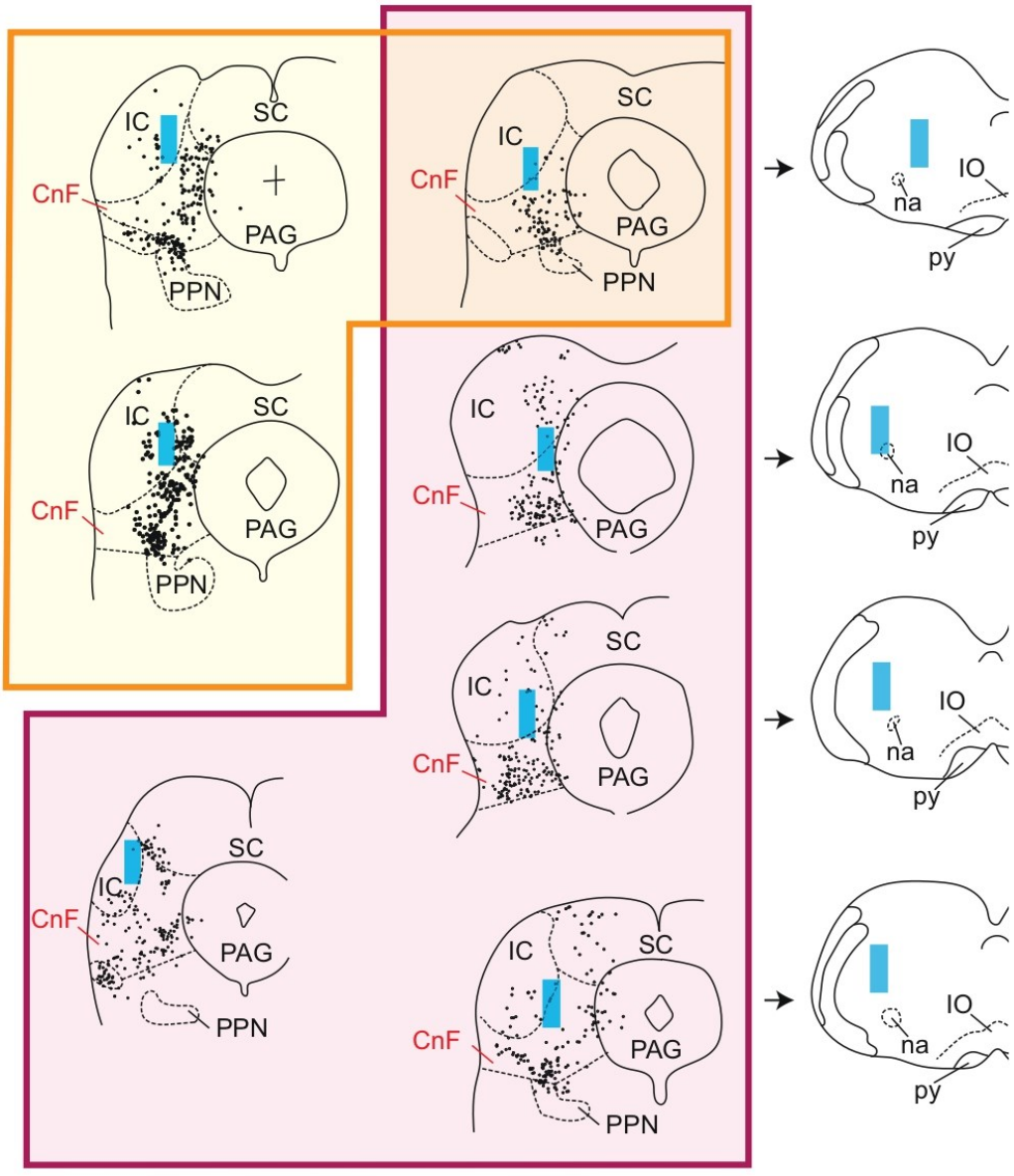

Supplementary Figure 1. Viral transfection and optic fiber implantation sites in the CnF and preBötC. Related to Figures 1, 2 and 3.
(a) Registration of transfected glutamatergic CnF cells (dots) and optic fiber placements (blue rectangles) in *Vglut2*^{Cre} adult mice used for Figures 1a-f (orange), 3 (pink), and 2a-c (all animals). One section represents one animal.
(b) In the 4 animals indicated by an arrow from (**a**), an additional optic fiber was placed in the ipsilateral preBötC to activate CnF projections in this region (experiments shown in Figure 2d-f).

Supplementary Figure 2

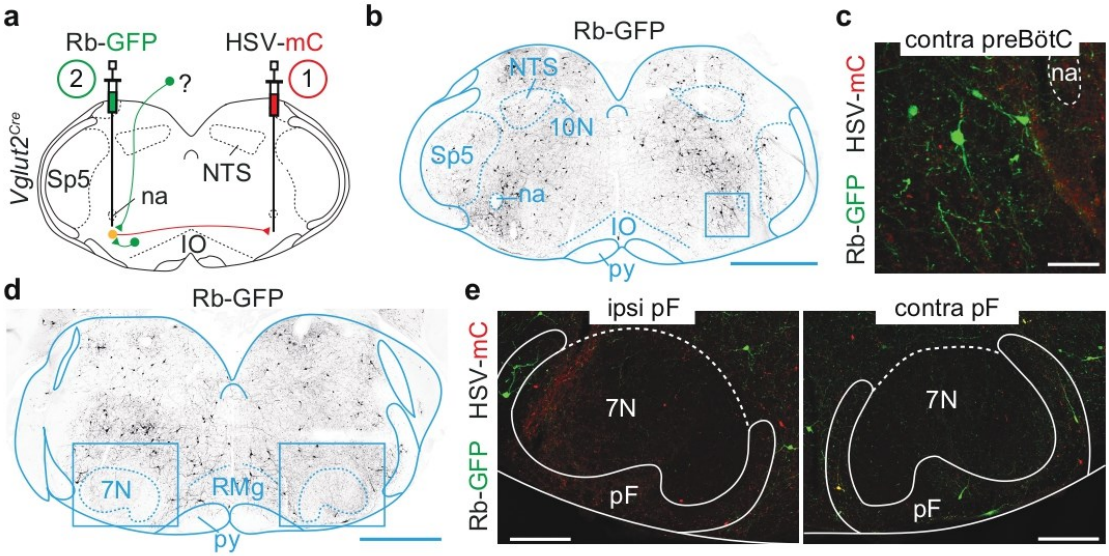

Supplementary Figure 2. Transsynaptic labelling from glutamatergic commissural preBötC neurons leads to only little labelling in the pF. Related to Figure 1.
(a) Experimental design for retrograde transsynaptic monosynaptic tracing from Glut^{+} commissural preBötC neurons in *Vglut2*^{Cre} adult mice. An HSV-LS1L-TVA-oG-mCherry (HSV-mC) is first injected in the contralateral preBötC followed by a G-deleted and EnvA pseudotyped Rb virus (Rb-GFP) in the ipsilateral preBötC.
(b) Transverse section at the preBötC level showing Rb-GFP putative presynaptic cells. Scale bar, 1 mm.
(c) Magnification over the contralateral preBötC showing Rb-GFP putative presynaptic cells. Scale bar, 100 µm.
(d) Transverse section at the level of the pF showing the scarcity of Rb-GFP presynaptic cells. Scale bar, 1 mm.
(e) Magnification over ipsilateral and contralateral pF areas. Scale bars, 250 µm.

Supplementary Figure 3

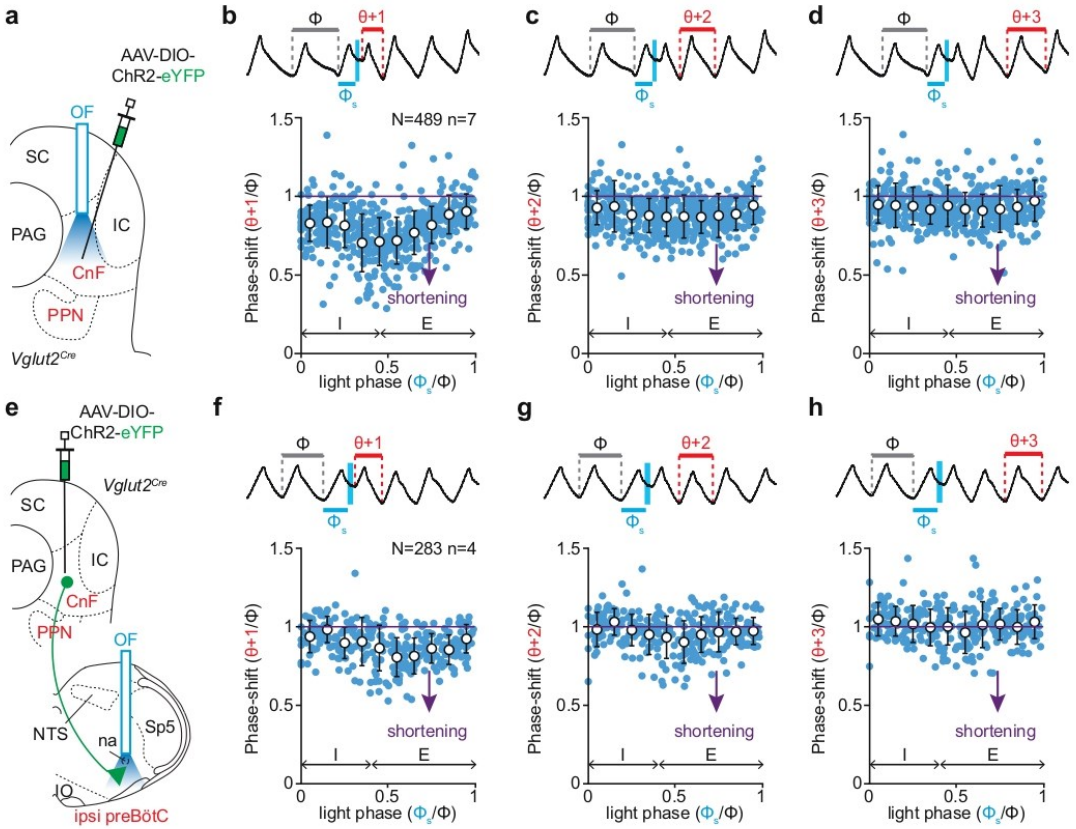

Supplementary Figure 3. Impact of photoactivating glutamatergic CnF neurons and their projection to the preBötC on respiratory cycles following the light-perturbed cycle. Related to Figure 2.
(a) Experimental strategy for photoactivating Glut⁺ CnF neurons on a *Vglut2*^{Cre} adult mouse.
(b) *Top*: whole body plethysmography (WBP) recordings of respiratory cycles around a single 50 ms photoactivation of Glut⁺ CnF neurons (inspirations are upwards, expirations are downwards). The control cycle (Φ, black), the phase of light-simulation (Φ_s, blue), and the cycle following the perturbed cycle (θ+1, red) are annotated. *Bottom*: plot of the phase-shift (cycle n+1 normalized to control cycle: θ+1/Φ) as a function of light phase (light cycle normalized to control cycle: Φ_s/Φ). Values < 1 (purple line) indicate a shortening of the cycle n+1. Blue circles represent individual data from N random trials from n mice and white circles are averages ± SD across all trials within 0.1 ms bins. Inspiration (I) and expiration (E) mean durations are annotated. See Figure 2 for details.
(c, d) Similar representations for cycles n+2 (θ+2, **c**) and n+3 (θ+3, **d**).
(e) Experimental strategy for photoactivating Glut⁺ CnF projections in the preBötC on a *Vglut2*^{Cre} adult mouse.
(f-h) Similar representations as in (**b-d**) when activating Glut⁺ CnF fibers in the preBötC.

Supplementary Figure 4

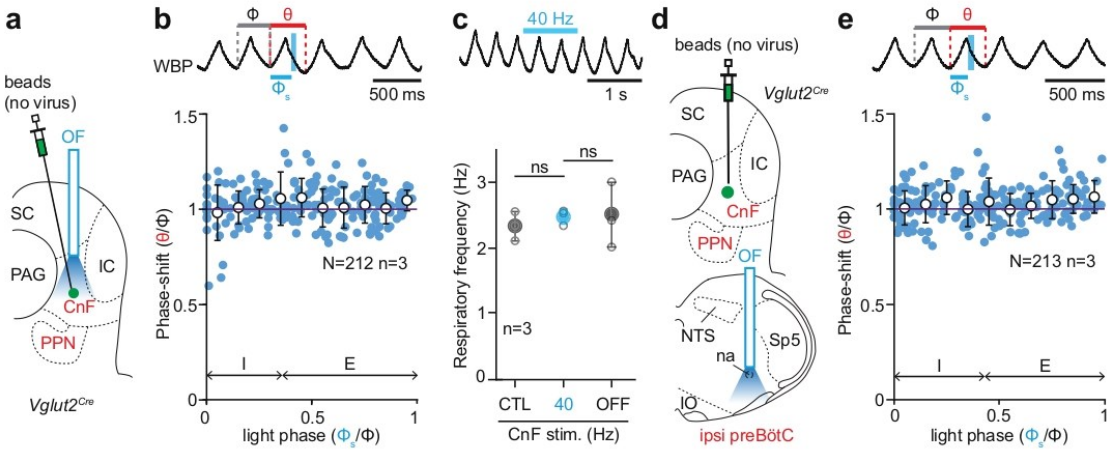

Supplementary Figure 4. Controls for optogenetic activations of glutamatergic CnF neurons. Related to Figures 2 and 3.

(a) *Vglut2*^{cre} adult mice were injected with fluorescent beads in the CnF, but no ChR2-coding virus. An optic fiber (OF) was implanted above the injection site.

(b) *Top*: whole body plethysmography (WBP) recordings of respiratory cycles around a single 50 ms light pulse delivered on control mice during the expiratory phase of one respiratory cycle (inspirations are upwards, expirations are downwards). The control cycle (Φ, black), the phase of light-simulation (Φ_s, blue), and the perturbed cycle (θ, red) are annotated (see Figure 2 for details). *Bottom*: plot of the phase-shift (perturbed cycle normalized to control cycle: θ/Φ) as a function of the phase of light-stimulation (Φ_s/Φ). Inspiration (I) and expiration (E) mean durations are indicated. Contrary to CnF light activations (see Figure 2), the respiratory cycle is not affected here in control mice (values close to 1, purple line). Blue circles represent individual data from N random trials from n mice. White circles are averages ± SD across all trials within 0.1 ms bins.

(c) *Top*: example WBP recording during a 1 s photoactivation (40 Hz train). *Bottom*: quantification of the diaphragm frequency showing no significant effect of the photoactivation in control mice (CTL: control; OFF: after light offset). Gray open circles are the means of individual animals and colored circles are the means ± SD across n mice. ns, not significant (Wilcoxon matched-pairs tests).

(d) Similar experimental design as in (**a**) but animals were implanted with an OF above the ipsilateral preBötC.

(e) Same as in (**b**) during a single 50 ms light delivery in the preBötC area. Contrary to light activations of CnF projections in the preBötC (see Figure 2), the respiratory cycle is not affected by photoactivations on these control mice (values close to 1, purple line).

Supplementary Figure 5

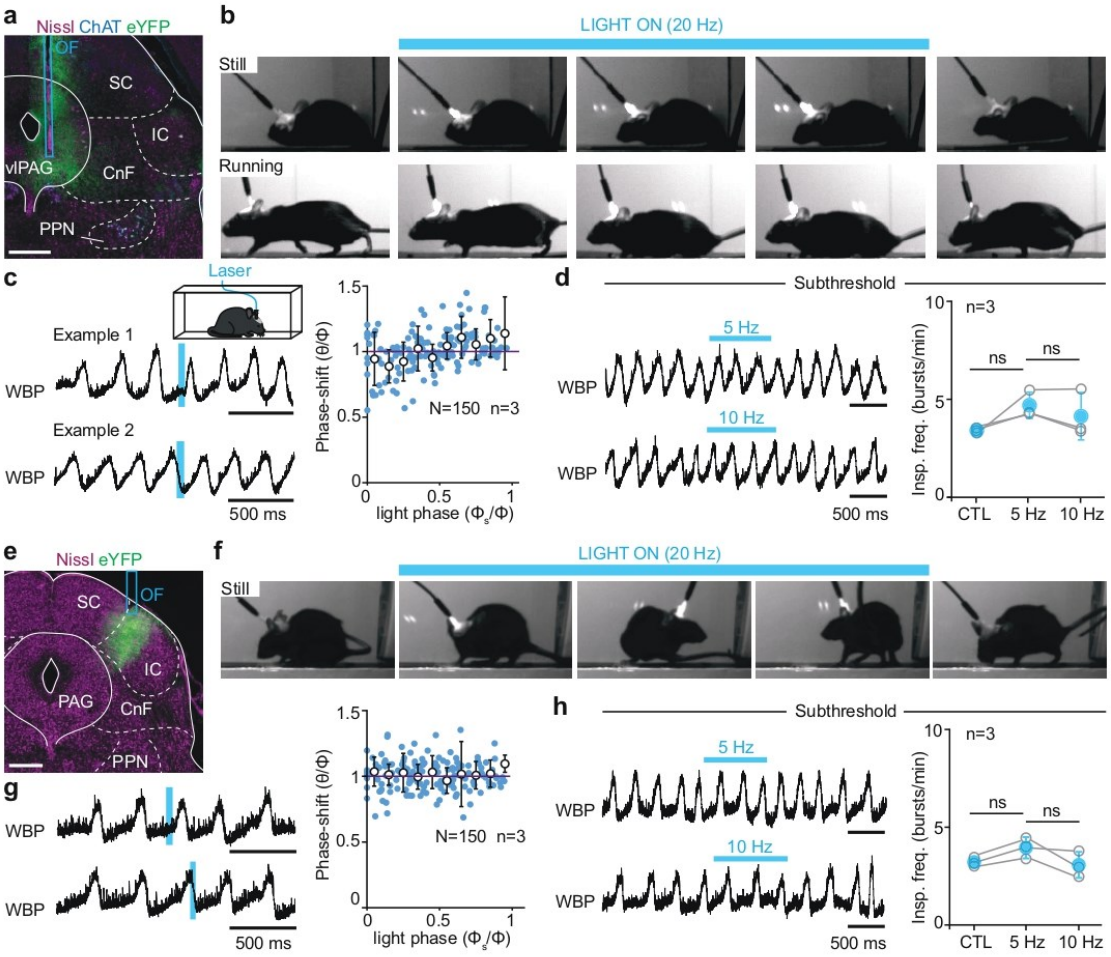

Supplementary Figure 5. Targeted photoactivations of adjacent structures to the CnF do not induce running nor modulate inspiratory rhythm mechanisms. Related to figures 2 and 3.
(a) Transverse section showing Glut⁺ ventrolateral periaqueductal gray (vlPAG) neurons, that reside more laterally but at the same dorso-ventral depth as the CnF, unilaterally-transfected with an AAV-DIO-eYFP on a *Vglut2*^{Cre} adult mouse. Scale bar, 0.5 mm.
(b) Photostimulation of Glut⁺ vlPAG neurons does not evoke running on resting mice and supresses running in moving mice.
(c) *Left*: WBP setup (top) and two example recordings (bottom) around a single 50 ms light stimulation of Glut⁺ vlPAG neurons at different phases of the respiratory cycle. *Right*: plot of the phase-shift as a function of the phase of light-stimulation. See Figure 2c for details. Note that the stimulation does not significantly perturb the respiratory cycle.
(d) *Left*: two examples of WBP recordings during vlPAG photostimulation at 5 and 10 Hz showing the absence of changes in breathing frequency. *Right*: quantifications of inspiratory frequency in control (CTL), and during the vlPAG photostimulation.
(e-h) Similar representations for targeted photostimulation of Glut⁺ neurons of the inferior colliculus (IC), that resides more dorsally, but at the same medio-lateral location, as the CnF. The photostimulation evokes a contralateral turning but no locomotor initiation in resting mice, and does not modulate inspiratory rhythm.
In graphs from panels **d** and **h**: ns, not significant (paired t-tests).

Supplementary Figure 6

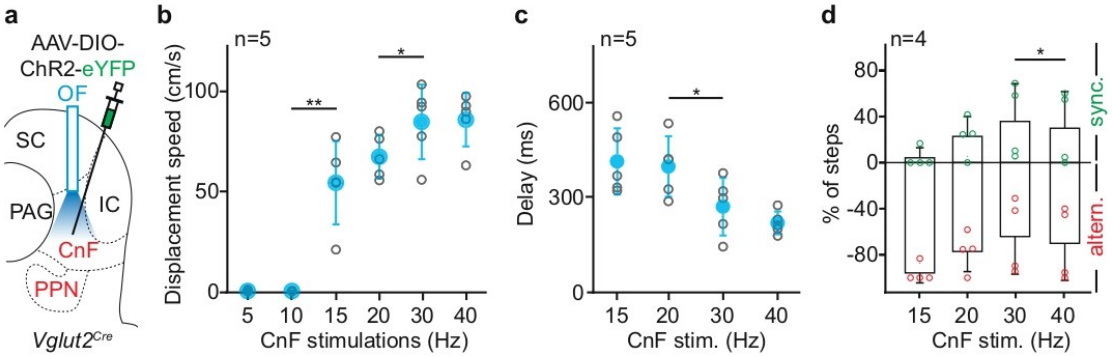

Supplementary Figure 6. Glutamatergic CnF neurons control locomotor speed, locomotor onset delay and hindlimb synchronicity rate. Related to Figure 3.
(a) Experimental strategy for photostimulating Glut^{+} CnF neurons in an adult *Vglut2*^{Cre} mouse.
(b, c) Quantification of the animal's displacement speed (**b**) and the delay to locomotor initiation (**c**) at increasing CnF photostimulations frequencies. Gray open circles are the means of individual animals and colored circles are the means ± SD across n mice.
(d) Quantification of the percent of hindlimb movements that show left-right alternation (negative values, indicative of trot) or left-right synchronicity (positive values, indicating of gallop) at increasing CnF photostimulation frequencies. Colored open circles are the means of individual animals and bar-graphs are the means ± SD across n mice.
*p < 0.05; **p < 0.01 (**b**, **c**, paired t-tests; **d**, Wilcoxon matched-pairs tests).

Supplementary Figure 7

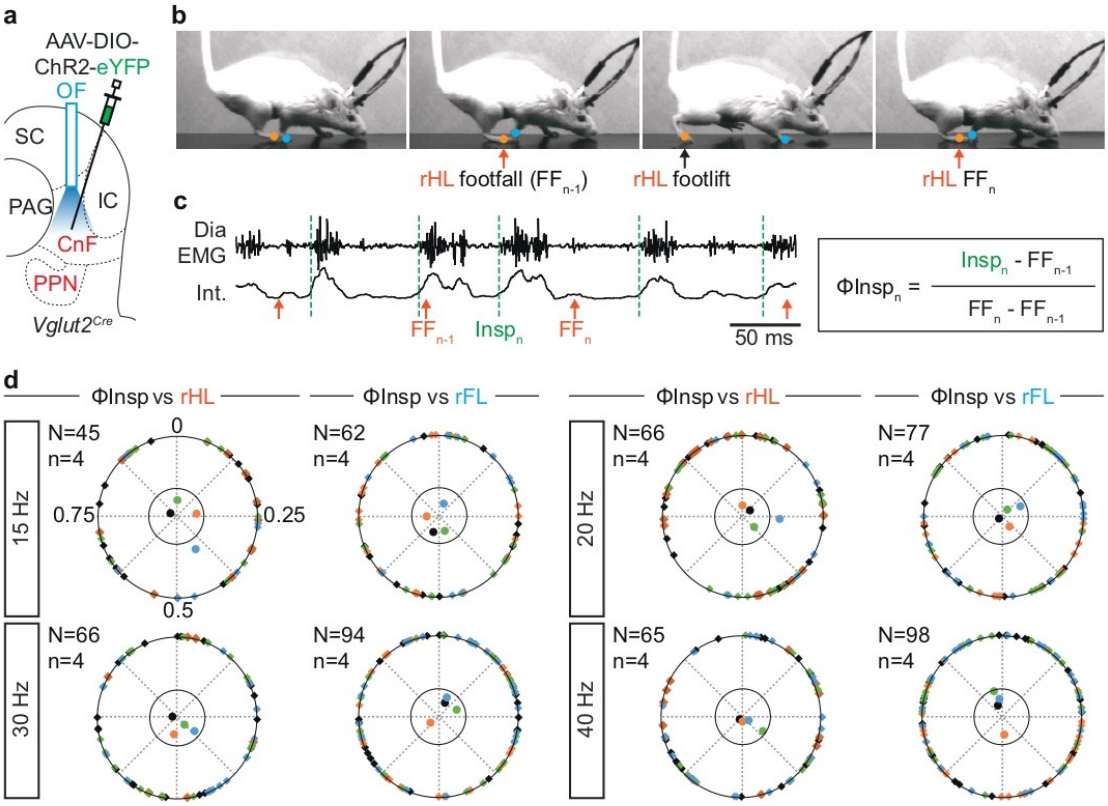

Supplementary Figure 7. Absence of phasing of respiratory and locomotor rhythms during CnF-evoked running. Related to Figures 2 and 3.

(a) Experimental strategy for photostimulating Glut$^+$ CnF neurons in an adult *Vglut2^{Cre}* mouse.

(b) Photostimulation of Glut$^+$ CnF neurons for 1 s at 20 Hz. The timing of footlifts and footfalls of the right hindlimb (rHL, orange) and the right forelimb (rFL, blue) were detected manually on the videos. One complete rHL locomotor cycle is shown, between two consecutive footfalls (FF_{n-1} and FF_n).

(c) Raw (EMG) and integrated (Int.) diaphragmatic electromyograms and occurrence of rHL footfalls (orange arrows) during CnF-evoked running. Dotted green lines indicate the onsets of inspirations, which can occur at any moment of the locomotor cycle. Occurrences of inspiratory bursts ($Insp_n$) within the locomotor cycle are then calculated and expressed as a phase value ($\Phi Insp_n$) from 0 (concomitant with FF_{n-1}) to 1 (concomittant with FF_n).

(d) Circular plots diagrams showing the phase-relationship between individual inspiratory bursts and the indicated reference limb for one representative animal in response to CnF photoactivations at 15, 20, 30, and 40 Hz. Diamonds on the outer circle indicate the phase of N individual inspirations pooled from n mice; values from each animal are given in the same color. Dots inside the circle indicate the mean orientation vector for each animal. The positioning of these mean values within the inner circle illustrates the absence of a significantly oriented phase preference ($R < 0.3$, R being the concentration of phase values around the mean as defined in Kjaerulff and Kiehn, 1996).

Supplementary Figure 8

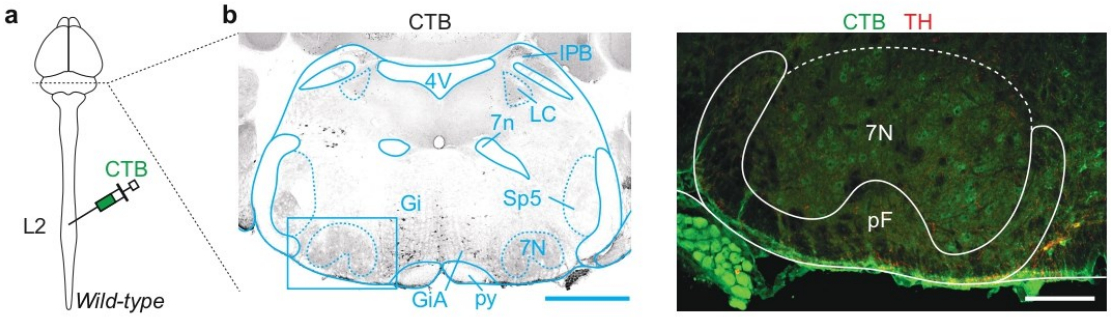

Supplementary Figure 8. Absence of spinally-projecting neurons in the pF. Related to Figure 4.
(a) Experimental strategy for labelling spinally-projecting neurons using a bilateral injection of the retrograde tracer Cholera Toxin B (CTB) at the second lumbar segment (L2) in a wild-type adult mouse.
(b) *Left*: transverse section at the level of the pF, showing CTB^+ spinally-projecting neurons in black. Scale bar, 1 mm. *Right*: magnification of the boxed area showing the absence of spinally-projecting neurons in the pF. CTB^+ cells are located more medially and include catecholaminergic cell-types (expressing tyrosine hydroxylase, TH). Scale bar, 200 µm. Representative of n = 3 animals.
IPB: lateral para-brachial nucleus. LC: locus coeruleus. See Figure 1 for other abbreviations.

Supplementary Figure 9

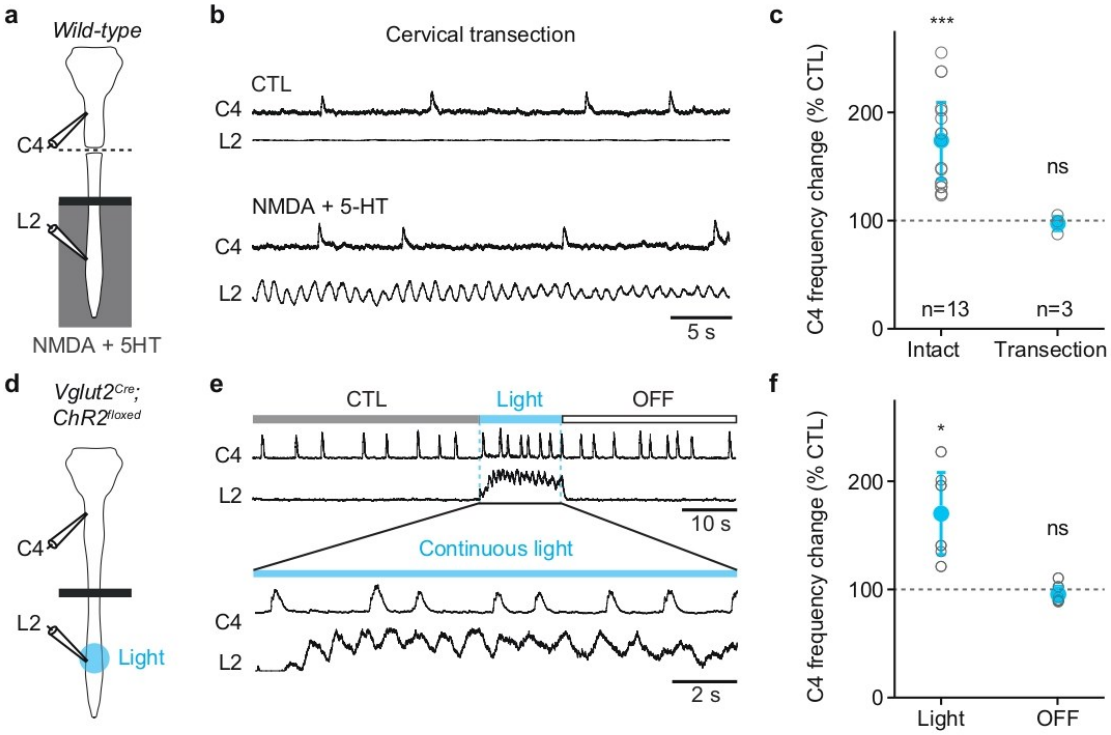

Supplementary Figure 9. Controls for *ex vivo* experiments and photoactivations of the glutamatergic lumbar spinal neurons. Related to Figure 5.

(a) Experimental strategy for recording respiratory (C4) and locomotor-like (L2) activities on *ex vivo* isolated brainstem-spinal cord preparations from neonatal wild-type mice. Preparation are separated in two compartments using a Vaseline barrier (black bar). The lumbar compartment is superfused with control or locomotor drugs enriched (NDMA and 5-HT) artificial cerebrospinal fluid (aCSF), while the brainstem compartment remains in control aCSF. Contrary to experiments in Figure 5, preparations underwent a complete transection at the cervical level.

(b) Recordings of respiratory and locomotor-like activities of one representative animal before (CTL) and during perfusion of NMDA and 5-HT in the lumbar compartment (only integrated traces are shown). The absence of change in C4 frequency following the transection rules out any leakage of NMDA and 5-HT from the lumbar to the brainstem compartment.

(c) Quantification of the respiratory frequency change during drug-induced locomotor-like activity as a percent change to CTL, in both intact and sectioned preparations. Grey open circles are the means of individual preparations, and blue circles are the means ± SD across n preparations.

(d) Experimental strategy for photostimulating lumbar Glut^{+} neurons in *Vglut2^{Cre};ChR2^{floxed}* neonatal *ex vivo* preparations. The blue light is delivered focally on the L2 segment, bilaterally.

(e) Recordings of respiratory and locomotor-like activities of one representative preparation before (CTL), during (Light) and after (OFF) a continuous 15 s photostimulation which triggers a substantial increase in respiratory frequency.

(f) Quantification of the respiratory frequency change during photo-evoked locomotor-like activity as a percent change to the CTL. In all graphs: ns, not significant. *, $p<0.05$; ***, $p<0.001$ (Wilcoxon matched-pairs tests).

Supplementary Figure 10

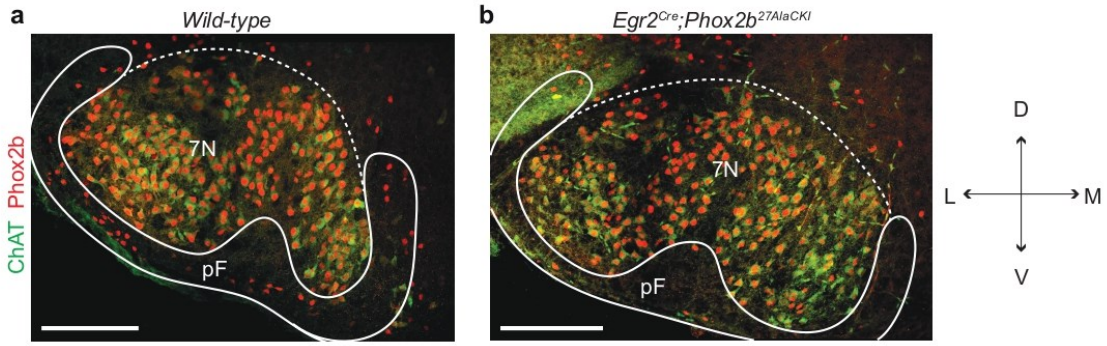

Supplementary Figure 10. Loss of RTN neurons in *Egr2^{Cre};Phox2b^{27AlaCKI}* mutant neonates.
Related to Figure 5.
(a) Magnification of the pF area on a transverse brainstem section of a wild-type neonatal mouse. RTN neurons are detected as Phox2b-expressing interneurons located in the pF area lying ventrally, ventro-medially, ventro-laterally and laterally to the facial motoneurons (7N) which also co-express the Choline Acetyl Transferase (ChAT).
(b) Similar imaging from a *Egr2^{Cre};Phox2b^{27AlaCKI}* neonate. Note the considerable loss of Phox2b-expressing RTN neurons, as demonstrated previously in Ramanantsoa et al., 2011 and in Ruffault et al., 2015. Scale bars, 200 µm. Representative of 2 animals.

Supplementary Figure 11

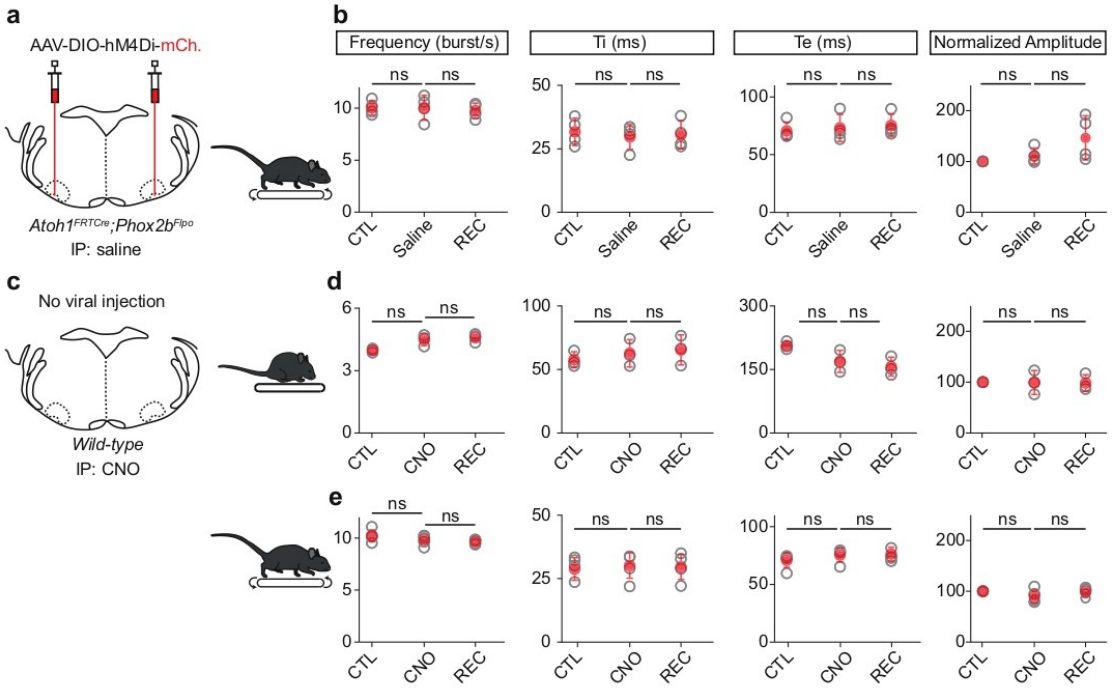

Supplementary Figure 11. Controls for chemogenetic silencing experiments. Related to Figure 6.
(a) Experimental strategy for the bilateral transfection of RTN$^{Phox2b/Atoh1}$ neurons using the inhibitory DREADD receptor hM4Di in *Atoh1*$^{FRTCre:}$*Phox2b*^{Flpo} adult mice. Injected mice were challenged to run on the motorized treadmill at 40 cm/s before, during and after intraperitoneal (IP) administration of saline solution.
(b) Quantifications of the diaphragm mean frequency, inspiratory (Ti) and expiratory (Te) times, and normalized amplitude before (CTL), during (Saline) and after (REC) IP administration of saline. Grey open circles are the means of individual mice, and filled red circles are the means ± SD across n mice. Saline administration alone does not alter the animals' capacity to modify its respiratory parameters during treadmill running.
(c) Experimental strategy to control for the effect of CNO administration alone, i.e., without expression of the hM4Di receptor, on breathing in resting and running mice.
(d, e) Similar respiratory parameters as in (**b**) during rest (**d**) and during treadmill running at 40 cm/s (**e**) before, during and after IP administration of CNO at 10 mg/kg.
In all graphs: ns, not significant (paired t-tests).

Supplementary Figure 12

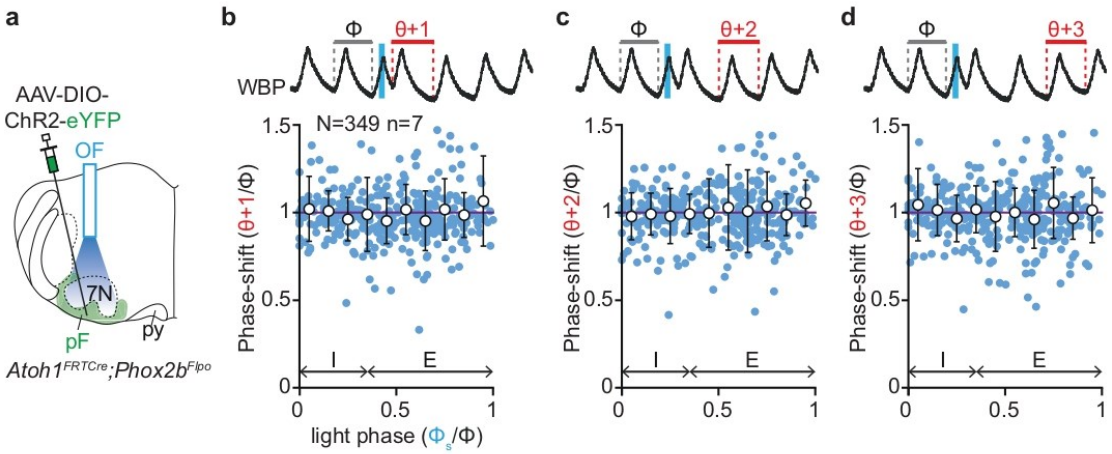

Supplementary Figure 12. Impact of photoactivating RTN$^{Phox2b/Atoh1}$ neurons on respiratory cycles following the light-perturbed cycle. Related to Figure 7.
(a) Experimental strategy for photoactivating RTN$^{Phox2b/Atoh1}$ neurons unilaterally in *Atoh1*^{FRTCre};*Phox2b*^{Flpo} adult mice.
(b) *Top*: whole body plethysmography (WBP) recording of respiratory cycles around a 50 ms stimulation. The cycle n+1 following the perturbed cycle is annotated on the trace (θ+1). *Bottom*: quantification of the perturbed cycle n+1 normalized to the control cycle (θ+1/Φ) as a function of the light phase (light cycle normalized to the control cycle: Φ_s/Φ). Values < 1 (purple line) indicate a shortening of the perturbed cycle (see Figure 2 for details). Blue circles represent individual data from N random trials from n mice and white circles are averages ± SD across all trials within 0.1 ms bins. Inspiration (I) and expiration (E) mean durations are annotated.
(c, d) Similar representations for cycles n+2 (θ+2, **c**) and n+3 (θ+3, **d**).

5. DISCUSSION

Our first interrogation focused on the behavioral significance of the locomotor arrests driven by V2a RS neurons (Bouvier et al., 2015). The results we obtained along the way raised new crucial questions that lead me to design specific experiments. To start exploring how the V2a neurons are engaged in arresting locomotion, first, we characterized anatomically their neuronal inputs with the highest selectivity. This showed that V2a Gi neurons receive most of their inputs from the contralateral Superior Colliculus. The inputs from the superior colliculus from the contralateral side made the V2a neurons candidates for relaying lateralized commands pertinent for orienting behaviors. We therefore performed unilateral photo-activations of V2a neurons in the Gi and found that the most striking response was a robust rotation of the head in the yaw axis and a displacement of the body orientation towards the stimulated side. We also observed an immediate horizontal deflection of the snout and the pupils tip towards the stimulated side. All these motor responses are known components of oriented attention in rodents (Kurnikova et al., 2017; Masullo et al., 2019; Sahibzada et al., 1986). Remarkably, when light stimulation was given during ongoing locomotion, the above orienting responses were accompanied by a bilateral arrest of all four limbs, followed by a pronounced change of locomotor trajectory towards the stimulated side. Moreover, we revealed the existence of at least three distinct V2a subsets: a lumbar-projecting subset whose activation arrests locomotion without changes in orientation nor pupil and snout movements, a cervical-projecting subset that evokes head rotation movements and whose activation alone imposes a change of locomotor direction, a facial-projecting subset that triggers an ipsilateral snout movement, but not head turning nor arrests of locomotion. Furthermore, we questioned the possibility that the divergent outcomes across muscular groups (e.g., ipsilateral excitation for the head and snout, bilateral inhibition for the hindlimbs) might reflect differences in V2a efferent connectivity at each executory module. Hence, using a rabies-based transsynaptic strategy on newborn

mice, we documented that the cervical and facial-projecting V2a neurons directly contact the motoneurons controlling neck and snout musculature, respectively.

Therefore, our work highlights that V2a Gi neurons orchestrate orienting motor actions and can be subdivided in at least two macro-categories, i) one controlling ocular and orofacial movements through supra-spinal projections, and ii) one controlling trunk and limb movements through spinal projections. Within each, a further specialization by projection site and postsynaptic target supports the control of individual motor components of a coherent multi-faceted behavior.

Additionally to my main PhD project, I participated to the main research of a former PhD student of the laboratory (Hérent et al., 2021). Results revealed that glutamatergic neurons of the MLR, and in particular that of the Cuneiform nucleus projects onto the PreBötC, the brainstem center that paces the inspiratory rhythm (Del Negro et al., 2018). Moreover, the activation of the CnF induces an increase of respiratory rate in a two-step sequential manner. Firstly, we observed a modest increase immediately at light onset but before the first locomotor movements. Secondly, the average respiratory rate was further augmented when the animal effectively engages in locomotion. These data suggest that glutamatergic CnF neurons can modulate respiratory activity independently of their action on limb movements, in line with what was reported in the lamprey (Gariepy et al., 2012). Yet the fact that the engagement in actual locomotor movements is associated with a stronger increase in breathing may reflect the mobilization, during actual running, of an additional activatory signal which could originate in executive lumbar locomotor circuits. We indeed show that the glutamatergic cells located ventrally in the lumbar spinal cord, send ascending projections to the brainstem. Furthermore, the activation of the lumbar segments increased the frequency of respiratory-like activities. However, in contrast to the anterograde tracings from the CnF glutamatergic neurons, these ascending projections were not targeted to the preBötC but rather to the parafacial respiratory region, another candidate of respiratory regulation during metabolic challenges including effort. Targeted chemogenetic silencing of these neurons demonstrated that they are required for setting the adapted ventilatory frequency during running exercise.

Altogether, these results thus uncover here two systems by which the central locomotor network can enable respiratory rate to be augmented in relation to running activity. These data expand, on the one hand, the functional implications of the MLR and the locomotor CPG beyond locomotor initiation and execution to *bona fide* respiratory modulation and on the other hand, the adaptive respiratory ambitions of the RTN beyond central $C0_2$ chemoception to “locomotor-ception”.

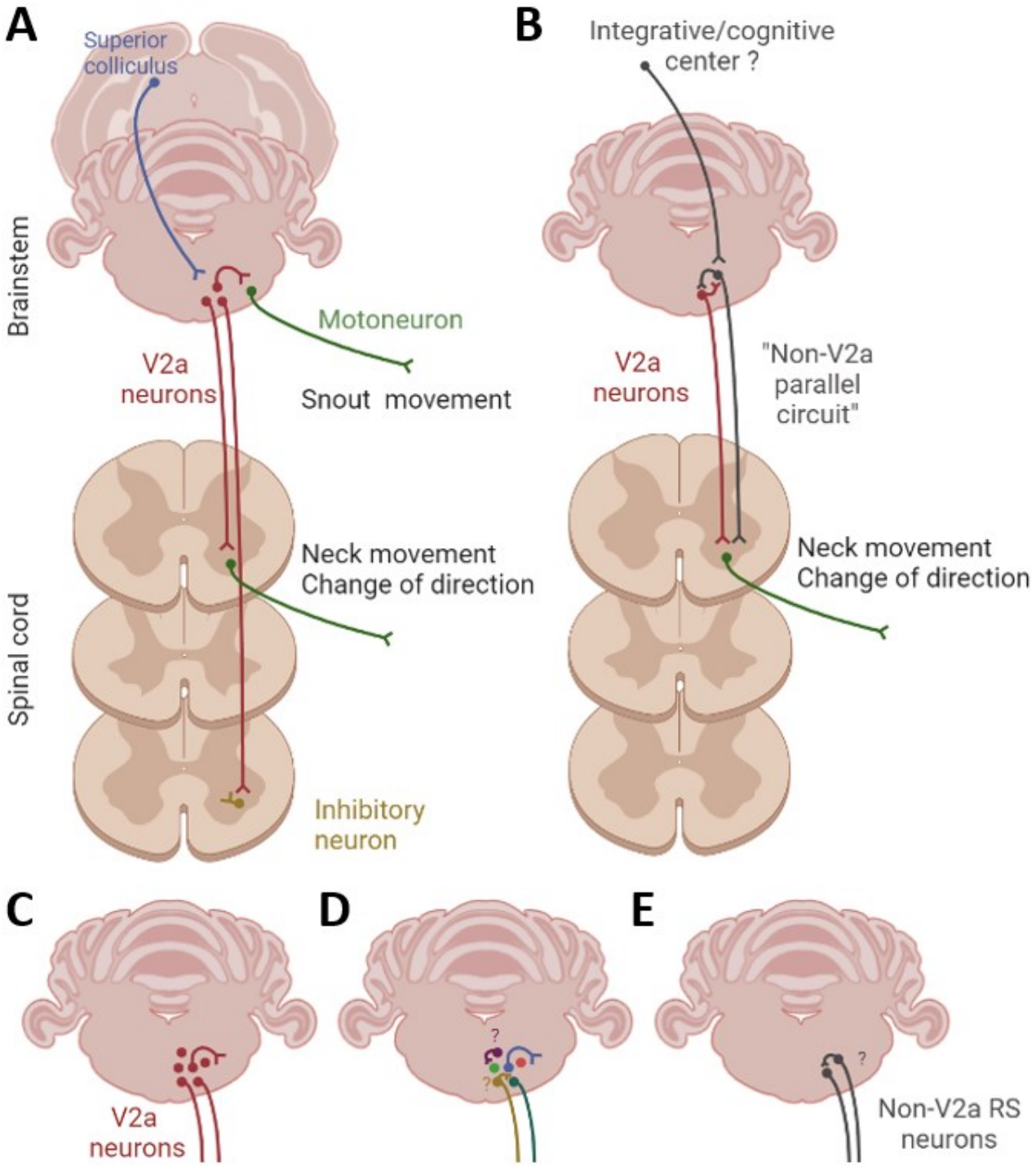

Figure 13. Overview of the circuits revealed in this work. (A) Schematic representation of the large-scale neural circuits: The superior colliculus projects to the V2a neurons (in red) that are organized in subsets controlling different components of orientation. The 7N-projecting subset contacts the motoneurons (in green) controlling snout musculature. The C2-projecting V2a neurons contacts motoneurons (in green) controlling axial musculature of the neck. The L2-projecting V2a neurons contacts inhibitory interneurons (in yellow) within the lumbar spinal cord. (B) Schematic representation of a neural circuits composed by non-V2a neurons that might be mobilized in other behavioral contexts. Furtheremore, there might be a reciprocal connection between V2a and non-V2a RS neurons contacting motoneurons that control neck muscles. (C) The V2a neurons (in red) control multiple motor components pertinent for orientation. (D) V2a neurons is a heterogeneous population (different colors) organized in subsets each controlling distinct a specific motor component. (E) RS neurons that are non-V2a might control other motor behaviors and could be organized in subsets. Image created using Biorender.

5.1. The head turning steers locomotor trajectory

The discovery of the cervical-projecting V2a subset that control head turning and its activation suffices to steer the animals' directional heading, placing the head orientation as the prime driver of locomotor trajectory is very important since the mechanical substrate for trajectory changes during ongoing locomotion, whether it is head orientation (Dollack et al., 2019; Grasso et al., 1996; Grasso et al., 1998), an asymmetric descending drive to limb controllers (Fagerstedt and Ullen, 2001; Oueghlani et al., 2018) or a combination of both, has remained speculative. Indeed, our investigations demonstrated that the unilateral activation of the entire population of the medullary V2a Gi neurons or the cervical-projecting V2a neurons leads to a change in direction, but that this change cannot be reproduced when activating only the lumbar-projecting V2a neurons. This argues that the impact of V2a neurons on locomotor trajectory is primarily supported by their capacity to impose the head orientation. It will be extremely interesting to examinate whether mice could change direction without the lead of the head. This might help to comprehend what are the neural circuits for the steering of the locomotion, which is a topic that is poorly studied. Indeed,

while the control of forward locomotion had progressed substantially over the last decades, our investigations provided here the first identification of a cellular substrate for the control of locomotor direction. Notably, as the head was already proposed and studied as an essential drive for steering trajectory in humans (Grasso et al., 1996; Grasso et al., 1998), the neural circuits controlling the head turning is poorly understood. Most of the studies focused on the superior colliculus/optic tectum (Basso and May, 2017; Isa et al., 2021; Saitoh et al., 2007). Here, we uncover a large-scale neural circuit that connect the superior colliculus, the V2a neurons that reach the cervical spinal cord, and the motoneurons controlling neck musculature, which contraction induces the head turning and the consequently change of the trajectory while the animal is locomoting (Figure 13A). For future research, as we observed also RS neurons that are not Chx10-positive contacting the motoneurons controlling axial musculature of the neck, it might be important to understand whether there are other neural substrates that control the head movements in order to change the trajectory (Figure 13B). One possibility is that such "parallel" neural circuits might be used for different behavioral situations, including escaping or hunting, that are controlled by different cognitive/integrative centers. Discovering whether these parallel neural circuits might be also reciprocally connected could be important (Figure 13B). Indeed, this anatomical finding could allow to understand how distinct behaviors are associated. Notably, the steering of the locomotor trajectory is an excellent example of composite/complex motor behavior that requires the involvement of multiple higher/cognitive and executive centers. Indeed, as the change of the trajectory might be due to avoid an obstacle or to a change of the destination, in both of the cases it is induced by a rapid integration of sensory inputs (vision, audition) to modify a motor behavior that was already ongoing (locomotion). Moreover, it requires further movements and postural adjustments of multiple parts of the body to avoid losing the equilibrium and fall.

During the second year of my PhD, we realized that another important laboratory was studying the same topic (Cregg et al., 2020). This situation represented an important point of my career since I found myself in a situation of "concurrency". Although it is clearly not optimal, it is common in research. It represented for me a difficult moment but the same

time an important situation for my professional training. Thanks to the motivation of my PhD supervisor for me to continue on my own path and to the support of the whole team, I continued my research and I am persuaded that this was an important step for my PhD formation. Indeed, I from one side lit forced me to be more efficient, on the other side, and probably this is the most important point, I learnt how to question my own research and to be more critical about my own work. Furthermore, even if some of the results we obtained coincided with the results acquired from the other laboratory, which is important sign of reproducibility, the two works diverged on many aspects. Indeed, we both demonstrated that the unilateral activation of V2a Gi neurons induces a change in direction. While the other laboratory claim that the steering of the trajectory is regulated by an asymmetric control of V2a neurons on lumbar locomotor circuits, we rather argued, and demonstrated, that this change cannot be reproduced when activating only the lumbar-projecting subset, even unilaterally. Furthermore, we demonstrated that the activation of the cervical-projecting V2a neurons, which induces the ipsilateral head turning, suffices to evoke a change of the trajectory toward the direction imposed by the head. This argues that the impact of the V2a neurons on locomotor trajectory is primarily supported by their capacity to impose the head orientation, rather than by their regulation of hindlimb controllers. The hindlimb asymmetry that indeed occurs during turning thus does not appear to be a primary consequence of activated descending V2a neurons but may rather be an adaptive adjustment to the displacement of the body axis, primed by the head, which is driven by cervical-projecting V2a neurons.

5.2. V2a neurons are organized in projection-based subsets

The mobilization of different motor actions controlled by medullary V2a neurons raises several questions: how are these motor actions controlled by the V2a neurons? Do the V2a neurons have access to the cervical and lumbar segments of the spinal cord where reside the circuits for the control of the head and hindlimb movements, respectively? Do they have access to the brainstem motor circuits in order to evoke the orofacial movements

observed? Do the medullary V2a neurons control all these motor responses as a unique entity through a wide collateralization of their axons, or instead through distinct subpopulations? Do the opposite motor outcomes triggered by this cell class (promoting effect for head/eye, or arrest for locomotion) reflect different cell types (inhibitory/excitatory) contacted at different executory centers along the brainstem and the spinal cord?

These questions are crucial for understanding the reasoning of our experiments during the past four years. Indeed, we proceeded our investigations starting from the idea that the V2a neurons might have access to the distinct brainstem and spinal cord regions for the control of the diversity of motor actions observed during their activation. However, and that is one of the most striking findings of my work, these distinct motor spinal cord segments are not predominantly contacted by a unique population of V2a neurons with branched collaterals. Conversely, as I described before, V2a neurons are organized in subsets controlling distinct motor actions (Figure 13A).

Our results reveal that multiple motor components of orientation are controlled by distinct reticular neurons that share a common genetic identity but that differ in their efferent connectivity. Therefore, our investigations underscore the organization of the reticular formation in functional modules defined by transcription factors, and at the same time argues for a further segregation within modules whereby a functional connectivity organized by muscle or muscle groups may underlie the execution of individual motor actions of a coherent and multi-faceted behavior (Fig 13 C,D). Indeed, similar specialization by projection has been proposed for other brain structures including cerebello-spinal neurons (Sathyamurthy et al., 2020), cortico-spinal neurons (Nelson et al., 2021; Sahni et al., 2021) and for the MLR (Ferreira-Pinto et al., 2021). Moreover, in our study on exercise hyperpnoea, we demonstrated that the MLR does not control only locomotion, but also respiratory centers. Whether these functional outcomes are controlled by one neural population sending collaterals to the distinct executory centers or there are distinct subpopulations each controlling one functions, is still unknown. We postulate for the second

hypothesis. Indeed, it has been showed, in lampreys that the MLR contacts the locomotor and respiratory centers with distinct subpopulations (Gariepy et al., 2012).

Such specialization and diversification of motor actions controlled by specific projections could represent an important entry point to further decipher the neuronal basis for the diversity of motor repertoires and how the brain elaborates complex movements. Indeed, this diversification might allow the nervous system to control one motor component independently from the others, when needed, and to increase the degree and versatility in the execution of composite motor behaviors. Furthermore, these subsets might be interconnected. Indeed, it has been shown that locally-projecting V2a neurons contact spinally-projecting V2a neurons (Chopek et al., 2021). However, whether different spinally-projecting V2a subsets are connected, is still not known. If so, there could be a reciprocal control between different subsets. Moreover, as the V2a neurons represent only a fraction of the RS neurons, it is crucial to focus in addition to the other types of RS neurons on order to decipher whether the organization of the V2a neurons is unique for this cell type, or whether the other cell types share similar configuration in controlling actions of composite motor behaviors. Indeed, studies on other brainstem and spinal cell types defined by transcription factors demonstrated that they might contain distinct functional subtypes (Sweeney et al., 2018; Talpalar et al., 2013; Wu et al., 2017). On this basis, from our study on the V2a neurons, we hypothesize that there might be a further specialization also in other RS cell types, that still remain to identify genetically (Fig 13E).

An approach that might be potentially groundbreaking in the investigation of the genetic diversity of the reticular formation is represented by the single cell RNA-sequencing. Indeed, as we saw above, the identification and the study of a class of neurons by transcription factors has limitations. Indeed, transcription factors might be expressed only transiently at birth or with different degree of expression at early postnatal stages and adult animal. There might even be cells sharing the same genetic history with different levels of expression of the common transcription factor, which seems to be the case of the V2a neurons (Hayashi et al., 2018). Furthermore, this classification with one single transcription factor cannot recapitulate a further functionally and anatom²ical classification within a so-

called “cell type”. Regarding V2a neurons, the diversification highlighted throughout my doctoral work is bound to reflect differences in gene expression that go well beyond the classification by the expression of Chx10. Moreover, single cells RNA sequencing can help to identified cell types by sequencing the RNA of hundreds of cells simultaneously (Jaitin et al., 2014), in order to reveal and explore heterogeneity in complex structures. For instance, such strategy has been used to delineate cell types with the spinal cord (Blum et al., 2021; Sathyamurthy et al., 2018). In our case, we could use it not only to reveal a possible genetic code underlying the diversity of the V2a neurons, but help study RS neurons in general. We might, first, identify a genetic signature that is associated to all reticulospinal neurons but that may be not shared with neurons of the reticular formation that do not project to the spinal cord. We could also reveal genetic determinants of other RS neurons besides the V2a ones. We might also identify the genetic underpinnings for the existence of different subsets of V2a neurons that differ by their projections. Applying the scRNA-seq on investigating the transcriptomic profiles of the reticular neurons, together with the study of projection profiles, soma position, developmental origin, might be fundamental to allow scientists to further progress in the understanding the neuronal heterogeneity of the reticular formation, and in general the entire brainstem, and its functions. Moreover, scRNA-seq strategy might allow scientists to identify the homologous cellular population in primate, and make comparison between rodents and primates, including humans.

5.3. Impact on clinical research

An important follow up of all the research focusing on reticulospinal neurons and their role in motor control, is represented by the investigation of the neural plasticity (sprouting and regeneration) of the descending fibers occurring after spinal cord injuries. The term “sprouting” typically refers to new connections established by an axon that was not itself damaged. This is notably illustrated in hemi-section models of SCI, where descending axons reaching the non-lesioned side often branch new collaterals to the lesioned side (Engmann et al., 2020; Raineteau and Schwab, 2001; Zorner et al., 2014). On

the other hand, “regeneration” relates to the growth of cut axons and their extension into or beyond the lesioned tissue. There is general agreement that the greatest hope for functional recovery after spinal cord injury involves regeneration of descending motor tracts (Siddiqui et al., 2015; Tuszynski and Steward, 2012). Addressing the capacity of medullary descending tracts to sprout and/or regenerate is therefore essential and, together with understanding the anatomy of the RS neurons and their correlation with motor actions, represents a major challenge and a crucial necessary background to developed new efficient therapies aimed to motor recoveries after spinal cord injuries. Therefore, unveiling the link from the upper motor center involved in action planning and circuits in the brainstem and spinal cord leading the execution of body movements will help design protocols to restore post-traumatic motor disabilities. In particular, such protocols could led to locomotor recovery following spinal cord injury (SCI), an incurable condition in which the interruption or weakening of axonal tracts leads to highly debilitating loss of motor and sensory functions, including the ability to stand and walk, (Sekhon and Fehlings, 2001; Varma et al., 2013; Wilson et al., 2012). Indeed, following SCI, the locomotor CPG in the spinal cord is denervated from its obligatory descending signals but it retains much of the capacity to produce a locomotor-like output if activated adequately. In fact, some degree of motor function is often regained spontaneously from the first clinical assessment. This is thought, at least from correlations studies, to owe to spared descending tracts and/or a potential regrowth of the severed ones (Fouad and Tse, 2008; Hilton et al., 2017; Zorner et al., 2014). Establishing means of providing locomotor-relevant descending inputs below the lesion is thus an absolute requirement.

6. CONCLUSION

Our investigations reveal therefore that the V2a Gi neurons form a functional module of the reticular formation that globally controls orienting motor actions but that, within this module, projection-defined subsets are in charge of the individual component motor actions. This possibility is well in line with the idea of the reticular formation as a key getaway for the regulation of motor actions and its organization into functional “clusters” with specialized outputs (Humphries et al., 2007). These results contribute to the elucidation of the organization of the reticular formation, in line with the proposition that the brainstem is stratified in channels that must be combined to generate the motor signal to the execution of a composed behavior (Arber and Costa, 2022). A crucial point for next investigations might be to focus on the local connectivity within the reticular formation, whether there is a crosstalk between different modules, or even between different subsets at the level of the reticular formation in order to uncover whether the reticular formation has a role in refining motor programs, in action selection and commitment to action. Importantly, to understand the functioning of the reticular formation in controlling motor behaviors, it will be essential to consider the reticular formation part of a system-wide network that is connected to other supraspinal brain areas that control motor actions. Indeed, I am persuaded that uncovering how individual motor areas are bound into coordinated networks to perform the desired movements, is essential to understand how the brain control motor behaviors. Altogether, these supraspinal motor-related areas might concur to the high level of diversity, versatility and flexibility of the execution of the motor repertoires.

If we go back to the shaolin monk represented within the first page of this manuscript, we can now, comprehend the enormous efforts that are done by his nervous system to correctly accomplish such composite motor behavior. Indeed, as we saw, performing multiple motor actions simultaneously, requires the activity of multiple neural centers that span throughout the brain, and a crucial role is played by the reticular formation. However, we are just at the beginning of understanding how all these centers are connected to form

large-scale neuronal circuits, and how the reticular formation, with its high neural heterogeneity, relays the motor signal and permits the execution of composite motor behaviors.

7. ENGLISH ABSTRACT

An essential function of the brain is to perform the desired motor actions. Our nervous system controls complex movements to execute coherent motor behaviors in response to our needs at every specific moment. Most studies focus on the executory centers in the brain and the spinal cord, or on the integrative/cognitive centers upstream. The main structure that conveys the motor command from the upstream centers to the downstream centers is the reticular formation. It is known that it acts as a relay and that it is involved in multiple motor actions. However, whether it is organized in different cell types controlling individual motor actions or whether it works as a unique entity controlling synergistically multiple movements has to be addressed.

My PhD project attempts to understand how the reticular formation selects, initiates and combines multiple motor actions To address this we examined, in mice, the function and diversity of a genetically circumscribed class of glutamatergic neurons, the V2a neurons (Chx10-expressing).

Firstly, using rabies-based transsynaptic tracings, we reveal that V2a neurons receive abundant synaptic inputs from the contralateral superior colliculus, making them a candidate relay of orienting commands. Furthermore, we show that unilateral photo-activations of V2a neurons evoke multiple orienting-like motor responses, including a yaw rotation of the head and a displacement of the body axis towards the stimulated side. During locomotion, such activations lead to a transient locomotor arrest followed by a striking change in path trajectory.

Secondly, using retrograde tracers and circuit optogenetics we reveal that these multiple motor actions are supported by distinct projection-defined V2a subsets, with at least 1) a lumbar-projecting subset whose activation, even unilaterally, arrests locomotion but neither impacts trajectory nor evokes orienting movements, and 2) a cervical-projecting

subset dedicated to head orientation and whose activation suffices to change the animal's trajectory. This argues that the impact of V2a RS neurons on path trajectory owes to their capacity to impose the head orientation.

Thirdly, we reveal that V2a reticular neurons also control other motor components of orienting, including snout and eye, whose executory circuits are located in the brainstem. Importantly, these functions are supported by brainstem-projecting V2a subsets rather than by collaterals of the spinally-projecting ones. Indeed, we identified a V2a subset projecting to the facial motor nucleus (7N) whose activation elicits an ipsilateral snout displacement, but does not control neck and eye movements nor arrests locomotion.

Fourthly, we question the possibility that the divergent outcomes across muscular groups (e.g., ipsilateral excitation for the head and snout, bilateral inhibition for the hindlimbs) reflect differences in V2a efferent connectivity at each executory center. Hence, using a rabies-based transsynaptic strategy on newborn mice, we document the identity of the postsynaptic cells of the V2a neurons at different brainstem and spinal levels. Specifically, we demonstrate that some V2a reticulospinal neurons make monosynaptic connection with motoneurons controlling axial muscle of the neck, at the level of the upper cervical spinal cord. We also demonstrate that the V2a neurons directly contact facial motoneurons that control snout and orofacial movements.

Our work highlights that V2a Gi neurons orchestrate orienting motor actions and can be subdivided in at least two macro-categories, i) one controlling ocular and orofacial movements through supra-spinal projections, and ii) one controlling trunk and limb movements through spinal projections. Within each, a further specialization by projection site and postsynaptic target supports the control of individual motor components of the multi-faceted orienting behavior.

8. FRENCH ABSTRACT

La principale fonction du cerveau est d'exécuter les actions motrices nécessaires à nos besoins à chaque instant. La plupart des études se concentrent sur les centres exécutifs de la moelle épinière ou sur les centres intégratifs et cognitifs en amont. Cependant, la structure principale qui transmet les commandes motrices de multiples comportements vers les centres exécutifs spinaux est la formation réticulée. Il n'est toutefois pas connu si la formation réticulée est organisée en différents types cellulaires contrôlant chacun des actions motrices individuelles, ou bien si elle forme une entité unique contrôlant de manière synergique de multiples actions. Mon doctorat vise ainsi à comprendre l'organisation de la formation réticulée pour l'orchestration des multiples composantes d'un comportement global cohérent.

Je me suis intéressé en particulier aux neurones V2a, sous-population génétiquement définie de neurones excitateurs de la formation réticulée. Premièrement, nous révélons par traçages transsynaptiques que les neurones V2a du noyau gigantocellulaire (Gi) reçoivent de nombreuses entrées synaptiques du colliculus supérieur contralatéral, ce qui en fait des candidats pour orchestrer les commandes d'orientation. Corroborant cela, nous montrons que la photo-activation unilatérale des neurones V2a induit en effet de multiples réponses typiques de l'orientation, dont une rotation de la tête et un déplacement du corps vers le côté stimulé. Pendant la locomotion, l'activation de ces neurones entraîne un arrêt suivi d'un changement de direction.

Deuxièmement, par traçages rétrogrades et optogénétique, nous révélons que ces différentes actions motrices sont soutenues par des sous-ensembles de neurones V2a distincts selon leurs projections efférentes, avec au moins 1) un sous-ensemble qui projette vers la moelle lombaire et dont l'activation, même unilatérale, arrête la locomotion mais n'a pas d'impact sur la trajectoire et n'évoque pas de mouvements d'orientation, et 2) un sous-ensemble qui projette vers la moelle cervicale et dont l'activation suffit à changer la

trajectoire de l'animal. Ceci suggère que l'impact des neurones V2a sur la trajectoire est dû à leur capacité à imposer l'orientation de la tête.

Troisièmement, nous révélons que les neurones V2a contrôlent d'autres composantes motrices de l'orientation, notamment le museau et l'œil, dont les circuits exécutifs sont dans le tronc cérébral. Nous montrons surtout que ces fonctions sont soutenues par des sous-ensembles de V2a projetant localement dans le tronc cérébral plutôt que par des collatérales de ceux projetant dans la moelle épinière. En effet, nous avons identifié un sous-ensemble supraspinal de neurones V2a projetant vers le noyau moteur facial (7N) et dont l'activation déplace le museau, mais ne contrôle ni les mouvements du cou et des yeux, ni la locomotion.

Quatrièmement, nous interrogeons la possibilité que les finalités fonctionnelles différentes des neurones V2a entre centres exécutifs (par exemple, excitation ipsilatérale pour la tête et le museau, inhibition bilatérale pour les membres postérieurs) reflètent des différences dans la connectivité efférente. Par traçages transsynaptiques, nous démontrons que certains neurones V2a établissent une connexion monosynaptique avec les motoneurones contrôlant le muscle axial du cou. De plus, nous certains neurones V2a contactent directement les motoneurones contrôlant les mouvements du museau.

Notre travail met ainsi en évidence que les neurones V2a de la formation réticulée orchestrent les différentes composantes motrices de l’orientation et peuvent être subdivisés en au moins deux macro-catégories : une contrôlant les mouvements oculaires et orofaciaux par des projections supra-spinales, et une contrôlant les mouvements du tronc et des membres par des projections spinales. Dans chacune d'elles, une spécialisation par site de projection et cible postsynaptique soutient le contrôle indépendant de chaque composante.

9. BIBLIOGRAPHY

Akbarian, S., Grusser, O.J., and Guldin, W.O. (1993). Corticofugal projections to the vestibular nuclei in squirrel monkeys: further evidence of multiple cortical vestibular fields. J Comp Neurol *332*, 89-104.

Al-Mosawie, A., Wilson, J.M., and Brownstone, R.M. (2007). Heterogeneity of V2-derived interneurons in the adult mouse spinal cord. Eur J Neurosci *26*, 3003-3015.

Albano, J.E., Norton, T.T., and Hall, W.C. (1979). Laminar origin of projections from the superficial layers of the superior colliculus in the tree shrew, Tupaia glis. Brain Res *173*, 1-11.

Alstermark, B., Lundberg, A., Pinter, M., and Sasaki, S. (1987). Vestibular effects in long C3-C5 propriospinal neurones. Brain Res *404*, 389-394.

Alstermark, B., Ogawa, J., and Isa, T. (2004). Lack of monosynaptic corticomotoneuronal EPSPs in rats: disynaptic EPSPs mediated via reticulospinal neurons and polysynaptic EPSPs via segmental interneurons. J Neurophysiol *91*, 1832-1839.

Amiel, J., Laudier, B., Attie-Bitach, T., Trang, H., de Pontual, L., Gener, B., Trochet, D., Etchevers, H., Ray, P., Simonneau, M*., et al.* (2003). Polyalanine expansion and frameshift mutations of the paired-like homeobox gene PHOX2B in congenital central hypoventilation syndrome. Nat Genet *33*, 459-461.

Apter, J.T. (1946). Eye movements following strychninization of the superior colliculus of cats. J Neurophysiol *9*, 73-86.

Arber, S., and Costa, R.M. (2018). Connecting neuronal circuits for movement. Science *360*, 1403-1404.

Arber, S., and Costa, R.M. (2022). Networking brainstem and basal ganglia circuits for movement. Nat Rev Neurosci *23*, 342-360.

Asanuma, C., Thach, W.T., and Jones, E.G. (1980). Nucleus interpositus projection to spinal interneurons in monkeys. Brain Res *191*, 245-248.

Asboth, L., Friedli, L., Beauparlant, J., Martinez-Gonzalez, C., Anil, S., Rey, E., Baud, L., Pidpruzhnykova, G., Anderson, M.A., Shkorbatova, P*., et al.* (2018). Cortico-reticulo-spinal circuit reorganization enables functional recovery after severe spinal cord contusion. Nat Neurosci *21*, 576-588.

Azim, E., Jiang, J., Alstermark, B., and Jessell, T.M. (2014). Skilled reaching relies on a V2a propriospinal internal copy circuit. Nature.

Barlow, S.M. (2009a). Central pattern generation involved in oral and respiratory control for feeding in the term infant. Curr Opin Otolaryngol Head Neck Surg *17*, 187-193.

Barlow, S.M. (2009b). Oral and respiratory control for preterm feeding. Curr Opin Otolaryngol Head Neck Surg *17*, 179-186.

Barth, K.A., Kishimoto, Y., Rohr, K.B., Seydler, C., Schulte-Merker, S., and Wilson, S.W. (1999). Bmp activity establishes a gradient of positional information throughout the entire neural plate. Development *126*, 4977-4987.

Basso, D.M., Beattie, M.S., and Bresnahan, J.C. (2002). Descending systems contributing to locomotor recovery after mild or moderate spinal cord injury in rats: experimental evidence and a review of literature. Restor Neurol Neurosci *20*, 189-218.

Basso, M.A., Bickford, M.E., and Cang, J. (2021). Unraveling circuits of visual perception and cognition through the superior colliculus. Neuron *109*, 918-937.

Basso, M.A., and May, P.J. (2017). Circuits for Action and Cognition: A View from the Superior Colliculus. Annu Rev Vis Sci *3*, 197-226.

Batton, R.R., 3rd, Jayaraman, A., Ruggiero, D., and Carpenter, M.B. (1977). Fastigial efferent projections in the monkey: an autoradiographic study. J Comp Neurol *174*, 281-305.

Bellardita, C., and Kiehn, O. (2015). Phenotypic characterization of speed-associated gait changes in mice reveals modular organization of locomotor networks. Curr Biol *25*, 1426-1436.

Bickford, M.E., Zhou, N., Krahe, T.E., Govindaiah, G., and Guido, W. (2015). Retinal and Tectal "Driver-Like" Inputs Converge in the Shell of the Mouse Dorsal Lateral Geniculate Nucleus. J Neurosci *35*, 10523-10534.

Bjorklund, A., and Skagerberg, G. (1979). Evidence for a major spinal cord projection from the diencephalic A11 dopamine cell group in the rat using transmitter-specific fluorescent retrograde tracing. Brain Res *177*, 170-175.

Bjursten, L.M., Norrsell, K., and Norrsell, U. (1976). Behavioural repertory of cats without cerebral cortex from infancy. Exp Brain Res *25*, 115-130.

Blum, J.A., Klemm, S., Shadrach, J.L., Guttenplan, K.A., Nakayama, L., Kathiria, A., Hoang, P.T., Gautier, O., Kaltschmidt, J.A., Greenleaf, W.J*., et al.* (2021). Single-cell transcriptomic analysis of the adult mouse spinal cord reveals molecular diversity of autonomic and skeletal motor neurons. Nat Neurosci *24*, 572-583.

Bolton, P.S., Goto, T., Schor, R.H., Wilson, V.J., Yamagata, Y., and Yates, B.J. (1992). Response of pontomedullary reticulospinal neurons to vestibular stimuli in vertical planes. Role in vertical vestibulospinal reflexes of the decerebrate cat. J Neurophysiol *67*, 639-647.

Bouvier, J., Caggiano, V., Leiras, R., Caldeira, V., Bellardita, C., Balueva, K., Fuchs, A., and Kiehn, O. (2015). Descending Command Neurons in the Brainstem that Halt Locomotion. Cell *163*, 1191-1203.

Bouvier, J., Thoby-Brisson, M., Renier, N., Dubreuil, V., Ericson, J., Champagnat, J., Pierani, A., Chedotal, A., and Fortin, G. (2010). Hindbrain interneurons and axon guidance signaling critical for breathing. Nat Neurosci *13*, 1066-1074.

Bretzner, F., and Brownstone, R.M. (2013). Lhx3-Chx10 reticulospinal neurons in locomotor circuits. J Neurosci *33*, 14681-14692.

Briscoe, J., and Ericson, J. (2001). Specification of neuronal fates in the ventral neural tube. Curr Opin Neurobiol *11*, 43-49.

Briscoe, J., Pierani, A., Jessell, T.M., and Ericson, J. (2000). A homeodomain protein code specifies progenitor cell identity and neuronal fate in the ventral neural tube. Cell *101*, 435-445.

Briscoe, J., Sussel, L., Serup, P., Hartigan-O'Connor, D., Jessell, T.M., Rubenstein, J.L., and Ericson, J. (1999). Homeobox gene Nkx2.2 and specification of neuronal identity by graded Sonic hedgehog signalling. Nature *398*, 622-627.

Brodal, A., and Szikla, G. (1972). The termination of the brachium conjunctivum descendens in the nucleus reticularis tegmenti pontis. An experimental anatomical study in the cat. Brain Res *39*, 337-351.

Brown, G. (1911). Two Cases of Death from Post-Anaesthetic Acid Intoxication. Br Med J *1*, 429.

Brown, T.G. (1914). On the nature of the fundamental activity of the nervous centres; together with an analysis of the conditioning of rhythmic activity in progression, and a theory of the evolution of function in the nervous system. J Physiol *48*, 18-46.

Brownstone, R.M., and Chopek, J.W. (2018). Reticulospinal Systems for Tuning Motor Commands. Frontiers in neural circuits *12*, 30.

Brownstone, R.M., and Wilson, J.M. (2008). Strategies for delineating spinal locomotor rhythm-generating networks and the possible role of Hb9 interneurones in rhythmogenesis. Brain Res Rev *57*, 64-76.

Caggiano, V., Leiras, R., Goni-Erro, H., Masini, D., Bellardita, C., Bouvier, J., Caldeira, V., Fisone, G., and Kiehn, O. (2018). Midbrain circuits that set locomotor speed and gait selection. Nature *553*, 455-460.

Caldeira, V., Dougherty, K.J., Borgius, L., and Kiehn, O. (2017). Spinal Hb9::Cre-derived excitatory interneurons contribute to rhythm generation in the mouse. Sci Rep *7*, 41369.

Capelli, P., Pivetta, C., Soledad Esposito, M., and Arber, S. (2017). Locomotor speed control circuits in the caudal brainstem. Nature *551*, 373-377.

Carbo-Tano, M., Lapoix, M., Jia, X., Auclair, F., Dubuc, R., and Wyart, C. (2022). Functional coupling of the mesencephalic locomotor region and V2a reticulospinal neurons driving forward locomotion. bioRxiv, 2022.2004.2001.486703.

Carrea, R.M., and Mettler, F.A. (1954). The anatomy of the primate brachium conjunctivum and associated structures. J Comp Neurol *101*, 565-689.

Cazalets, J.R., Grillner, P., Menard, I., Cremieux, J., and Clarac, F. (1990). Two types of motor rhythm induced by NMDA and amines in an in vitro spinal cord preparation of neonatal rat. Neurosci Lett *111*, 116-121.

Cazalets, J.R., Sqalli-Houssaini, Y., and Clarac, F. (1992). Activation of the central pattern generators for locomotion by serotonin and excitatory amino acids in neonatal rat. J Physiol *455*, 187-204.

Chau, C., Giroux, N., Barbeau, H., Jordan, L., and Rossignol, S. (2002). Effects of intrathecal glutamatergic drugs on locomotion I. NMDA in short-term spinal cats. J Neurophysiol *88*, 3032-3045.

Chopek, J.W., Zhang, Y., and Brownstone, R.M. (2021). Intrinsic brainstem circuits comprised of Chx10-expressing neurons contribute to reticulospinal output in mice. J Neurophysiol *126*, 1978-1990.

Clower, D.M., West, R.A., Lynch, J.C., and Strick, P.L. (2001). The inferior parietal lobule is the target of output from the superior colliculus, hippocampus, and cerebellum. J Neurosci *21*, 6283-6291.

Cordes, S.P. (2001). Molecular genetics of cranial nerve development in mouse. Nat Rev Neurosci *2*, 611-623.

Corneil, B.D., Olivier, E., and Munoz, D.P. (2002). Neck muscle responses to stimulation of monkey superior colliculus. II. Gaze shift initiation and volitional head movements. J Neurophysiol *88*, 2000-2018.

Courjon, J.H., Olivier, E., and Pelisson, D. (2004). Direct evidence for the contribution of the superior colliculus in the control of visually guided reaching movements in the cat. J Physiol *556*, 675-681.

Courjon, J.H., Zenon, A., Clement, G., Urquizar, C., Olivier, E., and Pelisson, D. (2015). Electrical stimulation of the superior colliculus induces non-topographically organized perturbation of reaching movements in cats. Front Syst Neurosci *9*, 109.

Cowley, K.C., and Schmidt, B.J. (1994). A comparison of motor patterns induced by N-methyl-D-aspartate, acetylcholine and serotonin in the in vitro neonatal rat spinal cord. Neurosci Lett *171*, 147-150.

Cowley, K.C., and Schmidt, B.J. (1997). Regional distribution of the locomotor pattern-generating network in the neonatal rat spinal cord. J Neurophysiol *77*, 247-259.

Cregg, J.M., Leiras, R., Montalant, A., Wanken, P., Wickersham, I.R., and Kiehn, O. (2020). Brainstem neurons that command mammalian locomotor asymmetries. Nat Neurosci *23*, 730-740.

Crone, S.A., Quinlan, K.A., Zagoraiou, L., Droho, S., Restrepo, C.E., Lundfald, L., Endo, T., Setlak, J., Jessell, T.M., Kiehn, O*., et al.* (2008). Genetic ablation of V2a ipsilateral interneurons disrupts left-right locomotor coordination in mammalian spinal cord. Neuron *60*, 70-83.

Crone, S.A., Viemari, J.C., Droho, S., Mrejeru, A., Ramirez, J.M., and Sharma, K. (2012). Irregular Breathing in Mice following Genetic Ablation of V2a Neurons. J Neurosci *32*, 7895-7906.

Dale, N., and Roberts, A. (1984). Excitatory amino acid receptors in Xenopus embryo spinal cord and their role in the activation of swimming. J Physiol *348*, 527-543.

Decety, J. (1993). Analysis of actual and mental movement times in graphic tasks. Acta Psychol (Amst) *82*, 367-372.

Degtyarenko, A.M., Simon, E.S., and Burke, R.E. (1998). Locomotor modulation of disynaptic EPSPs from the mesencephalic locomotor region in cat motoneurons. J Neurophysiol *80*, 3284-3296.

Deisseroth, K. (2015). Optogenetics: 10 years of microbial opsins in neuroscience. Nat Neurosci *18*, 1213-1225.

Dejours, P., Raynaud, J., and Flandrois, R. (1959). [Control of respiration by certain neurogenic stimuli during muscular exercise in human]. C R Hebd Seances Acad Sci *248*, 1709-1712.

Del Negro, C.A., Funk, G.D., and Feldman, J.L. (2018). Breathing matters. Nature reviews *19*, 351-367.

Delcomyn, F. (1980). Neural basis of rhythmic behavior in animals. Science *210*, 492-498.

Deliagina, T.G., Zelenin, P.V., and Orlovsky, G.N. (2002). Encoding and decoding of reticulospinal commands. Brain Res Brain Res Rev *40*, 166-177.

Deschenes, M., Takatoh, J., Kurnikova, A., Moore, J.D., Demers, M., Elbaz, M., Furuta, T., Wang, F., and Kleinfeld, D. (2016). Inhibition, Not Excitation, Drives Rhythmic Whisking. Neuron *90*, 374-387.

DiGiovanna, J., Dominici, N., Friedli, L., Rigosa, J., Duis, S., Kreider, J., Beauparlant, J., van den Brand, R., Schieppati, M., Micera, S*., et al.* (2016). Engagement of the Rat Hindlimb Motor Cortex across Natural Locomotor Behaviors. J Neurosci *36*, 10440-10455.

DiMarco, A.F., Romaniuk, J.R., Von Euler, C., and Yamamoto, Y. (1983). Immediate changes in ventilation and respiratory pattern associated with onset and cessation of locomotion in the cat. J Physiol *343*, 1-16.

Dollack, F., Perusquia-Hernandez, M., Kadone, H., and Suzuki, K. (2019). Head Anticipation During Locomotion With Auditory Instruction in the Presence and Absence of Visual Input. Front Hum Neurosci *13*, 293.

Dougherty, K.J., Zagoraiou, L., Satoh, D., Rozani, I., Doobar, S., Arber, S., Jessell, T.M., and Kiehn, O. (2013). Locomotor rhythm generation linked to the output of spinal shox2 excitatory interneurons. Neuron *80*, 920-933.

Douglas, J.R., Noga, B.R., Dai, X., and Jordan, L.M. (1993). The effects of intrathecal administration of excitatory amino acid agonists and antagonists on the initiation of locomotion in the adult cat. J Neurosci *13*, 990-1000.

Drew, T., Dubuc, R., and Rossignol, S. (1986). Discharge patterns of reticulospinal and other reticular neurons in chronic, unrestrained cats walking on a treadmill. J Neurophysiol *55*, 375-401.

Dubuc, R., Brocard, F., Antri, M., Fenelon, K., Gariepy, J.F., Smetana, R., Menard, A., Le Ray, D., Viana Di Prisco, G., Pearlstein, E*., et al.* (2008). Initiation of locomotion in lampreys. Brain Res Rev *57*, 172-182.

Edelman, J.A., and Goldberg, M.E. (2001). Dependence of saccade-related activity in the primate superior colliculus on visual target presence. J Neurophysiol *86*, 676-691.

Edelman, J.A., and Goldberg, M.E. (2003). Saccade-related activity in the primate superior colliculus depends on the presence of local landmarks at the saccade endpoint. J Neurophysiol *90*, 1728-1736.

Eldridge, F.L., Millhorn, D.E., Kiley, J.P., and Waldrop, T.G. (1985). Stimulation by central command of locomotion, respiration and circulation during exercise. Respir Physiol *59*, 313-337.

Eldridge, F.L., Millhorn, D.E., and Waldrop, T.G. (1981). Exercise hyperpnea and locomotion: parallel activation from the hypothalamus. Science *211*, 844-846.

Engmann, A.K., Bizzozzero, F., Schneider, M.P., Pfyffer, D., Imobersteg, S., Schneider, R., Hofer, A.S., Wieckhorst, M., and Schwab, M.E. (2020). The Gigantocellular Reticular Nucleus Plays a Significant Role in Locomotor Recovery after Incomplete Spinal Cord Injury. J Neurosci *40*, 8292-8305.

Ericson, J., Briscoe, J., Rashbass, P., van Heyningen, V., and Jessell, T.M. (1997). Graded sonic hedgehog signaling and the specification of cell fate in the ventral neural tube. Cold Spring Harb Symp Quant Biol *62*, 451-466.

Esposito, M.S., Capelli, P., and Arber, S. (2014). Brainstem nucleus MdV mediates skilled forelimb motor tasks. Nature *508*, 351-356.

Fagerstedt, P., and Ullen, F. (2001). Lateral turns in the Lamprey. I. Patterns of motoneuron activity. J Neurophysiol *86*, 2246-2256.

Feldman, J.L., and Del Negro, C.A. (2006). Looking for inspiration: new perspectives on respiratory rhythm. Nat Rev Neurosci *7*, 232-242.

Feldman, J.L., Del Negro, C.A., and Gray, P.A. (2013). Understanding the rhythm of breathing: so near, yet so far. Annu Rev Physiol *75*, 423-452.

Feldman, J.L., Mitchell, G.S., and Nattie, E.E. (2003). Breathing: rhythmicity, plasticity, chemosensitivity. Annu Rev Neurosci *26*, 239-266.

Fenno, L.E., Mattis, J., Ramakrishnan, C., Hyun, M., Lee, S.Y., He, M., Tucciarone, J., Selimbeyoglu, A., Berndt, A., Grosenick, L*., et al.* (2014). Targeting cells with single vectors using multiple-feature Boolean logic. Nat Methods *11*, 763-772.

Ferreira-Pinto, M.J., Kanodia, H., Falasconi, A., Sigrist, M., Esposito, M.S., and Arber, S. (2021). Functional diversity for body actions in the mesencephalic locomotor region. Cell *184*, 4564-4578 e4518.

Ferreira-Pinto, M.J., Ruder, L., Capelli, P., and Arber, S. (2018). Connecting Circuits for Supraspinal Control of Locomotion. Neuron *100*, 361-374.

Flandrois, R., Lacour, J.R., and Osman, H. (1971). Control of breathing in the exercising dog. Respir Physiol *13*, 361-371.

Fouad, K., and Tse, A. (2008). Adaptive changes in the injured spinal cord and their role in promoting functional recovery. Neurol Res *30*, 17-27.

Franklin, K.B., and Paxinos, G. (2007). The Mouse Brain in stereotaxic Coordinates. Elsevier.

Fuchs, A.F., and Robinson, D.A. (1966). A method for measuring horizontal and vertical eye movement chronically in the monkey. J Appl Physiol *21*, 1068-1070.

Fukushima, K. (1997). Corticovestibular interactions: anatomy, electrophysiology, and functional considerations. Exp Brain Res *117*, 1-16.

Fukushima, K., Peterson, B.W., Uchino, Y., Coulter, J.D., and Wilson, V.J. (1977). Direct fastigiospinal fibers in the cat. Brain Res *126*, 538-542.

Gabbay, H., and Lev-Tov, A. (2004). Alpha-1 adrenoceptor agonists generate a "fast" NMDA receptor-independent motor rhythm in the neonatal rat spinal cord. J Neurophysiol *92*, 997-1010.

Gale, S.D., and Murphy, G.J. (2014). Distinct representation and distribution of visual information by specific cell types in mouse superficial superior colliculus. J Neurosci *34*, 13458-13471.

Gariepy, J.F., Missaghi, K., Chevallier, S., Chartre, S., Robert, M., Auclair, F., Lund, J.P., and Dubuc, R. (2012). Specific neural substrate linking respiration to locomotion. Proc Natl Acad Sci U S A *109*, E84-92.

Gariepy, J.F., Missaghi, K., and Dubuc, R. (2010). The interactions between locomotion and respiration. Prog Brain Res *187*, 173-188.

Ghosh, M., and Pearse, D.D. (2014). The role of the serotonergic system in locomotor recovery after spinal cord injury. Front Neural Circuits *8*, 151.

Giber, K., Diana, M.A., Plattner, V., Dugue, G.P., Bokor, H., Rousseau, C.V., Magloczky, Z., Havas, L., Hangya, B., Wildner, H.*, et al.* (2015). A subcortical inhibitory signal for behavioral arrest in the thalamus. Nat Neurosci *18*, 562-568.

Giroux, N., Chau, C., Barbeau, H., Reader, T.A., and Rossignol, S. (2003). Effects of intrathecal glutamatergic drugs on locomotion. II. NMDA and AP-5 in intact and late spinal cats. J Neurophysiol *90*, 1027-1045.

Gnadt, J.W., Bracewell, R.M., and Andersen, R.A. (1991). Sensorimotor transformation during eye movements to remembered visual targets. Vision Res *31*, 693-715.

Goldberg, M.E., and Wurtz, R.H. (1972). Activity of superior colliculus in behaving monkey. II. Effect of attention on neuronal responses. J Neurophysiol *35*, 560-574.

Goulding, M. (2009). Circuits controlling vertebrate locomotion: moving in a new direction. Nat Rev Neurosci *10*, 507-518.

Graham, J., Lin, C.S., and Kaas, J.H. (1979). Subcortical projections of six visual cortical areas in the owl monkey, Aotus trivirgatus. J Comp Neurol *187*, 557-580.

Grantyn, A., Ong-Meang Jacques, V., and Berthoz, A. (1987). Reticulo-spinal neurons participating in the control of synergic eye and head movements during orienting in the cat. II. Morphological properties as revealed by intra-axonal injections of horseradish peroxidase. Exp Brain Res *66*, 355-377.

Grasso, R., Glasauer, S., Takei, Y., and Berthoz, A. (1996). The predictive brain: anticipatory control of head direction for the steering of locomotion. Neuroreport *7*, 1170-1174.

Grasso, R., Prevost, P., Ivanenko, Y.P., and Berthoz, A. (1998). Eye-head coordination for the steering of locomotion in humans: an anticipatory synergy. Neurosci Lett *253*, 115-118.

Gray, P.A., Rekling, J.C., Bocchiaro, C.M., and Feldman, J.L. (1999). Modulation of respiratory frequency by peptidergic input to rhythmogenic neurons in the preBotzinger complex. Science *286*, 1566-1568.

Grillner, S., and El Manira, A. (2020). Current Principles of Motor Control, with Special Reference to Vertebrate Locomotion. Physiol Rev *100*, 271-320.

Grillner, S., McClellan, A., and Perret, C. (1981). Entrainment of the spinal pattern generators for swimming by mechano-sensitive elements in the lamprey spinal cord in vitro. Brain Res *217*, 380-386.

Guldin, W.O., Mirring, S., and Grusser, O.J. (1993). Connections from the neocortex to the vestibular brain stem nuclei in the common marmoset. Neuroreport *5*, 113-116.

Guthrie, S. (2007). Patterning and axon guidance of cranial motor neurons. Nat Rev Neurosci *8*, 859-871.

Guyenet, P.G., Mulkey, D.K., Stornetta, R.L., and Bayliss, D.A. (2005). Regulation of ventral surface chemoreceptors by the central respiratory pattern generator. J Neurosci *25*, 8938-8947.

Hagglund, M., Borgius, L., Dougherty, K.J., and Kiehn, O. (2010). Activation of groups of excitatory neurons in the mammalian spinal cord or hindbrain evokes locomotion. Nat Neurosci *13*, 246-252.

Hall, N.J., and Colby, C.L. (2016). Express saccades and superior colliculus responses are sensitive to short-wavelength cone contrast. Proc Natl Acad Sci U S A *113*, 6743-6748.

Haouzi, P., Chenuel, B., and Chalon, B. (2004). Frequency response of the input reaching the respiratory centres during moderate intensity exercise. Adv Exp Med Biol *551*, 287-290.

Harting, J.K., Huerta, M.F., Hashikawa, T., and van Lieshout, D.P. (1991). Projection of the mammalian superior colliculus upon the dorsal lateral geniculate nucleus: organization of tectogeniculate pathways in nineteen species. J Comp Neurol *304*, 275-306.

Hayashi, M., Hinckley, C.A., Driscoll, S.P., Moore, N.J., Levine, A.J., Hilde, K.L., Sharma, K., and Pfaff, S.L. (2018). Graded Arrays of Spinal and Supraspinal V2a Interneuron Subtypes Underlie Forelimb and Hindlimb Motor Control. Neuron *97*, 869-884 e865.

Hemelt, M.E., and Keller, A. (2008). Superior colliculus control of vibrissa movements. J Neurophysiol *100*, 1245-1254.

Hentall, I.D., and Gonzalez, M.M. (2012). Promotion of recovery from thoracic spinal cord contusion in rats by stimulation of medullary raphe or its midbrain input. Neurorehabil Neural Repair *26*, 374-384.

Herent, C., Diem, S., Fortin, G., and Bouvier, J. (2020). Absent phasing of respiratory and locomotor rhythms in running mice. Elife *9*.

Hérent, C., Diem, S., Fortin, G., and Bouvier, J. (2021). Upregulation of breathing rate during running exercise by central locomotor circuits. bioRxiv, 2021.2007.2028.453983.

Hernandez-Miranda, L.R., Ruffault, P.L., Bouvier, J.C., Murray, A.J., Morin-Surun, M.P., Zampieri, N., Cholewa-Waclaw, J.B., Ey, E., Brunet, J.F., Champagnat, J.*, et al.* (2017). Genetic identification of a hindbrain nucleus essential for innate vocalization. Proc Natl Acad Sci U S A *114*, 8095-8100.

Hikosaka, O., and Wurtz, R.H. (1985). Modification of saccadic eye movements by GABA-related substances. II. Effects of muscimol in monkey substantia nigra pars reticulata. J Neurophysiol *53*, 292-308.

Hilton, B.J., Moulson, A.J., and Tetzlaff, W. (2017). Neuroprotection and secondary damage following spinal cord injury: concepts and methods. Neurosci Lett *652*, 3-10.

Hultborn, H. (1976). Transmission in the pathway of reciprocal Ia inhibition to motoneurones and its control during the tonic stretch reflex. Prog Brain Res *44*, 235-255.

Humphries, M.D., Gurney, K., and Prescott, T.J. (2006). The brainstem reticular formation is a small-world, not scale-free, network. Proc Biol Sci *273*, 503-511.

Humphries, M.D., Gurney, K., and Prescott, T.J. (2007). Is there a brainstem substrate for action selection? Philos Trans R Soc Lond B Biol Sci *362*, 1627-1639.

Isa, T., Marquez-Legorreta, E., Grillner, S., and Scott, E.K. (2021). The tectum/superior colliculus as the vertebrate solution for spatial sensory integration and action. Curr Biol *31*, R741-R762.

Isa, T., and Sasaki, S. (2002). Brainstem control of head movements during orienting; organization of the premotor circuits. Progress in neurobiology *66*, 205-241.

Iscoe, S. (1998). Control of abdominal muscles. Progress in neurobiology *56*, 433-506.

Iwamoto, Y. (1990). Disynaptic tectal and pyramidal excitation of hindlimb motoneurons mediated by pontine reticulospinal neurons in the cat. Exp Brain Res *79*, 175-186.

Jahn, K., Deutschlander, A., Stephan, T., Kalla, R., Wiesmann, M., Strupp, M., and Brandt, T. (2008). Imaging human supraspinal locomotor centers in brainstem and cerebellum. Neuroimage *39*, 786-792.

Jaitin, D.A., Kenigsberg, E., Keren-Shaul, H., Elefant, N., Paul, F., Zaretsky, I., Mildner, A., Cohen, N., Jung, S., Tanay, A.*, et al.* (2014). Massively parallel single-cell RNA-seq for marker-free decomposition of tissues into cell types. Science *343*, 776-779.

Jankowska, E. (2008). Spinal interneuronal networks in the cat: elementary components. Brain Res Rev *57*, 46-55.

Jasmin, L., Boudah, A., and Ohara, P.T. (2003). Long-term effects of decreased noradrenergic central nervous system innervation on pain behavior and opioid antinociception. J Comp Neurol *460*, 38-55.

Jenkin, S.E.M., and Milsom, W.K. (2014). Chapter 8 - Expiration: Breathing's other face. In Progress in brain research, G. Holstege, C.M. Beers, and H.H. Subramanian, eds. (Elsevier), pp. 131-147.

Jessell, T.M. (2000). Neuronal specification in the spinal cord: inductive signals and transcriptional codes. Nat Rev Genet *1*, 20-29.

Jordan, L.M., Liu, J., Hedlund, P.B., Akay, T., and Pearson, K.G. (2008). Descending command systems for the initiation of locomotion in mammals. Brain research reviews *57*, 183-191.

Josset, N., Roussel, M., Lemieux, M., Lafrance-Zoubga, D., Rastqar, A., and Bretzner, F. (2018). Distinct Contributions of Mesencephalic Locomotor Region Nuclei to Locomotor Control in the Freely Behaving Mouse. Curr Biol *28*, 884-901 e883.

Karachi, C., Grabli, D., Bernard, F.A., Tande, D., Wattiez, N., Belaid, H., Bardinet, E., Prigent, A., Nothacker, H.P., Hunot, S.*, et al.* (2010). Cholinergic mesencephalic neurons are involved in gait and postural disorders in Parkinson disease. J Clin Invest *120*, 2745-2754.

Kawahara, K., Nakazono, Y., Yamauchi, Y., and Miyamoto, Y. (1989). Coupling between respiratory and locomotor rhythms during fictive locomotion in decerebrate cats. Neurosci Lett *103*, 326-330.

Kiehn, O. (2006). Locomotor circuits in the mammalian spinal cord. Annu Rev Neurosci *29*, 279-306.

Kiehn, O. (2016). Decoding the organization of spinal circuits that control locomotion. Nat Rev Neurosci *17*, 224-238.

Kiehn, O., and Kjaerulff, O. (1996). Spatiotemporal characteristics of 5-HT and dopamine-induced rhythmic hindlimb activity in the in vitro neonatal rat. J Neurophysiol *75*, 1472-1482.

Kiehn, O., Sillar, K.T., Kjaerulff, O., and McDearmid, J.R. (1999). Effects of noradrenaline on locomotor rhythm-generating networks in the isolated neonatal rat spinal cord. J Neurophysiol *82*, 741-746.

Kimura, Y., Satou, C., Fujioka, S., Shoji, W., Umeda, K., Ishizuka, T., Yawo, H., and Higashijima, S. (2013). Hindbrain V2a neurons in the excitation of spinal locomotor circuits during zebrafish swimming. Curr Biol *23*, 843-849.

Kleinfeld, D., Deschenes, M., Wang, F., and Moore, J.D. (2014). More than a rhythm of life: breathing as a binder of orofacial sensation. Nat Neurosci *17*, 647-651.

Klier, E.M., Wang, H., and Crawford, J.D. (2001). The superior colliculus encodes gaze commands in retinal coordinates. Nat Neurosci *4*, 627-632.

Krogh, A., and Lindhard, J. (1913). The regulation of respiration and circulation during the initial stages of muscular work. J Physiol *47*, 112-136.

Kudo, N., and Yamada, T. (1987). Morphological and physiological studies of development of the monosynaptic reflex pathway in the rat lumbar spinal cord. J Physiol *389*, 441-459.

Kurnikova, A., Moore, J.D., Liao, S.M., Deschenes, M., and Kleinfeld, D. (2017). Coordination of Orofacial Motor Actions into Exploratory Behavior by Rat. Curr Biol *27*, 688-696.

Kuypers, H.G. (1964). The Descending Pathways to the Spinal Cord, Their Anatomy and Function. Prog Brain Res *11*, 178-202.

Kuypers, H.G. (1981). Anatomy of the descending pathways. Compr Physiol *2*, 597-666.

Lanuza, G.M., Gosgnach, S., Pierani, A., Jessell, T.M., and Goulding, M. (2004). Genetic identification of spinal interneurons that coordinate left-right locomotor activity necessary for walking movements. Neuron *42*, 375-386.

Le Gal, J.P., Colnot, E., Cardoit, L., Bacque-Cazenave, J., Thoby-Brisson, M., Juvin, L., and Morin, D. (2020). Modulation of respiratory network activity by forelimb and hindlimb locomotor generators. Eur J Neurosci *52*, 3181-3195.

Le Gal, J.P., Juvin, L., Cardoit, L., Thoby-Brisson, M., and Morin, D. (2014). Remote control of respiratory neural network by spinal locomotor generators. PLoS One *9*, e89670.

Leiras, R., Cregg, J.M., and Kiehn, O. (2022). Brainstem Circuits for Locomotion. Annu Rev Neurosci *45*, 63-85.

Lemieux, M., and Bretzner, F. (2019). Glutamatergic neurons of the gigantocellular reticular nucleus shape locomotor pattern and rhythm in the freely behaving mouse. PLoS Biol *17*, e2003880.

Lemon, R.N. (2008). Descending pathways in motor control. Annu Rev Neurosci *31*, 195-218.

Liang, H., Paxinos, G., and Watson, C. (2011). Projections from the brain to the spinal cord in the mouse. Brain Struct Funct *215*, 159-186.

Liu, J., and Jordan, L.M. (2005). Stimulation of the parapyramidal region of the neonatal rat brain stem produces locomotor-like activity involving spinal 5-HT7 and 5-HT2A receptors. J Neurophysiol *94*, 1392-1404.

Lu, P., Blesch, A., Graham, L., Wang, Y., Samara, R., Banos, K., Haringer, V., Havton, L., Weishaupt, N., Bennett, D*., et al.* (2012). Motor axonal regeneration after partial and complete spinal cord transection. J Neurosci *32*, 8208-8218.

Lyon, D.C., Nassi, J.J., and Callaway, E.M. (2010). A disynaptic relay from superior colliculus to dorsal stream visual cortex in macaque monkey. Neuron *65*, 270-279.

Marlinskii, V.V., and Voitenko, L.P. (1992). Participation of the medial reticular formation of the medulla oblongata in the supraspinal control of locomotor and postural activities in the guinea pig. Neurosci Behav Physiol *22*, 336-342.

Masullo, L., Mariotti, L., Alexandre, N., Freire-Pritchett, P., Boulanger, J., and Tripodi, M. (2019). Genetically Defined Functional Modules for Spatial Orienting in the Mouse Superior Colliculus. Curr Biol *29*, 2892-2904 e2898.

Mateika, J.H., and Duffin, J. (1992). Changes in ventilation at the start and end of moderate and heavy exercise of short and long duration. Eur J Appl Physiol Occup Physiol *65*, 234-240.

Mateika, J.H., and Duffin, J. (1995). A review of the control of breathing during exercise. Eur J Appl Physiol Occup Physiol *71*, 1-27.

Matsushita, M., and Hosoya, Y. (1978). The location of spinal projection neurons in the cerebellar nuclei (cerebellospinal tract neurons) of the cat. A study with the horseradish peroxidase technique. Brain Res *142*, 237-248.

Matsuyama, K., Nakajima, K., Mori, F., Aoki, M., and Mori, S. (2004). Lumbar commissural interneurons with reticulospinal inputs in the cat: morphology and discharge patterns during fictive locomotion. J Comp Neurol *474*, 546-561.

Mattis, J., Tye, K.M., Ferenczi, E.A., Ramakrishnan, C., O'Shea, D.J., Prakash, R., Gunaydin, L.A., Hyun, M., Fenno, L.E., Gradinaru, V*., et al.* (2011). Principles for applying optogenetic tools derived from direct comparative analysis of microbial opsins. Nature methods *9*, 159-172.

May, P.J. (2006). The mammalian superior colliculus: laminar structure and connections. Prog Brain Res *151*, 321-378.

McCall, A.A., Miller, D.M., and Yates, B.J. (2017). Descending Influences on Vestibulospinal and Vestibulosympathetic Reflexes. Front Neurol *8*, 112.

McClellan, A.D., and Grillner, S. (1984). Activation of 'fictive swimming' by electrical microstimulation of brainstem locomotor regions in an in vitro preparation of the lamprey central nervous system. Brain Res *300*, 357-361.

Mellen, N.M., Janczewski, W.A., Bocchiaro, C.M., and Feldman, J.L. (2003). Opioid-induced quantal slowing reveals dual networks for respiratory rhythm generation. Neuron *37*, 821-826.

Meyer, A.F., O'Keefe, J., and Poort, J. (2020). Two Distinct Types of Eye-Head Coupling in Freely Moving Mice. Curr Biol *30*, 2116-2130 e2116.

Michaiel, A.M., Abe, E.T., and Niell, C.M. (2020). Dynamics of gaze control during prey capture in freely moving mice. Elife *9*.

Mitchell, R.A., Loeschcke, H.H., Massion, W.H., and Severinghaus, J.W. (1963). Respiratory responses mediated through superficial chemosensitive areas on the medulla. J Appl Physiol (1985) *18*, 523-533.

Moore, J.D., Deschenes, M., Furuta, T., Huber, D., Smear, M.C., Demers, M., and Kleinfeld, D. (2013). Hierarchy of orofacial rhythms revealed through whisking and breathing. Nature *497*, 205-210.

Moore, J.D., Kleinfeld, D., and Wang, F. (2014). How the brainstem controls orofacial behaviors comprised of rhythmic actions. Trends Neurosci *37*, 370-380.

Moreno-Lopez, Y., Bichara, C., Delbecq, G., Isope, P., and Cordero-Erausquin, M. (2021). The corticospinal tract primarily modulates sensory inputs in the mouse lumbar cord. Elife *10*.

Mori, S., Matsui, T., Kuze, B., Asanome, M., Nakajima, K., and Matsuyama, K. (1998). Cerebellar-induced locomotion: reticulospinal control of spinal rhythm generating mechanism in cats. Ann N Y Acad Sci *860*, 94-105.

Mori, S., Sakamoto, T., Ohta, Y., Takakusaki, K., and Matsuyama, K. (1989). Site-specific postural and locomotor changes evoked in awake, freely moving intact cats by stimulating the brainstem. Brain Res *505*, 66-74.

Morin, D., and Viala, D. (2002). Coordinations of locomotor and respiratory rhythms in vitro are critically dependent on hindlimb sensory inputs. J Neurosci *22*, 4756-4765.

Mulkey, D.K., Stornetta, R.L., Weston, M.C., Simmons, J.R., Parker, A., Bayliss, D.A., and Guyenet, P.G. (2004). Respiratory control by ventral surface chemoreceptor neurons in rats. Nat Neurosci *7*, 1360-1369.

Mutolo, D., Bongianni, F., Einum, J., Dubuc, R., and Pantaleo, T. (2007). Opioid-induced depression in the lamprey respiratory network. Neuroscience *150*, 720-729.

Nelson, A., Abdelmesih, B., and Costa, R.M. (2021). Corticospinal populations broadcast complex motor signals to coordinated spinal and striatal circuits. Nat Neurosci *24*, 1721-1732.

Noga, B.R., Kriellaars, D.J., Brownstone, R.M., and Jordan, L.M. (2003). Mechanism for activation of locomotor centers in the spinal cord by stimulation of the mesencephalic locomotor region. J Neurophysiol *90*, 1464-1478.

Nudo, R.J., and Masterton, R.B. (1988). Descending pathways to the spinal cord: a comparative study of 22 mammals. J Comp Neurol *277*, 53-79.

Onimaru, H., Arata, A., and Homma, I. (1987). Localization of respiratory rhythm-generating neurons in the medulla of brainstem-spinal cord preparations from newborn rats. Neurosci Lett *78*, 151-155.

Onimaru, H., and Homma, I. (2003). A novel functional neuron group for respiratory rhythm generation in the ventral medulla. J Neurosci *23*, 1478-1486.

Onimaru, H., Ikeda, K., and Kawakami, K. (2008). CO2-sensitive preinspiratory neurons of the parafacial respiratory group express Phox2b in the neonatal rat. J Neurosci *28*, 12845-12850.

Opris, I., Dai, X., Johnson, D.M.G., Sanchez, F.J., Villamil, L.M., Xie, S., Lee-Hauser, C.R., Chang, S., Jordan, L.M., and Noga, B.R. (2019). Activation of Brainstem Neurons During Mesencephalic Locomotor Region-Evoked Locomotion in the Cat. Front Syst Neurosci *13*, 69.

Orlovskii, G.N. (1970a). [Cerebellar influence on the reticulo-spinal neurons during locomotion]. Biofizika *15*, 894-901.

Orlovskii, G.N. (1970b). [Work of reticulo-spinal neurons during locomotion]. Biofizika *15*, 728-737.

Oueghlani, Z., Simonnet, C., Cardoit, L., Courtand, G., Cazalets, J.R., Morin, D., Juvin, L., and Barriere, G. (2018). Brainstem Steering of Locomotor Activity in the Newborn Rat. J Neurosci *38*, 7725-7740.

Pantaleo, T., Mutolo, D., Cinelli, E., and Bongianni, F. (2011). Respiratory responses to somatostatin microinjections into the Botzinger complex and the pre-Botzinger complex of the rabbit. Neurosci Lett *498*, 26-30.

Pearce, D.H., and Milhorn, H.T., Jr. (1977). Dynamic and steady-state respiratory responses to bicycle exercise. J Appl Physiol Respir Environ Exerc Physiol *42*, 959-967.

Pearse, D.D., Pereira, F.C., Marcillo, A.E., Bates, M.L., Berrocal, Y.A., Filbin, M.T., and Bunge, M.B. (2004). cAMP and Schwann cells promote axonal growth and functional recovery after spinal cord injury. Nat Med *10*, 610-616.

Perrins, R., Walford, A., and Roberts, A. (2002). Sensory activation and role of inhibitory reticulospinal neurons that stop swimming in hatchling frog tadpoles. J Neurosci *22*, 4229-4240.

Peterson, B.W., and Abzug, C. (1975). Properties of projections from vestibular nuclei to medial reticular formation in the cat. J Neurophysiol *38*, 1421-1435.

Peterson, B.W., Pitts, N.G., Fukushima, K., and Mackel, R. (1978). Reticulospinal excitation and inhibition of neck motoneurons. Exp Brain Res *32*, 471-489.

Pierani, A., Moran-Rivard, L., Sunshine, M.J., Littman, D.R., Goulding, M., and Jessell, T.M. (2001). Control of interneuron fate in the developing spinal cord by the progenitor homeodomain protein Dbx1. Neuron *29*, 367-384.

Pogossian, V.I., and Fanardjian, V.V. (1992). Organization of afferent projections to the ventral and dorsal regions of the cat lateral vestibular nucleus: an HRP study. J Vestib Res *2*, 107-122.

Qu, S., Ondo, W.G., Zhang, X., Xie, W.J., Pan, T.H., and Le, W.D. (2006). Projections of diencephalic dopamine neurons into the spinal cord in mice. Exp Brain Res *168*, 152-156.

Raineteau, O., and Schwab, M.E. (2001). Plasticity of motor systems after incomplete spinal cord injury. Nature reviews *2*, 263-273.

Ramanantsoa, N., Hirsch, M.R., Thoby-Brisson, M., Dubreuil, V., Bouvier, J., Ruffault, P.L., Matrot, B., Fortin, G., Brunet, J.F., Gallego, J*., et al.* (2011). Breathing without CO(2) chemosensitivity in conditional Phox2b mutants. J Neurosci *31*, 12880-12888.

Ramirez, J.M. (2011). The human pre-Botzinger complex identified. Brain *134*, 8-10.

Ramirez, J.M., Quellmalz, U.J., and Richter, D.W. (1996). Postnatal changes in the mammalian respiratory network as revealed by the transverse brainstem slice of mice. J Physiol *491 (Pt 3)*, 799-812.

Ribotta, M.G., Provencher, J., Feraboli-Lohnherr, D., Rossignol, S., Privat, A., and Orsal, D. (2000). Activation of locomotion in adult chronic spinal rats is achieved by transplantation of embryonic raphe cells reinnervating a precise lumbar level. J Neurosci *20*, 5144-5152.

Riddle, C.N., Edgley, S.A., and Baker, S.N. (2009). Direct and indirect connections with upper limb motoneurons from the primate reticulospinal tract. J Neurosci *29*, 4993-4999.

Roberts, A., Li, W.C., Soffe, S.R., and Wolf, E. (2008). Origin of excitatory drive to a spinal locomotor network. Brain Res Rev *57*, 22-28.

Robinson, N.E. (1985). Respiratory adaptations to exercise. Vet Clin North Am Equine Pract *1*, 497-512.

Roelink, H., Porter, J.A., Chiang, C., Tanabe, Y., Chang, D.T., Beachy, P.A., and Jessell, T.M. (1995). Floor plate and motor neuron induction by different concentrations of the amino-terminal cleavage product of sonic hedgehog autoproteolysis. Cell *81*, 445-455.

Roh, J., Cheung, V.C., and Bizzi, E. (2011). Modules in the brain stem and spinal cord underlying motor behaviors. J Neurophysiol *106*, 1363-1378.

Romer, S.H., Seedle, K., Turner, S.M., Li, J., Baccei, M.L., and Crone, S.A. (2017). Accessory respiratory muscles enhance ventilation in ALS model mice and are activated by excitatory V2a neurons. Exp Neurol *287*, 192-204.

Ronzano, R., Skarlatou, S., Barriga, B.K., Bannatyne, B.A., Bhumbra, G.S., Foster, J.D., Moore, J.D., Lancelin, C., Pocratsky, A., Özyurt, M.G*., et al.* (2022). Spinal premotor interneurons controlling antagonistic muscles are spatially intermingled. bioRxiv, 2021.2002.2010.430608.

Roth, B.L. (2016). DREADDs for Neuroscientists. Neuron *89*, 683-694.

Ruder, L., and Arber, S. (2019). Brainstem Circuits Controlling Action Diversification. Annu Rev Neurosci *42*, 485-504.

Ruder, L., Schina, R., Kanodia, H., Valencia-Garcia, S., Pivetta, C., and Arber, S. (2021). A functional map for diverse forelimb actions within brainstem circuitry. Nature *590*, 445-450.

Ruffault, P.L., D'Autreaux, F., Hayes, J.A., Nomaksteinsky, M., Autran, S., Fujiyama, T., Hoshino, M., Hagglund, M., Kiehn, O., Brunet, J.F*., et al.* (2015). The retrotrapezoid nucleus neurons expressing Atoh1 and Phox2b are essential for the respiratory response to CO(2). Elife *4*.

Ryczko, D., and Dubuc, R. (2013). The multifunctional mesencephalic locomotor region. Curr Pharm Des *19*, 4448-4470.

Ryczko, D., and Dubuc, R. (2017). Dopamine and the Brainstem Locomotor Networks: From Lamprey to Human. Front Neurosci *11*, 295.

Sahibzada, N., Dean, P., and Redgrave, P. (1986). Movements resembling orientation or avoidance elicited by electrical stimulation of the superior colliculus in rats. J Neurosci *6*, 723-733.

Sahni, V., Shnider, S.J., Jabaudon, D., Song, J.H.T., Itoh, Y., Greig, L.C., and Macklis, J.D. (2021). Corticospinal neuron subpopulation-specific developmental genes prospectively indicate mature segmentally specific axon projection targeting. Cell Rep *37*, 109843.

Saitoh, K., Menard, A., and Grillner, S. (2007). Tectal control of locomotion, steering, and eye movements in lamprey. J Neurophysiol *97*, 3093-3108.

Sakatani, T., and Isa, T. (2007). Quantitative analysis of spontaneous saccade-like rapid eye movements in C57BL/6 mice. Neurosci Res *58*, 324-331.

Sasaki, S., Yoshimura, K., and Naito, K. (2004). The neural control of orienting: role of multiple-branching reticulospinal neurons. Prog Brain Res *143*, 383-389.

Sathyamurthy, A., Barik, A., Dobrott, C.I., Matson, K.J.E., Stoica, S., Pursley, R., Chesler, A.T., and Levine, A.J. (2020). Cerebellospinal Neurons Regulate Motor Performance and Motor Learning. Cell Rep *31*, 107595.

Sathyamurthy, A., Johnson, K.R., Matson, K.J.E., Dobrott, C.I., Li, L., Ryba, A.R., Bergman, T.B., Kelly, M.C., Kelley, M.W., and Levine, A.J. (2018). Massively Parallel Single Nucleus Transcriptional Profiling Defines Spinal Cord Neurons and Their Activity during Behavior. Cell Rep *22*, 2216-2225.

Schiller, P.H., and Stryker, M. (1972). Single-unit recording and stimulation in superior colliculus of the alert rhesus monkey. J Neurophysiol *35*, 915-924.

Schmidt, B.J., and Jordan, L.M. (2000). The role of serotonin in reflex modulation and locomotor rhythm production in the mammalian spinal cord. Brain Res Bull *53*, 689-710.

Schor, R.H., and Yates, B.J. (1995). Horizontal rotation responses of medullary reticular neurons in the decerebrate cat. J Vestib Res *5*, 223-228.

Schwarzacher, S.W., Rub, U., and Deller, T. (2011). Neuroanatomical characteristics of the human pre-Botzinger complex and its involvement in neurodegenerative brainstem diseases. Brain *134*, 24-35.

Schwenkgrub, J., Harrell, E.R., Bathellier, B., and Bouvier, J. (2020). Deep imaging in the brainstem reveals functional heterogeneity in V2a neurons controlling locomotion. Sci Adv *6*.

Sekhon, L.H., and Fehlings, M.G. (2001). Epidemiology, demographics, and pathophysiology of acute spinal cord injury. Spine (Phila Pa 1976) *26*, S2-12.

Shapovalov, A.I. (1972). [The evolution of neuronal systems for suprasegmentary motor control (review)]. Neirofiziologiia *4*, 453-470.

Shefchyk, S.J., Jell, R.M., and Jordan, L.M. (1984). Reversible cooling of the brainstem reveals areas required for mesencephalic locomotor region evoked treadmill locomotion. Exp Brain Res *56*, 257-262.

Shik, M.L., and Orlovsky, G.N. (1976). Neurophysiology of locomotor automatism. Physiol Rev *56*, 465-501.

Shik, M.L., Severin, F.V., and Orlovskii, G.N. (1966). [Control of walking and running by means of electric stimulation of the midbrain]. Biofizika *11*, 659-666.

Shik, M.L., Severin, F.V., and Orlovsky, G.N. (1969). Control of walking and running by means of electrical stimulation of the mesencephalon. Electroencephalography and clinical neurophysiology *26*, 549.

Shimamura, M., and Kogure, I. (1983). Discharge patterns of reticulospinal neurons corresponding with quadrupedal leg movements in thalamic cats. Brain Res *260*, 27-34.

Shimamura, M., Kogure, I., and Wada, S. (1982). Reticular neuron activities associated with locomotion in thalamic cats. Brain Res *231*, 51-62.

Siddiqui, A.M., Khazaei, M., and Fehlings, M.G. (2015). Translating mechanisms of neuroprotection, regeneration, and repair to treatment of spinal cord injury. Prog Brain Res *218*, 15-54.

Sinnamon, H.M., and Stopford, C.K. (1987). Locomotion elicited by lateral hypothalamic stimulation in the anesthetized rat does not require the dorsal midbrain. Brain Res *402*, 78-86.

Sivertsen, M.S., Perreault, M.C., and Glover, J.C. (2016). Pontine reticulospinal projections in the neonatal mouse: Internal organization and axon trajectories. J Comp Neurol *524*, 1270-1291.

Skarlatou, S., Herent, C., Toscano, E., Mendes, C.S., Bouvier, J., and Zampieri, N. (2020). Afadin Signaling at the Spinal Neuroepithelium Regulates Central Canal Formation and Gait Selection. Cell Rep *31*, 107741.

Smith, J.C., Ellenberger, H.H., Ballanyi, K., Richter, D.W., and Feldman, J.L. (1991). Pre-Botzinger complex: a brainstem region that may generate respiratory rhythm in mammals. Science *254*, 726-729.

Smith, J.C., Morrison, D.E., Ellenberger, H.H., Otto, M.R., and Feldman, J.L. (1989). Brainstem projections to the major respiratory neuron populations in the medulla of the cat. J Comp Neurol *281*, 69-96.

Sparks, D.L., and Mays, L.E. (1990). Signal transformations required for the generation of saccadic eye movements. Annu Rev Neurosci *13*, 309-336.

Stanek, E.t., Cheng, S., Takatoh, J., Han, B.X., and Wang, F. (2014). Monosynaptic premotor circuit tracing reveals neural substrates for oro-motor coordination. Elife *3*, e02511.

Stanford, T.R., Freedman, E.G., and Sparks, D.L. (1996). Site and parameters of microstimulation: evidence for independent effects on the properties of saccades evoked from the primate superior colliculus. J Neurophysiol *76*, 3360-3381.

Steeves, J.D., Schmidt, B.J., Skovgaard, B.J., and Jordan, L.M. (1980). Effect of noradrenaline and 5-hydroxytryptamine depletion on locomotion in the cat. Brain Res *185*, 349-362.

Steeves, J.D., Sholomenko, G.N., and Webster, D.M. (1987). Stimulation of the pontomedullary reticular formation initiates locomotion in decerebrate birds. Brain Res *401*, 205-212.

Stepien, A.E., Tripodi, M., and Arber, S. (2010). Monosynaptic rabies virus reveals premotor network organization and synaptic specificity of cholinergic partition cells. Neuron *68*, 456-472.

Stornetta, R.L., Moreira, T.S., Takakura, A.C., Kang, B.J., Chang, D.A., West, G.H., Brunet, J.F., Mulkey, D.K., Bayliss, D.A., and Guyenet, P.G. (2006). Expression of Phox2b by brainstem neurons involved in chemosensory integration in the adult rat. J Neurosci *26*, 10305-10314.

Stornetta, R.L., Rosin, D.L., Wang, H., Sevigny, C.P., Weston, M.C., and Guyenet, P.G. (2003). A group of glutamatergic interneurons expressing high levels of both neurokinin-1 receptors and somatostatin identifies the region of the pre-Botzinger complex. J Comp Neurol *455*, 499-512.

Sugiuchi, Y., Kakei, S., Izawa, Y., and Shinoda, Y. (2004). Functional synergies among neck muscles revealed by branching patterns of single long descending motor-tract axons. Prog Brain Res *143*, 411-421.

Suzuki, D.G., Perez-Fernandez, J., Wibble, T., Kardamakis, A.A., and Grillner, S. (2019). The role of the optic tectum for visually evoked orienting and evasive movements. Proc Natl Acad Sci U S A *116*, 15272-15281.

Sweeney, L.B., Bikoff, J.B., Gabitto, M.I., Brenner-Morton, S., Baek, M., Yang, J.H., Tabak, E.G., Dasen, J.S., Kintner, C.R., and Jessell, T.M. (2018). Origin and Segmental Diversity of Spinal Inhibitory Interneurons. Neuron *97*, 341-355 e343.

Szokol, K., Glover, J.C., and Perreault, M.C. (2008). Differential origin of reticulospinal drive to motoneurons innervating trunk and hindlimb muscles in the mouse revealed by optical recording. J Physiol *586*, 5259-5276.

Takatoh, J., Nelson, A., Zhou, X., Bolton, M.M., Ehlers, M.D., Arenkiel, B.R., Mooney, R., and Wang, F. (2013). New modules are added to vibrissal premotor circuitry with the emergence of exploratory whisking. Neuron *77*, 346-360.

Takatoh, J., Park, J.H., Lu, J., Li, S., Thompson, P.M., Han, B.X., Zhao, S., Kleinfeld, D., Friedman, B., and Wang, F. (2021). Constructing an adult orofacial premotor atlas in Allen mouse CCF. Elife *10*.

Talpalar, A.E., Bouvier, J., Borgius, L., Fortin, G., Pierani, A., and Kiehn, O. (2013). Dual-mode operation of neuronal networks involved in left-right alternation. Nature *500*, 85-88.

Talpalar, A.E., Endo, T., Low, P., Borgius, L., Hagglund, M., Dougherty, K.J., Ryge, J., Hnasko, T.S., and Kiehn, O. (2011). Identification of minimal neuronal networks involved in flexor-extensor alternation in the mammalian spinal cord. Neuron *71*, 1071-1084.

Thornton, J.M., Guz, A., Murphy, K., Griffith, A.R., Pedersen, D.L., Kardos, A., Leff, A., Adams, L., Casadei, B., and Paterson, D.J. (2001). Identification of higher brain centres that may encode the cardiorespiratory response to exercise in humans. J Physiol *533*, 823-836.

Tolbert, D.L., Bantli, H., Hames, E.G., Ebner, T.J., McMullen, T.A., and Bloedel, J.R. (1980). A demonstration of the dentato-reticulospinal projection in the cat. Neuroscience *5*, 1479-1488.

Tsuchiya, N., Iwase, M., Izumizaki, M., and Homma, I. (2012). Dopaminergic modulation of exercise hyperpnoea via D(2) receptors in mice. Experimental physiology *97*, 228-238.

Tupal, S., Rieger, M.A., Ling, G.Y., Park, T.J., Dougherty, J.D., Goodchild, A.K., and Gray, P.A. (2014). Testing the role of preBotzinger Complex somatostatin neurons in respiratory and vocal behaviors. Eur J Neurosci *40*, 3067-3077.

Tuszynski, M.H., and Steward, O. (2012). Concepts and methods for the study of axonal regeneration in the CNS. Neuron *74*, 777-791.

Usseglio, G., Gatier, E., Heuze, A., Herent, C., and Bouvier, J. (2020). Control of Orienting Movements and Locomotion by Projection-Defined Subsets of Brainstem V2a Neurons. Curr Biol *30*, 4665-4681 e4666.

Valverde, F. (1961). Reticular formation of the pons and medulla oblongata. A Golgi study. J Comp Neurol *116*, 71-99.

van den Brand, R., Heutschi, J., Barraud, Q., DiGiovanna, J., Bartholdi, K., Huerlimann, M., Friedli, L., Vollenweider, I., Moraud, E.M., Duis, S.*, et al.* (2012). Restoring voluntary control of locomotion after paralyzing spinal cord injury. Science *336*, 1182-1185.

Van Opstal, A.J., Van Gisbergen, J.A., and Smit, A.C. (1990). Comparison of saccades evoked by visual stimulation and collicular electrical stimulation in the alert monkey. Exp Brain Res *79*, 299-312.

Varma, A.K., Das, A., Wallace, G.t., Barry, J., Vertegel, A.A., Ray, S.K., and Banik, N.L. (2013). Spinal cord injury: a review of current therapy, future treatments, and basic science frontiers. Neurochem Res *38*, 895-905.

Vavrek, R., Pearse, D.D., and Fouad, K. (2007). Neuronal populations capable of regeneration following a combined treatment in rats with spinal cord transection. J Neurotrauma *24*, 1667-1673.

Vetrivelan, R., Fuller, P.M., Tong, Q., and Lu, J. (2009). Medullary circuitry regulating rapid eye movement sleep and motor atonia. J Neurosci *29*, 9361-9369.

Wang, Z., Maunze, B., Wang, Y., Tsoulfas, P., and Blackmore, M.G. (2018). Global Connectivity and Function of Descending Spinal Input Revealed by 3D Microscopy and Retrograde Transduction. J Neurosci *38*, 10566-10581.

Wenger, N., Moraud, E.M., Gandar, J., Musienko, P., Capogrosso, M., Baud, L., Le Goff, C.G., Barraud, Q., Pavlova, N., Dominici, N.*, et al.* (2016). Spatiotemporal neuromodulation therapies engaging muscle synergies improve motor control after spinal cord injury. Nat Med *22*, 138-145.

Wenninger, J.M., Pan, L.G., Klum, L., Leekley, T., Bastastic, J., Hodges, M.R., Feroah, T., Davis, S., and Forster, H.V. (2004). Small reduction of neurokinin-1 receptor-expressing neurons in the pre-Botzinger complex area induces abnormal breathing periods in awake goats. J Appl Physiol (1985) *97*, 1620-1628.

Whelan, P.J. (1996). Control of locomotion in the decerebrate cat. Prog Neurobiol *49*, 481-515.

White, B.J., Boehnke, S.E., Marino, R.A., Itti, L., and Munoz, D.P. (2009). Color-related signals in the primate superior colliculus. J Neurosci *29*, 12159-12166.

Wickersham, I.R., Finke, S., Conzelmann, K.K., and Callaway, E.M. (2007). Retrograde neuronal tracing with a deletion-mutant rabies virus. Nat Methods *4*, 47-49.

Wilson, J.R., Cadotte, D.W., and Fehlings, M.G. (2012). Clinical predictors of neurological outcome, functional status, and survival after traumatic spinal cord injury: a systematic review. J Neurosurg Spine *17*, 11-26.

Wilson, V.J., Zarzecki, P., Schor, R.H., Isu, N., Rose, P.K., Sato, H., Thomson, D.B., and Umezaki, T. (1999). Cortical influences on the vestibular nuclei of the cat. Exp Brain Res *125*, 1-13.

Wu, J., Capelli, P., Bouvier, J., Goulding, M., Arber, S., and Fortin, G. (2017). A V0 core neuronal circuit for inspiration. Nat Commun *8*, 544.

Wurtz, R.H., and Goldberg, M.E. (1972). Activity of superior colliculus in behaving monkey. IV. Effects of lesions on eye movements. J Neurophysiol *35*, 587-596.

Yamamoto, N., Nakayama, T., and Hagio, H. (2017). Descending pathways to the spinal cord in teleosts in comparison with mammals, with special attention to rubrospinal pathways. Dev Growth Differ *59*, 188-193.

Zampieri, N., Jessell, T.M., and Murray, A.J. (2014). Mapping sensory circuits by anterograde transsynaptic transfer of recombinant rabies virus. Neuron *81*, 766-778.

Zhang, J., Lanuza, G.M., Britz, O., Wang, Z., Siembab, V.C., Zhang, Y., Velasquez, T., Alvarez, F.J., Frank, E., and Goulding, M. (2014). V1 and v2b interneurons secure the alternating flexor-extensor motor activity mice require for limbed locomotion. Neuron *82*, 138-150.

Zorner, B., Bachmann, L.C., Filli, L., Kapitza, S., Gullo, M., Bolliger, M., Starkey, M.L., Rothlisberger, M., Gonzenbach, R.R., and Schwab, M.E. (2014). Chasing central nervous system plasticity: the brainstem's contribution to locomotor recovery in rats with spinal cord injury. Brain *137*, 1716-1732.

université PARIS-SACLAY

ÉCOLE DOCTORALE
Signalisations et réseaux intégratifs en biologie (BIOSIGNE)

Titre : Circuits du tronc cérébral pour les mouvements locomoteurs et d'orientation : étude fonctionnelle et connectomique des neurones V2a

Mots clés : circuit neuronal, formation réticulée, neurones réticulospinaux, optogénétique, traçage viral, souris

Resumé : Ce projet porte sur les mécanismes cérébraux qui nous permettent de nous mouvoir. En particulier, nous avons cherché à comprendre l'origine et le rôle des signaux nerveux qui relient le cerveau et la moelle épinière, dont l'interruption est une cause principale des pertes de motricité après lésion médullaire.
Nous avons identifié le type de cellule dans le cerveau postérieur (les neurones V2a) qui forme le lien entre un centre sensoriel du cerveau et la moelle épinière. Nous avons également constaté que ces neurones présentent une diversité inattendue : il en existe plusieurs catégories qui contactent chacune une seule région de la moelle épinière pour contrôler indépendamment les mouvements des membres, de la tête, du nez et des yeux.
Notre étude fournit ainsi des informations nouvelles sur les signaux nerveux descendants qui coordonnent les mouvements. Ces résultats devraient, à terme, aider à développer des stratégies ciblées de restauration motrice.

Title: Brainstem circuits for locomotor and orienting movements: a functional and connectivity study of V2a neurons

Keywords: neural circuit, reticular formation, reticulospinal neurons, optogenetics, viral tracing, mouse

Abstract: This project focuses on the brain mechanisms that allow us to move. The nerve signals that connect the brain and the spinal cord are vital for controlling movements. It is therefore essential to understand the origin and role of these signals.
We identified the specific cell type in the caudal brain (the V2a neurons) that forms the link between an important sensory center in the brain and the spinal cord which dictates muscular contractions. We also found that these neurons show an unexpected diversity: there are several categories and each contacts a single region of the spinal cord for independently controlling the limbs, the head, the nose, and eye movements.
Our study provides important new information on descending nerve signals for coordinating movements. The interruption or weakening of these descending connections is a main cause of loss of motor autonomy after spinal cord injury. Our findings should therefore ultimately help to develop targeted motor restoration strategies.